Advancing Nanocrystal-based Infrared Imaging : Exploring Novel Strategies in the Design and Characterization

Adrien Khalili Lazarjani

THESE DE DOCTORAT DE SORBONNE

Spécialité : Physique

Ecole doctorale 397 : Physique et Chimie des Matériaux

réalisée

à l'Institut des Nanosciences de Paris (Sorbonne Université)

présentée par

Adrien KHALILI LAZARJANI

pour obtenir le grade de

DOCTEUR DE SORBONNE UNIVERSITE

Sujet de la thèse :

Advancing Nanocrystal-based Infrared Imaging: Exploring Novel Strategies in the Design and Characterization

Soutenue le 4 octobre 2023

devant le jury composé de

M. Thierry TALIERCIO (IES, Montpellier)	Rapporteur
M. Hervé RINNERT (IJL, Nancy)	Rapporteur
M. Phillippe GUYOT-SIONNEST (U.Chicago, Chicago)	Examinateur
Mme. Eva IZQUIERDO (Thales, Palaiseau)	Examinatrice
M. Christophe TESTELIN (INSP, Paris)	Président du jury
M. Grégory VINCENT (ONERA, Palaiseau)	Co-encadrant de thèse
M. Emmanuel LHUILLIER (INSP, Paris)	Directeur de thèse

Remerciements

Cette thèse se termine après trois années passées au laboratoire, et c'était avant tout un travail d'équipe. Elle n'aurait pas pu aboutir sans un bon nombre de personnes que j'aimerais remercier dans ces quelques paragraphes.

Avant tout, je tiens à exprimer ma gratitude envers les membres de mon jury de thèse. Merci à mes deux rapporteurs, Thierry TALIERCIO et Hervé RINNERT, pour avoir lu attentivement mon manuscrit, et aussi pour votre patience quant à la résolution de cette roadmap en 12 étapes pour organiser votre venue. Je remercie également mes examinateurs, Philippe GUYOT-SIONNEST, Eva IZQUIERDO et Christophe TESTELIN. J'aimerais remercier l'ensemble de mon jury de thèse pour avoir évaluer mon travail doctoral, et pour ces discussions stimulantes lors de ma soutenance.

Je tiens à adresser mes remerciements les plus chaleureux à mes deux encadrants de thèse.

Tout a commencé en décembre 2019, lorsque j'ai déposé une candidature spontanée pour un stage de M2 dans ton groupe, Emmanuel. Deux jours plus tard, je t'ai rencontré et le mois suivant j'ai commencé mon stage. Je n'y connaissais pas grand-chose en *HgTe*, et j'ai tellement appris à tes côtés, aussi bien sur le schéma complet pour fabriquer une caméra que sur Franck ou sur la vidange de pompe à vide. Tu as su trouver la bonne formule pour faire tourner ton groupe, et cela passe d'abord par un encadrement exemplaire. On pouvait toujours discuter ensemble autour d'un café à 8h du matin ou d'une bière à 0h, et on trouvait toujours solution aux problèmes. Merci Emmanuel, grâce à toi, j'ai pu grandir de 14 à 17 ans, et j'espère encore continuer pour un temps dans cette voie à tes côtés pour espérer atteindre la vingtaine.

Grégory, il est vrai que mon amour pour la simulation m'a fait passer un peu (beaucoup, passionnément ?) moins de temps à l'ONERA. Néanmoins, tu as été d'une aide précieuse dans le déroulement de ma thèse. Tu as su m'expliquer les fondamentaux pour que j'y comprenne quelque chose sur la simulation et sur ces structures que vous aimez tant appeler « nano-résonateurs optiques ». Merci pour toutes ces heures de simulations que tu as faites et qui ont été indispensables à l'écriture de nos articles. On s'est même aventuré en duo dans l'alignement de cette pointe avec ce laser du SNOM, et après une journée, on a pu entrevoir un signal qu'on tente encore d'expliquer… Merci Grégory, sans toi cette thèse n'aurait pas pu aboutir.

Ma thèse n'aurait pas pu avoir lieu sans cette collaboration avec U. Chicago. Merci Philippe GUYOT-SIONNEST pour ta confiance, et pour nous avoir accueilli chez toi et dans ton groupe à Chicago. J'ai apprécié nos discussions scientifiques sur *HgTe*, et j'ai même eu la chance d'en apprendre plus sur l'électrochimie.

Je tiens ensuite à remercier les anciens doctorants du groupe OCN. Audrey, tu as été comme une maman à mon arrivée, en me prenant sous ton aile et en m'apprenant tout ce qu'il fallait savoir, notamment sur la lithographie avec une attention particulière sur le fait qu'un masque vaut plus qu'un étudiant (RIP petit masque GMR..). Chaque fois que je rencontrais des difficultés ou des interrogations au cours de mes expériences, Charlie, tu étais toujours là pour trouver une solution, au point que ça en devenait presque trop facile (et puis difficile parce qu'il a fallu apprendre à se passer de toi). Au-delà de ça, j'ai toujours apprécié nos discussions du matin ou du soir, sur la science, les avions, les voitures, les missions spatiales ou encore (surtout) de ragots. Audrey, Charlie, vous avez été une source d'inspiration, et je suis chanceux d'avoir pu travailler à vos côtés.

Puis, je voudrais exprimer ma gratitude envers mes partenaires de thèse, ceux avec qui j'ai pu partager cette aventure doctorale. Tung, it feels like yesterday when you spent 6

months measuring E_a only to change material at the end. It has been a real pleasure working with you, and I wish you the best in your new quest to build a QD laser! Coco, au-delà du labo, on a pu vivre le rêve américain ensemble, toi qui travaillais à Argonne et moi qui me promenait dans Chicago, le pied ! Ou même dans cette ville de la côte ouest qui était riche en Captain et boite hors de prix… Je te souhaite le meilleur dans ton aventure Singapourienne, et n'oublie pas : pas de nourriture crue la première semaine.

Merci à tous les membres du groupe OCN. Je commencerai par Yoan(n), je te remercie chaleureusement pour toutes ces synthèses de particules, sans toi le groupe avancerait beaucoup moins vite. Et merci aussi pour toutes ces discussions partagées en salle de chimie, parlant de séries, de France Gall, ou encore de notre sujet préféré…
Huichen, you own the chemistry room now, and what a painful pleasure but to drink your very famous spicy alcohol! Erwan, nous avons réussi une grande prouesse ensemble, *cling*, *regard inquiet* l'un pour l'autre, et pouf une chambre d'analyseur ouverte à 1h du matin… Que nous réservera le prochain run… Mariarosa, il t'a fallu un stage, puis un CDD pour te décider à enfin commencer une thèse au sein du groupe. Tu es devenue la reine de Blender (mille merci, sans toi et Charlie, ma thèse aurait été bien plus fade), et d'Igor en étant capable de manipuler des matrices à 42 dimensions. J'attends avec impatience de lire ta thèse rédigée en français !

Eva, je me dois de te remercier deux fois. La première, pour ton passage de quelques mois chez nous, où on a pu profiter de pastis, de diodes, d'encres reproductibles ou encore de problèmes de dents. Tu n'as passé qu'un bout de temps, et pourtant tu as définitivement réussi à apporter ton savoir. Puis, je te remercie aussi d'avoir accepté de faire partie de mon jury pour qu'on puisse partager ensemble le même anniversaire de thèse !

J'aimerais remercier toutes les personnes avec qui j'ai pu interagir à l'INSP. Je tiens également à remercier l'ensemble de l'équipe Physuf. En particulier, merci Sébastien pour ton aide précieuse en mécanique, promis je te paye la facture à la fin. Hervé, merci pour ces bons moments passés autour d'un café, à discuter du dernier ragot du labo. Durant ma thèse, j'ai passé un bon nombre d'heures dans la salle blanche, et pour cela je tiens à remercier Erwan Dandeu et Loïc pour leur aide.

Ce travail de thèse est le résultat de collaborations fructueuses. Merci à Baptiste Fix de l'ONERA, pour ton aide sur Hyperion et surtout sur le SNOM. Merci à Ludovic Desplanque de l'IEMN pour l'épitaxie des fils d'InGaAs. Au cours de ces trois années, j'ai pu passer quelques nuits (merci à Red Bull) sur TEMPO au synchrotron SOLEIL, merci à Mathieu Silly d'avoir été aussi gentil, même quand je faisais malencontreusement tomber tes portes-échantillons… Merci aussi à José Avila de la ligne ANTARES. Je souhaiterais aussi remercier Davide Boschetto et son équipe, pour vos nuits passées sur ces échantillons de *HgSe/HgTe*. Enfin merci à Pierre Potet, Victor Parahyba et David Darson, sans vous, l'imagerie IR avec HgTe n'aurait pas été possible.

Merci à tous mes amis présents lors de ma soutenance (et même ceux qui n'ont pas pu venir, parce qu'il est vrai que c'était un mercredi). Je pense aux groupes de La Miff, des Abeilles, à Thomas P. (mon ami de toujours), Alexis, Zicho, Nico, Hichem, Alaeddine, Lucas C. (on fera la course avec ton A1 s-line), Guigui, Antoine, Jérémie Z.
Germain et Jean, des WEI en licence Sciences pour la santé à la thèse, on a pu en voir des belles. J'attends avec impatience vos soutenances afin de pouvoir vous appeler Docteur !

A ma famille et *Cousinerie*, merci pour tous ces beaux dimanches midi partagés autour d'une raclette, d'un barbecue et de soupes bien évidemment… En particulier, j'aimerais remercier *Cousinerie x Boisson* pour toutes ces soirées au Nix Nox avec le Capitaine, où l'on décidait sur le qui-vive le déroulé de la nuit sans penser aux lendemains…

Je ne peux continuer ces remerciements sans penser à mes parents. Papa, Maman, merci pour tout, c'est grâce à vous, votre éducation, votre soutien, vos conseils, si j'en suis là aujourd'hui. Je vous aime.

En 2019, au tout début de ma thèse, tu es entrée dans ma vie, Noa. C'était à l'époque du Covid-19, et il me fallait donc une attestation de sortie pour aller te rencontrer chez toi à Bezons. Je me rappelle encore de cette côte de bœuf avec ses fameuses pâtes crémeuses à la moutarde. Depuis ce jour, on ne s'est jamais lâché, et c'est bien parce que tu es la plus belle chose qui me soit arrivée (même Mamie le dit, wow). Je suis convaincu que tu réussiras brillamment dans ta quête à Taïwan, et j'espère que tu continueras à me faire des pestacles même à 10 000 km de distance. Je t'aime infiniment.

Enfin, je terminerai cette liste par remercier celle qui m'a accompagnée au jour le jour durant toutes ces années. Merci à ma 407 SW, tu as su prendre l'A4 et l'A86 avec brio chaque matin et chaque soir. 325 000 km se sont écoulés depuis que tu es arrivé dans la famille en 2008, et malgré ça tu as toujours l'air aussi jeune !

Contents

Remerciements....4
Notations and abbreviations....9
Introduction....12
1. Infrared photodetection with colloidal nanocrystals....15
1.1- Infrared range....16
1.1-1 Spectrum and applications....16
1.1-2 Thermal detectors....17
1.1-3 Photodetectors....18
1.2- Addressing the infrared range with colloidal nanocrystals....20
1.2-1 Quantum confinement....21
1.2-2 Colloidal quantum dot synthesis....23
1.2-3 Transport in a nanocrystal array....25
1.3- From nanocrystals to an optoelectronic device....29
1.3-1 Type of photodetectors....30
1.3-2 Figure of merits for IR detection....32
1.4- Advanced infrared technologies....37
1.4-1 Wave-function engineering at the nanoscale....37
1.4-2 Enhanced light-matter coupling....38
1.4-3 Infrared focal plane arrays....39
1.5- Conclusion....42
2 Intraband photodetection with an enhanced light-matter coupling....43
2.1- HgSe for intraband detection....45
2.1-1 Self-doped HgSe nanocrystals....45
2.1-2 The doping issue for intraband detection....47
2.2 HgSe-HgTe heterostructure for infrared sensing....49
2.2-1 Uncoupling the optical from transport properties....49
2.2-2 Enhanced transport properties of HgSe/HgTe metamaterial....51
2.2-3 Exploring the ultrafast carrier dynamics in HgSe/HgTe....53
2.3 Enhanced light-matter coupling for intraband detection....56
2.3-1 State-of-the-art of resonators applied to NC-based infrared photodetectors....57
2.3-2 Guided-mode resonator: history and principle....58
2.3-3 Toward a HOT intraband-based photodetector....60
2.4 Conclusion....66
3 Extending the InGaAs spectral response through the coupling of bulk III-V and colloidal II-VI semiconductors....67
3.1 Mixed-dimensional van der Waals heterostructures....68
3.2 Expansion up to 2 µm of InGaAs spectral response....70

3.2-1 Design of the InGaAs/HgTe infrared sensor 71
3.2-2 Lifting the epitaxial constraint on the spectral response. 76
3.2-3 High electrical bandwidth hybrid photodetector 77
3.3 Toward a MWIR-sensitized InGaAs photodetector 79
3.3-1 Fabrication of the InGaAs – HgSe/HgTe heterostructure 80
3.3-2 Design of a planar p-n junction in the mid-infrared 82
3.3-3 Detection performances of the MWIR photodiode 85
3.4 Conclusion 86
4 Exploring *in-operando* and *in-situ* a short-wave infrared camera based on HgTe nanocrystals 87
4.1 Focal plane array based on HgTe nanocrystals 88
4.1-1 Toward cost-efficient infrared cameras 88
4.1-2 NC-based camera operated in a photoconductive mode 90
4.2 Inside an HgTe-based readout circuit 92
4.2-1 Fabrication of a model 92
4.2-2 Transport characterization 93
4.3 In-situ mapping of a HgTe-based focal plane array 95
4.3-1 X-ray Photoemission Spectroscopy: history and principle 96
4.3-2 Energy landscape of HgTe-based camera 99
4.3-3 Revealing the photocurrent spatial distribution in HgTe-based FPA 103
4.4 Conclusion 107
Conclusion and perspectives 109
Appendix 111
List of publications 113
References 118

Notations and abbreviations

Constants

Symbol	Value	Description
$\boldsymbol{e}$	1.609×10^{-19} C	Elementary charge
$\boldsymbol{c}$	299 792 458 m.s^{-1}	Speed of light
$\boldsymbol{h}$	6.62×10^{-34} J.s	Planck constant
$\boldsymbol{\hbar}$	1.05×10^{-34} J.s	Reduced Planck constant
$\boldsymbol{k_B}$	1.38×10^{-23} J.K^{-1}	Boltzmann constant
$\boldsymbol{m_0}$	9.11×10^{-31} kg	Electron mass
$\boldsymbol{\varepsilon_0}$	8.85×10^{-12} m^{-3}.kg^{-1}.s^4.A^2	Vacuum permittivity

Abbreviations

Abbreviation	Signification
NC	Nanocrystal
CQD	Colloidal quantum dot
IR	Infrared
NIR	Near infrared
SWIR, eSWIR	Short-wave infrared, extended short-wave infrared
MWIR	Mid-wave infrared
LWIR	Long-wave infrared
FIR	Far infrared
VB	Valence band
CB	Conduction band
FET	Field-effect transistor
TEM	Transmission electron microscopy
SEM	Scanning electron microscopy
SNOM	Scanning near-field optical microscopy
FTIR	Fourier-transform infrared spectroscopy
XPS	X-ray photoemission spectroscopy

BE	Binding energy
KE	Kinetic energy
FPA	Focal plane array
CMOS	Complementary metal-oxyde-semiconductor
ROIC	Read-out integrated circuit
MCT	Mercury cadmium telluride
QWIP	Quantum well infrared photodetector
QDIP	Quantum dot infrared photodetector
T2SL	Type II superlattice
QCD	Quantum cascade detector
QCL	Quantum cascade laser
PC	Photoconductor
PD	Photodiode
PV	Photovoltaic
GMR	Guided mode resonator
TM	Transverse magnetic polarization
TE	Transverse electric polarization
NW	Nanowire
EDT	Ethanedithiol
DDT	Dodecanethiol
MPOH	Mercaptoethanol
TOP	Tri-octylphosphine
DMF	Dimethylformamide
PEG	Polyethylene glycol

Notations

Symbol	Description
T	Temperature

$h\nu$	Photon energy
k	Wavevector
λ	Wavelength
R	Nanocrystal radius
a_0	Bohr radius
E_{bulk}	Bulk bandgap
E_G	Bandgap
m_e^*, m_h^*	Electron and hole effective masses
τ_{hop}	Hopping time
L_D	Diffusion length
μ	Mobility
V_{DS}	Drain-source voltage
V_{GS}	Gate-source voltage
I_{DS}	Drain-source current
I_{GS}	Gate-source current
I_{dark}	Dark current
I_{light}	Current under illumination
I_{photo}	Photocurrent
V_{OC}	Open-circuit voltage
I_{SC}	Short-circuit current
E_a	Dark current activation energy
R	Responsivity
S_I	Dark current spectral density
D^*	Specific detectivity
n	Refractive index

Introduction

Our first contact with infrared dates back to our early years when we experienced the sensation of warmth emanating from hot objects, despite being unable to visually perceive the responsible rays. The journey of infrared radiation began in the early 19th century, when the astronomer Sir Frederik William Herschel made the pioneering discovery of its existence. Born in Hanover, Germany, Herschel initially pursued a career as a musician and composer, rather than a scientist. However, his passion for astronomy inspired him and his sister Caroline to purchase a book on the subject and construct their own telescopes. Their collaborative efforts resulted in various catalogs detailing double stars and nebulae. In 1781, Herschel achieved worldwide approval with his remarkable discovery of Uranus, marking the first identification of a new planet since Antiquity. In 1800, Herschel achieved another significant breakthrough in his scientific journey.[1] He conducted an experiment wherein he directed sunlight through a glass prism, thereby generating a spectrum of colors, known as rainbow in everyday life. Employing a crafted monochromator, he measured the temperature associated with each color, and observed that the temperature increased gradually from the violet to the red portion of the spectrum. Intrigued by these findings, Herschel decided to explore the temperature just beyond the red region of the spectrum, which appeared devoid of sunlight. To his surprise, he discovered that this unilluminated domain exhibited the highest temperature of all. He invented the term "*calorific rays*" to refer to this region. Herschel's experiment held great significance as it marked the first instance of demonstrating the existence of light that escapes human visual perception.

Approximately a century after Herschel's discovery, a notable advancement in the realm of infrared sensing occurred in 1880 when Samuel Pierpont Langley conceived the first infrared sensor, that he named "*the Bolometer*".[2] This device featured a configuration comprising two thin platinum strips arranged in a manner similar to the arms of a Wheatstone bridge. When subjected to infrared illumination, these metallic strips would heat up, consequently leading to an increase in their electrical resistance, a parameter subsequently quantified by means of a galvanometer. Alongside, in 1873, Willoughby Smith made a significant discovery, unveiling the inaugural photon effect, the photoconductive effect, while conducting investigations involving Selenium as an insulating material for submarine cables.[3] Smith's remarkable work laid the foundation for the development of infrared quantum photon detectors, which possess a sensitivity based on the detection of photon flux as opposed to temperature differentials.

The field of infrared detection gained significant attention during World War II, primarily driven by the ability to detect and monitor thermal signatures emanating from objects and individuals without exposing oneself. This necessity led to the development of infrared photodetectors based on narrow bandgap semiconductors like InSb or HgCdTe. Subsequently, in the 1970s, the development of Molecular Beam Epitaxy marked a breakthrough in the realm of infrared technology, allowing for the epitaxial growth of monocrystalline semiconductors alongside precise doping control, thereby enabling the realization of heterostructures such as quantum wells. Consequently, highly sensitive infrared photodetectors covering the short- to long-wavelength infrared spectra were brought to realization. However, the inherent cost associated with epitaxially grown infrared sensors has restricted their use to defense and astronomical applications. Concurrently, advancements in technology over the past two decades within industries involving smartphones, automobiles, and agriculture have engendered a growing demand for cost-effective and highly sensitive infrared sensors.

During the 1990s, the field of Colloidal Quantum Dots, also known as Nanocrystals, emerged as promising materials for optoelectronics, building upon the research conducted on narrow bandgap bulk semiconductors. Notably, in 1993, a team of scientists at the Massachusetts Institute of Technology achieved a significant milestone by demonstrating the chemical synthesis of cadmium selenide nanocrystals in an apolar solvent.[4] This chemical growth technique offers several advantages over epitaxial growth, including ease of production

and cost-efficiency, making it well-suited for large-scale manufacturing. Since this pioneering work, the nanocrystal field has rapidly evolved, with Nanocrystals have already found their way into civilian applications, notably in television technology where they serve as bright sources for the red and green colors in displays (QLED TV). Moreover, research on nanocrystals for infrared applications has mainly been driven by the pursuit of efficient solar cells capable of harnessing the infrared portion of sunlight, particularly in the near-infrared range. In this context, substantial progress has been achieved with the utilization of lead sulfide (PbS) nanocrystals. However, the demand for next-generation applications in everyday life, including industrial vision, LiDAR in autonomous vehicles, and agricultural monitoring, necessitates addressing wavelengths beyond the near-infrared, notably the short- and mid-infrared region.

In this context, my PhD thesis was conducted at Institut des Nanosciences de Paris (Sorbonne Université) in the group of Emmanuel Lhuillier, and at the Département d'Optique et Techniques Associées (ONERA) under the supervision of Grégory Vincent. My PhD is supported by the CNRS for the collaboration with the research group led by Philippe Guyot-Sionnest at the University of Chicago. Over the course of my thesis, I had the privilege of visiting the University of Chicago to conduct electrochemical measurements and participate in a seminar related to nanocrystals. The majority of my doctoral work took place at INSP, where the focus lies in fabricating an infrared optoelectronic system, starting from the chemical synthesis of nanocrystals to the characterization of single sensor element, and ultimately integrating them into advanced infrared technologies such as multipixel cameras. Throughout my doctoral journey, I had the opportunity to delve into various aspects of nanocrystal-based infrared photodetector production. Specifically, I explored novel concepts relating to both material properties and the design of complex device geometries with enhanced light-matter coupling.

Organization of the manuscript

This doctoral thesis comprises four chapters. The **first chapter** serves as an introduction, providing an in-depth overview of the infrared range, particularly in relation to colloidal quantum dots. This section will delve into the various types of infrared detectors, existing sensing technologies, and the figure of merits (quantitative metrics) employed to evaluate their performance. Furthermore, it will elucidate the fundamental aspects of nanocrystals, including their growth mechanisms, optical characteristics, and transport properties. Lastly, a comprehensive examination of the experimental setups utilized throughout the three years of my PhD to characterize the developed infrared detectors will be presented.

The **second chapter** of this thesis focuses on the comprehensive exploration and integration of intraband-based nanocrystals within intricate device architectures designed for mid-infrared detection applications. Specifically, the aim is to engineer the carrier wave-functions at the device level, thereby creating a hybrid nanocrystal material. This hybrid material will be integrated into a complex device geometry, where the light-matter coupling is precisely tailored to enhance light absorption. This light management strategy allows for the realization of a High Operating Temperature detector.

The **third chapter** of this thesis is dedicated to demonstrating the remarkable synergistic properties that emerge from the strategic coupling of mercury chalcogenide HgX II-VI nanocrystals with bulk III-V InGaAs materials. Historically, these two communities have been perceived as distinct and separate. However, in this chapter, instead of pitting these technologies against each other, they are coupled to design a SWIR detector and a MWIR sensor. This approach aims to capitalize on the unique advantages offered by each material system.

The **fourth chapter** of this thesis is dedicated to the development of the most sophisticated infrared device, compared to the ones of the preceding chapters. Specifically, significant advancements in the design and implementation of an infrared camera based on HgTe

nanocrystals will be discussed. Notably, this imager will undergo *in-situ* and *in-operando* investigations to probe its energy and photocurrent landscapes. This innovative approach represents a crucial departure from the conventional practice of studying the material and the device independently, instead focusing on the material within the context of the device itself. By examining the material within its operational framework, a deeper understanding of the underlying mechanisms and performance characteristics can be attained, propelling the field of infrared imaging towards remarkable levels of sophistication and functionality.

The **appendix** serves as a "Material and Methods" section, providing detailed information on the synthesis of the nanocrystals employed in this thesis, including their transformation into an ink form. Furthermore, a general protocol outlining the fabrication of the electrodes through optical and e-beam lithography will be presented.

1. Infrared photodetection with colloidal nanocrystals

Related articles:

- *Lhuillier, E.; Dang, T. H.; Cavallo, M.; Abadie, C.; **Khalili, A**.; Gréboval, C. Electronic Structure of Mercury Chalcogenides Nanocrystals. In Handbook of II-VI Semiconductor-Based Sensors and Radiation Detectors: Volume 1, Materials and Technology; Korotcenkov, G., Ed.; Springer International Publishing: Cham, 2023; pp 133–156.*

- *Lhuillier, E.; Dang, T. H.; Cavallo, M.; Abadie, C.; **Khalili, A**.; Peterson, J. C.; Gréboval, C. Infrared Sensing Using Mercury Chalcogenide Nanocrystals. In Handbook of II-VI Semiconductor-Based Sensors and Radiation Detectors: Volume 2, Photodetectors; Korotcenkov, G., Ed.; Springer International Publishing: Cham, 2023; pp 155–181.*

1. Infrared photodetection with colloidal nanocrystals 15
1.1- Infrared range 16
1.1-1 Spectrum and applications 16
1.1-2 Thermal detectors 17
1.1-3 Photodetectors 18
1.2- Addressing the infrared range with colloidal nanocrystals 20
1.2-1 Quantum confinement 21
1.2-2 Colloidal quantum dot synthesis 23
1.2-3 Transport in a nanocrystal array 25
1.3- From nanocrystals to an optoelectronic device 29
1.3-1 Type of photodetectors 30
1.3-2 Figure of merits for IR detection 32
1.4- Advanced infrared technologies 37
1.4-1 Wave-function engineering at the nanoscale 37
1.4-2 Enhanced light-matter coupling 38
1.4-3 Infrared focal plane arrays 39
1.5- Conclusion 42

1.1- Infrared range

1.1-1 Spectrum and applications

Infrared detection has become an integral component in numerous applications such as night vision, remote sensing, spectroscopy, medical imaging and telecommunication. The earliest IR detectors were thermal, which relied on material absorption of IR radiation and temperature rise to produce a measurable signal. In the 1950s, photoconductive detectors were developed that used semiconductors to convert infrared light into a change in electrical conductivity. On the heels of this innovation came photovoltaic detectors, which use semiconductors to directly convert IR radiation into electrical current. These early detectors had limited sensitivity and response speed, but advances in materials and device design have enabled significant progress in IR detection over the last decades. Nowadays, various types of IR detectors exist such as bolometers, pyroelectric detectors, quantum well detectors, and nanocrystal-based ones.

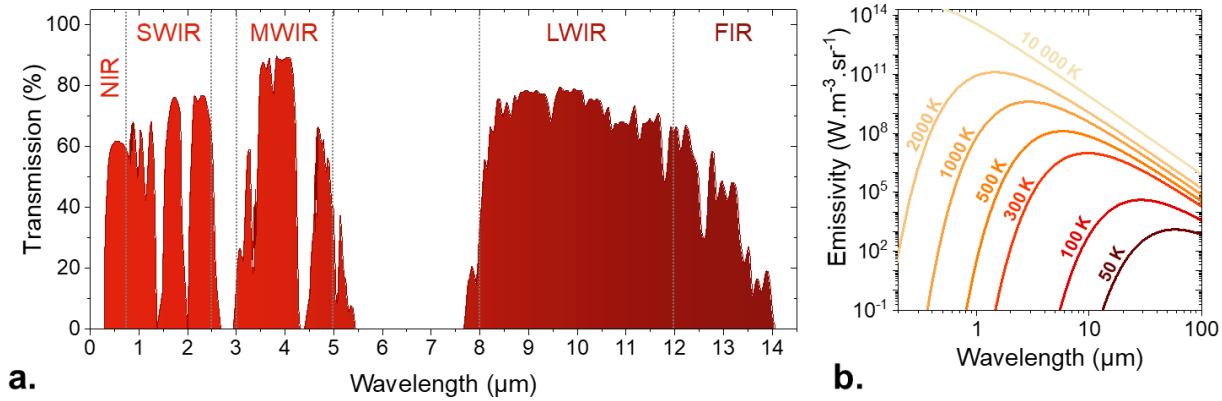

Figure 1 Infrared spectral range. a. Earth atmospheric transmission spectra with each infrared subregion. b. Blackbody spectral radiation at different temperatures.

The infrared part of the electromagnetic spectrum extends from 800 nm to 100 µm and is conventionally divided into various subregions depending on the intended application. One widely accepted scheme utilized by academic and industrial communities is based on atmospheric transparency windows and the corresponding sensor response. Notably, the earth's atmosphere is mostly opaque to specific infrared radiations due to the presence of water vapor and carbon dioxide, which limits their detection in certain regions (2.7 - 3 µm and 5.5 - 8 µm). The subregions can be classified beginning from the longer wavelengths of the visible spectrum as:

- The **Near-Infrared** (NIR) region spans from 0.7 µm to 1 µm and is accessible using technologies developed for the visible spectrum, such as silicon. This region is particularly attractive for solar-cell materials since it can harvest both the visible and a significant portion of the infrared spectrum. NIR is useful for night vision and facial recognition applications due to the availability of cheap and powerful light sources such as AlGaAs at 808 nm and Nd:YAG at 1064 nm. It is also of interest for biological imaging as skin tissue is transparent to wavelengths around 900 nm.

- The **Short-Wave-Infrared** (SWIR) region spans from 1 µm to 1.7 µm and is close to the visible for imaging. Objects in this region can act as secondary sources by reflecting and diffusing light, which is useful for active imaging with proper illumination sources. The transparency of the atmosphere over the entire SWIR range, combined with high-performance sources and detectors (such as InGaAs), makes long-range imaging possible, and is used in military applications for target acquisition and surveillance. In recent years, SWIR has gained a lot of attraction in civilian applications such as machine vision systems and quality control for sorting products in the food industry. LiDAR (light

detection and ranging) are also widely used in newer generations of smartphones and autonomous cars. Additionally, telecommunications wavelengths fall in the SWIR range, as it offers the lowest attenuation for glass-based optical fibers around 1.5 µm. The extended SWIR, known as eSWIR, extends up to 2.5 µm, which is a region of interest for several space applications.

- The **Mid-Wave-Infrared** (MWIR) region spans from 3 µm to 5 µm, where blackbody emission from objects becomes dominant over the reflection of secondary sources. Blackbody emission at the temperature T is given by:

$$L(\lambda, T) = \frac{2hc^2}{\lambda^5} \frac{1}{e^{hc/(\lambda k_B T)} - 1}$$

Where $L(\lambda, T)$ is the spectral radiance in W.m^{-3}.sr^{-1}, c is the speed of light, h the Planck constant, k_B the Boltzmann constant and λ the wavelength. Objects in this region act as light sources, allowing for thermal (passive) imaging without requiring a secondary source, making them ideal for stealthy applications. MWIR is widely used in gas detection, as many molecules absorb in this range of wavelengths, including C-H and CO_2 with peaks at 2900 cm^{-1} and 2349 cm^{-1}, respectively.

- The **Long-Wave-Infrared** (LWIR) spans from 8 µm to 12 µm. LWIR imaging is commonly used for room-temperature objects since the latter's maximum emission is found to be at 10 µm. Therefore, the LWIR is the historical region of interest for defense applications with missile- and airplane-seeking. Moreover, LWIR cameras can detect temperature differences as small as 10 mK, making them useful for detecting overheating in electrical components and other systems.

- The **Far-Infrared** (FIR) spans between 15 µm and 100 µm and overlaps with the THz range. FIR is capable of penetrating deeper than other wavelengths through certain materials without ionizing hazards, making it useful for surveillance applications. FIR is the range of choice in astronomy for studying cooler objects in the universe, such as dust and gas clouds.

1.1-1. Infrared detectors

This section discusses infrared detectors, which are devices designed to detect and measure infrared radiation. It presents the leading technologies and materials used in the detection of infrared light. It is important to differentiate the two types of infrared detectors: thermal detectors and photodetectors.

1.1-2 Thermal detectors

Infrared thermal detectors are a type of infrared detector that operates by measuring the temperature rise resulting from the absorption of infrared radiation by a material. These detectors have been used since the early days of infrared detection and are still widely used today in a variety of applications, including temperature measurement, surveillance, and industrial process control. The earliest infrared thermal detectors were based on thermocouples, which are junctions between two dissimilar metals that produce a voltage proportional to the temperature difference between the junctions. These detectors had limited sensitivity and were largely replaced by bolometers in the early 20th century. Bolometers are a type of thermal detector that measures the temperature rise of a thin film of material in response to absorbed infrared radiation. They are highly sensitive and can operate over a wide range of wavelengths, but their bandwidth is limited to around 25 Hz since they are based on the cooling/heating of the absorber.

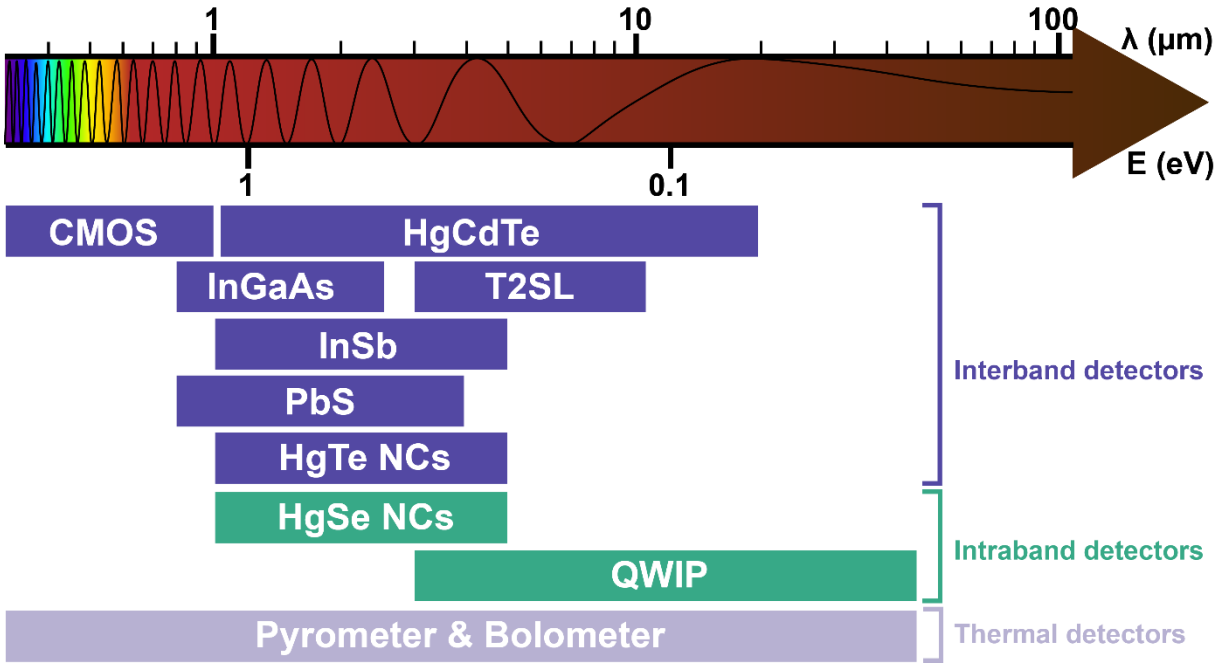

Figure 2 Overview of the main technologies for infrared detection depending on the spectral region of interest.

In the 1960s, pyroelectric detectors were developed, which are based on the property of certain materials to generate a voltage when their temperature changes. The metal pair platinum-rhodium is widely used in pyrometers for high temperature measurements that typically exceed 1000°C. Pyroelectric detectors are faster and more sensitive than bolometers. Recent advances in materials science and microfabrication techniques have led to the development of new types of infrared thermal detectors, such as microbolometers and thermopiles, which offer improved sensitivity, response time, and spatial resolution. Nowadays, low-cost thermal imaging devices typically employ microbolometers based on vanadium oxide (VO_x) technology.

1.1-3 Photodetectors

The operation of photodetectors is based on the conversion of the photon's energy into an electrical signal. This is achieved by using electronic transitions between bands or levels in semiconductor materials. Upon the absorption of an infrared photon by the semiconductor material, an exciton, which is an electron-hole pair, is generated. The generated electron and hole can move through the material under the influence of an electric field, creating a measurable photocurrent across the device. The energy of the absorbed infrared photon must match the energy difference between the hole and electron levels of the semiconductor to detect it. A crucial factor in the design of infrared photodetectors is the operating temperature. As the electronic transitions have low energies due to the low energy of infrared photons, carriers start being activated thermally (25 meV at room temperature) resulting in an increase in dark current and decrease in signal-to-noise ratio. To address this problem, most infrared detectors are cooled to decrease dark current and improve performances. However, this comes at the expense of a costly, heavy, and high energy consumption cooling mechanism (cryostat). Infrared photodetectors can be divided into two types based on the nature of their electronic transitions: interband and intraband detectors.[5,6] In the following, we will provide an overview of the leading detection technologies in each infrared region.

Interband detectors are based on semiconductor materials with electronic transitions between the valence and conduction bands. These types of photodetectors are the most widespread among the infrared community. Narrow bandgap semiconductors such as Ge, PbS

and InSb, as well as alloys like InGaAs and HgCdTe, are used to achieve low energy interband transitions for detecting infrared light.

In the near-infrared (NIR) range, silicon-based complementary metal-oxide-semiconductor (CMOS) technology is the most popular option, offering low-cost and high-performance (silicon cutoff wavelength at 1.1 µm).

In the SWIR, the dominant technology for photodetection is based on the use of a ternary alloy consisting of indium, gallium, and arsenic atoms, known as InGaAs. This semiconductor material can be epitaxially grown as a single crystal on an indium phosphide substrate using either molecular beam epitaxy (MBE) or metal organic chemical vapor deposition (MOCVD). The bandgap energy of $In_{0.53}Ga_{0.47}As$ is 0.75 eV, corresponding to a cutoff wavelength of approximately 1.65 µm, which can be extended up to 2.6 µm by tuning the indium content to 0.83. InGaAs photodetectors exhibit low dark current, low noise, and high sensitivity, with detectivity values reaching 10^{13} Jones (10^{11} for 2.6 µm cut-off), and can be operated at room temperature. The process of integrating the InGaAs thin film into a large focal plane array is well-established and involves the hybridization of the active material to the readout circuit (ROIC) using indium beads. This fabrication process is complex and hence increases the cost of an InGaAs camera, which typically ranges from 10 to 50 k€. Other alternatives for photodetection that are less expensive and less sensitive than InGaAs include PbS, PbSe, and Ge.

In the MWIR, there are two dominant interband technologies: InSb and HgCdTe. InSb is a narrow bandgap III-V semiconductor with a bandgap of 230 meV, which corresponds to a wavelength of 5.4 µm at 80 K. Typically, InSb is grown using MOCVD, and it provides high sensitivity in the 1-5 µm range with detectivities of 10^{11} Jones at 77K. However, its fixed bandgap prevents its spectral tuning over a wider range. In contrast, the HgCdTe (or MCT) alloy allows spectral response tuning over the SWIR to the LWIR range (1-30 µm) by adjusting the cadmium content.[7] To ensure a lattice match, HgCdTe thin film must be grown using liquid-phase epitaxy on a CdZnTe substrate. Additionally, MCT photodetectors require cooling to 80K (for MWIR) or 4K (for THz) to maintain detectivities of 10^{10}-10^{11} Jones. Due to their high performance and complex fabrication processes, MWIR detectors are primarily used in defense applications and are expensive, with a basic MCT camera costing around 100 k€.

In recent years, a new category of interband detectors has emerged, known as type II superlattice (T2SL) detectors.[8] These detectors are composed of multiple monolayers of InAs and GaSb, which are arranged alternately, thereby forming a superlattice structure. In T2SLs, the valence band of GaSb and the conduction band of InAs are separated in energy by a type II alignment, allowing for spatial separation of electrons and holes. The confinement of the carriers in two different materials results in an extended lifetime of the electron-hole pair. When a photon is absorbed, an electron-hole pair is generated, and the electron is excited to the conduction band of InAs, while the hole is left in the valence band of GaSb. The photogenerated carriers can then move, creating a photocurrent under the influence of an applied electric field. T2SL photodetectors are regarded as a promising candidate that can compete with MCTs in terms of spectral tunability, high sensitivity, and photovoltaic mode.

Intraband detectors are based on doped heterostructured semiconductors where electronic transitions can occur within the same band or energy level. These detectors emerged in the 1990s with the development of molecular beam epitaxy (MBE) technology, which facilitated wave-function engineering. The most prevalent types of intraband detectors are quantum well infrared photodetectors (QWIPs) and quantum dot infrared photodetectors (QDIPs).[9] The first QWIP was developed in 1987 by Levine *et al.*[10] at AT&T Bell Laboratories, where thin layers of doped GaAs were grown epitaxially and sandwiched between two wider bandgap AlGaAs layers. In QWIPs, the electrons and holes are confined to a 2D layer of discrete energy levels that can be excited by the absorption of infrared photons. The excited electrons are then transferred to the continuum and drift to the electrode under an applied electric field, owing to the alignment of energy levels of the QWs and the AlGaAs barriers.

QDIPs, on the other hand, are the 0D counterpart of QWIPs, where small clusters of InAs are embedded in a wider bandgap material such as GaAs.

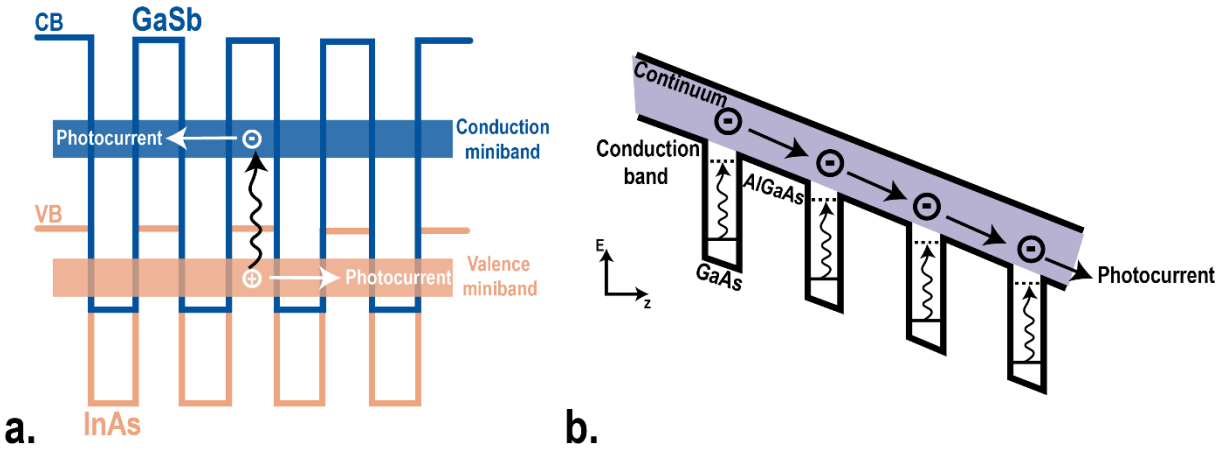

Figure 3 Exploiting the interband and intraband absorption to design infrared photodetectors. a. Scheme of the band diagram of a typical InAs/GaSb type II superlattice interband detector. b. Scheme of the band diagram of the conduction band in a QWIP made of GaAs/AlGaAs.

Despite the high performance exhibited by intraband-based detectors, their operation is restricted to cryogenic temperatures due to the high dark current that they generate. Furthermore, when compared to Type-II superlattice detectors, QWIPs have a narrower spectral bandwidth. Additionally, the optical selection rules in 2D structures of QWIPs prohibit normal incidence absorption. Consequently, light management strategies (*i.e.*, diffraction grating) must be implemented, resulting in increased fabrication complexity and cost of intraband photodetectors.

1.2- Addressing the infrared range with colloidal nanocrystals

Infrared detection has a long history, but it was during World War II that its development accelerated significantly. The need to detect enemy planes, ships, and soldiers under low light or nighttime conditions in a stealthy manner pushed the advancement of infrared technology. In the 1940s, the Germans developed the first practical infrared system, the *Spanner Anlage,* consisting of a detector photomultiplier placed in front of the pilot, and a large searchlight fitted with a filter to limit the output to the IR range. This provided enough light to see the target at a short range.

During the second half of the XXth century, the 8-12 µm spectral range, which aligns with the peak emission of a blackbody at room temperature, became a subject of interest. Infrared sensors initially emerged in the 1950s, but those based on lead chalcogenide materials had a large bandgap (0.3 - 0.4 eV), rendering them unsuitable for thermal imaging. In order to satisfy the requirements for LWIR passive imaging, the investigation of semiconductors with very narrow bandgap (100 meV) was necessary. While InSb was a promising candidate due to its high carrier mobility (78000 $cm^{-2}.V^{-1}.s^{-1}$),[11] its 0.17 eV direct bandgap limited it to the 1-5 µm range. At the time, semimetallic materials (0 eV bandgap) such as gray tin, HgTe, and HgSe were investigated, but they did not exhibit photoconduction properties in their bulk form. In 1959, Lawson *et al.*[12] demonstrated photoconduction properties in HgCdTe alloys for the first time at the Royal Radar Establishment in the UK. MCT detectors showed similar performance to InSb with spectral tunability. Hence, HgCdTe met the military's requirements and propelled the research on infrared detection for an extended period. Even now, MCT detectors are widely used and for instance integrated into the latest NASA space telescope, James Webb.[13]

Infrared detectors, such as HgCdTe, InSb, and QWIP, require complex and expensive fabrication techniques using MBE or MOCVD. However, for the first time in 1993 at the MIT, Murray *et al.*[4] demonstrated a monodisperse colloidal synthesis of cadmium chalcogenides

nanocrystals *via* a hot injection method. This approach allowed for the solution growth of semiconductor nanoparticles as a quantum confined material with an atom-like structure. Although the semiconductor community was initially skeptical of colloidal syntheses due to lower control and carrier mobilities, intensive research over the past three decades has shown comparable size, shape,[14,15] and composition control to traditional growth methods. Today, nanocrystals have achieved a global market status, with a market worth of 1 billion dollars per year,[16,17] and are used in various applications, including display,[18,19] detection, and lasing.

Mercury chalcogenides (HgX) have emerged as a promising alternative to epitaxially grown semiconductors for pushing the nanocrystals optical features in the red and infrared range.[20] In particular, mercury telluride (HgTe) nanocrystals were first utilized in the telecommunications domain in the early 2000s.[21] The semimetallic nature of HgTe allows for tuning of its spectral response from 1.5 eV for the most confined form[22,23] to virtually zero, thus addressing the entire infrared range. Additionally, nanocrystals provide higher flexibility in the design of infrared detectors compared to their epitaxially grown III-V and II-VI counterparts, which must be lattice-matched to the substrate, limiting their bandgap tunability. In the following section, we will examine why HgX NCs are an attractive candidate for infrared detection by discussing their fundamental properties in terms of electronic structure, synthesis, and transport.

1.2-1 Quantum confinement

The band theory is a fundamental concept used to explain the electronic properties of bulk semiconductors. It characterizes the energy levels available for electrons, where the highest occupied energy band is known as the valence band (VB), and the lowest unoccupied energy band is called the conduction band (CB). The energy difference between these two bands is referred to as the bandgap energy (E_g). If E_g is greater than a few electron volts (eV), the material is classified as an insulator. However, if E_g is in the order of 1 eV, the material is considered a semiconductor. In contrast, when E_g is zero, the material is classified as a semi-metal.

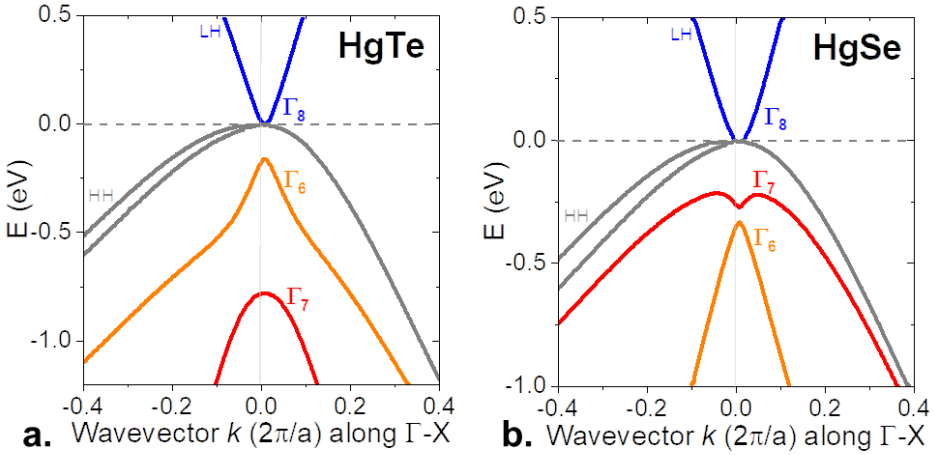

Figure 4 Calculated band structure for HgTe (a) and HgSe (b) near the Γ point. The horizontal axis is $2\pi/a$ with $a = 6.47$ Å for HgTe and $a = 6.08$ Å for HgSe. Adapted from ref.[24]

The spectral tunability of mercury telluride (HgTe) and selenide (HgSe) can be attributed to their unique band structures, which are distinct from classical semiconductors. Specifically, HgTe and HgSe have inverted band structures[24] in which the usual conduction band with symmetry Γ_6 is located below the Γ_8 bands. Moreover, HgSe has Γ_7 located between the Γ_6 and Γ_8 levels, whereas in HgTe, the Te spin-orbit coupling is so strong that Γ_7 falls below Γ_6. The bandgap energy usually defined as $E_G = E(\Gamma_6) - E(\Gamma_8)$, is a negative bandgap for both materials. Furthermore, in their bulk form, the valence and conduction Γ_8 bands meet at the center of the Brillouin zone, classifying them as semi-metals.

Therefore, the bandgap energy in HgTe and HgSe semiconductor only arises in their nanocrystal form throughout quantum confinement. Considering a simple model of *particle in a box* (infinite square well), the behavior of electrons and holes can be explained by two parabolic dispersion relations for the conduction and valence bands. Assuming a direct bandgap, both bands are separated in energy by the bulk bandgap energy E_{bulk} at the Γ point. The dispersion relations for electrons and holes are as follows:

$$E_{CB}(k) = E_{bulk} + \frac{\hbar^2 k^2}{2m_e^*} \;\; and \;\; E_{VB}(k) = -\frac{\hbar^2 k^2}{2m_h^*}$$

With $\hbar$ the reduced Planck constant, k the wavevector, m_e^* and m_h^* the effective electron and hole masses, respectively. Those parabolic bands are represented in Figure 5.

Upon absorption of a photon, an electron is excited from the valence to the conduction band, creating an electron-hole pair or exciton. When one dimension of the crystal falls below the average distance between both photogenerated charges (Bohr radius), the quantum confinement arises in this direction. The exciton Borh radius is given by:

$$a_0 = \frac{4\pi\varepsilon_0\varepsilon_r\hbar^2}{m_0 m_{eh}^* e^2} \quad with \quad \frac{1}{m_{eh}^*} = \frac{1}{m_e^*} + \frac{1}{m_h^*}$$

Where e is the elementary charge, ε_0 is the absolute dielectric permittivity, ε_r is the material dielectric constant, and m_{eh}^* is the reduced mass. Table 1 presents the Bohr radius for different semiconductors.

Table 1 Electronic structure parameters of some semiconductors in their nanocrystal form

Material	$E_{bulk}\ (eV)$	$m_e^*\ (\times m_0)$	$m_h^*\ (\times m_0)$	$a_0\ (nm)$	References
HgTe	0	0.013	0.5 – 0.7	40	25
HgSe	0	0.04	0.78	17	26
PbS	0.4	0.087	0.083	21	27
CdSe	1.7	0.18	0.89	5.6	15

Considering a spherical particle with a radius $R < a_0$, solving the Schrödinger equation results in confined and discrete energy levels. The discrete energy states $E_{n,l}$ and their wavevectors $k_{n,l}$ are then given by:[28]

$$E_{n,l} = \frac{\hbar^2 \phi_{n,l}^2}{2m^* R^2} \quad and \quad k_{n,l} = \frac{\phi_{n,l}}{R}$$

With m^* the effective electron or hole mass, $\phi_{n,l}$ the n-th root of the l-th Bessel function. The resulting energy states are denoted nl with $n = 1, 2, 3 \ldots$ and $l = S, P, D, F \ldots$ Furthermore, an index h or e is added to indicate if the energy state is located in the valence (h) or conduction (e) band.

From above equation, we can also see that the effective mass affects the spacing of energy states. In II-VI semiconductors, particularly in HgTe and HgSe, the hole effective mass is largely greater than the electron one ($m_h^* = 25 m_e^*$ for HgTe).[29] Therefore, the dispersion of the energy levels is higher in the conduction than the valence band. The latter is referred as a quasi-continuum. Figure 5 illustrates the band diagram of a nanocrystal (spherical particle with $R < a_0$) with its discrete energy states. The nanocrystal's bandgap energy is then given by subtracting the energy of the conduction band ($1S_e$) and the valence band ($1S_h$) as:

$$E_g^0 = E_{1S_e} - E_{1S_h} = E_{bulk} + \frac{\hbar^2\pi^2}{2R^2 m_e^*} + \frac{\hbar^2\pi^2}{2R^2 m_h^*} = E_{bulk} + \frac{\hbar^2\pi^2}{2R^2 m_{eh}^*}$$

In nanocrystals, the Coulombic interaction between the electron and hole is small compared to the confinement energy. As a result, the nanocrystal bandgap is inversely proportional to the particle size, indicating that larger particles emit at longer wavelengths in the infrared spectrum.

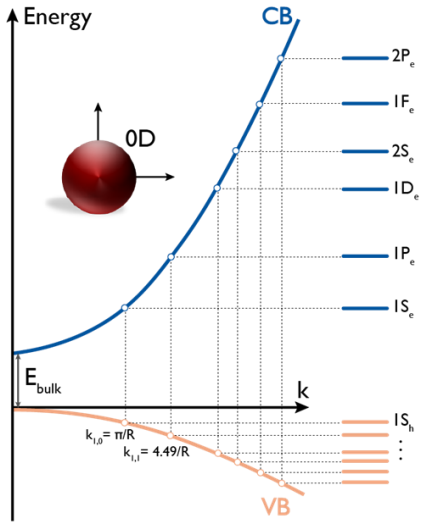

Figure 5 Effect of quantum confinement on a spherical particle with dimension below the Bohr radius. Band diagram of a colloidal nanocrystal in the parabolic approximation.

1.2-2 Colloidal quantum dot synthesis

The introduction of quantum confined nanoparticles in the semiconductor community brought a novel appealing material for optoelectronics. By growing nanocrystals in solution, and only tailoring their size, their optical properties could be tuned throughout the electromagnetic spectrum, considerably easing the material growth in contrast to traditional semiconductors that require precise doping or alloying. 30 years ago, the Bawendi group[4] established the initial II-VI nanocrystal synthesis utilizing a hot injection technique, which involves the rapid injection of semiconductor precursors into a hot coordinating solvent. The authors succeeded in synthetizing CdSe nanocrystals covering the entire visible spectrum with this growth method.

Currently PbS is the main material used for achieving absorption in the infrared range, but its 0.41 eV bandgap prevents its use in the MWIR. HgTe, on the other hand, can address the whole infrared range with its 0 eV bandgap. The first synthesis of HgTe NCs was developed in the early 2000s by Rogach *et al.*[21] in aqueous medium with a gaseous H_2Te precursor. Few years later, Kovalenko *et al.*[30] improved the synthesis and extend the cut-off wavelength of HgTe to 4 µm. In 2011 at the University of Chicago, Keuleyan et *al.*[31] introduced a more straightforward synthesis in organic solvents, which is the one typically used by the group at INSP. Each step of the HgTe colloidal synthesis is depicted in Figure 6a. Firstly, the semiconductor precursor TOP:Te is formed by dissolving tellurium (Te) in trioctylphosphine (TOP), whereas mercury chloride ($HgCl_2$) and oleylamine are degassed under magnetic stirring in a three-neck flask at 110°C. It is crucial to remove water and oxygen during the degassing stage to prevent any undesirable reactions with the precursors. Subsequently, under an inert atmosphere (N_2 or Argon) and at the reaction temperature (60 – 120°C), TOP:Te precursor is quickly injected. The reaction is quenched with dodecanethiol (DDT) in toluene after a few minutes. Finally, the resulting solution is washed (precipitation and redispersion) several times to remove unreacted precursors and oleylamine. The nanocrystals are precipitated with a polar solvent like ethanol or methanol and redispersed in toluene. They are then stored in a freezer at -20°C to avoid any sintering of the particles and are stable for months. The crucial parameters to control the nanocrystal size in this process are the reaction temperature and time. The particle size increases with the rise in temperature or reaction time. Figure 6b presents an image of HgTe with a cut-off at 2 µm, captured with transmission electron microscopy. The nanoparticles are branched rather than spherical. Shen *et al.*[32] proposed to replace the TOP:Te chalcogenide precursor by a more reactive one which is bis-trimethylsilyl-telluride $(TMS)_2Te$ to obtain spherical HgTe NCs. A synthetic route *via* a seeded growth method was also demonstrated by Prado *et al.*[33] to obtain a spherical form.

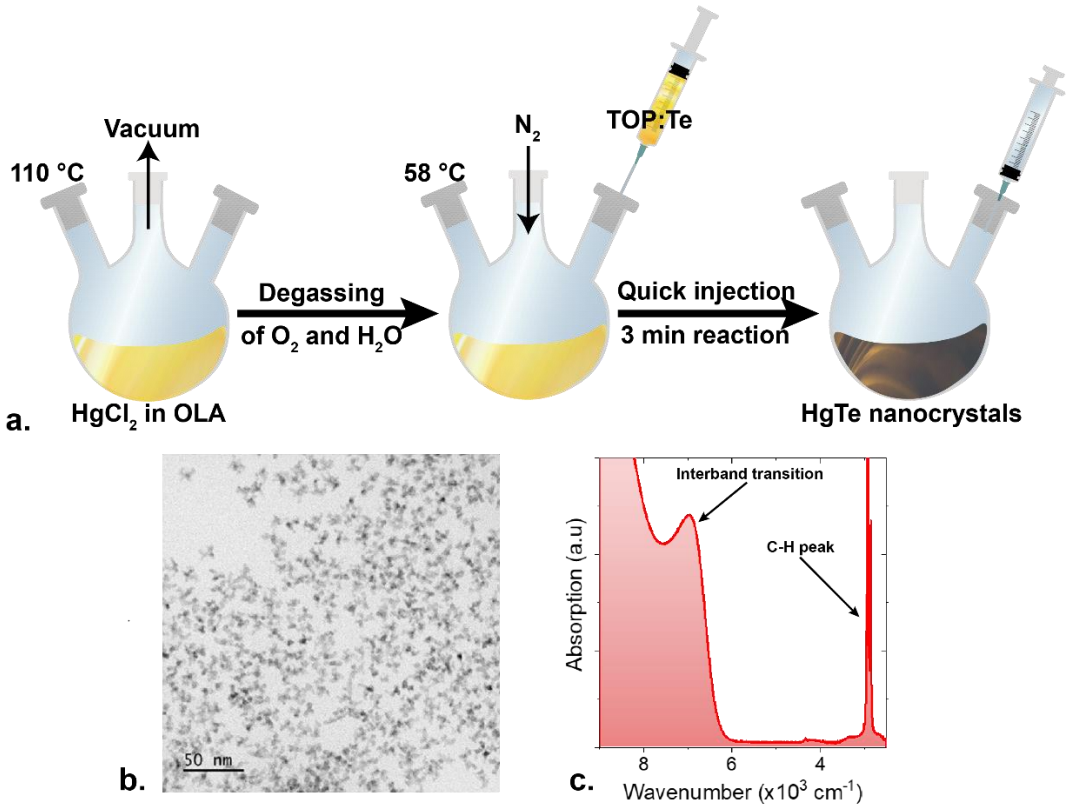

Figure 6 HgTe colloidal quantum dot synthesis. a. Scheme illustrating the main steps to synthetize HgTe nanocrystals. b. Transmission electronic microscopy image of HgTe nanocrystals. c. Absorption spectrum of HgTe nanocrystal with a cut-off wavelength at 1.7 µm.

Interband transitions in HgTe nanocrystals

The bandgap of HgTe nanocrystals is determined by the interband optical transition between $1S_h$ and $1S_e$ levels (as depicted in Figure 7a) and is exclusively controlled by quantum confinement. Thus, tuning the nanocrystal size allows to cover the whole infrared spectrum. Optical spectra of various sizes of HgTe NCs are presented in Figure 7b. The smallest particles, which are a few nanometers in diameter, exhibit an excitonic peak at 9000 cm^{-1} (1.1 µm, 1.1 eV), while increasing the size up to 20 nm shifts the peak to the mid-infrared at 2000 cm^{-1} (5 µm, 0.25 eV). Furthermore, these spectra display well-defined band-edges (a flat baseline above the excitonic peak, and a sharp transition at the cut-off), which signifies a controlled size dispersion of <10%. The presence of C-H bonds due to the organic ligands (DDT) covering the nanocrystals can be inferred from a fine and intense peak at around 2900 cm^{-1}, as shown in Figure 6c.

During the 2010s, a number of research groups from various regions of the world, including Europe[34,35], Asia[36,37], and the United States[38,39], were able to successfully integrate HgTe nanocrystals into photoconductive devices. And in the decade since, HgTe NC-based devices have achieved state-of-the-art performance with integration into more complex structures such as photodiodes[40–43] and focal plane arrays.[44–47] Despite the presence of numerous non-radiative decay paths in the infrared that lead to low photoluminescence quantum yield, HgTe NCs also feature interband emission.[20,48]

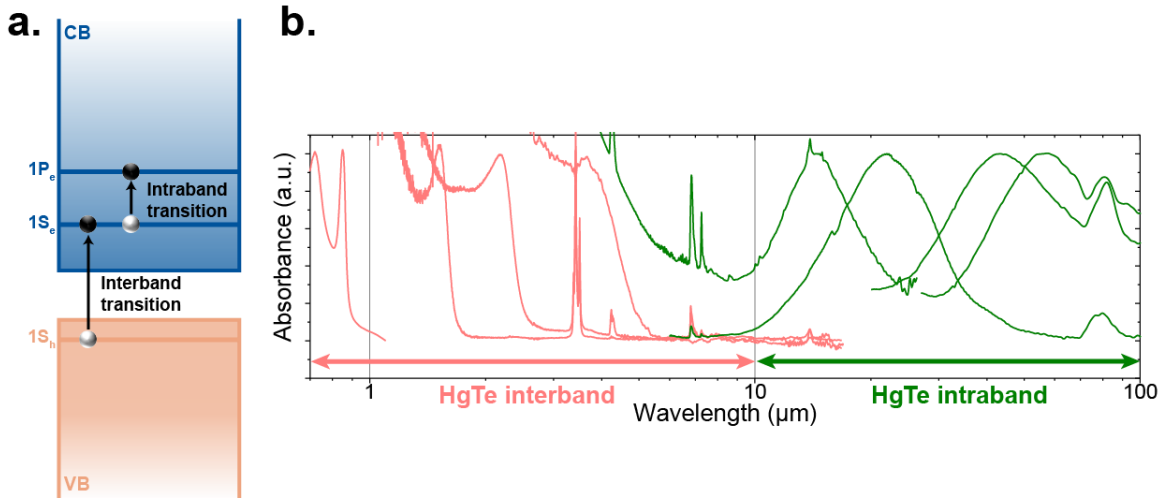

Figure 7 Addressing the entire infrared spectrum with mercury chalcogenide nanocrystals. a. Scheme of available optical transitions in a self-doped nanocrystal. b. Absorption spectra over the whole infrared range for undoped and doped HgTe nanocrystals. Adapted from ref.[49]

Intraband transition in self-doped nanocrystals

Despite the potential to achieve any desired bandgap energy with HgTe, there are numerous challenges that hinder further progress beyond the mid-infrared range. One significant obstacle is the difficulty of obtaining large, colloidally stable HgTe nanocrystals that do not aggregate. Consequently, like their epitaxially grown counterparts (QWIP, T2SL), one may consider intraband transitions in the upper levels of the conduction band. In HgTe and HgSe mercury chalcogenides nanocrystals, intraband absorption is dependent on electronic transitions between the first levels of the conduction band ($1S_e$ to $1P_e$) and only occurs when the system is doped so that the ground level of the conduction band is filled with electrons. The first demonstrations of intraband absorption in nanocrystals were achieved by heavily doping them using electrochemistry[50,51] or by pumping them to strong optical excitation.[52,53] In 2014, the Guyot-Sionnest group succeeded in synthesizing self-doped HgS[54] and HgSe[55] nanocrystals that could achieve intraband photodetection in the MWIR. The doping in these nanocrystals resulted from the surface composition and the nature of the ligand used.[54,56] Later, in 2016, Lhuillier *et al*.[57] refined the synthesis and achieved intraband absorption up to 20 µm with HgSe NCs. Finally, intraband absorption in HgTe was achieved through high-temperature (> 120°C) synthesis, in which the authors achieved absorption up to the THz range (100 µm) with large and unconfined HgTe NCs.

Mercury chalcogenides nanocrystals such as HgTe and HgSe, are viable building blocks for infrared photodetection. Rather than adjusting material properties through complex methods as alloying, by tailoring the NC size, the whole infrared spectrum from 1 to 100 µm can be addressed (see Figure 7b).

1.2-3 Transport in a nanocrystal array

An infrared photodetector serves as an optical transducer, relying on its capacity to absorb infrared photons and convert them into an electrical signal. As previously detailed, the former capability is crucial, while the latter depends on the ability to conduct charges in an array of independent nanocrystals. This aptitude is the initial step towards fabricating an infrared sensor, and in this section, we will discuss the transport properties of nanocrystals.

Hopping transport

At the end of the colloidal synthesis, the nanocrystals are composed of an inorganic core surrounding by an organic layer. Although, these ligands are critical to ensure colloidal stability, controlled size dispersion and surface passivation, they are long and insulating

organic chains (12 to 18 carbons). This “organic shell” effectively separates one nanocrystal from the next by several nanometers (2 nm) and behaves as a tunnel barrier, leading to a hopping mechanism for transport in a nanocrystal array.

In the situation where a potential difference is applied across an array of randomly distributed nanocrystals positioned between two electrodes (source and drain), a charge must hop between nanocrystals to cross the tunnel barrier induced by the organic ligands in order to be transported from one electrode to the other. The carrier mobility is primarily determined by this tunnel barrier, which is represented by the barrier coefficient of transmission:[58]

$$\mathcal{T} = \mathrm{e}^{-2l\sqrt{\frac{2m^*V_B}{\hbar^2}}} = e^{-\beta l}$$

Where β is the attenuation of the wavefunction probability in the barrier with length l and height V_B. m^* is the carrier effective mass. Then, using Einstein’s relation between carrier mobility μ and diffusion in three dimensions gives:

$$\mu = \frac{ed^2}{6\tau_{hop}k_BT}$$

With d the hopping distance corresponding to the nanocrystal size, k_BT the thermal energy, and τ_{hop}^{-1} the effective hopping rate. If the hopping follows an exponential decay, then the hopping rate can be rewritten in function of the barrier transmission coefficient as:

$$\tau_{hop}^{-1} = \frac{2E_a}{h}\mathcal{T}e^{-\frac{E_a}{k_BT}}$$

Where E_a is the activation energy of the hopping process depending on the tunnel barrier energy. Finally, the mobility in three dimensions for one conductance channel can be expressed as:

$$\mu = \frac{ed^2E_a}{3hk_BT}e^{-\beta l-\frac{E_a}{k_BT}}$$

From this expression, we can observe that the carrier mobility depends exponentially on the barrier height and length. Those two parameters are thus crucial for the design of infrared sensors. In a typical photodetector, to go from one electrode to the other, the carrier will have to hop through ten to a few thousands tunnel barriers.

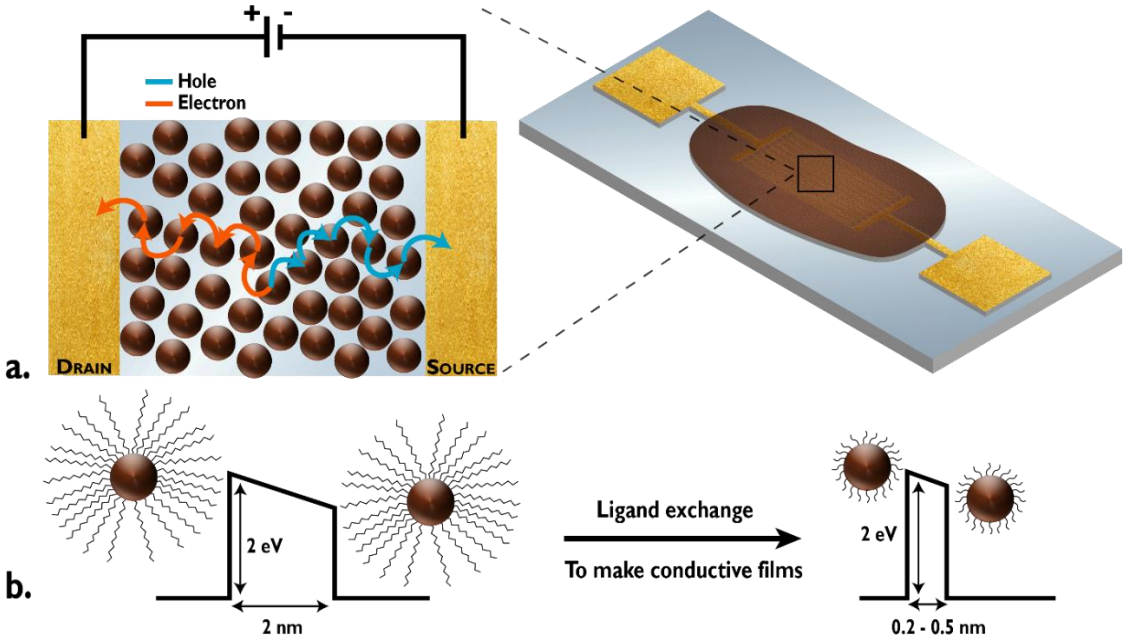

Figure 8 Hopping transport in a nanocrystal array. a. Scheme of a nanocrystal film deposited between two gold electrodes (drain and source) with the hopping of carriers. b. Principle of a ligand exchange procedure, where the long capping organic ligands (DDT) are replaced by short ligands (MPOH).

Controlling the tunnel barrier *via* ligand exchange

As outlined in the previous section, an array of nanocrystals with long organic ligands demonstrates low carrier mobility, rendering it non-conductive. Initially, the solution to enhance conduction was to strip off[59] the organic layer surrounding the nanocrystals, leading to close packing of the particles and improved conduction. However, stripping the organic ligands also prevented their function in passivating surface defects, causing a negative impact on transport properties. Instead of removing the long organic ligands, a ligand exchange method was developed wherein they were substituted with shorter ligands,[60,61] allowing for efficient surface passivation. Currently, the ligand exchange process can be accomplished through two methods: in a solid-state or liquid-phase (ink).

The solid-state ligand exchange process involves the direct treatment of a thin film deposited on a substrate by spin-coating, drop-casting, or dip-coating. The substrate is immersed in a solution of short ligands (such as ethanedithiol, EDT) that are present in excess to replace the long ligands. The solvent is chosen to dissolve the short ligands without affecting the nanocrystal film. The exchange process is completed in a few tens of seconds, after which the substrate is rinsed to remove the free ligands. The effectiveness of the exchange is confirmed by a drop in film resistance and a significant decrease in C-H bond amplitude on the absorption spectrum. However, this procedure is limited to thin films (20-30 nm) as ligand diffusion is not efficient in thicker films. Also, there is a contraction in the film resulting in cracks as the nanocrystals get closer. These issues can be partly resolved by repeating the procedure multiple times to fill the cracks and create thicker films.

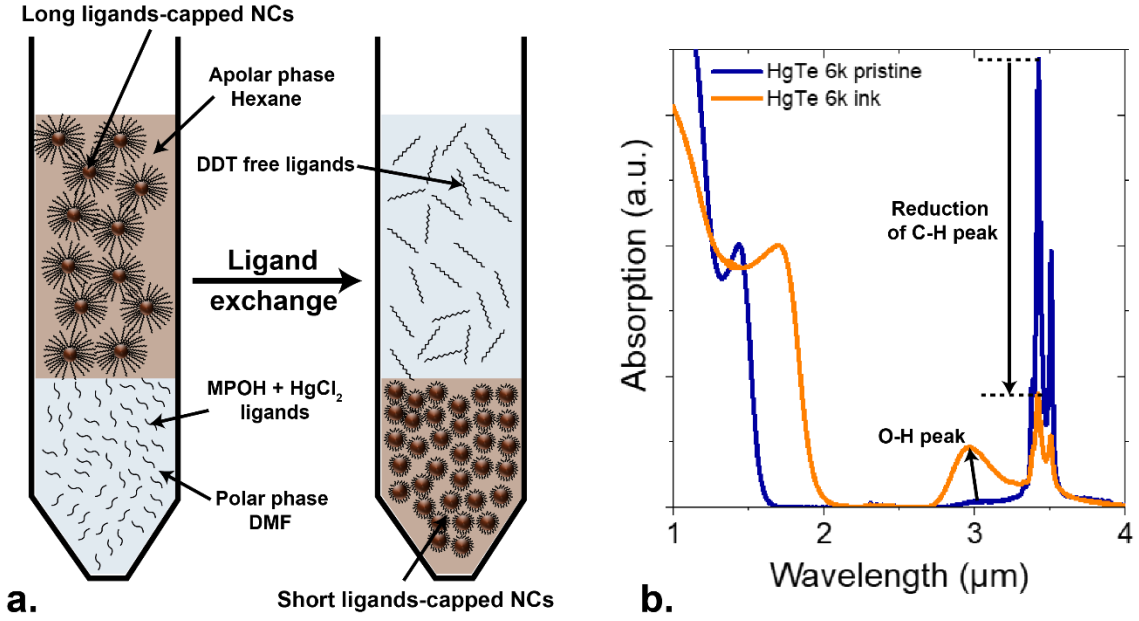

Figure 9 Controlling the tunnel barrier in colloidal nanocrystals. a. Scheme of a liquid-phase ligand exchange procedure. b. Absorption spectrum of HgTe nanocrystals after a ligand exchange process (ink). The O-H peak indicates the presence of MPOH ligands. The reduction of the C-H peak confirms the efficiency of the ligand exchange.

The alternative strategy initially employed shorter ligands with small ions, such as sulfide S^{2-}, halides Cl^-, I^-, Br^-, or hydroxide OH^-.[62,63] This approach reduces the length of the tunnel barrier and lowers its height compared to the carbon chain due to the small size of the ions. As these ions are only soluble in polar solvents, a liquid-phase exchange procedure was

developed. The nanocrystals in their apolar solvent, such as toluene or hexane, are added to a tube containing a solution of short ligands in a polar solvent, typically dimethylformamide (DMF). Upon agitation, both phases come into contact and the ligand exchange takes place. The nanocrystals are capped with ions, which stabilizes them in the polar solvent. The apolar phase, containing the long free ligands, can then be removed, resulting in a final solution called ink that can be deposited on electrodes. The liquid-phase ligand exchange method is more efficient than the solid-state process and can produce a high-quality (homogenous and without cracks) film with a thickness range of 20 to 600 nm in a single step by adjusting the ink concentration and to a small extent the spin-coating speed parameters. With this approach, high carrier mobilities up to 1 $cm^2.V^{-1}.s^{-1}$ have been achieved,[64,65] whereas they were only in the range of 10^{-4} - 10^{-2} $cm^2.V^{-1}.s^{-1}$ for the solid-state process[66].

Investigating the interparticle coupling with field-effect transistors

The advancement in conductive NC films raised the need for the investigation of the electronic coupling among nanocrystals. Although absorption spectra provide information about the bandgap energy, it is unable to reveal the carriers nature and mobility. In the context of bulk semiconductors, Hall effect measurements are typically used to extract the carrier mobilities. However, such measurements are challenging to apply to nanocrystal films because their mobilities are significantly lower than those of bulk semiconductors leading to very small Hall bias. Consequently, the nanocrystal community prefers to use a Field-Effect Transistor (FET) geometry to investigate the coupling between nanoparticles.

Field-effect transistors are electronic devices that control the flow of current through a channel by applying an electric field to a gate electrode. In this device, a film of nanocrystals is deposited between two terminals called source and drain. When a voltage V_{DS} is applied to this channel, a current I_{DS} flows through it. A gate electrode, typically made of strongly doped silicon (Si), is placed close to the channel, separated from it by a thin insulating layer typically made of silica (SiO_2). This can be seen as a capacitor that allows for the modulation of the carrier density in the nanocrystal channel by injecting charge carriers in the latter. When a voltage is applied to the gate, there is a charge accumulation at the capacitor surface in contact with the nanocrystal film. Therefore, to ensure the system neutrality, charges with an opposite sign will be injected in the channel. As a result, the energy bands of the semiconductor will bend enabling a control over the Fermi level in the bandgap. As a positive voltage (resp. negative bias) is applied between the gate and source electrodes, the conduction band (resp. valence band) bends toward the Fermi level resulting in an electron injection (resp. hole). In order to determine the nature of the majority carrier, the evolution of the channel current I_{DS} as a function of the gate bias, named transfer curve, is followed. A material is *n-type* (resp. *p-type*) as the conduction increases under electron (resp. hole) injection, revealing that the electrons (resp. holes) are the majority carriers. If the material conduction increases under both carrier injection, then it is considered as *ambipolar*. Considering a channel of length L and width W, under a bias V_{DS}, the carrier mobility μ can be expressed as:

$$\mu = \frac{1}{CV_{DS}} \frac{L}{W} \frac{\partial I_{DS}}{\partial V_{GS}}\Big|_{V_{DS}}$$

Where C is the gate capacitance, and $\partial I_{DS}/\partial V_{GS}$ is the slope of the transfer curve in the region of interest. In a conventional back-gated FET, the low capacitance of the Si/SiO_2 gate (10 $nF.cm^{-2}$ for a thickness of 400 nm) prevents efficient charge injection in the nanocrystal film. Hence, the electric field required to inject electrons into the material can exceed the dielectric breakdown of the SiO_2. Additionally, because the gate effect is confined to the interface between the capacitor and the NC film, carrier density modulation only occurs within the first tens of nanometers of the film thickness.[67]

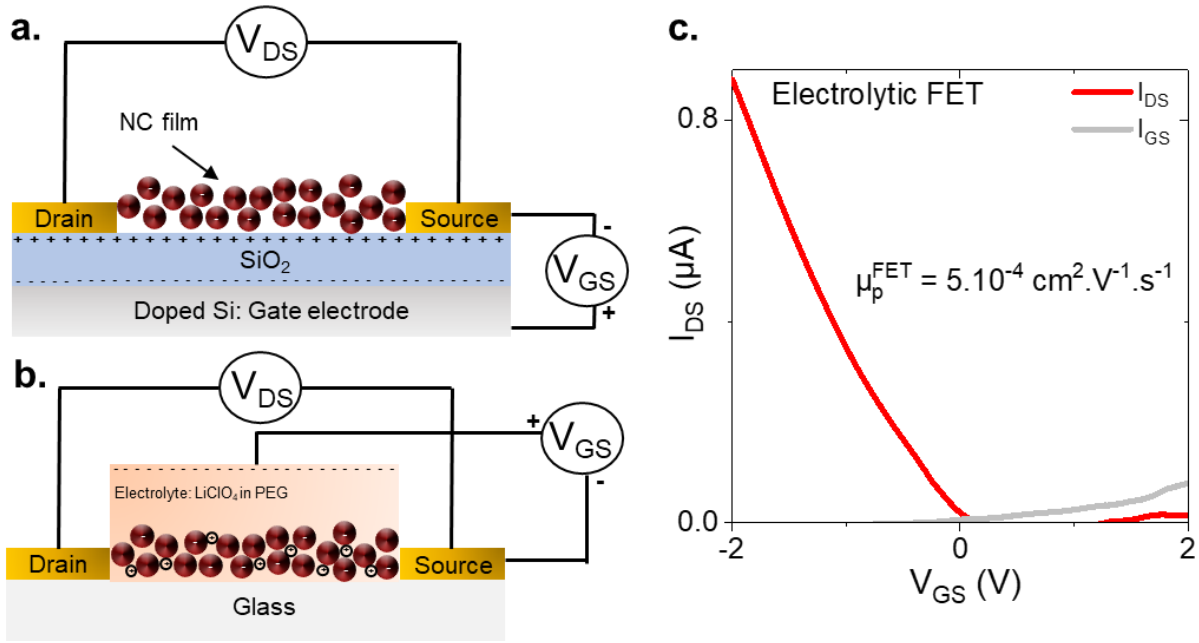

Figure 10 Field-effect transistors to probe the coupling between nanocrystals. a. Conventional Si/SiO_2 back-gated FET. b. Electrolytic top-gated FET with lithium perchlorate in PEG as electrolyte. c. Transfer curve with an electrolytic FET of HgTe nanocrystals with a 2 µm cut-off wavelength.

To address these difficulties, an alternative method was developed, which employs an electrolyte as a gate dielectric instead of a solid-state material. This strategy is a simple air operable method in order to achieve high capacitance gating. In this approach, a lithium perchlorate ion ($LiClO_4$) electrolyte embedded in a polyethylene glycol (PEG) matrix is deposited on the nanocrystal film. When a voltage is applied to the gate electrode, the ions in the electrolyte solution are attracted ($V_{DS} > 0$) or repelled ($V_{DS} < 0$) toward the surface of the nanocrystal film, allowing for modulation of their carrier density. This configuration greatly increases the gate capacitance, to approximately 1 µF.cm^{-2}, due to the ion size. As a result, an electrolytic top-gated FET can be performed at room temperature and under a smaller gate bias than a back-gated FET (< 3 V). Moreover, this method is not limited in thickness and can be applied to the gating of thick NC films. Nonetheless, this approach has a few drawbacks (i) ions must diffuse in the PEG matrix requiring a slow scanning speed of around 1 mV.s^{-1} (ii) the operating temperature should be high enough (> 280K) to avoid freezing of the matrix as well as the displacement, and (iii) applied voltages must be restricted to the electrochemical stability window (-3 V – 3 V typically) to prevent any electrochemical reactions within the electrolyte. Despite these limitations, the electrolytic FET is a valuable tool to investigate the carrier density in nanocrystal films. Its high capacitance enables the assessment of both wide and narrow energy bandgap nanocrystals. As a result, the electrolytic transistor is routinely used in the group to characterize new colloidal materials.

1.3- From nanocrystals to an optoelectronic device

In the previous section, we understood the reason why HgX NCs emerged as an appealing candidate for infrared detection with their wide bandgap tunability over the electromagnetic spectrum. We discussed their cost-efficient growth through colloidal synthesis, as well as their surface chemistry modification making them compatible with electronic transport. Here, we will discuss one of the current challenges in the community, which is the integration of nanocrystals into infrared detectors where they are electrically and optically active.

1.3-1 Type of photodetectors

As stated earlier, infrared photodetectors are optical transducers that absorb infrared radiation and convert it into an electrical signal. They can be classified along with their geometry in two types: photoconductive and photovoltaic detectors. In the following, we will explain both structure properties and their advantages.

1.3-1.1 Photoconductor

The history of photoconductors can be traced back to the discovery of the photoelectric effect by Heinrich Hertz in 1887. He observed that shining an ultraviolet light on electrodes caused a change in the voltage between them. In 1902, Philipp Lenard, who was Hertz assistant, demonstrated that illuminating a metal surface liberated electrically charged particles that he called *quanta of electricity*, which eventually became *electrons* in the everyday term.[68] The first photoconductors were made using metals such as selenium, which exhibited changes in electrical conductivity when exposed to light. In the mid-1900s, the use of semiconductor materials such as silicon and germanium revolutionized the field of photoconductors.[69] These materials were found to exhibit much stronger changes in conductivity when exposed to light than the earlier metal-based photoconductors. In these devices, a thin film of semiconductor material (typically < 1 µm) is deposited between two electrodes in a planar geometry. When exposed to light, the detector absorbs photons, creating electrons and holes, which are then collected by the electrodes under an applied electric field. This results in an increase of the photodetector electrical conductivity, named photocurrent. The current-voltage (I-V) characteristic of a photoconductor based on HgTe NCs is depicted in Figure 11b, it follows and Ohmic law and is linear.

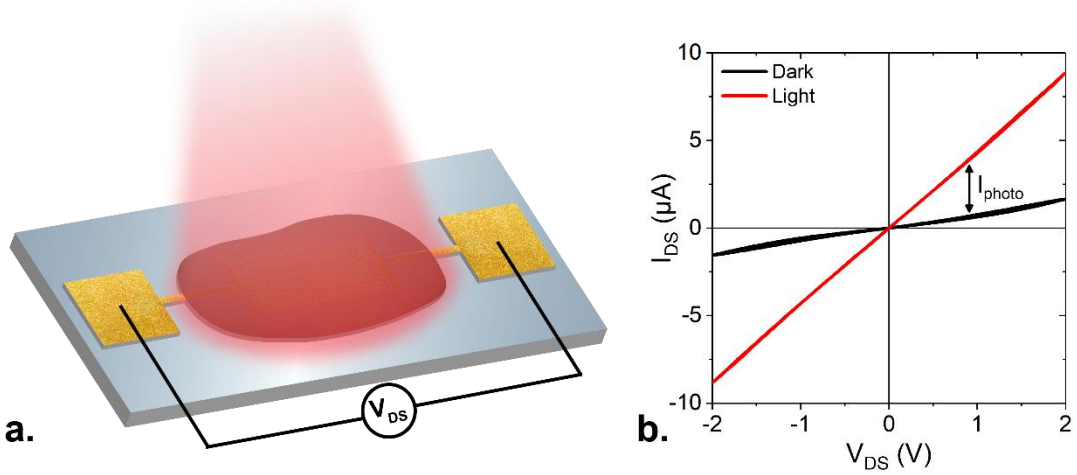

Figure 11 Infrared detection in a photoconductor geometry. a. Scheme of a nanocrystal film deposited on a photoconductor with interdigitated electrodes. b. I-V characteristics of a typical HgTe NC film under dark and illumination with a 1.55 µm laser diode.

The photoconductor geometry offers the advantage of a simple fabrication process and a strong tolerance toward defects in a thin film such as pinholes and thickness variations. As such, it was the first geometry developed for nanocrystal-based photodetectors. The interdigitated electrodes configuration represents the most popular design in photoconductive devices[38,70,71] because it acts as a current amplifier in a first place. Then electrical gain[72–75] is possible in such geometry. This phenomenon occurs when one carrier has a higher mobility than the other. In such cases, the former reaches the electrode before the latter and is subsequently reinjected in the channel to preserve charge neutrality. Hence, the absorption of one photon can contribute to the photocurrent multiple times. However, the electrical gain increases carrier lifetime, resulting in reduced detector bandwidth. Therefore, depending on the intended application, a gain/bandwidth product trade-off must be considered during photoconductor design.

The major limitation for nanocrystal-based photoconductors is their limited signal-to-noise ratio. One significant reason is inherent to the planar geometry, where the electrode spacing is much larger (µm scale) than the intrinsic short carrier diffusion length in nanocrystals (10 – 200 nm). Therefore, most of the photogenerated carriers recombine or get trapped, leading to a weak collection efficiency and a weak signal-to-noise ratio. Recently, Chu *et al.*[76] demonstrated an HgTe nanocrystal-based photoconductor with an electrode spacing (< 100 nm) corresponding to the diffusion length. The authors achieved state-of-the-art performances (detectivity of 10^{12} Jones and MHz bandwidth) comparable to those of photovoltaic detectors. However, the complex fabrication of such photoconductor hinders its transfer into a large array of pixels. The second reason explaining a weak signal-to-noise ratio in photoconductors relates to the dark current which is proportional to the noise. Although the interdigitated configuration allows for a reduced electrode spacing and for an electrical gain, it also amplifies the dark current and thereby the noise in the system. One path to address this signal-to-noise issue is to introduced a light-matter coupling management strategy (*i.e.*, light resonator) in the system. In the course of my thesis, I investigated such strategies, which will be discussed later in the manuscript.

A phototransistor is a unique type of photoconductor that incorporates a field-effect transistor in its structure. By doing so, the material's carrier density can be finely controlled, which significantly enhances the detector's responsivity. This is achieved by applying a gate voltage, which essentially transforms the device into a switch with a predetermined threshold, capable of suppressing or amplifying the photocurrent. This attribute makes phototransistors highly desirable for applications that require distinct ON and OFF states.

The phototransistor geometry has been applied to colloidal nanocrystals, particularly HgTe[77–79] and PbS[80]. While this setup can enhance the photoresponse, the dark current behaves similarly and reaches a maximum at the point where the photocurrent is at a maximum. Therefore, the gain in signal-to-noise ratio is modest. The gate is used more as a tool to tailor the doping in nanocrystals, which is challenging to control during synthesis. An optimized operating point can then be determined to maximize phototransistor sensitivity. Additionally, the time-response of phototransistors decreases as the photocurrent increases, leading to reduced device bandwidths. Finally, a current challenge in phototransistors concerns film thickness. In such an architecture, the gating effect only takes place in the proximity of the NC film, typically the first 70 nm.[67] Consequently, the incident light is not absorbed effectively, limiting the device's photoresponse.

1.3-1.2 Photodiode

In 1839, the French physicist Edmond Becquerel discovered the photovoltaic effect.[81,82] In his experiment, he used silver chloride or silver bromide to coat platinum electrodes. He observed that once the electrodes were exposed to light, voltage and current were generated and thereby created the world's first solar cell. However, it was not until a century after, in 1954, that Bell Laboratories scientists D. Chapyl, C. Fuller, and G. Pearson invented the first silicon photovoltaic cell.[83] They grew a µm-thick layer of *p-doped* silicon over a *n-type* substrate and measured a 6% conversion efficiency, which was an order of magnitude higher than the commercial photocells at the time. Unlike the planar geometry of photoconductors, photodiodes rely on vertical stacking of materials and are not symmetrical. Hence, upon absorption of light, the generated electron-hole pairs are separated by the device internal electric field, leading to a current flow. This is reflected in the typical I-V characteristics of a photodiode, where dark conditions and the absence of an applied electric field result in close-to-zero current and voltage measurements, while exposure to light generates measurable short-circuit current I_{SC} and open-circuit voltage V_{OC}, as shown in Figure 12b.

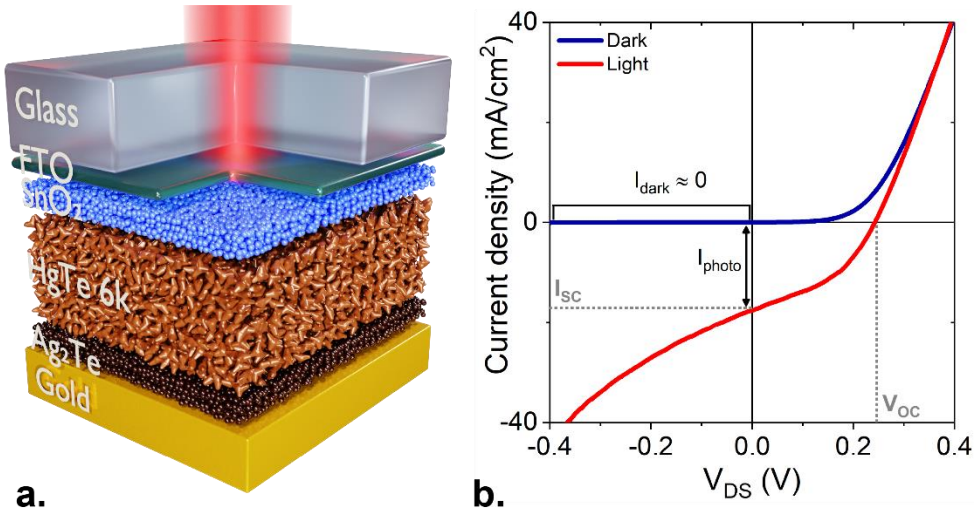

Figure 12 HgTe nanocrystal-based photodiode. a. Scheme of the photodiode structure. Adapted from ref.[42] *b. I-V characteristics under dark conditions and exposed to a 1.55 µm laser diode.*

In the previous part, we have seen that the photoconductor geometry exhibits a modest signal-to-noise ratio. In contrast, the photovoltaic configuration can operate at 0 V, which significantly reduces the dark current and hence, the noise. Nowadays, most high-performance photodetectors in the global market are based on photodiodes. However, the fabrication of photodiodes is more complex. The nanocrystal film must be of high quality without pinholes that could lead to short-circuits upon depositing the top metallic contact. Moreover, one of the electrodes must be transparent in the targeted spectral range. For example, thin layers (< 100 nm) of conductive oxides such as ITO (tin-doped indium oxide) and FTO (fluorine-doped tin oxide) inherited from the Liquid Crystal Display community are commonly used up to the SWIR. However, in the MWIR, these materials absorb most of the light, and alternative strategies have to be considered. Recently, Dang *et al*.[84] demonstrated that a metallic grid acting both as an electrode and a light resonator could efficiently replace traditional conductive oxides. Lastly, the band alignment between the different materials in a photodiode must be carefully designed to facilitate carrier collection and induce an internal electric field. To determine the material band alignment, X-ray photoemission[85–87] and electrochemistry[88] experiments are commonly used in the nanocrystal community.

In the early 2000s, the first photodiodes based on PbS nanocrystals were developed to harvest the NIR tail of the solar spectrum. Later, to access the SWIR and MWIR, photodiodes based on HgTe NCs were developed. The first high-performance HgTe NCs-based photovoltaic detector was demonstrated by Ackermann *et al.*[40] with a vertical stacking of ITO/HgTe/Ag_2Te/Au. ITO serves as the transparent conductive electrode and collects electrons. HgTe is the MWIR absorbing material with *n-type* character for promoting electron conduction. Ag_2Te with its *p-type* character favors hole extraction, leading to decreased dark current. A gold electrode is deposited on top to collect holes. The *p-n* junction in this vertical stacking leads to a significant increase in signal-to-noise ratio compared to the photoconductive mode. The authors demonstrated a detectivity of 10^9 Jones at 230K with a 5 µm cut-off wavelength. Today, most infrared photodiode based on HgTe rely on this HgTe/Ag_2Te interface.

1.3-2 Figure of merits for IR detection

We have seen that infrared photodetectors could be built based on a wide range of materials and geometries. To accurately assess and compare their performance, the infrared sensing community uses a distinct set of figures of merit pertinent to the infrared range. In this context, we will elaborate on the IR figure of merits, along with the experiment set-up used at the laboratory to measure them.

Spectral response

Infrared photodetectors are designed based on the specific spectral range required for the intended application, such as SWIR or MWIR. Fourier-transform spectroscopy (FTIR) is commonly used to measure absorption or transmission in the infrared and can be utilized to spectrally resolve the detector response. A typical set-up used during my thesis is shown in Figure 13. The FTIR light source illuminates the device, and the resulting output current is amplified using a low noise transimpedance amplifier. This signal is then processed by the FTIR electronic to perform a Fourier transform. The resulting signal is a product between the spectral response of the light source and the photodetector. The former can be measured using a flat-response DTGS (deuterated triglycine sulfate) detector that is integrated into the FTIR. Therefore, by dividing the light source spectra to the one obtained, the detector spectral response can be extracted.

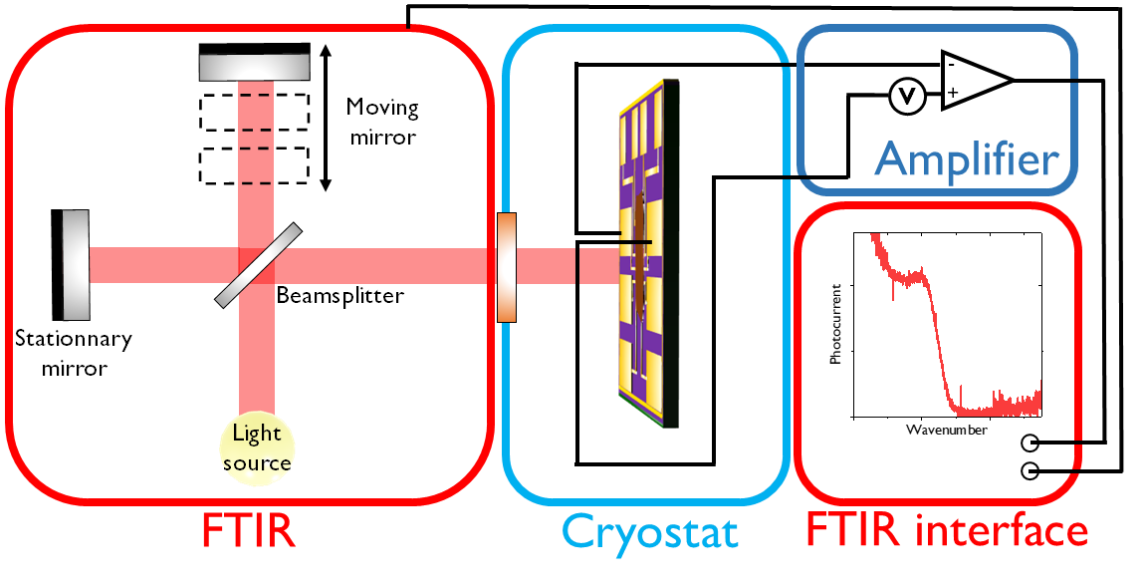

Figure 13 Experiment setup used to measure a photodetector spectral response.

Responsivity

A photodetector transduces a photon flux into an electrical signal. The responsivity R is a direct measure of the optical-to-electrical conversion efficiency. Considering, an incident optical power P_{opt} and a device photocurrent $I_{photo} = I_{illu} - I_{dark}$, the responsivity can be written as:

$$R = \frac{I_{photo}}{P_{opt}}$$

With R expressed in $A.W^{-1}$. From this equation, we can retrieve another figure of merit, which is the quantum efficiency. It is a measurement of incident photon to converted electron ratio. At a wavelength λ, it can be written as:

$$EQE = \frac{R}{\lambda}\frac{hc}{e} \approx \frac{R}{\lambda} \times (1240\ W.nm.A^{-1})$$

Where EQE is the external quantum efficiency, h is the Planck constant, c is the speed of light and e is the elementary charge. Hence, for SWIR detectors, 100% of EQE at 2 µm correspond to a responsivity of approximately $2.5\ A.W^{-1}$. Experimentally, the photodetector is illuminated with a pulsed light source, which can be either monochromatic, typically a 1.55 µm laser diode, or polychromatic, typically a blackbody for infrared. The acquired signal is processed using a lock-in amplifier, which multiplies the input signal with the reference signal,

obtained by modulating the light frequency, and integrates it over time. The resulting DC component corresponds to the detector responsivity at the reference signal frequency. The responsivity is commonly measured using a blackbody due to its broadband emission in the infrared and its small output powers that are representative of real detection conditions. The blackbody incident power can be determined analytically using the following formula:

$$P(W) = A_D.\pi.cos(\beta).sin^2(\alpha).\int_{\lambda_{min}}^{\lambda_{max}} \frac{2hc^2}{\lambda^5}.\frac{1}{e^{hc/\lambda k_B T}-1}d\lambda$$

With α the half solid angle illuminated, β the incident light angle, A_D the device area, and T the temperature. The responsivity of nanocrystal-based photodetectors highly depends on the incident photon flux. Generally, the responsivity increases as the photon flux decreases.

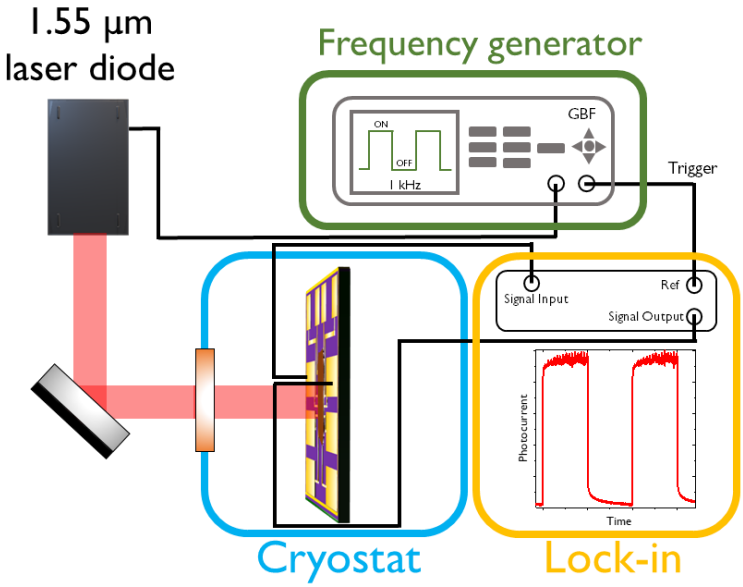

Figure 14 Experimental setup used to determine a photodetector responsivity.

Noise

Infrared photodetectors rely on narrow bandgap semiconductors which energies are in the order of the thermal activation $k_B T$ (25 meV at room temperature). Hence, compared with visible photodetectors, carriers are thermally activated resulting in weaker signal-to-noise ratios. The noise is directly proportional of these carriers, and can be induced by three main sources:

- The thermal noise or Johnson noise, relates to the mobility fluctuation of carriers due to the thermal agitation. Assuming a device of resistance R_0, operating in an electrical bandwidth Δv at a temperature T, the thermal is written as:

$$i_{th}^2 = \frac{4k_B T}{R_0}\Delta v$$

- The shot noise or generation-recombination noise, relates to random carrier density fluctuations due to the current flowing in the device. Considering a photoconductor operated at an electrical bandwidth Δv with a dark current I_{dark} and a gain g, the shot noise is expressed as:

$$i_{GR}^2 = 2egI_{dark}$$

- These two contributions are referred as *white noises* because they are independent from the frequency. A perfect photodetector would have his performances limited by these two sources of noise. However, in practice, nanocrystals-based devices are neither limited by thermal nor shot noises. The main contribution is a Flicker noise characterized a $1/f$ power spectral density.[38,89] Analytical determination of this noise is not possible, and it needs to be measured experimentally for each device. For conductors with a $1/f$ power law, Hooge[90] proposed an empirical expression:

$$i_{1/f}^2 = \frac{\alpha I^2}{Nf}$$

Where N is the number of carriers in the conductor, I is the current, f is the frequency, and α which was initially introduced a constant because metallic films displayed comparable values ($\alpha \sim 10^{-3}$). However, nanocrystal films showed very different values from one another. In this system, α is independent from the nature of the material and the particle size,[89] and is rather affected by the film quality and the interparticle coupling. As the coupling increases, α is reduced down toward its bulk value.

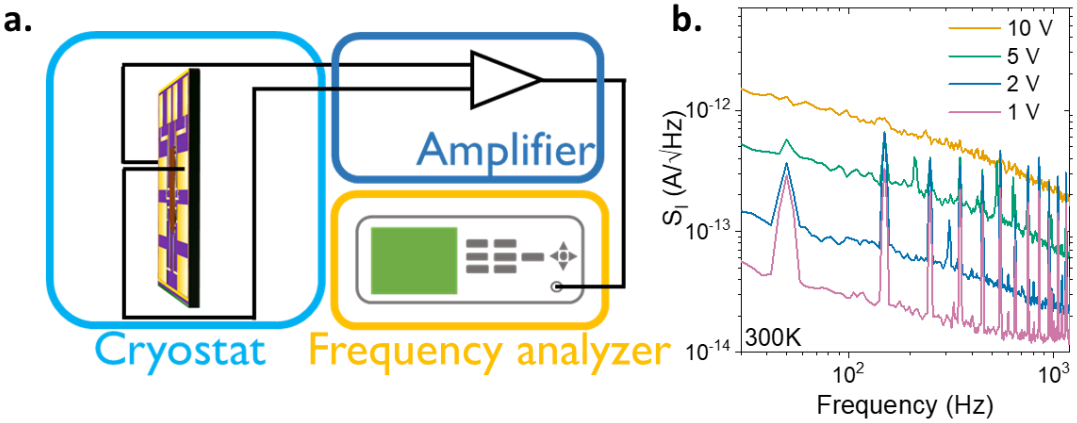

Figure 15 Noise current density determination. a. Scheme of the experimental setup used to measure noise. b. Measured noise current density for HgTe-based photodetector at 300 K.

Figure 15a illustrates a typical experimental setup utilized for assessing the noise characteristics of infrared photodetectors. It should be noted that the electrical bandwidth of the amplifier must be taken into consideration based on the frequency used to determine the noise current density value. Typically, this value is obtained at or below 1000 Hz, and therefore the amplifier bandwidth should exceed this frequency. In Figure 15b, the noise current density of an HgTe-based photoconductor is displayed at different voltages. The noise exhibits a 1/f dependence in this configuration, and when reducing the bias, the signal at 50 Hz, as well as its harmonics, significantly increases. At such low noise levels, typically in the range of a few fA.Hz$^{-1/2}$, the electrical environment surrounding (any objects connected to an electrical plug) the detector generates a parasitic 50 Hz signal. Consequently, the noise current density is determined based on the spectrum's baseline, which is clearly distinguishable in this case.

Noise equivalent power (NEP) and detectivity (D*)

The noise equivalent power (NEP) relates to a signal-to-noise ratio by measuring the minimal optical power that can be detected. Hence, the lower the NEP is, the more sensitive the detector will be. The NEP is typically measured over 1 Hz and can be written as:

$$NEP = \frac{S_I}{R}$$

Where the NEP is expressed in $W.Hz^{-1/2}$, S_I is the noise current density, and R is the responsivity. The detectivity D^* is considered the most crucial figure of merit for evaluating infrared photodetectors, as it normalizes the signal-to-noise ratio with respect to the sensor's area, thereby allowing for a fair comparison between detectors. The detectivity can be expressed as:

$$D^* = \frac{R}{S_I}\sqrt{A}$$

With D^* in $cm.Hz^{-1/2}.W^{-1}$ or Jones, and A the device's area. The detectivity is dependent on the frequency since the noise follows a 1/f power law. Consequently, one should select higher frequency values, provided they are within the electrical bandwidth of the system. The detectivity is consistently provided with the frequency used, the temperature, the applied voltage, and the device cut-off wavelength. Typically, the desired range of detectivity for infrared detection is on the order of 10^{11} Jones at room temperature for SWIR and 10^{11} Jones at 80 K for MWIR.

Time-response

The photodetector time-response relates to the time it takes for the sensor to respond to a change in the incident radiation. The experimental setup employed is comparable to that of the responsivity measurement and a high-speed pulsed (usually GHz) laser may be utilized. In addition to the high-speed source, it is necessary for the bandwidth of the entire electrical chain to match the laser bandwidth. Hence, the amplifier, oscilloscope, and photodiode used to trigger the laser must exhibits a GHz electrical bandwidth. Figure 16 depicts a typical experimental setup used to measure a photodetector time-response. The cut-off frequency (the frequency at which the responsivity is reduced by -3 dB) is determined by calculating the rise and decay times of the photocurrent. The time-response serves as a significant performance indicator for photodetectors, depending on the intended application. For instance, detectors with a GHz bandwidth are necessary for applications in remote sensing like LiDARs with targeted wavelengths at 940, 1064, or 1550 nm.

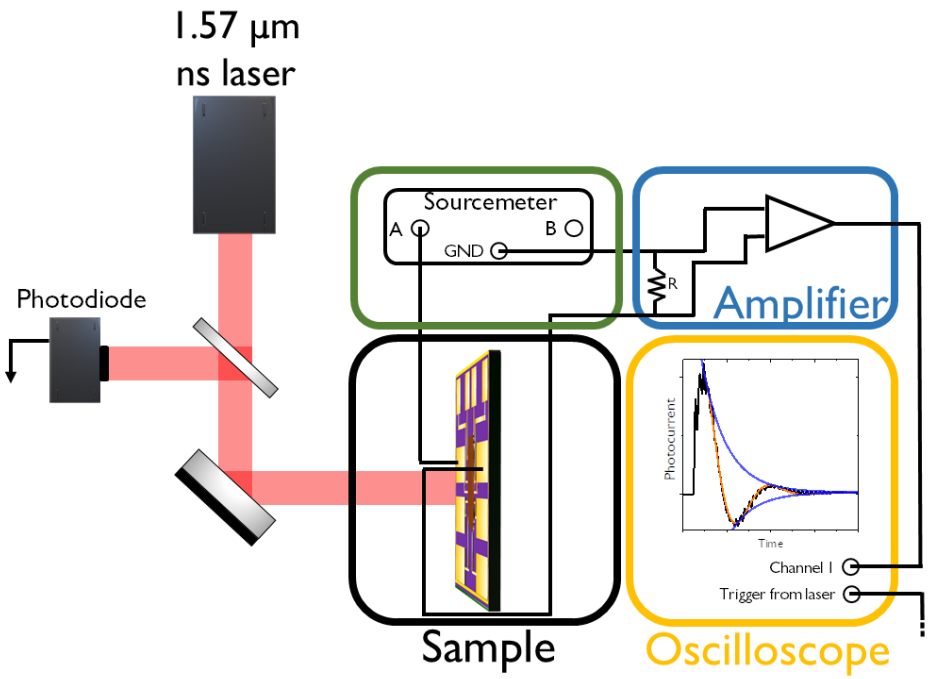

Figure 16 Experiment setup used to measure the time-response of a detector.

Operating temperature

Due to the narrow bandgap semiconductors involved in infrared photodetectors, the carriers are thermally activated, leading to a large dark current. To reduce this, one can lower the temperature of the system using various techniques such as Peltier cells or cryostat cooling. Most infrared sensors require cooling, and integrating such systems increases the overall cost, weight, and power consumption. Consequently, a pressing concern in the infrared community is to develop sensors with high operation temperatures (HOT) while maintaining high performance. Regarding SWIR sensing, the objective is to attain optimal performance at room temperature with a tenfold increase in performances at a temperature of 200 K. On the other hand, MWIR detection capabilities are currently confined to cryogenic operations within the temperature range of 80 to 150 K. In my thesis, I examined various strategies to increase the operation temperature of infrared photodetectors in the MWIR and the SWIR, which will be discussed further in the manuscript.

1.4- Advanced infrared technologies

Infrared technologies have found widespread applications across many fields, from aerospace and defense at the beginning, to biomedical imaging and machine vision systems nowadays. Infrared detection is a powerful tool that can reveal information about objects and materials that are invisible to the naked eye, allowing for non-destructive and non-invasive investigation. In this context, we have discussed the fundamental properties of mercury chalcogenides nanocrystals and their potential for infrared detection. In the following, we will examine different strategies to carefully design an infrared sensor for an efficient detection.

1.4-1 Wave-function engineering at the nanoscale

During the latter half of the 20th century, rapid progresses in the development of epitaxial growth techniques allowed for semiconductor structures to be grown with high accuracy, achieving atomic resolution. This progress enabled device structures to be dimensioned similar to relevant electron or wave functions in the growth direction,[6] allowing for electrical engineering at the quantum mechanical level. In 1970, IBM scientists, Esaki and Tsu[91] introduced the concept of a superlattice, which is a periodic structure composed of alternating monolayers of two different semiconductors. This paper was highly influential and led to the development of new types of infrared technologies based on superlattices, including QWIP[92], T2SL, or QCL[93] (quantum cascade laser). In these heterostructures, the thickness and composition of each monolayer could be precisely controlled to achieve a desired bandgap and electronic properties. Superlattices provided a new approach to engineer the electron and hole wave-functions at the atomic level. Depending on the band alignment between both semiconductors, the heterointerface can be classified into different groups. For instance, QWIPs features a type I heterostructure where both electron and hole are confined in the same quantum wells allowing for efficient transfer of photogenerated carriers from the QW into the adjacent barrier layers. In contrast, T2SLs have a type II structure where the electron and the hole are localized in different parts of the structure. This spatial separation of charge carriers leads to a strong built-in electric field which enhances the separation and collection of photogenerated carriers.

Similarly to the III-V semiconductor field, the development of heterostructures of colloidal nanocrystals arose from the necessity to achieve greater control over the optical and electrical properties, with a particular focus on enhancing the photoluminescence. A simple structure composed of a single population of nanocrystal results in optical properties that are primarily influenced by the size of the nanocrystal and to a lesser extent, its surface chemistry. However, the introduction of another colloidal material allows for the transition from bandgap engineering to wave-function engineering in nanocrystals. The most commonly employed type of heterostructures in nanocrystals is based on core-shell structures, which enables the realization of different types of band alignment through the careful selection of materials.

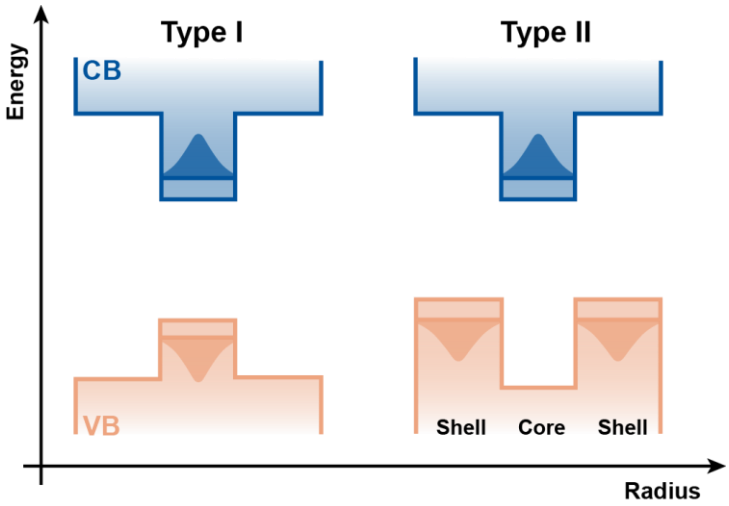

Figure 17 Classification of the core-shell heterostructures band alignment. In a type I configuration, electron and hole are confined within the core nanocrystal. While in a type II architecture, the electron is localized in the core, and the hole in the shell material.

In the 1990s, the group of P. Guyot-Sionnest[94] successfully capped CdSe nanocrystals with a shell composed of a larger bandgap ZnS semiconductor.[95] This type I configuration leads to a confinement of the carrier wave-function in the core, with the shell protecting the core material from oxidation and the exciton from trapping at the surface states. As a result, type I nanocrystal heterostructures are mostly utilized in applications that necessitate high photoluminescence quantum yield, and among them, CdSe/ZnS heterostructures are the most widely used. Their infrared counterparts are based on PbS/CdS,[96,97] HgSe/CdS,[98–100] or HgS/CdS[101]. However, type I heterostructures have certain limitations in their optoelectronic properties, restricting their integration into infrared detectors. To overcome this issue, type II core-shell heterostructures with improved optoelectronic properties have been developed. In this configuration, the spatial separation of electrons and holes leads to a significant increase in the exciton lifetime, which can reach several µs. Some examples of this type II heterostructures include PbSe/PbS,[102,103] CdS/ZnSe,[104] CdTe/CdSe[105].

Over the course of the past thirty years, significant developments have been made in colloidal synthesis, leading to the ability to grow core-shell heterostructures at the monolayer resolution and thereby enabling the engineering of wave-functions at the particle level. Recently, the concept of using a mixture of nanoparticles[106] with on-demand electronic spectrum has emerged for the design of solar cells,[107,108] light-emitting diodes,[109] and to tune the average doping magnitude in a nanocrystal array.[110] Through careful consideration of material size, proportion, and interdot coupling, the optical and electrical properties of the photodetector can be tailored, ultimately allowing for wave-functions engineering at the nanoscale (*i.e.*, at the device level). Additionally, recent advanced in the design of heterostructures for infrared detection have included the use of novel materials with mixed-dimensionalities, such as 2D materials like graphene,[77,80,111] transition metal dichalcogenides (TMDC),[35,112] or even bulk III-V semiconductor as InGaAs,[113,114] to further enhance the device performance. The main topic of my thesis is to explore the engineering of wave-functions at the nanoscale through the use of either Van der Waals heterostructures or mixture of nanocrystals, specifically for the design of infrared photodetectors. I will detail this topic in the second and third chapters of the manuscript.

1.4-2 Enhanced light-matter coupling

Light-matter coupling plays a crucial role in determining the efficiency of infrared photodetectors. This concept gained significant attention with the development of Quantum Well Infrared Photodetectors (QWIPs), which cannot be operated under normal incident light. However, illuminating the detector at an angle of 45° restricts detector geometries to single

elements and 1D arrays. To address this issue and further enhance device performance, light management strategies had to be incorporated into QWIP design. Initially, researchers at Siemens[115,116] and Bell[117] Laboratories developed a method to efficiently couple light in a 2D array by placing a metallic grating on top of the detector, deflecting the incoming light away from the normal direction to the surface. This grating provided low quantum efficiency (10-20%) as only one polarization of light is absorbed. To overcome this limitation, two-dimensional gratings were introduced for QWIPs operating in the 8-10 µm range,[118–120] allowing for the absorption of light in both polarizations and an increase in device performance. Lastly, a new detector structure known as the Corrugated Quantum Well Infrared Photodetector (c-QWIP) was proposed by scientists at the U.S. Army Research Laboratory to simplify array production.[121–123] The c-QWIP utilizes total internal reflection to couple normal incident light into the photodetector.

Infrared detectors based on nanocrystals also necessitate the development of light management strategies, albeit for different reasons than their III-V thin film counterparts. As explained earlier, the transport in a nanocrystal array occurs through a hopping mechanism limiting the carrier mobilities values. The diffusion length L_D is proportional to the carrier mobility μ as:

$$L_D = \sqrt{\frac{\mu k_B T \tau}{e}}$$

Where τ is the time-response, $k_B T$ is the thermal activation, and e is the elementary charge. Considerable progress has been achieved to increase the mobility values[62,124,125] of nanocrystals from below 10^{-4} to around 1 $cm^2.V^{-1}.s^{-1}$. Despite these advances, these values remain 2 to 3 orders of magnitude lower than those of bulk materials. As a result, the charge diffusion length is limited to a few nanocrystals (10-100 nm corresponding to 1 to 10 NC size) and is shorter than the absorption depth of a thin nanocrystal film. The latter must be a few micrometers thick[126] to achieve full absorption of the incident light, while a typical nanocrystal film is in the 200-300 nm range, resulting in a mere 10-20% absorption. To tackle this issue, the first strategy involves developing higher quality (mirror-like with a film roughness on the order of the NC size), thick films (>500 nm) with improved interparticle coupling (higher mobility) by working on the material. This approach has been applied to the design of photodiodes using HgTe-based inks.

The second approach to increase absorption in a thin nanocrystal film (200 nm) involves modifying the light-matter coupling within it, similar to its epitaxial counterpart. The electromagnetic field is modified to concentrate it into the NC film. Optical resonators are coupled to the nanocrystal film for light trapping[127–131] and, in turn, increase the probability of photon absorption. Initially developed in the early 2010s for solar cell applications[132,133] in the visible and near-infrared range, these resonators were later extended to NC-based infrared photodetectors. Most detectors rely on plasmonic resonances induced by the introduction of a nanostructured metallic layer. Plasmonic resonators use the light-matter interaction between light and surface plasmons to enhance the electromagnetic field. Plasmons are collective oscillations of electrons at the surface of a metal that can interact with light to create a strongly confined electromagnetic field near the metal surface. By shaping the resonant structure, the plasmonic resonance can be tuned to a specific wavelength, creating a localized electromagnetic field that enhances light absorption from the adjacent material. Plasmonic resonators have been successfully integrated into HgTe-based infrared photodetectors in photoconductor[134–136] and photovoltaic[137–139] geometries. In my thesis, I integrated these optical resonators to enhance light-matter coupling in infrared sensors. Therefore, in the second chapter of this manuscript, I will elaborate on their principle and current state-of-the-art.

1.4-3 Infrared focal plane arrays

Infrared focal plane arrays have a broad range of applications such as surveillance, imaging, remote sensing, and target tracking. FPAs consist of an array of individual IR detectors, or pixels, arranged in a two-dimensional format capable of detecting the presence and intensity of IR radiation. Currently, the global market for infrared cameras is dominated by two primary types: microbolometers and epitaxial photodetectors. Microbolometers, which are mostly used for civilian applications such as building thermography, fire detection, and surveillance, are uncooled cameras that are compatible with CMOS technology, making mass production relatively easy and leading to low-cost imaging systems that cost less than 1 k€. However, since they operate on the principle of a temperature change, their sensitivity and frame rate are lower compared to their photodetector equivalent. As a result, microbolometers cannot be used for applications that require a fast response time, such as LiDAR, or missile and airplane seeking. Quantum photodetectors, on the other hand, address these issues and are typically used in high-performance, cooled infrared cameras. Depending on the targeted infrared spectral range, these photodetectors can be made of various materials such as MCT, InSb or InGaAs. Nevertheless, the entire complex fabrication chain of these photodetectors leads to high costs ranging from 10 to a few 100 k€.

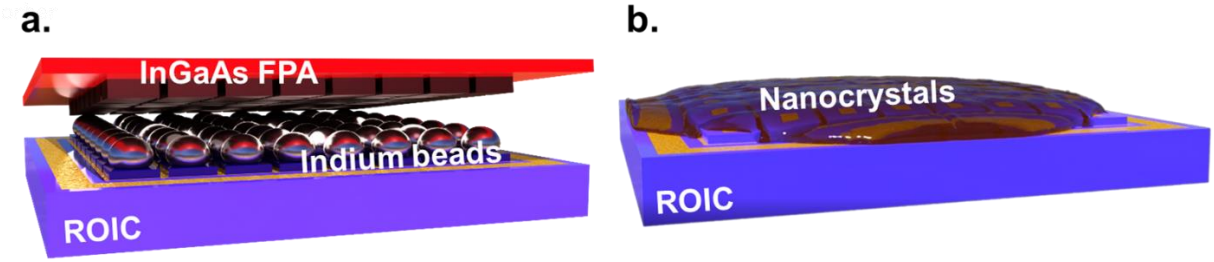

Figure 18 Coupling of the absorbing infrared layer to the readout circuit. a. Hybridization of an InGaAs focal plane array to a ROIC through indium beads. b. Deposition in a single step of a nanocrystal film on a ROIC. The deposition is typically done with a spin-coating process.

Historically, the development of infrared detection was primarily for military applications, which later expanded to astronomy. The infrared range was considered a niche market where the focus was on performance rather than cost-effectiveness. In recent years, significant technological advancements have been made in various fields such as electronics in smartphones or automobiles. This has brought new players and industries into the infrared field where the demand is mainly centered on the cost of a detector for integration into everyday civilian applications. These include quality sorting of food products, night driving assistance in autonomous cars, or LiDAR in new generations of smartphones. While the silicon industry dominates the visible electronics market with high performance and low cost, its indirect bandgap makes it unsuitable for optoelectronics applications. Moreover, since silicon has a 1.1 eV bandgap, it cannot access the infrared range. As a result, the infrared counterpart of silicon is still in the process of being fully realized, and traditional epitaxially grown III-V and II-VI semiconductors remain the costly materials of choice for IR detection.

Throughout this initial chapter, it has become apparent that colloidal nanocrystals have emerged as a promising candidate for optoelectronic applications. Specifically, HgTe nanocrystals have gained significant attention due to their capacity for continuous spectral tunability across the infrared spectrum, state-of-the-art single-element performance, and cost-effective synthesis. The shortwave infrared (SWIR) range of 1-2.5 µm is the key spectral range for emerging civilian applications, and the current industry-leading technology is based on InGaAs alloys. The cost of an InGaAs camera falls within the range of 10-100 k€, with a substantial portion of the cost attributable to detector fabrication. Epitaxial growth of InGaAs alloys is carried out using molecular beam epitaxy (MBE), which demands an ultra-high vacuum environment, ultimately increasing costs. In contrast, HgTe nanocrystals satisfy emerging demands for infrared detection with their cost-effective colloidal synthesis. High-quality nanocrystal films can be produced, and their growth does not necessitate an ultra-high

vacuum environment. Moreover, nanocrystal films can be deposited onto conventional, less toxic substrates such as silicon, which are less expensive than those used for epitaxial detectors (CdZnTe for MCT and InP for InGaAs).

Another crucial aspect of detector fabrication is the coupling of the active material to the read-out circuit (ROIC), which collects and processes signals generated by the FPA. Acting as an intermediary between the detectors and the camera's output stage, the ROIC converts the detector signal into a usable image format. ROICs are silicon-based, and traditional epitaxial detectors grown on their specific substrates require a hybridization step, during which small indium bumps are typically deposited onto the surface of the ROIC. The detector array is then aligned and bonded to the bumps, creating electrical connections between the detector pixels and the ROIC, which allows for charge collection, see Figure 18. The hybridization step is a critical and delicate phase in the manufacturing process, which is poorly efficient, leading to increased costs for a camera. However, nanocrystals do not have any constraints on the hybridization step since they can be directly deposited onto the ROIC via spin-coating. Finally, NC-based infrared cameras exhibit great promise in achieving high-resolution images by decreasing pixel size. In a traditional camera, the hybridization step typically restricts pixel sizes to no less than 10 µm, as alignment between the FPA and ROIC becomes increasingly difficult, further decreasing manufacturing yield.

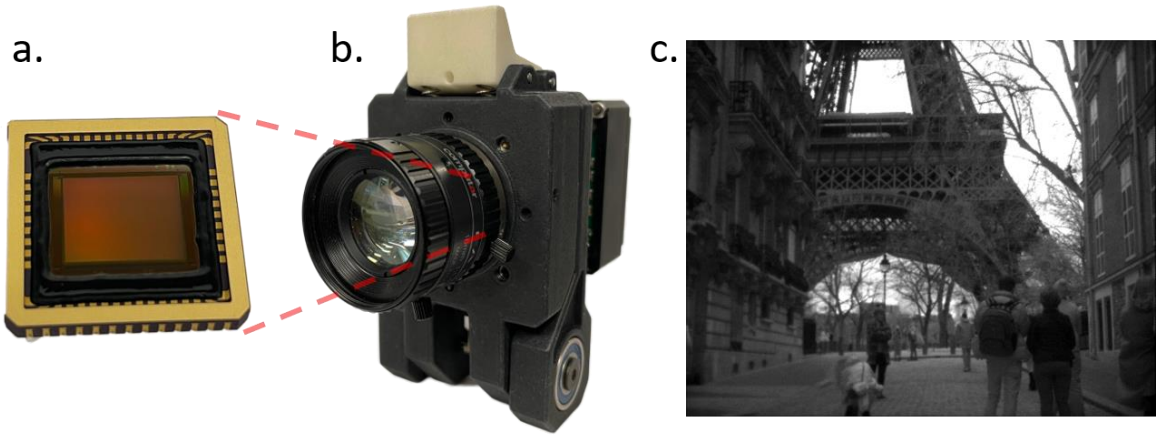

Figure 19 Nanocrystal-based infrared camera. a. Readout circuit in a VGA format with 15 µm pitch from New Imaging Technology. b. Camera with an infrared objective. c. Picture of the Eiffel Tower taken with the HgTe-based infrared camera.

Colloidal nanocrystals, which can be synthesized cost-effectively and coupled easily to the ROIC while reducing pixel size, represent a unique platform for the development of infrared cameras. PbS nanocrystals were the first to be integrated into infrared cameras, and several industrial companies, including SWIR Vision Systems,[140] IMEC,[141] and Emberrion,[142] have brought them to the global market over the past decade. However, the 0.41 eV bandgap of PbS limits the spectral range to the near-infrared (NIR). In contrast, HgTe offers a large spectral tunability that covers the entire infrared spectrum. Demonstrations of HgTe-based cameras are relatively recent, as the material had to achieve stability and high-quality film deposition over an area of at least 1 cm².

Tang *et al.*[138] developed a strategy that did not rely on multipixel detectors for HgTe nanocrystals. They coupled a single pixel device with a moving optical lens that scanned the photocurrent signal at each position to reconstruct an image. The authors demonstrated MWIR imaging, but the method is inherently slow due to mechanical displacements and long-time acquisition. Therefore, it cannot be applied to live imaging where the minimum frame rate is 24 fps. Aberrations from the lens were also an issue, but the authors overcame it by designing a device with enhanced light-matter coupling on a flexible substrate to obtain an eye-like sensor.[143]

The first infrared images using an HgTe-based FPA were obtained in the MWIR.[46,47] HgTe nanocrystals with a cut-off wavelength at 5 µm were deposited on a ROIC with 320x256 pixels and a 30 µm pitch, followed by a solid-state ligand exchange. The camera was cooled down to cryogenic temperatures and exhibits quantum efficiency below 1%. Last year, in 2022, Gréboval *et al.*[44] and Zhang *et al.*[45] successfully integrated HgTe nanocrystals with a cut-off wavelength of around 2 µm in a half VGA format ROIC for SWIR imaging. They used HgTe-based inks to deposit a high-quality, thick film in a single step. As a result, infrared images from both cameras presented only a few dead pixels, which were primarily located on the border of the image. The ROIC runs in a photoconductive mode where the polarization is applied in-plane, and the authors demonstrated quantum efficiencies in the order of 5-10%.

Despite the promising performance of CQD cameras, they still lag behind their epitaxial equivalents, which typically exhibit 90% QE for SWIR imaging in an InGaAs camera. Colloidal nanocrystals are an emerging field, having only been studied for 30 years, while epitaxially grown semiconductors benefit from more than 70 years of intense research. The next challenge for HgTe-based cameras is the integration of a diode stack onto the ROIC. The photovoltaic mode of the imaging system would enable 0 V operation, which would considerably decrease the dark current and increase the signal-to-noise ratio. Such integration is delicate, as it requires (i) vertical stacking of high-quality NC layers without pinholes that could lead to a short circuit, (ii) inversion of the diode structure or electrodes since the top metallic contact reflects light, and (iii) redesign of the ROIC to efficiently integrate the nanocrystal layers. Hence, because of these challenges, an HgTe-based infrared camera in a photovoltaic mode has not yet been realized, and certainly current research of several groups focuses on this topic.

1.5- Conclusion

In this chapter, fundamental concepts concerning colloidal nanocrystals have been presented, including their growth, transport, and integration into optoelectronics systems. These nanocrystals represent one of the few nanotechnologies that have achieved mass market penetration, with an estimated annual revenue of one billion dollars. They are commonly used as downconverters for red and green sources in displays such as quantum light-emitting diodes (QLEDs) televisions. Beyond the visible spectrum, mercury chalcogenides HgX nanocrystals offer a promising alternative for infrared optoelectronics due to their continuous spectral tunability across the entire infrared range, coupled with cost-effective synthesis. This makes them well-suited for integration into next-generation detectors and emitters.

Over the past three decades, significant progress has been made in the field of nanocrystals, which has led to the ability to engineer carrier wave-functions at the particle level, particularly with the development of core-shell heterostructures. Today, this concept has been extended to the device level, where nanocrystals can be coupled to other types of NCs or to other materials with any dimensionalities. In the following two chapters, we will focus on these new types of heterostructures that allow for wave-function engineering at the nanoscale. The second chapter will present a mixture of nanocrystals made of HgSe and HgTe with intraband absorption in the MWIR. Additionally, a light-matter coupling strategy was designed to enable close-to HOT operation. The third chapter will introduce the concept of Van der Waals heterostructures, where for the first time, mercury chalcogenides nanocrystals are coupled to nanowires of bulk InGaAs allowing for SWIR and MWIR detection. Finally, the last chapter will focus on the integration of HgTe NCs in an advanced infrared technology, which is a SWIR camera. The device properties were investigated through operando photoemission microscopy conducted at Soleil Synchrotron and near-field mapping of the photocurrent.

2 Intraband photodetection with an enhanced light-matter coupling

This chapter is dedicated to the integration of intraband HgX nanocrystals into a mid-infrared photodetector. The primary objective of this work is to introduce the concept of a hybrid nanocrystal material, which allows for the engineering of carrier wave-functions at the device level. Additionally, a light-matter coupling management strategy will be introduced in the photodetector to enable close-to-HOT (high operating temperature) operation. The experimental aspects of this study involved the theoretical calculations of the hybrids' spectroscopic properties as well as infrared microscopy conducted by Gregory Vincent and Audrey Chu, and the nanoparticle growth carried out by Yoann Prado.

Related article:

- ***Khalili, A**.; Weis, M.; Mizrahi, S. G.; Chu, A.; Dang, T. H.; Abadie, C.; Gréboval, C.; Dabard, C.; Prado, Y.; Xu, X. Z.; Péronne, E.; Livache, C.; Ithurria, S.; Patriarche, G.; Ramade, J.; Vincent, G.; Boschetto, D.; Lhuillier, E. Guided-Mode Resonator Coupled with Nanocrystal Intraband Absorption. ACS Photonics 2022, 9, 985–993.*

2 Intraband photodetection with an enhanced light-matter coupling.....43
2.1- HgSe for intraband detection.....45
2.1-1 Self-doped HgSe nanocrystals.....45
2.1-2 The doping issue for intraband detection.....47
2.2 HgSe-HgTe heterostructure for infrared sensing.....49
2.2-1 Uncoupling the optical from transport properties.....49
2.2-2 Enhanced transport properties of HgSe/HgTe metamaterial.....51
2.2-3 Exploring the ultrafast carrier dynamics in HgSe/HgTe.....53
2.3 Enhanced light-matter coupling for intraband detection.....56
2.3-1 State-of-the-art of resonators applied to NC-based infrared photodetectors.....57
2.3-2 Guided-mode resonator: history and principle.....58
2.3-3 Toward a HOT intraband-based photodetector.....60
2.4 Conclusion.....66

Intraband detectors are a type of photodetector that operates on the principle of absorbing light within the same band of a material. Unlike conventional interband photodetectors, which detect light by promoting electrons from the valence band to the conduction band, intraband detectors commonly use transitions within the conduction band. This allows for detection of photons with energies below the bandgap of the material, enabling detection in the mid-wave infrared (MWIR) and long-wave infrared (LWIR) regions where interband detectors suffer from complex, low-yield and expensive fabrication processes.

The most commonly used materials for intraband detectors are doped III-V semiconductors, such as n-type GaAs/AlGaAs superlattices. In these materials, the conduction band is populated with a high density of electrons, allowing for efficient intraband absorption. Intraband detectors can be designed in various configurations, including photoconductors, photodiodes, quantum well infrared photodetectors (QWIPs), and quantum dot infrared photodetectors (QDIPs). Among these, QWIPs have gained significant attention due to their high detection sensitivity and the ability to engineer the optical properties by changing the quantum well thickness. In QWIPs, the absorption occurs in the quantum well, where electrons are confined in two dimensions, resulting in a sharp absorption peak in the MWIR or LWIR. Nevertheless, QWIPs demonstrate large dark current, and the inherent optical selection rules prevent absorption under normal incidence conditions. Consequently, QDIPs emerged as a viable alternative to address these limitations.

Quantum Dot Infrared Photodetectors (QDIPs) operate in a similar manner to Quantum Well Infrared Photodetectors (QWIPs) since both rely on intraband transitions in the upper levels of the conduction band. However, in a QDIP, electrons are confined in all three dimensions, which should lead to an increase in the electron relaxation time due to the phonon bottleneck[144]. This effect should have significantly reduced the thermal generation of carriers, leading to a decrease in the dark current. Despite the original purpose of QDs being for semiconductor laser development[145], their potential for MWIR photodetection quickly gained interest. The first QDIPs were composed of narrow bandgap self-assembled quantum dots of InAs buried between GaAs barriers, leading to mid- and long-wave infrared photoconductivity.[146–149] Since then, epitaxial QDs have been integrated into various semiconductor heterostructures and device designs, such as dot-in-well (DWELL)[150,151] or lateral QWIP, in order to improve their performance. Quantum cascade photodetectors (QCDs),[152] which are based on resonant tunneling through quantum wells, have also gain significant attention over the last years. QWIPs and QDIPs were considered as potential replacements for Mercury Cadmium Telluride (MCT) detectors in MWIR sensing, which is still the leading technology for mid-infrared detection. Despite long-standing concerns regarding HgCdTe uniformity and toxicity,[153] it remains the leading technology driving mid-infrared detection.

Intraband detectors based on QWIP and QDIP technologies have been successfully integrated into focal plane arrays[154–156] and QWIPS have even achieved commercial status with companies such as Thales[157]. However, the coupling of the active layer to the readout integrated circuit (ROIC) requires a complex hybridization process through indium bonding, which reduces manufacturing yield and hinders the possibility of reducing pixel size. Despite achieving performance levels comparable to MCT detectors, epitaxial QWIPs/QDIPs have not brought about other advantages such as cost reduction or direct integration with silicon electronics. On the other hand, these motivations have driven research into microbolometer detectors[158–161], which can be directly integrated onto CMOS without any hybridization step. Advances in nano-fabrication and micro-electrochemical (MEMS) technology have led to the commercialization of cost-effective microbolometer cameras. However, bolometric detection falls short in terms of sensitivity and time-response compared to photodetectors, rendering them unsuitable for emerging IR applications in automotive sectors or product sorting in food industries.

Three decades ago, a novel material surfaced that held the potential to combine the photodetectors' performance and CMOS compatibility of microbolometers. Colloidal quantum dots (CQDs) or nanocrystals (NCs), have emerged as attractive contenders for next-generation optoelectronics due to their cost-effective growth and size-tunable optical properties.[162,163] The majority of the nanocrystal-based detector advancements in visible and near-infrared have been achieved using CdSe or PbS. However, broadening the spectral range of nanocrystals to mid-infrared was challenging because the bandgap of PbS limits its range to NIR. In the early 2000s, mercury chalcogenides HgX nanocrystals were developed, showcasing continuous spectral tunability over the IR and exemplary performances at the single element level.[49] Specifically, mercury selenide HgSe NCs features an intraband transition[55] that allows for tunability of photoconductivity throughout the mid-infrared region.

In this context, the present chapter will provide a detailed account of the integration of self-doped HgSe NCs in advanced heterostructures and device architecture design. To begin with, the limitations of a doped material for transport will be introduced. Next, the concept of hybrid material, which enables an engineering of the wave-functions at the nanoscale, willl be explained. This metamaterial, comprising HgSe and HgTe nanocrystals, will be examined with respect to the charge dynamics between these two populations of NCs using pump-probe experiments. Finally, the light-matter coupling management strategy aimed at achieving a close-to-HOT photodetector in the MWIR (at 4.4 µm) will be elaborated.

2.1- HgSe for intraband detection

In the history of infrared devices, the transition from interband to intraband materials led to the development of detectors based on quantum engineering. To address low energies using interband transitions in colloidal materials, large nanoparticles (*i.e.*, weakly confined) must be grown, which are poorly colloidally stable. Therefore, intraband transitions in nanocrystals are appealing for MWIR/LWIR detection since they allow for absorption below the material bandgap. Moreover, this transition presents significant prospects for developing an efficient strategy to reduce the toxicity. Currently, the observation of narrow bandgap interband transitions is predominantly confined to materials composed of lead (Pb), mercury (Hg), and other heavy atom-containing compounds. Narrow bandgaps are more readily attainable in materials characterized by a higher electron count compared to those comprising lighter atoms, which exhibit a relatively smaller density of states. Consequently, the realization of doping in moderately doped nanocrystals holds the potential to achieve intraband transitions in materials featuring reduced toxicity as observed in Ag_2Se nanocrystals.[164–166] In the following section, we will review the fundamental properties of the intraband transition in self-doped HgSe nanocrystals. Additionally, challenges arising from a doped colloidal material will be discussed.

2.1-1 Self-doped HgSe nanocrystals

In nanocrystals, intraband transitions typically involve promoting an electron between two levels of the conduction band due to the quasi-continuum of states in the valence band resulting from the large hole effective mass. To initiate such a transition, the first level of the conduction band must be populated in the ground state, a process commonly referred to as doping. Intraband transitions have been observed in nanocrystals since the 1990s, with the initial demonstrations being in CdSe[167] nanocrystals through saturating the interband transition via optical pumping. This method has also been extended to CdSe/CdS[53] (core-shell) and PbSe[168], among others, with the former capable of intraband emission in the mid-infrared. However, these applications have predominantly focused on their utilization as spectroscopy tools. Alternatively, a second approach involves electrochemically charging electrons in the quantum-confined states of the nanocrystals. This has been observed in CdSe nanocrystals where the interband transition was bleached, leading to an intraband absorption at 300 meV in the MWIR.[51] However, neither of these techniques is compatible with device integration,

where the intraband transition must be available in the steady state. In the late 2010s, chemically doped PbS nanocrystals with silver[169] or iodine[170] were successfully used to occupy the $1S_h$ or $1S_e$ state, leading to tunable MWIR to LWIR absorption.

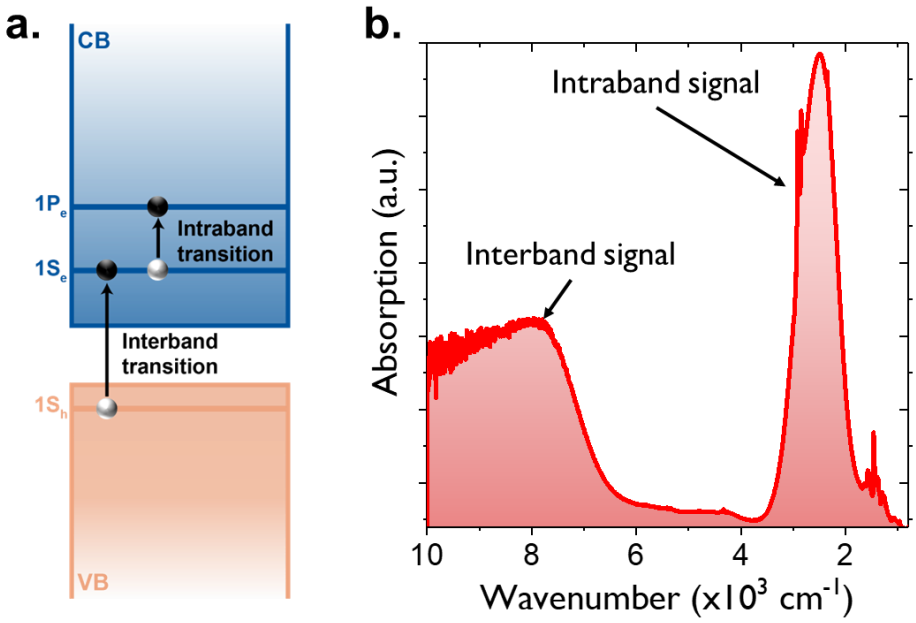

Figure 20 Intraband transition in HgSe nanocrystals. a. Scheme illustrating the optical transitions in a colloidal quantum dot. b. Absorption spectrum of HgSe NCs featuring an intraband signal in the MWIR, and an interband contribution at higher energies.

In 2014, a significant breakthrough occurred in the field of intraband colloidal semiconductors with the discovery of self-doping in mercury sulfide (HgS) nanocrystals.[54] This was the first instance where an intraband absorption was observed in the steady state due to a bleach of the interband transition by the nanocrystal's surrounding environment. Following this, intraband photoconductivity was explored in mercury selenide (HgSe)[55,57] nanocrystals, which are self-doped nanoparticles possessing an occupied $1S_e$ state, resulting in an intraband transition ($1S_e$ to $1P_e$) in addition to the interband transition, as illustrated in Figure 20a. Typically, the interband transition in HgSe is bleached as the first level of the conduction band is filled with electrons. Figure 20b depicts a typical spectrum of HgSe nanocrystals, where the intraband absorption is seen as a sharp peak in the mid-wave infrared (MWIR), while the interband absorption appears as a broad feature at higher energies. The energies of both optical transitions can be modified with the size of the nanocrystal, enabling tuning from the MWIR to THz.[57]

The doping in HgSe nanocrystals is self-generated, meaning it arises from the intrinsic properties of the material rather than being intentionally induced from an external source. Robin *et al.*[171] demonstrated that a reduction of CQD by the environment generates doping, and its magnitude can be tailored with its surface chemistry. Figure 21b shows the normalized absorption spectrum of HgSe nanocrystals with different surface chemistries (*i.e.*, ligands). When the original dodecanethiol (DDT) ligands (as-synthesized) are exchanged for a transport compatible surface chemistry, which is a mixture of thiol and mercury ions, the magnitude of the interband transition increases, as seen with the broad feature at around 6000 cm^{-1}. The initial DDT ligands lead to close-to-filled $1S_e$ states with two electrons per dot, whereas transport-compatible surface chemistries reduce the average number of electrons per dot (*i.e.*, doping reduction), resulting in the unbleaching of the $1S_h$ to $1S_e$ interband transition. This is due to a dipole effect where each ligand carries a different dipole, effectively tuning the absolute energy of the bands at the surface of the nanocrystal.[172] A similar dipole effect has also been observed in PbS nanocrystals, with a large tunability of the band-edge energy.[87,173]

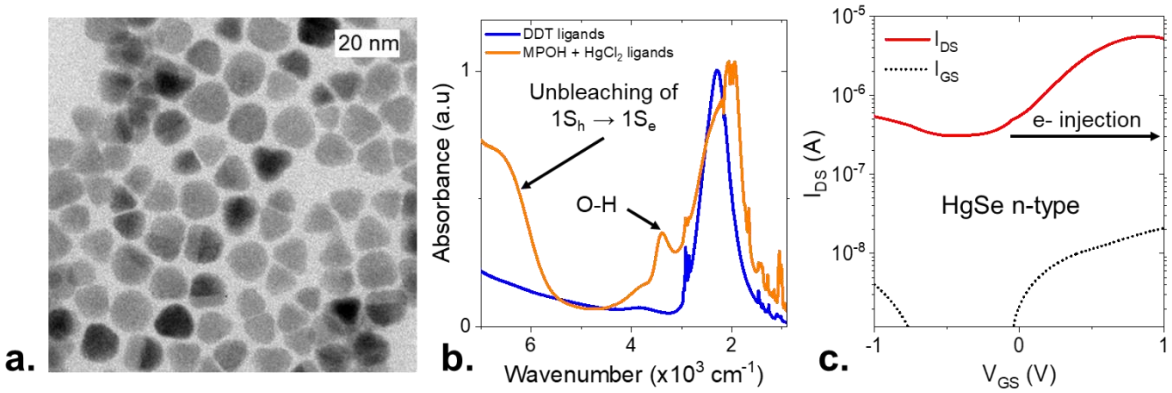

Figure 21 Properties of HgSe NCs. a. TEM image of HgSe nanocrystals with a size of 5 nm. b. Absorption spectra before and after a liquid-phase exchange procedure. c. Transfer curve of HgSe NCs deposited on a single digit electrode (electrolytic FET).

This chapter employs nearly spherical mercury selenide (HgSe) nanocrystals with a diameter of approximately 5 nm, synthesized following the procedure developed by Lhuillier *et al.*[57] Initially, a semiconductor precursor solution, consisting of selenium (Se) dissolved in trioctylphosphine (TOP), is formed, while mercury oleate ($Hg(OAc)_2$) and oleylamine are degassed under magnetic stirring in a three-neck flask at 85°C. Subsequently, under an inert atmosphere (N_2) and at a moderate temperature (100 °C), the TOP:Se precursor is rapidly injected. The reaction is then quenched with DDT in toluene after 3 minutes, and the resulting solution is washed several times to remove unreacted precursors and oleylamine. The nanocrystals are precipitated with a polar solvent such as ethanol or methanol and redispersed in toluene. TEM imaging of HgSe nanocrystals confirms their mean size of 5 nm and quasi-round shape, as shown in Figure 21b. These nanocrystals display a broadband interband feature above 6000 cm^{-1} (1.7 µm – 730 meV) and an intraband signal at around 2200 cm^{-1} (4.4 µm – 280 meV). The chosen particle size matches the intraband absorption with the 3 – 5 µm atmospheric transparency window, known as the mid-wave infrared (MWIR) region. The doping nature of HgSe nanocrystals is investigated using a field-effect transistor technique, as depicted in Figure 21c. A film of HgSe nanocrystals is spin-coated between two electrodes, and an electrolyte comprising $LiClO_4$ in PEG is deposited on top. The current of the nanocrystal channel arises under positive gate voltage (*i.e.*, injection of electrons), confirming the n-type character of HgSe. Furthermore, the transfer curve does not display any hole transport, and the minimum of conduction is found at negative gate bias, revealing the strong native doping in HgSe nanocrystals.

2.1-2 The doping issue for intraband detection

The use of intraband absorption in HgSe nanocrystals presents an attractive opportunity to develop colloidal counterparts of intraband detectors such as QDIPs and QWIPs. However, the development of colloidal QDIPs poses several challenges related to intraband detection. Figure 22 illustrates the typical transport properties of a photoconductor based on an HgSe nanocrystal array. In this device, HgSe NCs with long DDT ligands are replaced with a mix of mercaptoethanol (MPOH) and mercury chloride ($HgCl_2$) through a liquid-phase ligand exchange procedure. These short ligands partially reduce doping in HgSe, while preserving intraband absorption. A film of HgSe is then deposited on interdigitated electrodes using spin-coating, with the film thickness being controlled by the ink concentration and to a lesser extent, the speed parameters of the spin-coater.

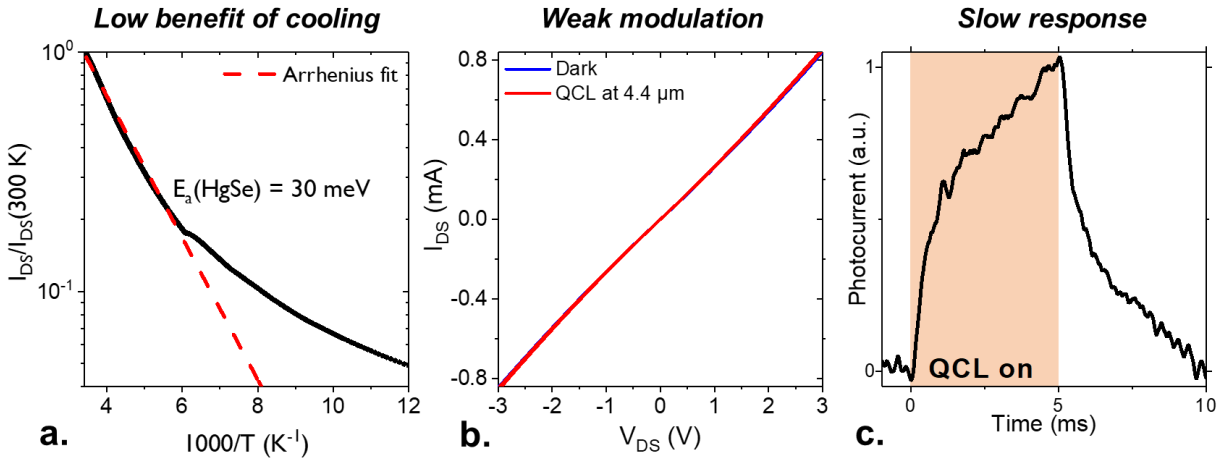

Figure 22 Transport properties of an HgSe-based photoconductor. a. Evolution of the dark current with temperature. The activation energy is extracted with an Arrhenius fit. b. I-V characteristics under dark conditions and exposed to a QCL matching the intraband absorption at 4.4 µm. c. Time-response of the HgSe detector under the illumination of a QCL.

The transport properties of a photoconductor based on HgSe are being examined by following its dark current, time-response, and activation energy. The activation energy is related to the enhancement of detector performance at lower temperatures. The temperature-dependent dark current of the device is shown in Figure 21a. At high temperatures, a decrease in the current can be observed, which can be characterized by an Arrhenius model, depicting an exponential decay, given by:

$$I(T) = I(300K)e^{\frac{-E_a}{k_B T}}$$

Where E_a is the activation energy, expressed in eV, that can have a maximum value of the bandgap for an intrinsic semiconductor. Therefore, a higher activation energy leads to a reduction in dark current upon cooling and a subsequent improvement in device performance. For an HgSe nanocrystal array with a bandgap of 300 meV, the activation energy is measured to be 30 meV, indicating minimal improvement in performance of HgSe upon cooling, as shown in Figure 21a. On the other hand, interband HgTe nanocrystals with a bandgap of 500 meV exhibit an activation energy close to 200 meV. Due to the intraband transition's low energy (300 meV), thermally activated carriers result in a high dark current. The photodetector is then illuminated with a quantum cascade laser MWIR source at 4.42 µm to match the intraband absorption. However, the high dark current in HgSe results in a weak signal-to-noise ratio, as evidenced by the small value of photocurrent I_{photo}, which indicates a weak modulation between the current under illumination and dark, as shown in Figure 22b. Additionally, the photoresponse of the device is extremely slow, with a time-response on the order of several seconds. Symmetrical response (*i.e.*, comparable rise and decay times) shown in Figure 22c indicates that the photoresponse is bolometric rather than photogenerated, *i.e.*, due to the heating of the nanocrystal film upon absorption of light. To summarize, an intraband detector operating in the mid-infrared with HgSe nanocrystals suffers from:

- A high dark current due to the degenerate doping of nanocrystals and the occupation of the $1S_e$ state.
- A poor responsivity, which coupled with high dark current leads to weak signal-to-noise ratio.
- A very slow photoresponse (> 1 s), suggesting a bolometric character.
- A low activation energy (30 meV) indicating that the photodetector performances would barely increase upon cooling of the system.

The presence of degenerate doping in nanocrystals enables intraband absorption, but it has a detrimental effect on the dark current. Moreover, many researchers were skeptical about the possibility of achieving high performance with intraband detection, which was also the case for intersubband transitions in quantum well infrared photodetectors (QWIPs). These two aspects explain why colloidal intraband detectors are not as advanced as their interband counterparts, with detectivities below 10^9 Jones at cryogenic temperatures. In the first demonstration of an HgSe-based intraband photodetector, the authors claimed that a fast response time could be achieved when the $1S_e$ state was fulfilled with 2 electrons per dot.[55] However, this is practically challenging to accomplish because the post-synthesis ligand exchange also affects the film's doping magnitude. Recently, Chen *et al.*[174] proposed a mixed-phase ligand exchange on HgSe NCs to fully occupy the $1S_e$ state (2 e- per dot). They were able to obtain an intraband photodetector with a time-response in the microsecond range and detectivity of 10^9 Jones at 80 K. However, the pursuit of achieving a two-electron-per-dot configuration through this strategy presents several challenges. Firstly, it is crucial to identify the specific surface chemistry required to attain this condition for each dot size, which necessitates empirical investigation. Secondly, it has been demonstrated by the same group that the two-electron-per-dot configuration holds true only in the case of a monodisperse synthesis. In my thesis, I focused on another approach to design an intraband photodetector based on the concept of a mixture of two different populations of nanocrystals, which allows for wave-function engineering of the carriers at the nanoscale.

2.2 HgSe-HgTe heterostructure for infrared sensing

Over the course of the past thirty years, colloidal nanocrystals have been predominantly utilized for their optical interband transitions.[49,175] In contrast, intraband and intersubband transitions have found extensive use in epitaxially grown III-V semiconductors. QDIPs and QWIPs have been some of the earliest implementations of these transitions and have now become viable commercial alternatives to conventional MCTs. For infrared emission, the advent of quantum cascade lasers (QCLs) has had a significant impact since their inception three decades ago.[93] These lasers employed precise engineering of intersubband energies and relaxation rates, leading to a significant breakthrough in semiconductor physics and device development. Consequently, this field has seen an enormous amount of activity, and QCLs have become the most widely utilized mid-infrared laser source. Despite their potential to revolutionize optoelectronics, intraband transitions in nanocrystals are still beset by several challenges. The previous section highlighted a major issue, namely, the degenerate doping of nanocrystals resulting in high dark current. In this regard, we present a novel strategy based on a heterostructure of nanocrystals that aims to overcome this challenge. The wave-functions of the carriers are engineered at the device level to reduce the dark current and enhance the time-response of the intraband-based infrared detector.

2.2-1 Uncoupling the optical from transport properties

Intraband-based CQDs face similar challenges as their III-V counterparts, owing to their degenerate doping, which is essential for inducing intraband transitions in nanocrystals with narrow bandgaps. However, this doping also leads to a transport mechanism driven by thermally activated carriers and a large dark current. Additionally, in the case of HgSe NCs, it is unclear whether the overall current should increase after the promotion of an electron from the $1S_e$ to $1P_e$ state upon illumination, given that this effect is unipolar and the photoinduced change in the carrier density is comparatively small compared to interband materials. While HgSe nanocrystals have been extensively studied for intraband-based photodetection, other colloidal semiconductors, such as Ag_2Se[166,176–178] or PbS[170], have also exhibited limited bandwidth and modest performances, characterized by weak signal-to-noise ratios.

At the outset, the feasibility of attaining high performance with intraband detection was met with skepticism by the infrared community, and this was also the case for intersubband

transitions in quantum well infrared photodetectors (QWIPs). However, the latter proved to be highly successful, leading to their commercialization and opening up new possibilities in the design of infrared photodetectors. Subsequently, the nanocrystal community was inspired by III-V heterostructures in which absorption and transport are spatially decoupled[152,179], and developed similar hybrid structures based on narrow bandgap materials, such as HgSe and HgTe. The guiding principle of such hybrids was to merge the intraband MWIR absorption properties derived from HgSe with the interband (*i.e.*, low dark current) transport properties of HgTe.

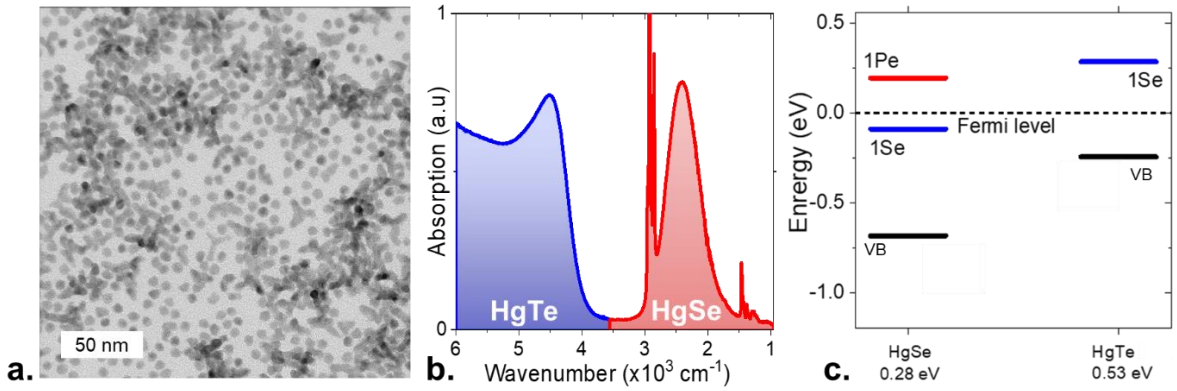

Figure 23 HgSe/HgTe mixture as a dye-sensitized infrared sensor. a. TEM image of the HgSe/HgTe mixture. b. Absorption spectrum of the mixture revealing the interband contribution from HgTe and the intraband signal from HgSe. Band alignment of HgSe and HgTe determined from x-ray photoemission, adapted from ref[106]*.*

Goubet *et al.*[180] initially proposed an approach to achieve high performance with intraband detection by growing epitaxially-connected HgSe/HgTe core-shell heterostructures. In this design, HgSe is responsible for driving the optical properties, while the promoted electrons are transported throughout the wider bandgap HgTe. While previous investigations had explored growing a wide bandgap protective shell made of CdSe or CdS on HgSe or HgS doped nanocrystals to enhance the intraband photoluminescence signal, this technique resulted in the vanishing of the intraband feature and exhibited limited optoelectronic properties, precluding their integration into infrared photodetectors.

HgSe/HgTe core-shell nanostructures, on the other hand, have a type II alignment favoring charge dissociation, where the intraband absorption is combined with a poor electron and hole wave-function overlap. Adding a HgTe shell does not significantly impact the intraband energy, but add an additional contribution due to the interband absorption of HgTe. This interband signal is found at higher energies than the one of the intraband. Additionally, the interband transition between the valence band of HgTe and the $1P_e$ state of HgSe provides a second path for absorption.

Despite the benefits of HgSe/HgTe core-shell nanostructures, growing epitaxially-coupled HgSe/HgTe core-shell heterostructures is a complex process, and the bandgap engineering of the HgTe shell is limited. Nonetheless, the authors[180] demonstrated that HgSe/HgTe core-shell nanostructures can significantly reduce the dark current while increasing the activation energy by up to 180 meV, which is half of the intraband gap value. By using a QCL that matches the intraband absorption at 4.4 µm, the authors showed that the time-response is greatly reduced from seconds to microseconds.

In recent years, there has been a growing interest in utilizing a blend of nanoparticles with a controllable electronic spectrum for the development of solar cells,[107,108] light-emitting diodes,[109] and for tuning the average doping magnitude in a nanocrystal matrix[110]. This approach involves careful consideration of the nanoparticle size, proportion, and interdot coupling to tailor the electrical and optical characteristics of the photodetector. These efforts enable the engineering of wave-functions at the nanoscale, thereby making it possible to fine-tune device-level properties. Livache *et al.*[106] followed a similar approach where they mixed

two population of nanocrystals: HgSe with its intraband absorption and HgTe with its interband properties. The energy landscape of this hybrid mimics the one of their III-V QWIPs/QDIPs counterpart, which uncouple the photon absorption from the carrier transport. Compare to the core-shell heterostructure, the mixture of nanocrystals allows for more freedom on the design by optimizing the bandgap of HgTe to favor charge transfer without generating dark current. This approach enables the fine-tuning of the interdot coupling and nanoparticle size distribution to optimize the device-level properties.

During the course of this project, I used this concept of mixture of HgSe and HgTe nanocrystals to create a type II alignment, in which the $1S_e$ state of HgTe is quasi-resonant with the $1P_e$ state of HgSe, as illustrated in Figure 23c. HgSe NCs were grown to a size of 5 nm to match the mid-infrared transparency window (3 – 5 µm), while the bandgap of HgTe was fixed at 0.5 eV. In conventional QWIPs or QDIPs, charge extraction and transport are ensured by tuning the barrier width and the energy of the excited state. However, in the HgSe/HgTe mixture, these parameters can be precisely controlled by varying the size of the HgTe nanocrystals. The difference between the $1P_e$ level of HgSe and the $1S_e$ level of HgTe determines the barrier height (ΔE), which can be adjusted by tuning the HgTe bandgap. If the energy difference between the excited state and the continuum is too large ($\Delta E \gg 0$), charge extraction is likely to be poor, as the excited state will not induce drift transport in the continuum. Conversely, if the energy difference is too small ($\Delta E \ll 0$), the promoted electron of HgSe is expected to be efficiently transferred to the HgTe barrier. However, this would lead to a substantial increase in the dark current due to the significant thermal activation of carriers through the HgTe band edge. In QWIPs, the well spacing is designed to minimize residual tunnel coupling and reduce the dark current. In the HgSe/HgTe hybrid, however, nanocrystals are randomly distributed, and a sufficient number of HgTe NCs must be introduced to prevent percolative hopping through HgSe NCs.

2.2-2 Enhanced transport properties of HgSe/HgTe metamaterial

The present project aims to optimize transport properties and intraband absorption in the MWIR of a hybrid composed of HgSe/HgTe. The foundation of this project was laid by C. Livache, a former PhD of the group, and I have subsequently expanded the work. Figure 23b displays the absorption spectra of the hybrid under investigation. It can be observed that at high energies (2.5 µm – 0.5 eV), interband contribution from HgTe is evident, while the intraband absorption of HgSe is observed at lower energies (4.4 µm – 0.3 eV). The small feature located in-between corresponds to an O-H peak originating from the MPOH ligands, which confirms the efficacy of the ligand exchange procedure. The ratio between HgTe and HgSe nanoparticles is established empirically to ensure that the magnitude in optical density (OD) of the interband signal of HgTe and the intraband signal of HgSe are nearly equivalent. To determine the nanoparticle ratio in the mixture, we utilize a combination of energy-dispersive X-ray spectroscopy (EDX) and transmission electronic microscopy (TEM). EDX is an analytical technique used for elemental analysis of a sample, which directly averages the Te/Se ratio over a large number of nanocrystals with a µm resolution. Based on the EDX analysis, we deduce that the atomic fraction of Se (n_{Se}) is approximately 3.2 times greater than that of Te (n_{Te}) as $n_{Te} = 3.2 \cdot n_{Se}$. Therefore, the ratio between HgTe and HgSe NCs can be expressed as follows:

$$\frac{N_{HgTe}}{N_{HgSe}} = \frac{n_{HgTe}}{n_{HgSe}} \times \frac{a_{QD-Se}}{a_{QD-Te}}$$

Where n_{HgTe}/n_{HgSe} is the atomic ratio determined from EDX, a_{QD-Se} (resp. a_{QD-Te}) is the number of Se (resp. Te) atoms in one nanoparticle. Figure 23a shows TEM images of the mixture indicating that HgSe is a 6.4 nm sphere and HgTe an 8 – 10 nm tripod (modeled as 3 spheres with 6 nm diameter). Hence, we have $V_{HgTe} = 3 \cdot V_{pod-HgTe}$, with V_{HgTe} the total volume of the tripodic HgTe and $V_{pod-HgTe}$ the volume of one arm of HgTe. Then, considering

the volume V_{HgSe} of a HgSe NC, and the unit cell volume $V_{Unit\ cell-HgSe}$ (or $V_{Unit\ cell-HgTe}$), we can write:

$$\frac{a_{QD-Se}}{a_{QD-Te}} = \frac{\frac{V_{HgSe}}{V_{Unit\ cell-HgSe}}}{\frac{V_{HgTe}}{V_{Unit\ cell-HgTe}}} \approx \frac{1}{2}$$

Finally, the nanoparticle ration between HgSe and HgTe is;

$$\frac{N_{HgTe}}{N_{HgSe}} \approx 1.5$$

This value should be regarded as an approximate estimation. When the nanoparticle ratio is too low (<< 1), the volume fraction of HgSe becomes insufficient to observe significant intraband absorption. Conversely, when the nanoparticle ratio is too high (>> 1), the percolation of photogenerated carriers through the HgTe matrix is hindered, resulting in no improvement in transport properties. Therefore, a nanoparticle ratio approaching 1 appears to be the most optimal for facilitating transport in HgTe and enhancing overall performance.

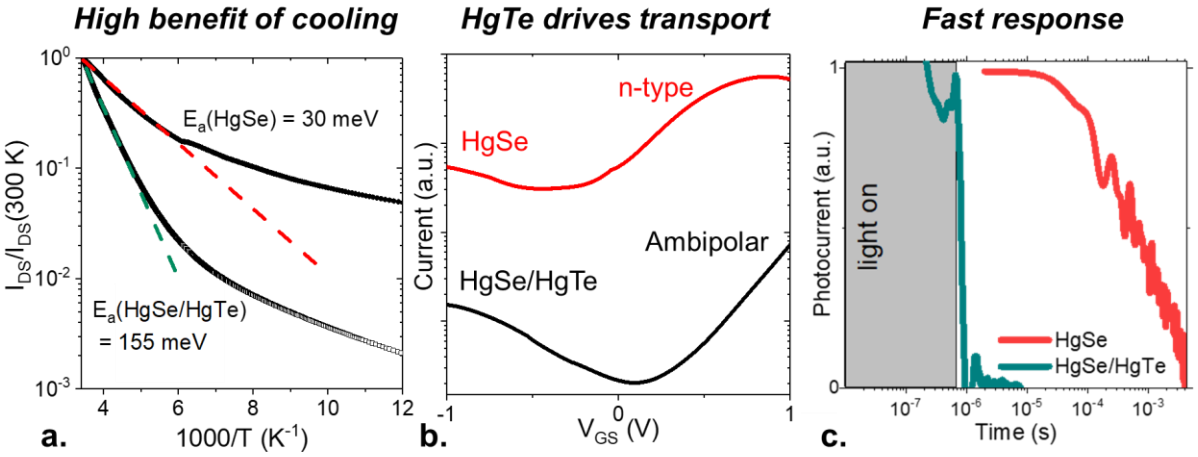

Figure 24 Transport properties of the HgSe/HgTe hybrid. a. Evolution of the dark current with the temperature of HgSe and the HgSe/HgTe mixture. b. Comparison of the electrolytic FET of HgSe and the hybrid. HgSe exhibits a n-type behavior while the mixture is ambipolar. c. Time-response of HgSe and the mixture.

Following the optimization of the nanoparticle ratio, the HgSe/HgTe metamaterial undergoes a ligand exchange procedure, wherein the initial long DDT ligands are substituted with a combination of mercaptoethanol and mercury chloride. A film of this mixture is then spin-coated onto conventional interdigitated electrodes and subsequently place in a closed-cycle cryostat for characterization. The evolution of dark current with temperature, $I(T)$, is monitored to extract the activation energy of the system, as presented in Figure 24a. An array of pure HgSe nanocrystals exhibits a weak thermal dependence, with an Arrhenius fit of the $I(T)$ resulting in an activation energy of 30 meV. This value indicates that cryogenic operation for pure HgSe NCs would scarcely reduce the dark current. However, for the HgSe/HgTe mixture, the activation energy increases to 155 meV, which is similar to the value obtained for a pure HgTe NC array. Consequently, the thermal generation of carriers in HgTe NCs drives the activation of the dark current. Moreover, the hybrid activation energy is close to half the energy of the optical transition (300 meV), which is expected for an intrinsic semiconductor. Notably, the dark current is significantly reduced upon the introduction of HgTe NCs into the system.

The investigation of transport properties in the HgSe/HgTe mixture is performed by means of an electrolytic field-effect transistor. The method involves deposition of a drop of $LiClO_4$ in a PEG matrix onto the photoconductor and monitoring the evolution of the NC channel current I_{DS} under injection of electrons (positive gate bias, $V_{GS} > 0$) and holes

(negative gate bias, $V_{GS} < 0$), as depicted in Figure 24b. A pure HgSe photoconductor exhibits an n-type character with only electron conduction and a minimum of conductance close to $V_{GS} = 0$. In contrast, the HgSe/HgTe mixture shows an ambipolar behavior with both electron and hole conduction. The hybrid is less doped compared to pure HgSe NCs, which is advantageous for reducing the dark current. Additionally, its ambipolar behavior is similar to that observed for a pure HgTe NC array, thus providing further evidence that transport in this system is governed by HgTe NCs.

The photocurrent dynamics of the HgSe/HgTe mixture in the MWIR range is then examined by resonantly exciting the intraband transition using a quantum cascade laser (QCL) operating at 2200 cm^{-1} (4.4 µm), as depicted in Figure 24c. The response time of the detector shifts from a few milliseconds in the case of a pure HgSe NC array to a few microseconds for the mixture. This acceleration in the device response confirms that the photoresponse is attributable to a photoconductive process rather than a bolometric effect.

Through the transport characterization of the HgSe/HgTe detector, we demonstrate a significant improvement in performance by decoupling the absorption from the transport properties, comparable to their III-V QWIP/QDIP epitaxial counterparts. This approach overcomes the issues related to the degenerate doping of nanocrystals necessary to observe an intraband transition. The HgSe/HgTe mixture yields results similar to those of the initial HgSe/HgTe core-shell nanostructure, while removing the constraint of epitaxial growth of HgTe and offering more flexibility in HgTe size. The enhanced performance of the HgSe/HgTe mixture results from precise engineering of the carrier wave-functions at the device level.

2.2-3 Exploring the ultrafast carrier dynamics in HgSe/HgTe

As mentioned previously, in the HgSe/HgTe mixture, the absorption of both materials was adjusted to achieve a similar optical density, as depicted in Figure 25a. However, the photocurrent spectrum exhibits significantly different contributions from HgSe and HgTe, as demonstrated in Figure 25b. Notably, the intraband photocurrent of HgSe experiences a significant reduction in the hybrid structure. While the absorption measurement was performed at room temperature, the photocurrent measurement was conducted at 80 K. Consequently, one could attribute this discrepancy to a temperature effect.

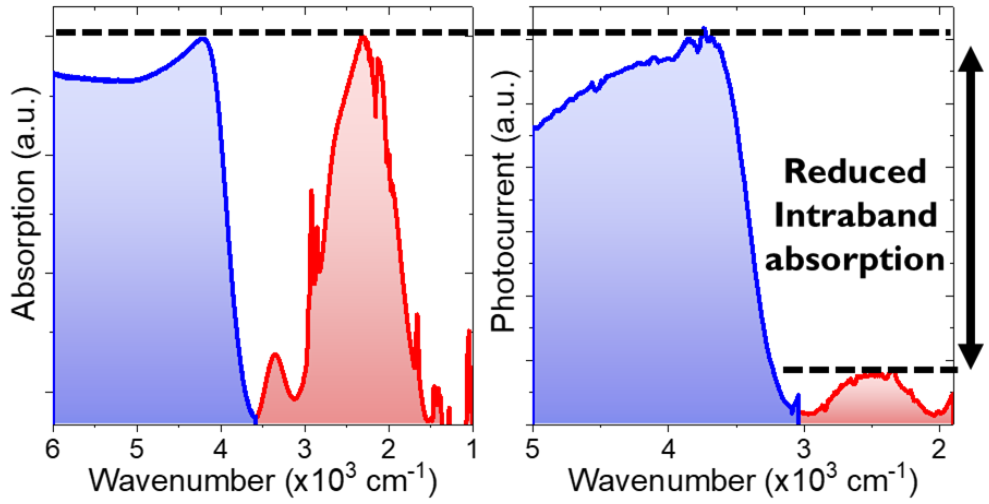

Figure 25 Charge transfer in the HgSe/HgTe mixture. Absorption and photocurrent spectra at 300 K of the HgSe/HgTe hybrid.

To explore this further, we performed a comprehensive analysis of the pristine HgSe, HgTe materials and their mixture's absorption behavior as a function of temperature. As the temperature is lowered[29], the interband gaps of HgTe and HgSe decrease, resulting in a redshift of +240 µeV.K^{-1} for HgTe, while the intraband gap of HgSe increases[181], leading to a blueshift of -115 µeV.K^{-1}, as depicted in Figure 26d-e. Similar shifts are also observed in the

HgSe/HgTe mixture, as illustrated in Figure 26f. Nonetheless, the temperature does not affect the relative absorption magnitude between the intraband and interband contributions, as shown in Figure 26c. Consequently, the observed reduction in the HgSe intraband peak in the photocurrent is attributed to a transport process.

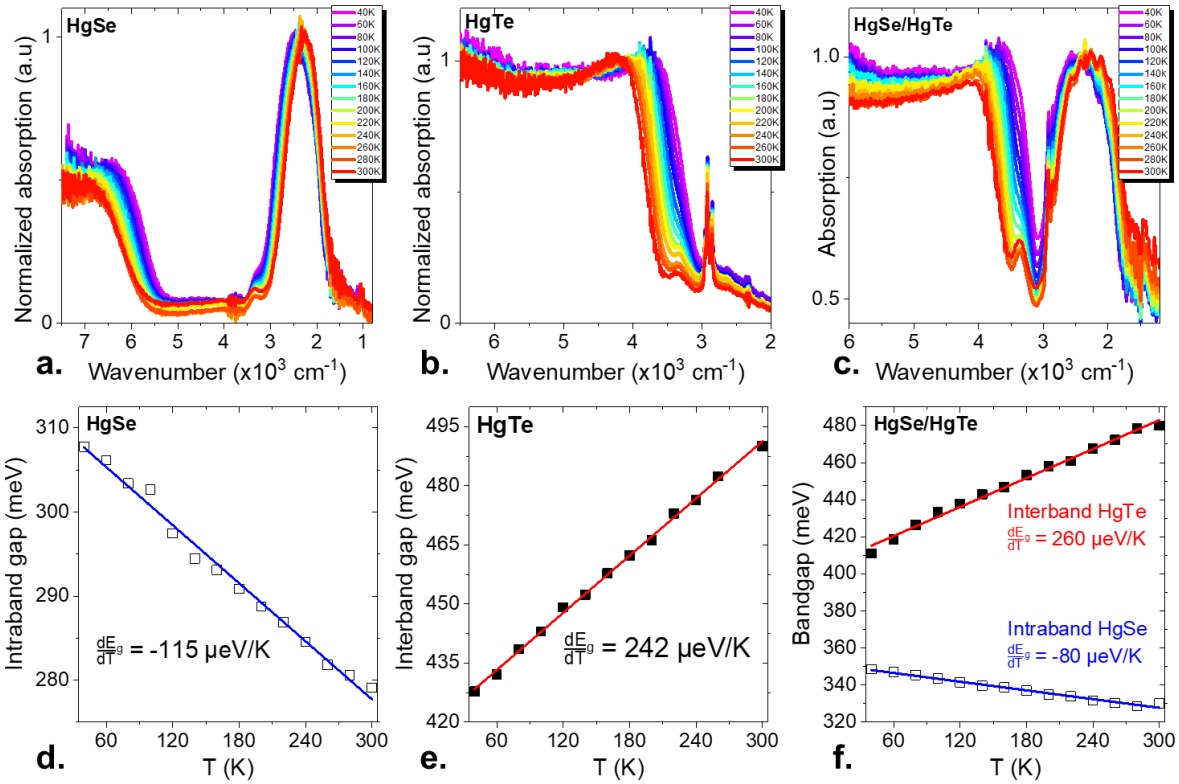

Figure 26 Temperature dependence of the pristine materials and the mixture. Normalized absorption spectrum of (a) HgSe NCs, (b) HgTe NCs and (c) HgSe/HgTe mixture. Measurements are conducted in a transmission configuration while the material is deposited on a double side polished undoped Si wafer. Bandgap shift as a function of temperature of HgSe NCs (d), HgTe NCs (e) and HgSe/HgTe mixture (f).

Upon absorption of a photon that matches the intraband transition, an electron from the conduction band ground state $1S_e$ is promoted to the excited state $1P_e$ in the HgSe nanocrystal. The HgSe/HgTe mixture is designed to facilitate the transport of the photogenerated carrier through the interband HgTe matrix to contribute to the photocurrent. The observed difference in the photocurrent spectrum of the mixture is attributed to the inefficient charge transfer between HgSe and HgTe nanocrystals, resulting in an intraband contribution from HgSe that is only 1/6 of the interband contribution from HgTe, yielding a charge transfer efficiency of around 17%. While the concept of the HgSe/HgTe mixture has been established, a detailed analysis of the coupling between the populations of both nanoparticles has not yet been performed. In collaboration with Davide Boschetto at the Laboratoire d'Optique Appliquée, we investigated the charge transfer dynamics using an infrared transient reflectivity measurement in a pump-probe configuration. The experimental setup operates in a non-degenerate mode, with the pump operating at 800 nm (Ti:sapphire laser - 1.55 eV - 35 fs pulse duration) and the probe set at 4 µm (optical parametric amplifier - 0.32 eV - 50 fs pulse duration), matching the intraband gap of HgSe. A comparative analysis of the transient signals measured for HgTe, HgSe, and the mixture is performed since the experimental configuration does not allow for an accurate determination of exciton lifetimes and intrinsic processes in each of the nanocrystal hosts. The HgTe, HgSe, and mixture nanocrystals undergoes the same liquid-phase ligand exchange procedure as for the photoconductive experiments. They are then deposited on sapphire substrates via spin-coating, with a film thickness of around 100 nm. The electronic structure of HgSe is shown in Figure 27b. In the steady state, the Fermi level lies in the

conduction band between the $1S_e$ and $1P_e$ states. This degenerate doping results in a valence band filled with electrons, while the 1Pe and upper states (called hot states HS) are unoccupied. As explained earlier, the $1S_e$ state of HgSe is mostly filled with two electrons per dot with their initial long DDT ligands, while the doping is reduced to 0.2 to 2 electrons per dot with their short ones.[171,172]

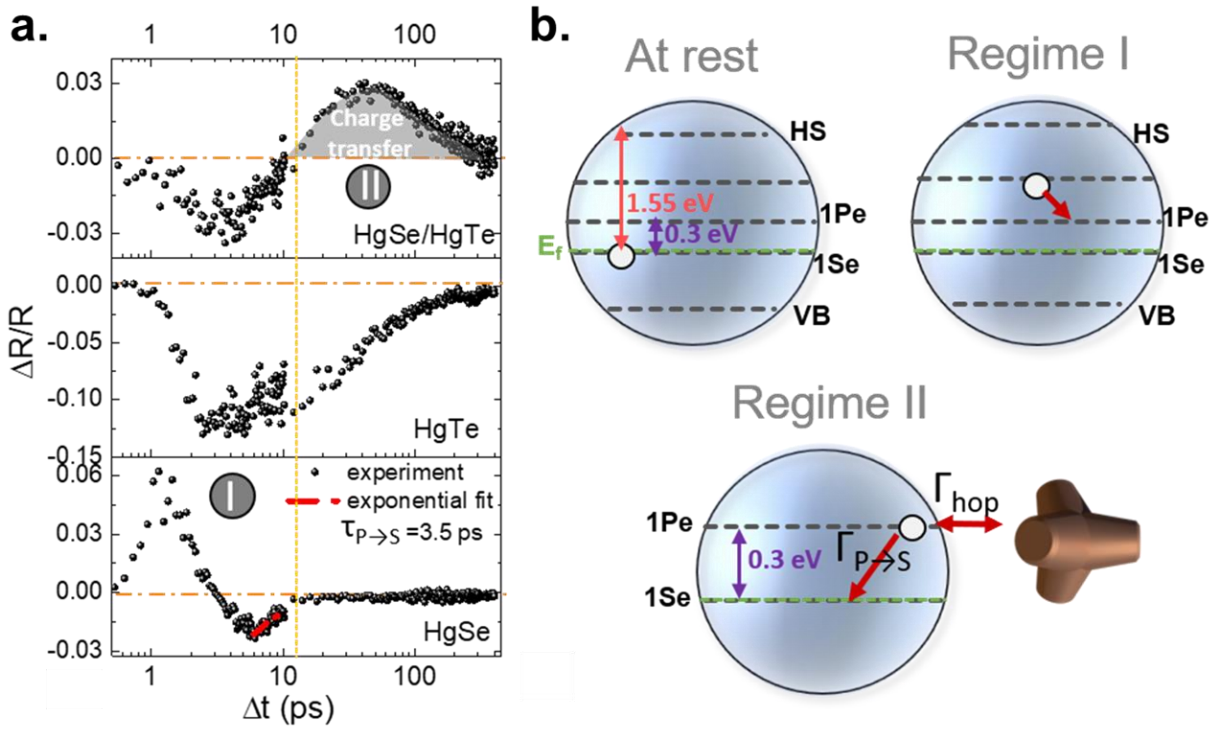

Figure 27 Dynamics of the carrier relaxation in HgX nanocrystals. a. Transient reflectivity signal as a function of time for the film made of HgSe (bottom), HgTe (middle) and HgSe/HgTe mixture (top). The yellow dashed line splits the regime I and II. b. Schematic of the HgSe NC electronic structure for different time ranges as defined in the bottom panel of part a.

The infrared (IR) transient reflectivity setup is employed to investigate the dynamics of charge transfer in HgSe/HgTe nanocrystal mixture. The setup consists of a pump which illuminates the samples, generating a hot electron with high energy (1.55 eV) compared to the interband gap. This energy is sufficient to excite electrons from either the $1S_e$ state or valence band states. In the latter case, carriers are excited to lower energy states and will thermalize on a shorter time scale, with the cooling rate appearing unaffected by the pump excitation in intraband nanocrystals.[182] Figure 27a displays the transient reflectivity signal $\Delta R/R$ for the HgSe/HgTe mixture, HgTe, and HgSe. In the case of pristine HgSe NCs (last panel corresponding to regime I in Figure 27b), a positive $\Delta R/R$ is observed from 0 to 3 ps, which is indicative of a photon-induced absorption (PIA). One plausible mechanism for this PIA is an energy shift of the intraband transition due to hot carriers generating a Stark effect. Other effects, such as hot intraband transitions or a shift resulting from exciton-exciton interactions, may also contribute to this PIA. Following this early PIA signal, electrons cool down to the $1P_e$ state (regime I), resulting in a negative $\Delta R/R$ signal since the number of arriving states for the $1S_e$ to $1P_e$ transition is reduced. Then, electrons relax from the $1P_e$ to the $1S_e$ state (end of regime I), and the corresponding time $\tau_{P\to S} = 3.5\ ps$ is extracted from an exponential fit, as demonstrated in the last panel of Figure 27a. This relaxation time is consistent with intraband dynamics observed in CdSe[183] or HgTe[182,184] nanocrystals, which typically range between 1 and 10 ps. In the case of pristine HgTe, only a negative transient reflectivity signal $\Delta R/R$ is observed, as illustrated in the top panel of Figure 27a.

The HgSe/HgTe mixture displays a negative $\Delta R/R$ at a short time scale of 1 – 10 ps, followed by a positive contribution at a long-time scale (> 10 ps, corresponding to regime II in

Figure 27b). The duration of this signal is longer than the intraband relaxation time of either pristine material and is not observed in either of the two pristine materials. This contribution can be interpreted as the signature of a charge transfer between HgSe and HgTe nanocrystals. In the hybrid, a new relaxation pathway becomes available for photogenerated carriers, where they can relax either within the initial nanoparticle or *via* charge transfer. The positive $\Delta R/R$ signal indicates that excited electrons transfer from HgTe to HgSe. An increase in the population of HgSe results from a photogenerated carrier in HgTe, which leads to an increase in intraband absorption (positive $\Delta R/R$). The charge transfer hypothesis can be modeled by calculating the characteristic hopping time. In a diffusive model, the hopping time is given by:

$$\tau_{hop} = \frac{eR^2}{\mu k_B T}$$

Where e is the proton charge, R is the nanoparticle radius, μ is the carrier mobility, and $k_B T$ is the thermal energy. Considering a charge transfer between two types of particles, the expression can be generalized as:

$$\boxed{\tau_{HgSe\rightarrow HgTe} = \frac{eR_{HgSe}R_{HgTe}}{\mu k_B T} \approx 50\ ps} \quad with \begin{cases} R_{HgSe} = 2.5\ nm \\ R_{HgTe} = 5.0\ nm \\ \mu = 10^{-2}\ cm^2.V^{-1}.s^{-1} \end{cases}$$

The charge transfer characteristic time scale is found in the 30 – 50 ps range in the IR transient reflectivity measurement, which matches our theoretical calculation. Moreover, the determined dynamics explains the relative magnitude of the intraband contribution in the photocurrent spectrum shown earlier in Figure 25b. An electron promoted to the $1P_e$ state in HgSe can relax throughout a charge transfer in 30 ps or an internal relaxation ($1P_e$ to $1S_e$) in 3.5 ps. The efficiency of the charge transfer is then given by:

$$\frac{\tau_{P\rightarrow S}}{\tau_{HgSe\rightarrow HgTe}} = 12\%$$

This value is considered as an order of magnitude given the temporal broadening of each feature. However, the 12% charge transfer efficiency is consistent with the 17% determined from the relative magnitude between intraband and interband signal determined in the photocurrent spectrum.

The limited efficiency of this transfer leads to a decrease in intraband absorption in the MWIR photodetector. In the subsequent sections, we will introduce a strategy for managing the coupling between light and matter, with the aim of boosting intraband absorption for close-to-HOT sensor operation.

2.3 Enhanced light-matter coupling for intraband detection

Infrared photodetectors are essential devices for a variety of applications, including telecommunication, gas sensing or imaging. High performances in these devices are crucial to achieve efficient and sensitive detection of infrared light. The introduction of light managements strategies in infrared detectors has been a key factor in achieving such goal. The concept of resonators has been applied in many fields, such as lasers, fiber optics, or microcavities. The resonator's ability to trap and confine light in a small volume results in an enhancement of the electromagnetic field, which in-turn leads to a higher probability of light-matter interaction. This concept gained significant attention in the infrared community with the development of QWIPs. Initially, it was used as a strategy to break the optical selection rule by coupling the incoming light away from the normal incidence in QWIPs, and then later to increase the quantum efficiency in these detectors. In the early 2010s, optical nanoresonators have been extended to nanocrystal-based infrared detectors to enhance their performances. This section will first discuss the various types of resonators employed in NC-based detectors. Secondly, we will demonstrate that utilizing a specific type of resonator, known as the guided-

mode resonator (GMR), close-to High Operating Temperature (HOT) operation can be achieved for a MWIR detector based on the HgSe/HgTe mixture.

2.3-1 State-of-the-art of resonators applied to NC-based infrared photodetectors

In nanocrystals, hopping transport results in a carrier diffusion length that is typically in the range of 10 – 100 nm, which is shorter than the absorption depth of the material (µm). Therefore, a thin film of nanocrystals, typically ranging from 100 – 200 nm, would only absorb a small percentage of the incoming light, generally around 10 – 20%. Although increasing the film thickness[185] may increase the absorption, it is usually limited by the short transport diffusion length[186]. Thicker films, despite their greater absorption, do not necessarily generate larger photocurrent. In recent years, researchers have turned to the concept of optical resonators to address this issue in NC-based sensors. By confining the incoming light within the thin film, the absorption is enhanced while maintaining the film thickness compatible with the transport diffusion length.

Various types of optical resonators have been implemented in infrared photodetectors based on epitaxially grown semiconductors, such as nanostructured interfaces[187,188], periodic nanophotonic structures[189–192], or the incorporation of metallic nanoparticles[193–196]. The main principle behind the former two strategies is to induce resonances in the absorbing layer through optical nanoresonators, which extend the optical path and increase the electromagnetic field, leading to an enhancement of photodetector absorption. The latter strategy relies on the interaction between light and surface plasmons in metallic nanoparticles to enhance the electromagnetic field. Near the resonant structure, a localized electromagnetic field is generated, which increases the light absorption from the adjacent material. The fabrication of nanocrystal-based infrared photodetectors requires a carefully designed top-down approach. Infrared nanocrystals are typically grown at low temperatures (< 100 °C), and cannot withstand high temperature operation as they would sinter. Therefore, the introduction of an optical resonator must be carried out prior to the deposition of nanocrystals, as the photodetector back-end undergoes several lithography processes that require high temperatures for resist baking, typically above 120 °C.

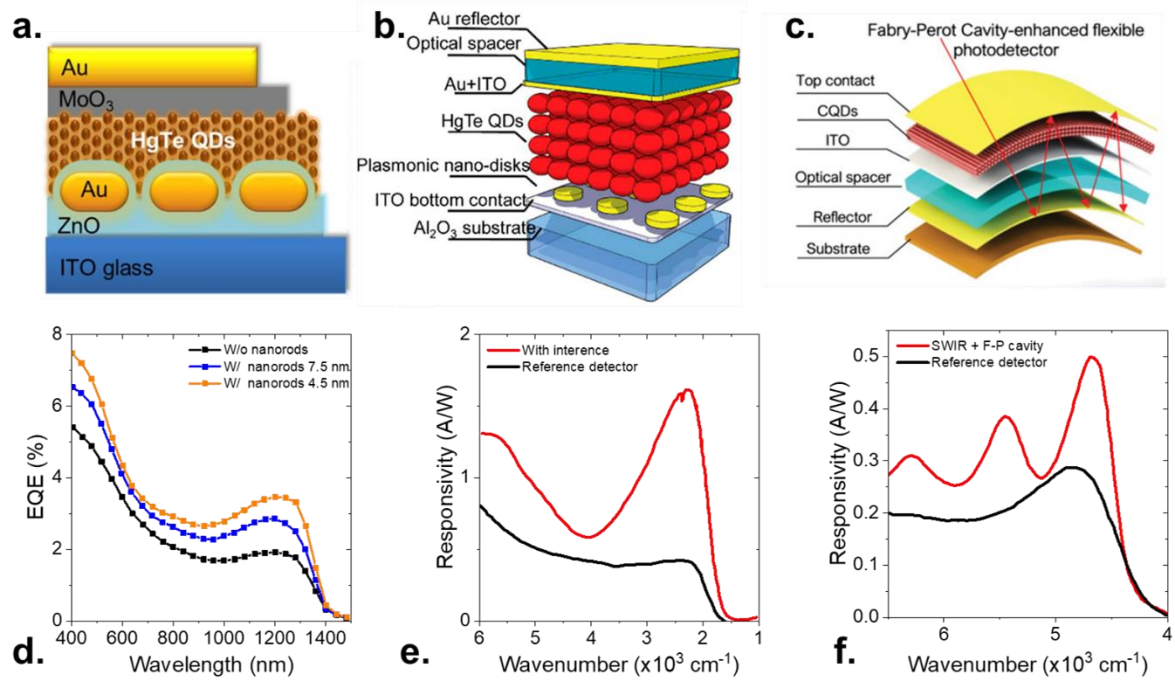

Figure 28 Optical resonators applied to NC-based infrared photodetector. a. HgTe NCs/ZnO heterojunction with gold nanorods embedded within the ZnO layer. d. External quantum efficiency of the same device as function of the wavelength. (a) and (d) are adapted from ref.[137]

b. Illustration of the HgTe NCs detector with interference structure and a plasmonic disk array. e. Measured spectral responsivity of the same sensor. (b) and (e) are adapted from ref.[138] *c. Illustration of a Fabry-Perot cavity enhanced HgTe photodetector. f. Spectral responsivity of the SWIR HgTe sensor with and without the F-P cavity. (c) and (f) are adapted from ref.*[143]

The coupling of resonators with mercury chalcogenide films is typically accomplished by introducing plasmonic resonances induced by gold nanodisks or nanorods localized beneath the NC film. In 2014, Chen *et al.*[137] were the first to couple gold nanorods to HgTe absorbing films in a photovoltaic device, as depicted in Figure 28a. These metallic nanorods exhibit two resonances, depending on the direction, and the one associated with the long direction falls in the near-infrared region around 900 nm. HgTe with small sizes were grown to match this wavelength, while a ZnO spacer was deposited on top of the gold nanorods in order to avoid any quenching of the exciton. The authors demonstrated a two-fold enhancement of the photodiode external quantum efficiency (EQE 2% → 4%), as shown in Figure 28d.

Following this work, Yifat *et al.*[134] extended this strategy to the mid-infrared (MWIR), using a photoconductive configuration. In their device, the MWIR HgTe layer is deposited on top of interdigitated electrodes and gold nanorods. The authors demonstrated a three-fold enhancement of the photocurrent. However, the latter is polarization-dependent since the structure is based on gold nanorods, and therefore only increases along the rod polarization. Using nanodisks instead of nanorods as a resonant structure avoids any polarization effects. In 2018, Tang *et al.*[138] integrated plasmonic gold nanodisks in an HgTe-based photodiode operating in the MWIR, as depicted in Figure 28b. In addition to a three-fold enhancement of the photocurrent, they showed that the spectral response could be tuned with the period of the resonant structure. This offers a new degree of freedom for post-synthesis design of photodetectors.

While plasmonic resonators have been successfully integrated into HgX-based infrared sensors, they introduce optical losses in the metallic electrodes due to the spatial localization of the mode near the metal. Hence, other types of light resonators have been proposed, including Fabry-Perot resonators[40,143]. The latter are optical cavities that consist of two parallel, partially reflecting mirrors. They are widely used in optics and photonics to enhance the intensity of light by confining it within the cavity and causing it to undergo multiple reflections and interference. Compared with plasmonic resonators, Fabry-Perot cavities are independent of the angle of incidence of the incoming light and can be integrated onto flexible substrates, as demonstrated by Guyot-Sionnest and coworkers.[143] In the same work, the authors achieved broadband absorption over the short-wavelength infrared (SWIR) by coupling a plasmonic resonator to a Fabry-Perot cavity, as shown in Figure 28d. This broadband absorption is certainly appealing for multispectral detection in the infrared range, which is achieved in solar cells where up to nine resonances can be implemented.[197]

Throughout my doctoral research, I extensively employed guided-mode resonators (GMRs), a type of optical resonator that utilizes periodic nanophotonic metallic structures. This resonator design for nanocrystals was developed at Onera by A. Chu and G. Vincent. In the subsequent section, I will explain the underlying principles of GMRs, in addition to elucidating their coupling with nanocrystal films.

2.3-2 Guided-mode resonator: history and principle

Guided mode resonators have a rich history that dates back to the early 1900s, when John Tyndall first observed light being guided through a falling stream of water. By directing a beam of sunlight at the path of water as it flowed from one container to another, Tyndall demonstrated that light followed a specific path using internal total reflection. Although he knew that light was temporarily trapped inside the stream of water, he could not explain the underlying mechanism at the time. In the late 1960s, integrated optics emerged as a field of study, where the use of optical fibers replaced traditional wired and radio links, enabling light-waveguiding rather than through-the-air optical paths.[198] The advent of the first lasers in the early 1960s provided a stable source of coherent light, making this technology possible. The concept of guided mode resonances was first proposed in the 1990s by S. S. Wang and R.

Magnusson, who introduced a high-efficiency resonant grating filter using the principle of waveguide-mode coupling.[199–201]

GMRs are optical resonators that confine light within a waveguide structure, allowing for strong light-matter interactions. The basic design of a GMR consists of a planar waveguide with a high-refractive index layer sandwiched between two lower-index layers. The high-refractive index layer forms a resonant cavity where light can be confined and resonated. In GMRs, the waveguide layer is patterned with a periodic array of structures acting as a diffraction grating, which couples the incoming light within a uniform waveguide layer or directly within the grating. The careful choice of material and geometrical parameters allows for precise control of the resonance wavelength and polarization, making GMRs ideal for wavelength-selective filtering and polarization-sensitive applications.

The concept of guided mode resonances has been successfully applied to nanocrystal-based photodetectors.[136,202,203] This particular structure comprises of a thin metallic grating and a thin dielectric film (nanocrystal film) serving as a waveguide. The metallic grating acts as a diffraction grating that facilitates the coupling of diffractive waves to the horizontal waveguide eigenmodes. In contrast to plasmonic resonators, where surface plasmons are evanescent waves and can result in thermal losses in the metal, GMR resonances are mainly localized in the nanocrystal film. This reduces thermal losses as resonances in GMRs, since they depend on the diffraction of propagative modes that can be localized in the nanocrystal film. However, GMR nanostructures exhibit a significant drawback in their strong dependence on the angle of incidence of the incoming light, leading to a considerable reduction of the resonance amplitude away from the normal incidence. Lemarchand *et al.*[204,205] have introduced metal-dielectric structures composed of bi-atomic grating coupled to GMR nanostructures in order to enhance the angular tolerance of GMR devices. However, implementing such an architecture[206] entails a lithography process on the dielectric layer, which is currently unfeasible for nanocrystals due to the potential sintering that would occur.

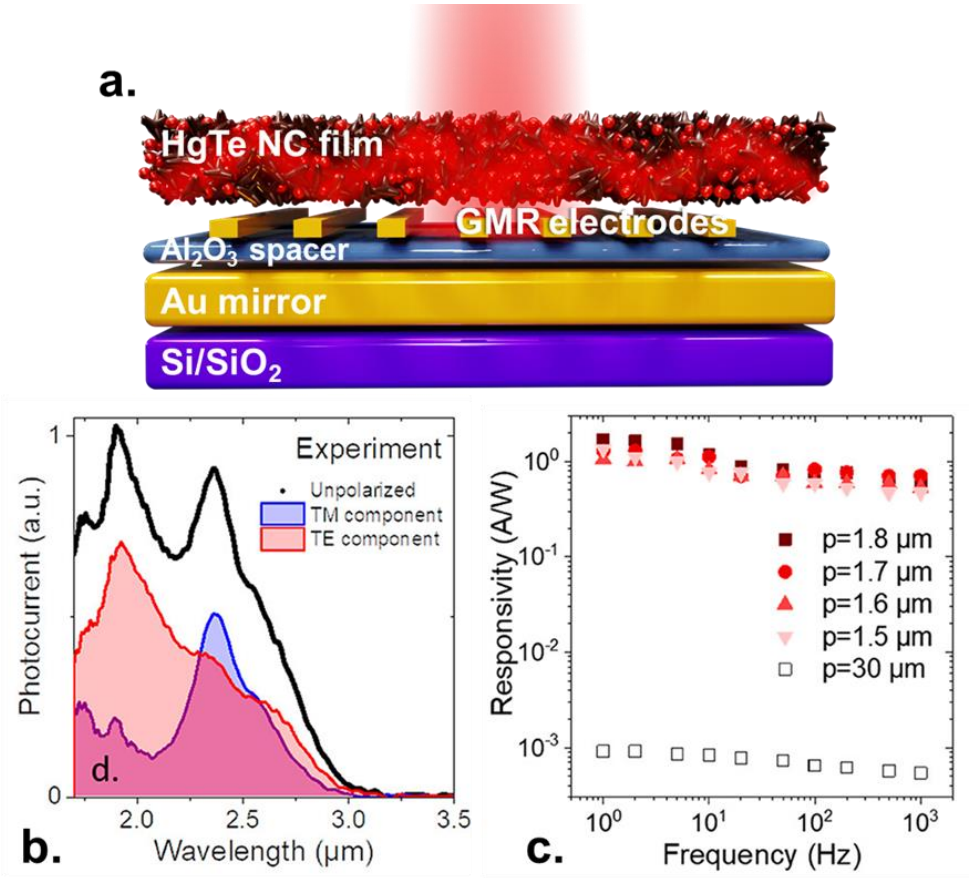

Figure 29 GMR nanostructures coupled with HgTe QDs for sensing at 2.6 µm. a. Illustration of the HgTe-based detector with the integration of GMR nanoelectrodes. b. Photocurrent spectra of the device in TM, TE polarizations and unpolarized. c. Responsivity as function of the light signal frequency for a reference interdigitated electrode (p = 30 µm) and the GMR structures. The light source is a blackbody at 980 °C. Adapted from ref.[136]

The initial integration of guided mode resonance (GMR) nanostructures in a NC-based infrared photodetector was accomplished by Chu *et al*.[136] In their study, they utilized an PbS- or HgTe-based photoconductor that operates in the short-wave infrared region. Unlike prior devices, where the transport was sustained by interdigitated electrodes that were entirely decoupled[134] from the array of resonators, Chu *et al.* proposed a combination of both functions within the same set of electrodes. The period and size of interdigitated electrodes were designed to induce the resonance and, to a lesser degree, fine-tune the cut-off wavelength of the material. A back-side gold mirror was also included in the design, which allowed for a second pass of light in the absorbing layer, as depicted in Figure 29a. The pattern of interdigitated electrodes resulted in a polarization-dependent photocurrent that could be utilized to broaden the spectral response. However, the key advantage of designing dual-function nanoelectrodes (*i.e.*, inducing resonance and collecting photogenerated carriers) is the generation of gain. By reducing the electrode spacing, the transit time follows the same trend, which in turn produces an electrical gain. The authors demonstrated a significantly higher enhancement of the photocurrent than the absorption, reaching a factor up to 1000.

During the course of my research, I investigated the integration of GMR nanostructures with HgSe/HgTe mixture for the purpose of designing a highly efficient mid-infrared photodetector. In the subsequent sections, I will elaborate on the design, fabrication and optoelectronic characterization of this intraband detector.

2.3-3 Toward a HOT intraband-based photodetector

2.3-3.1 Tailored structure for MWIR absorption

The initial GMR structure design was developed by A. Chu and G. Vincent at Onera, and we will discuss it along with its fabrication in the following sections. The design of the GMR structure is simulated with Reticolo code[207] on Matlab software. This program, developed by P. Lalanne and J.P. Hugonin at Institut d'Optique, computes the diffraction efficiencies and amplitudes of gratings composed of stacks of lamellar structures. The calculation and visualization of the electromagnetic fields inside and outside the grating can be performed. The Reticolo code is based on the Rigorous Coupled Wave Analysis (RCWA) method developed by Moharam and Gaylord.[208] The RCWA method solves Maxwell's equations in periodic structures by decomposing the fields into Fourier harmonics and matching boundary conditions between the layers. This allows the calculation of the reflection, transmission, and diffraction of light at various angles and wavelengths. The refractive index of each layer is taken into account in the numerical analysis. The refractive index is given by:

$$\underline{n} = n + ik$$

Where n (resp. k) is the real (resp. imaginary) part of the complex refractive index. The determination of the spectral dependence of k in NC films entails the measurement of the absorption spectrum, which is then normalized to the exciton band-edge using the absorption coefficient. Meanwhile, the refractive index's real component, n, is ascertained through ellipsometry measurements[209], with an approximate value of 2.35[139] for HgTe films. Geometric factors such as layer thickness and structuration (period and size) must also be taken into account. Many of the thicknesses are predetermined, such as the 80 nm-thick back-side gold mirror for total reflection or the 40 nm-thick Al_2O_3 dielectric layer for insulation. The NC film thickness ranges in the order of a few hundred nanometers. Thus, the size of the gold electrodes must be within the 100 ± 50 nm range, achieving a balance between high-quality film deposition and contact resistance. Finally, the driving parameter to tune the resonance in a GMR structure is the period of the interdigitated electrodes. At least one mode must be

diffracted within the waveguide and not in the air to induce a resonance in the structure. This requirement is satisfied if the following condition is met:

$$p < \lambda_R < pn_{NC}$$

With p the period of the grating, n_{NC} the nanocrystal film refractive index taken as 2.35 for the HgSe/HgTe mixture, and λ_R the resonant wavelength. To match the intraband absorption, a resonance at $\lambda_R = 4.4\ \mu m$ is targeted. Thus, the period can be adjusted within $1.9\ \mu m < p < 4.5\ \mu m$, depending on the nanocrystal film thickness, which is typically in the 200 – 300 nm range. Along with these parameters, the height and width of the gold electrodes are optimized to maximize the effective device absorption (*i.e.*, within the NC film). Figure 30a illustrates the device structure based the coupling of an HgSe/HgTe mixture to a guided-mode resonator, which I used during this project. From bottom to top, the infrared photodetector consists of:

- A Si/SiO_2 substrate.
- A back-side gold mirror allowing for a second pass of the incoming light.
- An Al_2O_3 dielectric electrical insulator between the back-side gold mirror and the electrodes.
- GMRs gold nanoelectrodes inducing the optical resonance matching the intraband transition and collecting the photogenerated carriers.
- A HgSe/HgTe nanocrystal film.

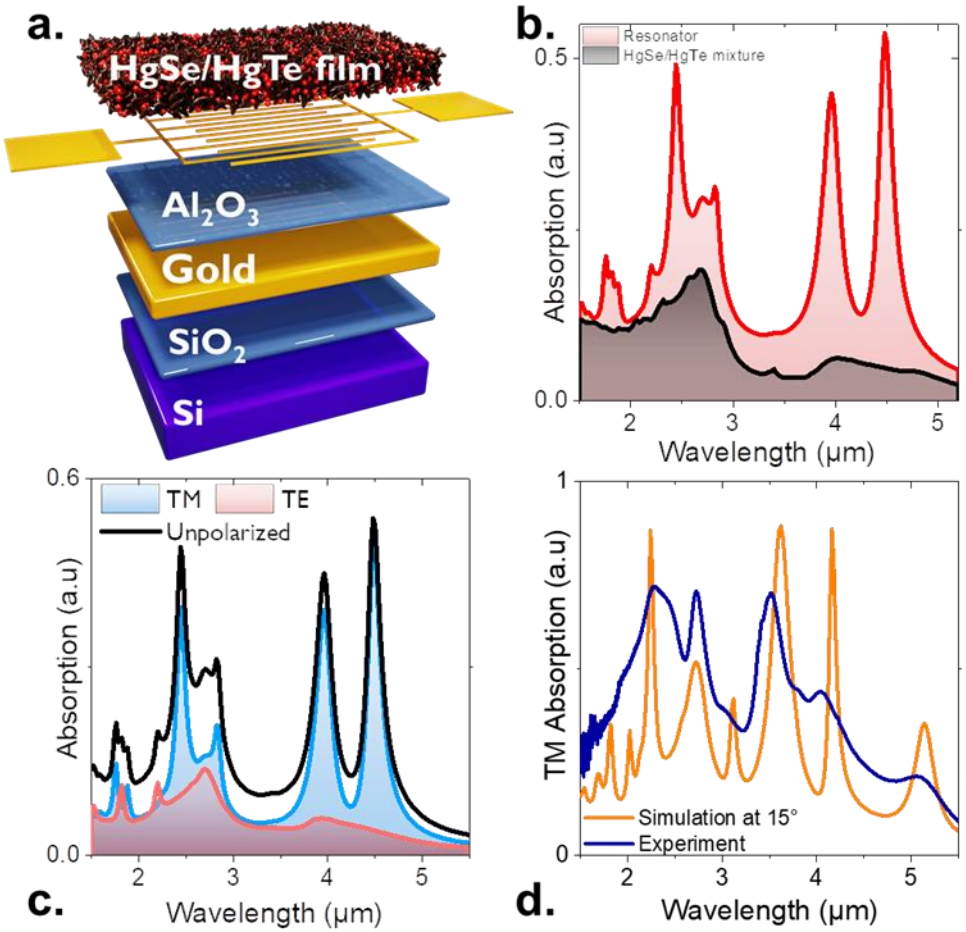

Figure 30 Guided-mode resonator for enhanced intraband absorption. a. Schematic of the GMR device coupled to an intraband absorbing film made of HgSe/HgTe NC mixture. b. Simulated absorption spectra for reference interdigitated electrodes (i.e., without resonance) and for GMR electrodes, under TM polarized wave. c. Simulated absorption spectrum for GMR electrodes for unpolarized light and its TE and TM component. d. Comparion of the measured absorption (mean collect angle is 15°, with 10° aperture) and simulated absorption with a 15 ° angle (plane wave) along TM polarization.

The absorption spectrum of the GMR device is simulated and compared with a reference device comprising interdigitated electrodes without any induced resonances, as depicted in Figure 30b. The GMR device exhibits a distinct resonance that matches the intraband absorption at 4.4 µm (2200 cm^{-1}). As the optical resonator is a one-dimensional grating, the absorption is strongly polarized and the resonance occurs in the transverse magnetic (TM) polarization, where the electric field lies in the plane of incidence, as illustrated in Figure 30c. Infrared microscopy is used to determine the device absorption. This method combines an FTIR and a microscope, enabling the measurement of the reflectivity of a sample. In the present device, a back-side gold mirror prohibits any transmission of the incoming light, and therefore, the total absorption can be determined as $Absorption = 1 - Reflection$, assuming that reflection does not involve diffracted orders. Additionally, the optics employed in the experimental setup introduce a mean angle of 15° for light collection. As previously mentioned, a standard GMR structure is highly dispersive and thus, the 15° angle causes a shift in the resonant peak. Figure 30d compares the experimental results with the simulated absorption and displays a good correlation between the energy of the resonance peaks.

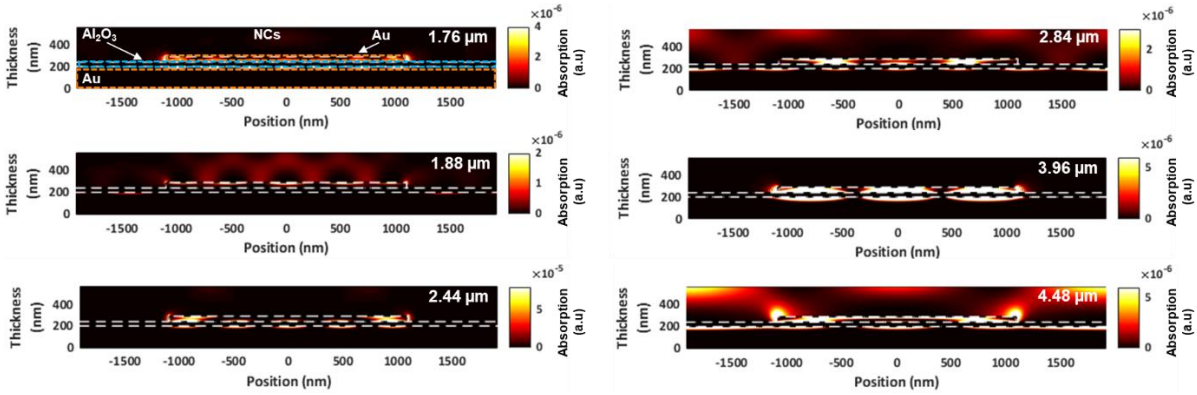

Figure 31 Spatial mapping of the different resonance peaks induced by the GMR structure.

In addition to the primary resonance intended to match the intraband absorption of HgSe in the MWIR, several other resonance peaks can be observed at 1.76, 1.88, 2.44, 2.84, and 3.96 µm, as illustrated in Figure 30c. As previously mentioned, in a GMR nanostructure, the propagative modes undergo diffraction, which can be localized far from the grating. Thus, a resonance would contribute to the photocurrent only if it is localized in the nanocrystal film. If the resonance is located in the metal, it leads to thermal losses. In Figure 31, we simulate a spatial mapping of the absorption loss for each resonance, and Table 2 provides an estimation of the absorption occurring in the nanocrystal film. Out of these six resonances, the main contributions expected are the resonance matching the intraband absorption of HgSe at 4.4 µm and the one matching the interband absorption of HgTe at 2.44 µm. The anticipated absorption for the intraband resonance is approximately 60%, which is a promising result that could improve the sensor's signal-to-noise ratio and its temperature of operation.

Table 2 Estimation of the absorption of the device and in the NC array for each resonance.

Peak position	% TM absorption	% absorption within NCs
1.76 µm	29%	42%

1.88 µm	22%	79%
2.44 µm	**79%**	**44.5%**
2.84 µm	41%	64%
3.96 µm	78%	12.5%
4.48 µm	**99%**	**60.80%**

The GMR nanostructure design has been established through an optimization process of its geometrical parameters using Reticolo code. The optimization aimed to maximize absorption at the intraband wavelength of 4.4 µm. Additionally, a spatial mapping analysis was performed to verify that the resonances matching both intraband and interband contributions are confined within the nanocrystal film, indicating the generation of photocurrent. This numerical analysis step is crucial for the successful integration of an optical nanoresonator in a photodetector, as it provides the necessary geometrical parameters. Once the simulation of the GMR structure to enhance intraband absorption was completed, I could begin the device fabrication process at the cleanroom facility located at the Institut des NanoSciences de Paris.

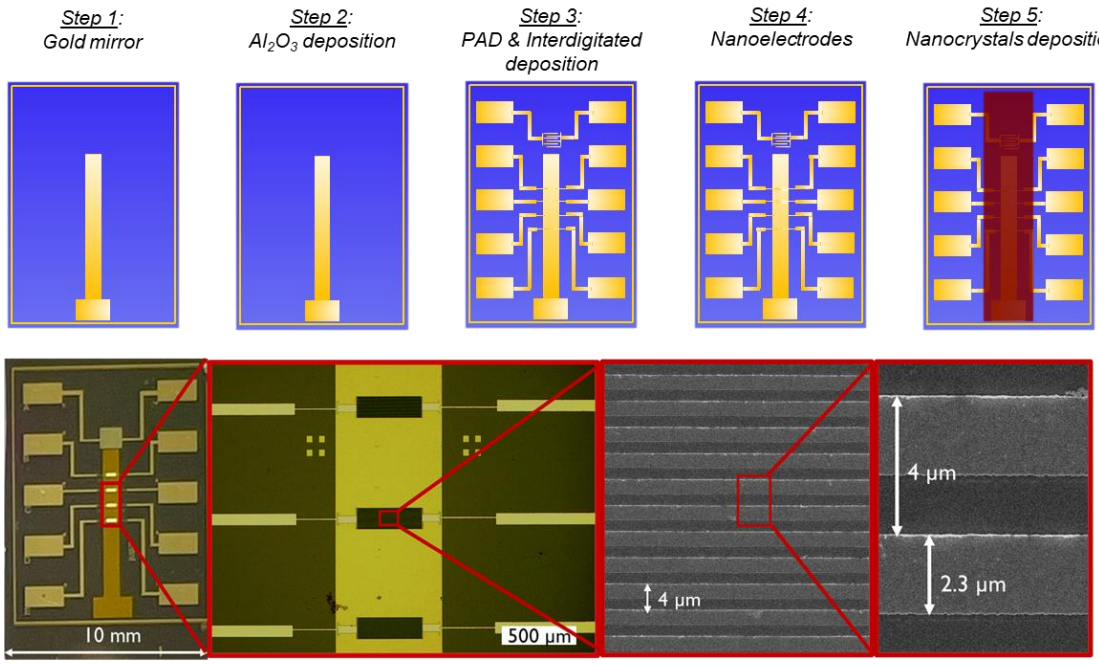

Figure 32 Integration of GMR nanostructures in a NC-based photodetector. The top part illustrates the main steps involved in the fabrication of the electrodes to induce a guided-mode resonance. The bottom part depicts a progressive zoom of the GMR device with optical and e-beam microscopy.

Figure 32 depicts the key stages involved in the fabrication of the mid-infrared photodetector. A Si/SiO_2 substrate with a dimension of 10x12 mm^2 is used. Firstly, a first UV lithography is conducted to deposit 5 nm of chromium (Cr - adhesive promoter) and 80 nm of gold (Au) to create a fully reflective back-side gold mirror. This is followed by an atomic layer deposition (ALD) process, in which 40 nm of alumina (Al_2O_3) is deposited to serve as an insulator between the mirror and the electrodes. The next step involves a second UV lithography process to align with the first one and deposit the contact pads (5 nm Cr + 150 nm Au) and the reference interdigitated electrodes. The latter are 1 mm long, 10 µm wide, and spaced 20 µm apart. Subsequently, the GMR nanostructures are fabricated between the

contact pads. The period of the interdigitated electrodes for the GMR is optimized through simulation and ranges from 3 to 4 µm to accommodate variations in the thickness of the NC film between 200 and 400 nm. Since these dimensions are at the limit of resolution for UV lithography, e-beam lithography is used to fabricate the GMR electrodes. The optoelectronic properties presented in the subsequent section correspond to a GMR structure comprising 20 pairs of electrodes, each 500 µm long, 2.2 µm wide, and spaced 3.85 µm apart. The final step involves the deposition of the HgSe/HgTe ink mixture, which is optimized for the spin-coater parameters and ink concentration to achieve a final film thickness of approximately 250 nm.

2.3-3.2 Mid-infrared photodetection performances

Characterizing the optoelectronic properties of an infrared detector is an essential step in the development and optimization of such devices. These detectors can operate based on different mechanisms, such as photovoltaic, photoconductive, and bolometric effects, which require different approaches in characterization. In this context, I characterized the HgSe/HgTe mixture-based sensor coupled with a light resonator operating a photoconductive mode. The detector is placed in a close-cycle cryostat and various techniques are used to determine its spectral response, electrical bandwidth, and detectivity.

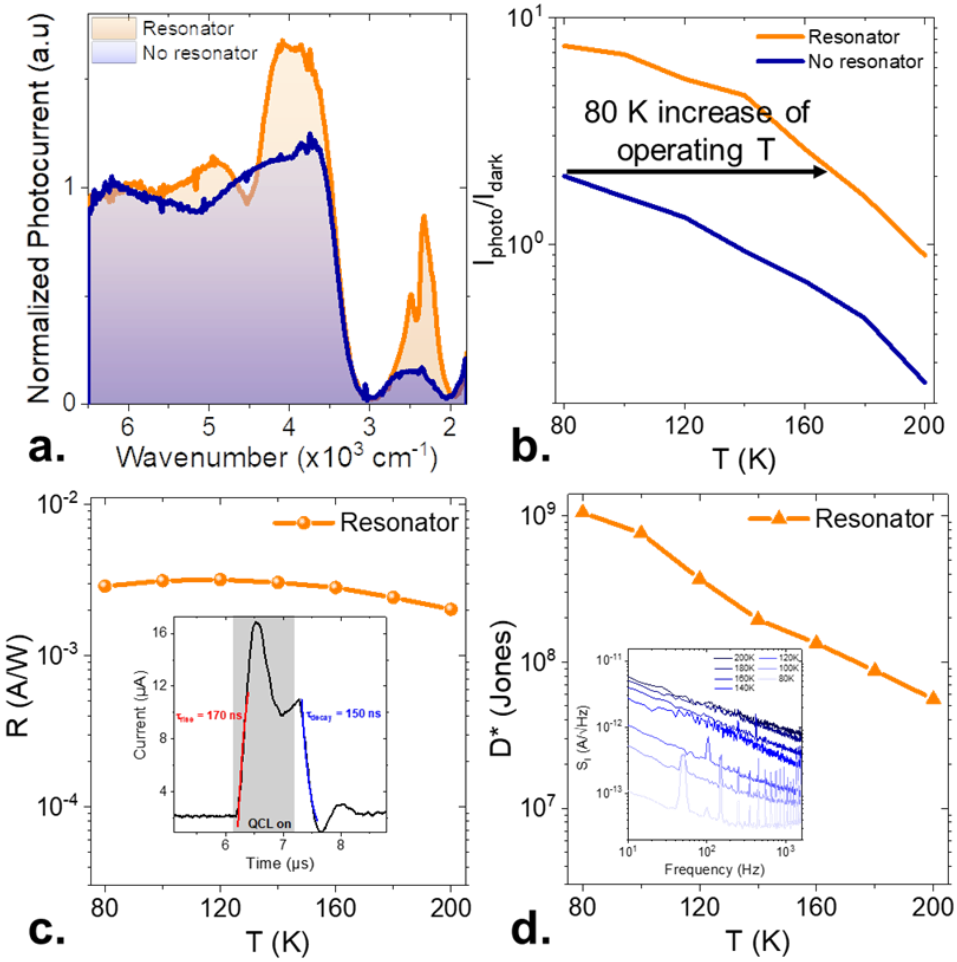

Figure 33 Photodetection performances of the intraband device coupled with GMRs. a. Photocurrent, under 0.1 V and at 80 K, spectrum for the GMR device and the reference one without resonances. b. Ratio of the intraband photocurrent (i.e., QCL illumination at 4.4 µm) over the dark current as a function of temperature for reference interdigitated electrodes (i.e., without resonance) and for GMR electrodes. c. Responsivity, at 1.5 V, under blackbody illumination for the GMR device as a function of temperature. The inset is the photocurrent time trace as a response to a 1 µs long pulse of light at 4.4 µm, spectrally matched with intraband absorption. d. Specific detectivity (at 1 kHz, under 1.5 V) for the GMR device as a

function of temperature under blackbody illumination. The inset is the noise current density for different temperatures under 1.5 V.

Figure 33 illustrates the performance of the mid-infrared photodetector with GMR nanostructures. The first characterization conducted was the spectral response of the device to verify the accuracy of the numerical simulation. The GMR device displayed two distinct signals that closely matched the intraband of HgSe and the interband of HgTe, in accordance with the simulation predictions. Figure 33a shows that the intraband absorption of HgSe was enhanced by a factor of 4 in comparison to the reference electrode. To provide a more detailed assessment of the benefits of GMR electrodes, the sample was illuminated with a quantum cascade laser that matched the intraband absorption signal, thus excluding the contributions from high-energy-absorbing transitions. The photocurrent-to-dark-current ratio was then plotted as a function of temperature, revealing a significant 4-fold improvement. Furthermore, as illustrated in Figure 33b, the GMR structure enabled an increase in the operating temperature of up to 80 K when compared to the device without light trapping (*i.e.*, reference electrodes). Achieving such a high operating temperature is crucial to the development of High Operating Temperature (HOT) MWIR sensors, which is currently a major challenge in the field of infrared detection. The cooling requirements for conventional infrared detectors result in additional power, size, and weight, which restrict the mobility and versatility of the sensors.

Table 3 Figure of merit for infrared photodetectors based on the intraband absorption of nanocrystals. PC = photoconductor, PD = photodiode.

Intraband absorbing material	Device structure	λ (μm)	R ($A.W^{-1}$)	D* (Jones)	Operating T (K)	Times response	Reference
HgSe	PC	4.4	$5x10^{-4}$	$8.5x10^{8}$	80	-	[55]
HgSe	PC	6	0.8	$\approx 10^{8}$	300	-	[57]
HgSe	PD	4	$5x10^{-3}$	10^{9}	80	<200 ns	[106]
HgSe	**PC + resonator**	**4.4**	**$3x10^{-3}$** **$2x10^{-3}$**	**10^{9}** **$6x10^{7}$**	**80** **200**	**<200 ns**	**This work**[210]
HgSe	PC	4.5	$8x10^{-2}$	$2x10^{9}$	80	μs	[174]
Ag_2Se	PC	4.8	$8x10^{-6}$	-	25	seconds	[166]
Ag_2Se	PC	4.5	$4x10^{-4}$	-	90	-	[176]
Ag_2Se	Barrier device	4.5	$13x10^{-3}$	$3x10^{5}$	300	seconds	[177]
Ag_2Se/PbS	PD	4.5	$2x10^{-2}$	$8x10^{6}$	300	-	[211]
PbS	PC	5-9	$\approx 10^{-4}$	$\sim 10^{4}$	80	>200 ms	[170]

The device responsivity was measured as a function of temperature under blackbody illumination, filtered with a germanium window to remove signals below 2 μm, as illustrated in Figure 33c. The sensor responsivity exhibited a weak temperature dependence and was approximately $3\ mA.W^{-1}$ for a bias of 1.5 V. The electrical bandwidth of the detector was then measured using a pulsed QCL that matched the intraband absorption. The rise and fall times were extracted with single exponential fits and were found to be 170 and 150 ns, respectively. These time-responses were among the best reported for nanocrystal (NC) intraband detection, and were orders of magnitude faster than photodetectors based on a single population of

nanocrystals, as detailed in Table 3. The inset of Figure 33d displays the noise current density of the GMR device at different temperatures. The noise was found to be $1/f^{89,212}$ limited, which is characteristic of NC-based photoconductors as discussed in the first chapter of this manuscript. Finally, the specific detectivity D* was calculated as 10^9 Jones at 80 K for a 5 µm cut-off wavelength, and dropped by a decade at 160 K. This MWIR photodetector based on a mixture of HgSe/HgTe NCs coupled to GMR nanostructures demonstrates state-of-the-art performances with a close-to-High Operating Temperature (HOT) prospect.

2.4 Conclusion

Since the discovery of colloidal nanocrystals, they have been primarily used for their optical interband transitions. However, intraband and intersubband transitions have been widely utilized in epitaxially grown III-V semiconductors. In nanocrystals, intraband transitions offer new possibilities for optoelectronics, but there are several challenges related to degenerate doping, such as high dark current, bolometric response, slow dynamics, and weak signal-to-noise ratio. In this study, we present a heterostructure of nanocrystals as a strategy to engineer the wave-functions of the carrier and overcome the challenges associated with doping.

This mixture of HgSe/HgTe nanocrystals acts as a dye-sensitized infrared sensor where the intraband absorption is uncoupled from the transport properties. The hybrid material maintains intraband absorption in the MWIR region while reducing dark current, increasing the activation energy, and accelerating the time-response. Furthermore, we studied the carrier dynamics in this metamaterial using infrared transient reflectivity measurements and found that the relaxation of a photogenerated carrier from the $1P_e$ to the $1S_e$ state in HgSe occurs within approximately 3.5 ps. A comparative study of the pristine materials (HgTe and HgSe) and the mixture reveals the presence of a new feature in the latter, which is attributed to charge transfer. This process occurs within a dynamic range of 30-50 ps related to hopping time from HgSe to HgTe.

Using a HgSe/HgTe mixture reduces the volume fraction of HgSe in the detector, leading to a reduction in intraband absorption. To address this issue, we designed an optical resonator based on guided-mode resonance to increase the intraband absorption. The photocurrent signal of the mid-infrared contribution is enhanced by a factor of four, which enables an increase in the operating temperature by 80 K compared to the reference device without light resonators. This close-to-HOT capability makes the sensor more portable and versatile by reducing power, weight, and size. Finally, the photodetector achieves a detectivity of 10^9 Jones at 80 K for a 5 µm cut-off wavelength and exhibits a time-response below 200 ns, which matches state-of-the-art performances for devices based on intraband absorption.

In the subsequent chapter, we will demonstrate that heterostructures composed of nanocrystals are not confined to colloidal materials alone, but can be expanded to materials possessing diverse dimensionalities. Specifically, we will couple mercury chalcogenide nanocrystals to bulk III-V InGaAs to increase the spectral response in the short-wave infrared (SWIR) and the mid-wave infrared (MWIR), while simultaneously lifting the limitations associated with epitaxial growth.

3 Extending the InGaAs spectral response through the coupling of bulk III-V and colloidal II-VI semiconductors

This chapter presents the first demonstration of the synergistic properties arising from the coupling of HgX nanocrystals with bulk III-V InGaAs. The experimental aspects of this study involved the growth of the InGaAs semiconductor by Ludovic Desplanque at IEMN, the theoretical calculations of the hybrids' spectroscopic properties conducted by Gregory Vincent at Onera, and the nanoparticle growth carried out by Yoann Prado at INSP.

Related articles:

- ***Khalili, A.**; Abadie, C.; Dang, T. H.; Chu, A.; Izquierdo, E.; Dabard, C.; Gréboval, C.; Cavallo, M.; Zhang, H.; Pierini, S.; Prado, Y.; Xu, X. Z.; Ithurria, S.; Vincent, G.; Coinon, C.; Desplanque, L.; Lhuillier, E. Colloidal II–VI—Epitaxial III–V Heterostructure: A Strategy to Expand InGaAs Spectral Response. Appl. Phys. Lett. 2022, 120, 051101.*

- ***Khalili, A**.; Cavallo, M.; Dang, T. H.; Dabard, C.; Zhang, H.; Bossavit, E.; Abadie, C.; Prado, Y.; Xu, X. Z.; Ithurria, S.; Vincent, G.; Coinon, C.; Desplanque, L.; Lhuillier, E. Mid-Wave Infrared Sensitized InGaAs Using Intraband Transition in Doped Colloidal II–VI Nanocrystals. J. Chem. Phys. 2023, 158, 094702*

3 Extending the InGaAs spectral response through the coupling of bulk III-V and colloidal II-VI semiconductors 67
3.1 Mixed-dimensional van der Waals heterostructures 68
3.2 Expansion up to 2 µm of InGaAs spectral response 70
3.2-1 Design of the InGaAs/HgTe infrared sensor 71
3.2-2 Lifting the epitaxial constraint on the spectral response. 76
3.2-3 High electrical bandwidth hybrid photodetector 77
3.3 Toward a MWIR-sensitized InGaAs photodetector 79
3.3-1 Fabrication of the InGaAs – HgSe/HgTe heterostructure 80
3.3-2 Design of a planar p-n junction in the mid-infrared 82
3.3-3 Detection performances of the MWIR photodiode 85
3.4 Conclusion 86

Heterostructures of nanocrystals have attracted significant attention in recent years due to their unique properties and potential for various applications such as efficient light-emitting diodes (LEDs) in displays. Combining nanocrystals with different properties offers great opportunities for advanced device design and performance. The formation of these heterostructure were initially achieved with core-shell structure. Then, as explained in the second chapter, the controlled assembly of two population of nanocrystals with different composition, and size, results in a hybrid material with enhanced optoelectronic properties while lifting the constraint on a complex shell growth. The majority of these heterostructures exclusively rely on the combination of colloidal nanocrystal materials.

One of the key advantages of nanocrystal heterostructures is the ability to engineer the band structure and electronic properties by combining materials with different bandgaps or energy levels. This provides opportunities for enhanced charge separation, and carrier transport, crucial for applications in photodetection. In this chapter, we will demonstrate that these nanocrystal-based heterostructure can be extended to other type of semiconductors, with the possibility to introduced different dimensionalities such as with 2D layered materials. In particular, we will discuss the synergistic coupling between 1D nanowires of bulk InGaAs and 0D HgX nanocrystals. We will show that this heterostructure allows for an expansion of the InGaAs spectral response up to the MWIR while lifting the constraint on the epitaxial growth.

3.1 Mixed-dimensional van der Waals heterostructures

Van der Waals (vdW) heterostructures have emerged as a novel class of materials with unique properties and versatile applications. These heterostructures are composed of atomically thin layers of different two-dimensional (2D) materials, such as graphene, transition metal dichalcogenides (TMDCs), hexagonal boron nitride (hBN), and other layered materials, which are stacked on top of each other through weak van der Waals interactions. The concept of van der Waals heterostructures was pioneered by Novoselov and Geim, the Nobel laureates who first isolated graphene[213], and it has since revolutionized the field of 2D materials. These heterostructures offer an exceptional degree of flexibility and tunability, enabling the combination of different materials with distinct properties, bandgaps, and lattice symmetries. This versatility allows researchers to design and engineer materials with tailored electronic, optical, magnetic, and mechanical characteristics, opening up exciting possibilities for fundamental scientific research and technological advancements.

The assembly of van der Waals heterostructures is typically achieved through a transfer technique, where individual 2D layers are mechanically stacked on top of each other, forming a precisely controlled heterostructure. The weak van der Waals forces between the layers ensure the preservation of the intrinsic properties of each material, while the weak interlayer coupling provides an ideal platform for studying and manipulating the interlayer interactions and electronic properties. Van der Waals interactions extend beyond interplanar interactions in layered materials. Instead, any surface that is passivated and free from dangling bonds can interact with another surface through van der Waals forces. As a result, it is possible to integrate various layered 2D materials with materials of different dimensionalities, creating mixed-dimensional van der Waals heterostructures.[214]

The integration of nanocrystals into mixed-dimensional van der Waals heterostructures with 2D material as graphene or TMDCs (MoS_2, $MoSe_2$) seemed appealing since the latter showed exceptional carrier mobilities and particular electronic structures. In the 2010s, a few demonstrations of mixed vdW heterostructures with nanocrystals have been achieved with PbS[80] and HgTe[35]. Such as with the concept of hybrid presented in the previous chapter, the driving idea of these mixed vdW is to decoupled the photon absorption from the transport of photogenerated carriers. Nanocrystals are used here as light sensitizer due to their easy growth and large spectral tunability, while 2D materials brings their exceptionally large mobilities (60 000 $cm^2.V^{-1}.s^{-1}$ for graphene[215] and 18 $cm^2.V^{-1}.s^{-1}$ for MoS_2[35]) for transport. In order to achieve infrared sensitivity in this phototransistor, a thin film of nanocrystals is

deposited onto the graphene channel. Consequently, upon photon absorption, an electron-hole pair is generated, and one of the carriers (either the hole as depicted in Figure 34a or the electron in Figure 34b) undergoes transfer to the high mobility 2D material, while the other carrier remains confined within the nanocrystal film. The trapping of one carrier facilitates multiple cycles of circulation for the other carrier within the channel, leading to the generation of electrical gain. The authors report gains ranging from 10^5 to 10^8 per absorbed photon. This significant enhancement is demonstrated in Figure 34c-d, where an exceptionally high responsivity of up to 10^7 $A.W^{-1}$ is achieved[35,80], in contrast to the responsivities of the nanocrystal films without the 2D material channel, which are typically in the range of $mA.W^{-1}$ to a few $A.W^{-1}$.[37–39]

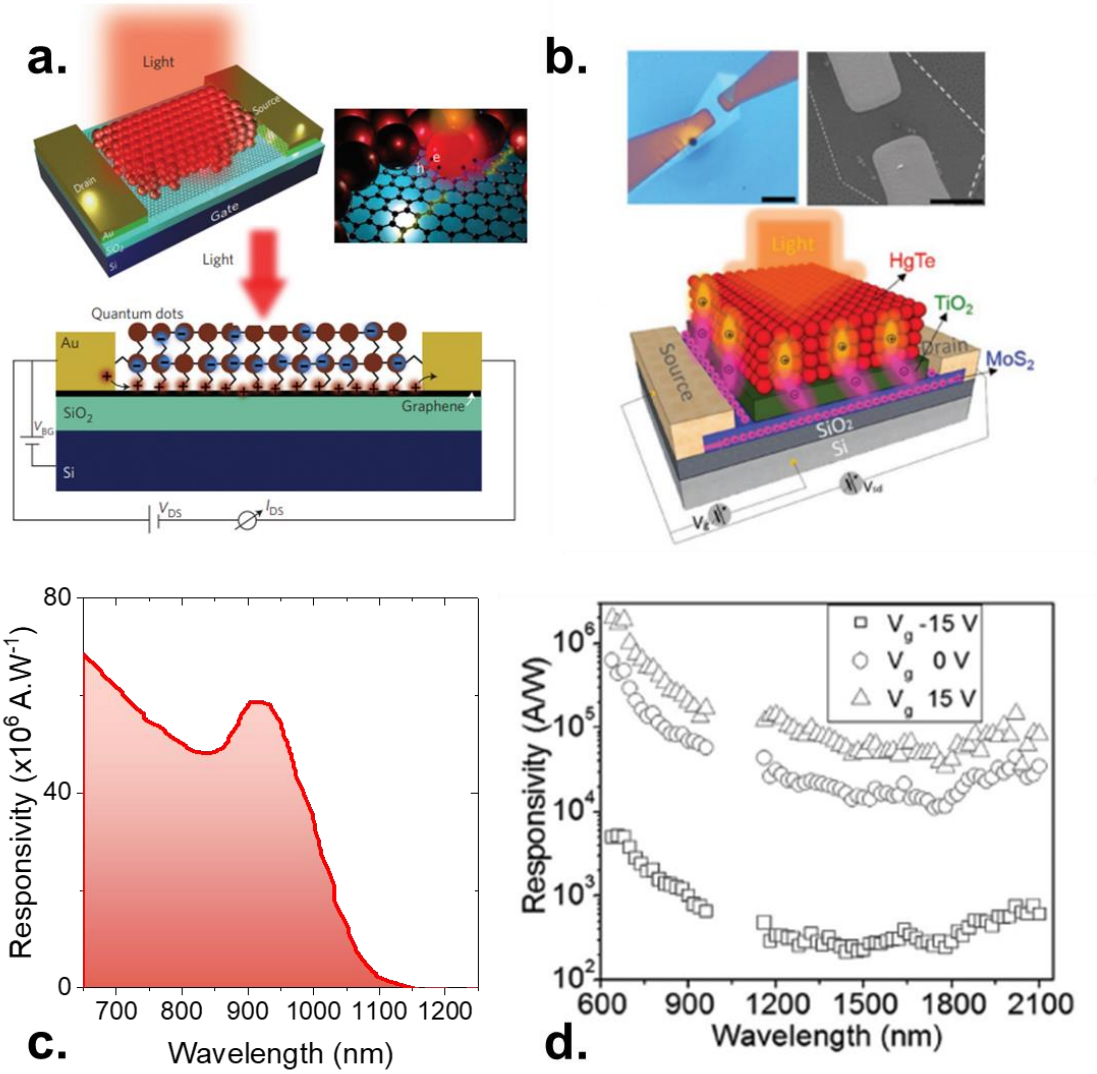

Figure 34 Mixed-dimensional Van der Waals heterostructures with 2D layered materials. a. Schematic of the graphene–quantum dot hybrid phototransistor, in which a graphene flake is deposited onto a Si/SiO2 structure and coated with PbS quantum dots. b. Top part are optical microscope and SEM images of typical $MoS_2/TiO_2/HgTe$ hybrid photodetectors, both scale bars are 5 µm. Bottom part is a schematic diagram of the hybrid device with light illumination and of the photogenerated carrier separation and transport in the hybrids photodetectors. c. Spectral responsivity of the phototransistor presented in part (a). d. Spectral responsivity of the hybrid photodetector presented in part (b). Part (a) and (c) are adapted from ref[80]. Part (b) and (d) are adapted from ref[35].

However, achieving such high gains comes with inherent trade-offs. While the specific detectivity of these devices can reach levels as high as 10^{12} Jones in the near-infrared region,

it is accompanied by a compromise in response time. The aforementioned detectivity values are attained at low frequencies (1 Hz in the given examples). Although the rise time can be relatively short, typically on the order of a few milliseconds, the fall time is considerably longer, extending up to one second. This prolonged response is primarily attributed to the slow dynamics of carrier depopulation within the absorptive layer. Once the carriers are trapped within the graphene channel, they exhibit a propensity to remain confined, contributing to gain enhancement while impeding recombination with the trapped carriers in the film. Consequently, the current exhibits a gradual decrease even after the excitation has been performed. One approach to mitigate this issue involves the application of electric pulses to the gate, thereby reducing the potential barrier that impedes recombination. Despite the implementation of these strategies aimed at minimizing relaxation time, the response time of these devices does not decrease below a few milliseconds, rendering them unsuitable for applications such as imaging that necessitate operation frequencies surpassing the kHz range.

Furthermore, it is important to acknowledge that these 2D materials also possess certain limitations. Graphene, for instance, lacks a bandgap leading to large dark current, while transition metal dichalcogenides (TMDCs) suffer from constraints related to flake size, typically in the range of a few tens of micrometers, which hampers the design of large-scale devices. In addition, large responsivities exhibited by these hybrid structures are predominantly observed under conditions of extremely low photon flux. Overcoming these challenges, such as ensuring material stability, achieving high mobility, precise doping control, and enabling large-scale processing, can be effectively addressed by leveraging the well-established maturity of Silicon[216] or III-V semiconductors[113,114]. However, the exploration of their combination with nanoparticles, specifically in the context of coupling them with nanocrystals, remains relatively unexplored.

In this study, we present the synergistic properties that emerge from the integration of III-V nanowire arrays with II-VI nanocrystals. By exploiting this hybrid structure, we demonstrate the ability to conveniently design the spectral response, enabling the absorption of longer wavelengths beyond the cut-off of bulk InGaAs

3.2 Expansion up to 2 µm of InGaAs spectral response

The history of InGaAs can be traced back to the mid-1950s along with the development of InSb, when researchers began exploring new semiconductor materials for photodetection in the IR region. During this time, the need for high-performance photodetectors capable of operating in the NIR and SWIR wavelengths became increasingly evident. It was recognized that traditional materials like silicon, which are efficient for visible light detection, are limited in their ability to absorb photons in the IR range.

The advantages of InGaAs for infrared photodetection are numerous. Firstly, its narrow bandgap enables the absorption of photons with energy levels corresponding to NIR and SWIR wavelengths, resulting in high responsivity and sensitivity to IR radiation. Additionally, InGaAs exhibits low dark current, which is crucial for achieving low noise levels and enhancing signal-to-noise ratio in photodetection systems. The material also demonstrates excellent carrier transport properties with mobilities reaching up to ≈10 0000 $cm^2.V^{-1}.s^{-1}$ at room temperature[217], enabling fast and efficient charge collection, leading to high-speed photodetection. However, the spectral tunability of InGaAs relies on an alloy content modification throughout molecular beam epitaxy (MBE), which is complex and reduce the manufacturing yield.

In this section, we propose to sensitize an array of 1D InGaAs nanowires by HgTe nanocrystals absorbing at 2 µm. Here, the nanowire geometry is used to prevent any absorption of the InGaAs layer in the photodetector. We will elaborate on the sensor fabrication as well as its infrared photodetection performance. Moreover, we will demonstrate that our strategy seamlessly leads to the formation of a *p-n* junction with a strongly rectifying I-V curve while such design relies on the complex choice of the surface chemistry and the coupling to carrier transport layers for all NC-based photodiodes.[40,42,218]

3.2-1 Design of the InGaAs/HgTe infrared sensor

The growth of InGaAs is carried out by our collaborator, L. Desplanque, at IEMN in Lille. To fabricate arrays of in-plane, p-doped InGaAs nanowires, atomic hydrogen-assisted selective area Molecular Beam Epitaxy (MBE) is employed.[217,219] The process begins with the preparation of a silicon dioxide mask on an InP(100) semi-insulating substrate. The mask is created using e-beam lithography and reactive ion etching techniques, resulting in a network of nano-trenches with a width of 100 µm and periodicity of 500 nm (Figure 35b). Each trench consists of openings that are 20 µm long and 130 nm wide, oriented along the [110] crystallographic direction (Figure 35c). To enable electrical conduction, two additional trenches, measuring 100 µm in length and 130 nm in width, are incorporated perpendicularly within the middle and at the opposite end of the nanowire arrays to account for potential discontinuities while minimizing the array resistance, as shown in the optical (Figure 36a) and electron microscopy images (Figure 36b-c). The nanowire arrays are electrically connected in parallel at one end through a larger 5x100 µm opening in the silicon dioxide mask.

Subsequently, the sample is introduced into the MBE chamber for surface deoxidization of InP using atomic hydrogen and arsenic flux at a temperature of 500 °C. The subsequent epitaxial growth involves depositing a 50 nm layer of InGaAs, which is lattice-matched to InP and n-doped with a targeted Silicon atom density of $3.5x10^{18}$ cm^{-3}. Due to the relatively large dimensions of the nanowires, quantum confinement effects are not expected to be significant in the InGaAs array. The resulting array consists of 200 nanowires, each 20 µm long and 130 nm wide. Different wire spacings (500, 700, and 1000 nm) were tested, but the results presented in this work focus on the smallest period. The elaboration parameters of InGaAs nanowires were chosen to reach a strong doping, and a high carrier mobility.

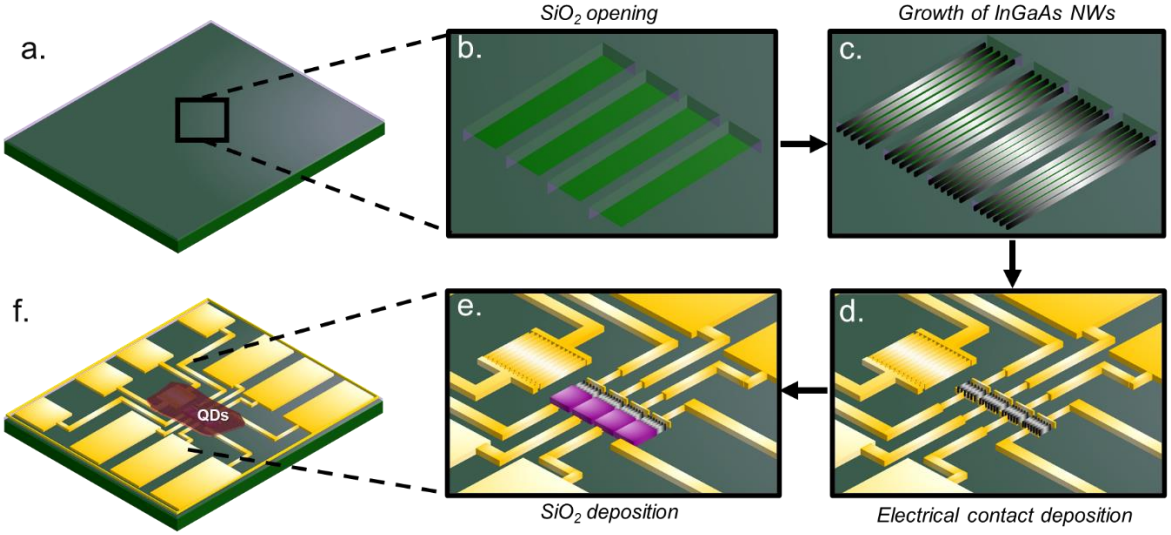

Figure 35 Main fabrication steps for the hybrid structure. a. Deposition of silica on InP substrate by sputtering. b. Opening of the silica layer by e-beam lithography and etching. c. Growth of the InGaAs wires by molecular beam epitaxy. d. Deposition of the metallic contacts after optical lithography. e. Protection of the metallic contacts by silica coating to avoid direct transport in the NC array. f. Deposition of the HgTe NC film.

Following the growth of nanowires, the sensor fabrication process is carried out in our laboratory at Institut des NanoSciences de Paris. The sample is dipped in an ammonia solution throughout the whole fabrication procedure to avoid any oxidation. Metal gold contact electrodes are deposited to define the diode area, as illustrated in Figure 35d. One electrode is designed to overlap with the nanowire array, while the second electrode is intentionally kept separate from the III-V semiconductor material.

Subsequently, an array of HgTe nanocrystals is uniformly coated onto the device surface. To ensure that charge transport occurs exclusively through the nanowire array, the

metallic electrode is insulated using a silica patch. This patch, indicated by the purple area in the false-color microscopy image (see Figure 35e and Figure 36a), effectively blocks conduction in the NC array while allowing for the desired nanowire conduction. The HgTe NCs are grown using the procedure developed by Keuleyan *et al.*[39], which is elaborated upon in the introduction chapter of this manuscript.

The HgTe nanocrystals have an average particle size of approximately 8 nm, chosen specifically to achieve a longer wavelength band edge (2 µm cut-off) compared to InGaAs (1.6 µm cut-off). The absorption and photoluminescence spectra of the HgTe NC material are depicted in Figure 36d. The band gap, determined at the peak of the photoluminescence signal, is approximately 1.75 µm (approximately 700 meV), and the cut-off wavelength extends to around 2 µm after a liquid-phase ligand exchange involving a mixture of $HgCl_2$ and MPOH to enhance film conductivity.

For the deposition of HgTe NCs, a spin-coating technique is employed, resulting in a layer thickness ranging from approximately 200 nm to 400 nm on the nanowire array. This thickness ensures a high film quality (homogenous thickness without any cracks) along with a relatively great light absorption.

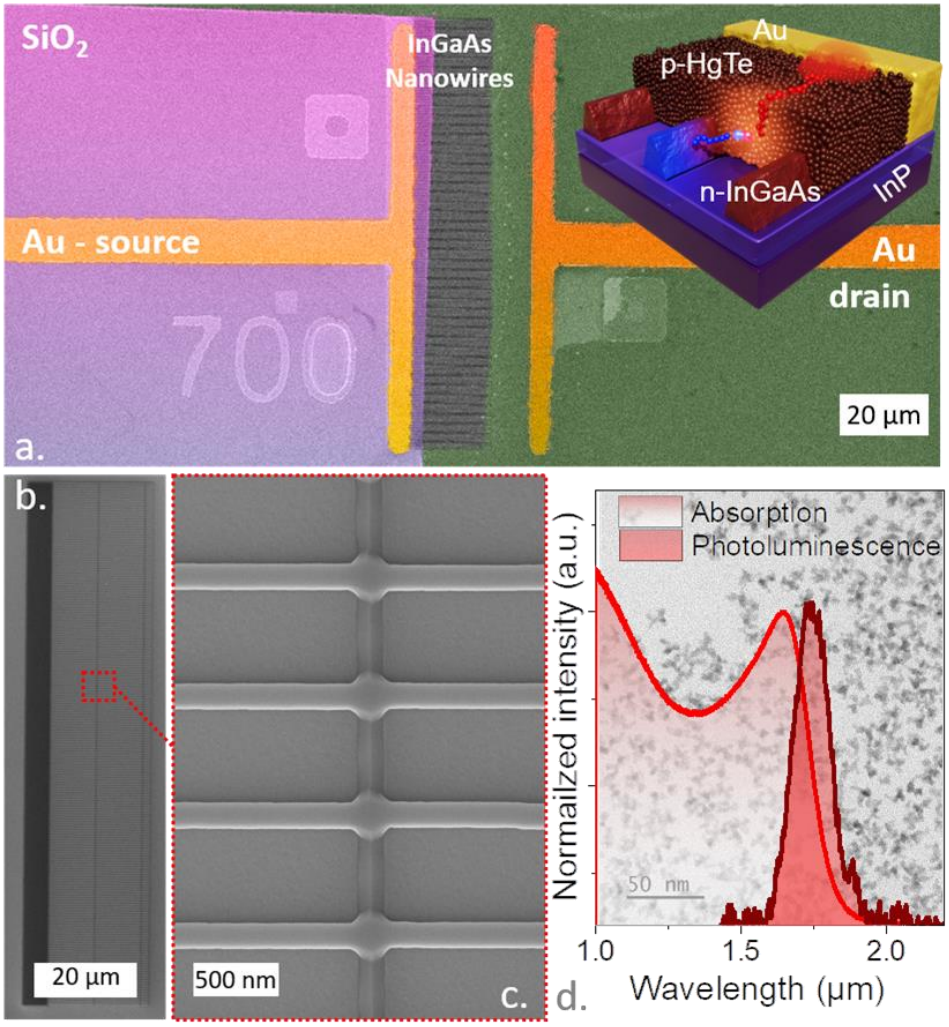

Figure 36 InGaAs wires/HgTe NCs hybrid device. a. False color microscopy image of the patterned nanowires. As a convention the wires are connected to the source in the following of the paper. The right-side inset is a schematic of the device once coated by a HgTe NCs film. b. SEM image of the InGaAs wires array. c. Zoom on the InGaAs wires array. d. Normalized absorption and photoluminescence spectra of HgTe NCs. The background is a TEM image of the same HgTe NCs.

Prior to delving into the transport and photo-transport characteristics of the hybrid structure, comprehensive characterizations are conducted to investigate the conduction properties of the individual materials. To isolate the conduction within the wires, a specific device was fabricated with InGaAs nanowires connected on both ends. The InGaAs nanowires, which possess a strong n-doping, exhibit a weak dependence on temperature. The observed reduction in resistance upon cooling (see Figure 37a) can be attributed to an enhancement in electron mobility resulting from reduced phonon scattering effects. The current-voltage (I-V) curve displays an ohmic behavior (see Figure 37b), and the Hall mobility is determined to be approximately ≈3000 $cm^2.V^{-1}.s^{-1}$.[217] The nature of the majority carriers in the InGaAs nanowire array is then investigated through an electrolytic field-effect transistor (FET). The n-doped nature of the array is further confirmed with a rise of conduction only under electron injection ($V_{GS} > 0$), as depicted in the inset of Figure 37b.

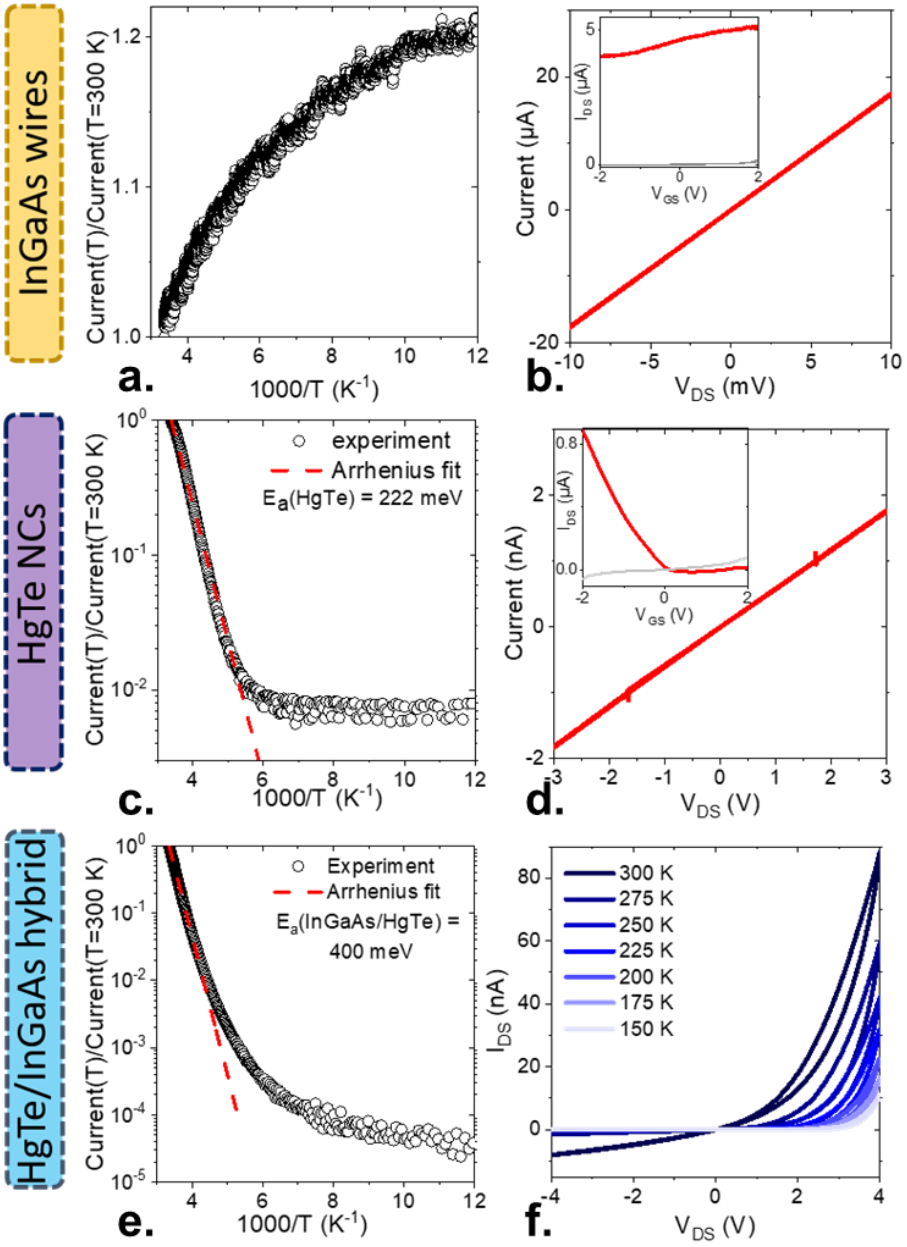

FIigure 37 Transport properties of the InGaAs wires array, of the HgTe NCs array and of the hybrid structure. a. Current (V_{DS}=1 mV) normalized by its value at room temperature as a function of the temperature for an array of InGaAs wires connected on both ends. b . Dark I-V curve, at room temperature, for the InGaAs wires array. The inset is the tranfer curve (drain current in red and gate current in grey) as a function of the applied gate bias (V_{DS}=3 mV). c.

Current (V_{DS}=1 V) normalized by its value at room temperature as a function of the temperature for an array of HgTe NCs. d. Dark I-V curve, at room temperature, for the HgTe NCs array. The inset is the transfer curve as a function of applied gate bias (V_{DS}=100 mV). Parts c and d are measured on gold interdigitated electrodes. e. Current (V_{DS}=1 V) normalized by its value at room temperature, as a function of the temperature for the hybrid structure made of the InGaAs wires (connected to only one end) coated by an HgTe NCs film. f. Dark I-V curves, at various temperatures, for the hybrid structure.

In the HgTe NC array-based device, the transport behavior also manifests as ohmic, consistent with a minimal offset between the material and the gold electrode (Figure 37d). FET measurements reveal a rise of conductance only under hole injection ($V_{GS} < 0$) highlighting the p-doped character of HgTe, as illustrated in the inset of Figure 37d. This phenomenon can be attributed to the localization of the Fermi level within the lower portion of the band gap, as supported by photoemission investigations conducted on HgTe NCs of similar size.[220] The temperature dependence of the current (Figure 37c) follows a thermally activated transport mechanism, and the activation energy of the current is approximately ≈220 meV, marginally smaller than half the value of the band gap ($E_G/2 = 350\,meV$) expected for an intrinsic semiconductor possessing the same band gap.

The doping of HgTe NCs results from two processes: self-doping and surface chemistry. Self-doping involves a reduction of the QD by its environment, whereas surface chemistry is intricately linked to the growth procedure and the ligands used. Small-sized HgTe NCs exhibit a p-type character, and as their size increases, a transition towards ambipolar behavior occurs, ultimately leading to an n-type character. The precise mechanism remains unclear, but it is likely correlated with the observed change in shape for HgTe as a function of size. The variation in exposed facets may induce a shift in the amount of excess Hg cation on the surface with particle size. To control the doping of HgTe NCs, one can act on its surface chemistry by adjusting the ligands used. Alternatively, doping control can be achieved through the application of a gate. This aspect has been a focal point of considerable effort in our research group, involving the exploration of different gate types such as ionic glass or ferroelectric materials.

The difference in doping nature for both HgTe and InGaAs array should result in a planar p-n junction for this infrared sensor. Upon deposition of the p-type HgTe NC array onto the n-type wire array, a diode is formed, evident from the highly rectifying nature of the current-voltage (I-V) curve obtained, as depicted in Figure 37f. At a temperature of 200 K, the current asymmetry between forward and reverse bias polarities reaches three orders of magnitude, as shown in Figure 38a. Another notable consequence of the interaction between the two materials is observed in the temperature dependence of the current. The current exhibits significant enhancement, with the activation energy of transport reaching 400 meV, as illustrated in Figure 37e. This increased activation energy reinforces the decrease in dark current upon cooling, and suggest that the device is not limited by trap states anymore.

Subsequently, our focus shifts to investigating the photoconductive properties of the hybrid structure, as presented in Figure 39. Under illumination, a significant modulation of the current is observed, particularly pronounced under reverse bias conditions, as depicted in Figure 39a. However, it is worth noting that the I-V curve under illumination does not exhibit an open-circuit voltage (V_{OC}).

As explained in the introductory chapter, a photodiode is a device that can convert light energy into an electrical current. The internal electric field in a diode allows for a separation of the electron-pair, creating a photocurrent. Typically, upon absorption of a photon, there is the generation of a current (short-circuit current I_{SC}) and a voltage (open-circuit voltage V_{OC}). The presence of an open-circuit voltage is an important characteristic of a photodiode as it indicates the potential difference that can be generated across the device terminals in the absence of an external load. However, in our bulk semiconductor/colloidal nanocrystals heterostructures, we observe the absence of a V_{OC}, preventing any operation at 0 V. In a photodiode, several factors can contribute to this phenomenon:

- Material Properties: The choice of semiconductor material used in the photodiode can influence the presence or absence of V_{OC}. Some materials may have a high recombination rate of charge carriers, which can limit the potential difference across the terminals. Additionally, the energy levels and band alignments of the materials within the photodiode can affect the separation and extraction of charge carriers, thereby influencing the generation of V_{OC}.

- Series Resistance: The presence of high series resistance within the photodiode circuit can limit the voltage generation. Series resistance can arise from the intrinsic resistance of the semiconductor material or from the resistance of other components within the device circuit such as the contact resistance of the metallic contacts. High series resistance can impede the flow of current and reduce the potential difference across the terminals, resulting in a lack of V_{OC}.

- Shunt resistance: The absence of V_{OC} can also be attributed to the presence of an external load (resistance) connected to the photodiode. In this context, the shunt resistance provides an alternate current path for the light-generated current. As a result, the amount of current flowing through the photodiode is reduced, and the voltage across the photodiode terminals decreases, potentially leading to a negligible or zero V_{OC}.

- Inefficient Charge Collection: If the photogenerated charge carriers do not efficiently reach the terminals of the photodiode, it can lead to a lack of V_{OC}. This can occur due to poor charge collection efficiency resulting from defects or recombination processes within the device structure.

The absence of an open-circuit voltage (V_{OC}) in the configuration discussed in this chapter can be attributed to the reasons elucidated above. The optimization of carrier collection is achieved through the presence of the InGaAs nanowire array, facilitating the efficient transport of one type of carrier. However, the other type of carriers must traverse the nanocrystal matrix to reach the second electrode via hopping mechanisms. The distance between the interface of InGaAs and nanocrystals to the electrode spans several tens of micrometers, significantly greater than the nanocrystals' hopping distance (10 - 100 nm). As a result, there is a high probability of photogenerated carriers recombining before reaching the contact electrode while being transported through the nanocrystal matrix, which results in a shunt resistance (Figure 38b). Furthermore, in this planar configuration (Figure 38a), the nanocrystals introduce substantial series resistance due to their significantly higher resistivity compared to the InGaAs nanowire array. For instance, in the InGaAs/HgTe hybrid, the nanocrystals exhibit resistivity 10^5 times greater than that of the InGaAs nanowires ($R_{InGaAs} = 10\ k\Omega \gg \mathrm{R_{HgTe}} = 1\ G\Omega$), which can account for the absence of V_{OC}. Lastly, in this geometry, a combination of nanowires and nanoparticles is employed, where the interface between them represents only a small fraction of the total volume. Given the hopping transport mechanism in nanocrystals, the carriers reaching the electrode within the nanocrystal matrix are likely generated near the wire tip closest to the electrode. Consequently, the p-n heterojunction interface in this hybrid accounts for only a few percent of the generated photocurrent, which could also contribute to the lack of V_{OC}.

The open-circuit voltage V_{OC} serves as a vital parameter in photodiodes as it allows for zero voltage operation, leading to a substantial enhancement in the signal-to-noise ratio of infrared photodetectors. To improve the performance of our hybrid structures, several potential enhancements can be considered. Firstly, employing a channel of InGaAs instead of an array of nanowires, while maintaining a single electrode connection, could augment the surface area of the heterojunction. This increased surface area would facilitate enhanced carrier generation and separation, thereby potentially elevating the V_{OC}. Additionally, reducing the distance between the electrode and the InGaAs pattern to less than a micrometer would contribute to an improved charge collection efficiency. By minimizing the separation, the photogenerated carriers would experience reduced recombination rates, resulting in a higher V_{OC} output. The

optimal approach to achieve this objective involves transitioning from a planar architecture to a vertical configuration.

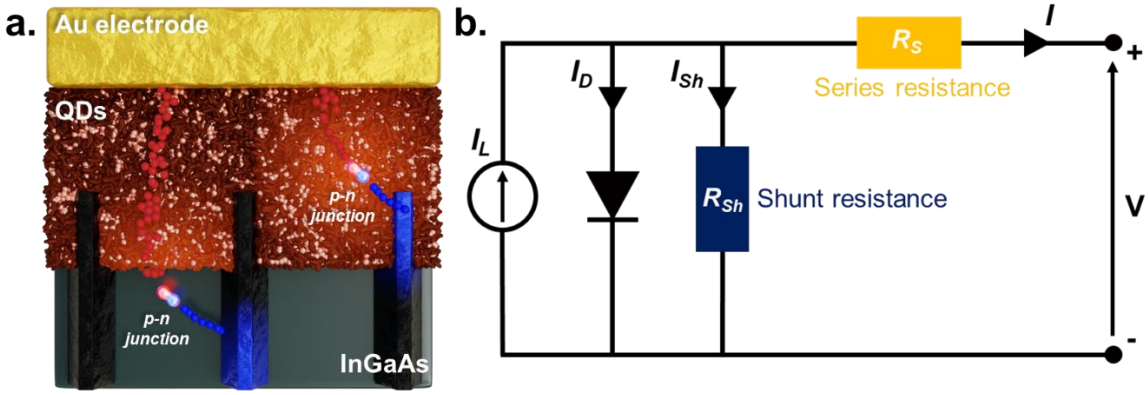

Figure 38 Planar p-n junction with InGaAs/HgTe hybrid. a. Scheme illustrating the top view of the hybrid device. The p-n junctions can be generated anywhere along InGaAs nanowires. The photogenerated carrier created at the tip of the nanowires is the most likely to contribute to the photocurrent while the one along the wire will most probably get recombined before reaching the gold contact. b. Equivalent circuit of a photodiode. I_L is the light-generated current, while I, I_D, and I_{Sh} are the output, diode and shunt current, respectively. V is the voltage across the output terminals.

3.2-2 Lifting the epitaxial constraint on the spectral response.

As elucidated in the previous sections, the fundamental principle underlying the design of these mixed-dimensional vdW heterostructures, comprised of InGaAs nanowires and HgTe nanocrystals, is to uncouple the optical properties from the transport characteristics. The selection of HgTe NCs with specific sizes is aimed at extending the spectral response of InGaAs by approximately 300 nm, thereby achieving a cut-off wavelength of 2 µm, while circumventing the constraints associated with epitaxial growth. Furthermore, the strategic implementation of a heterostructure composed of III-V and II-VI semiconductors may initially be perceived as a means to take away the cost-effectiveness associated with nanocrystals. However, it also yields significant advantages in terms of stability and precise control of doping through the utilization of InGaAs.

In order to provide further insight into the generation and behavior of photogenerated carriers, we employed photocurrent spectroscopy as an investigative tool. This spectroscopic technique enabled us to gain a deeper understanding of the origin and nature of the photoinduced charge carriers within the heterostructure. By carefully examining the photocurrent response as a function of incident light wavelength, we were able to elucidate the underlying mechanisms governing carrier generation and transport in this unique mixed-dimensional system.

Figure 39b presents the photocurrent spectrum obtained from the InGaAs/HgTe heterostructure. Notably, in the wavelength range slightly below 1 µm, a huge peak coming from the InP substrate is observed. Within the short-wavelength infrared (SWIR) region around 2 µm, an absorption signal corresponding to the HgTe nanocrystals is detected, while no discernible feature associated with the InGaAs is observed. Furthermore, despite the presence of a one-dimensional (1D) array of InGaAs nanowires, the photocurrent exhibits an unpolarized nature.

To gain insights into these characteristics, simulations of the absorption map and spectrum of the hybrid structure were conducted using a finite element tool, specifically COMSOL software. These simulations were performed by G. Vincent at Onera. Figures 38c and 38f illustrate the absorption map of the hybrid structure at wavelengths below and above the InGaAs bandgap, respectively.

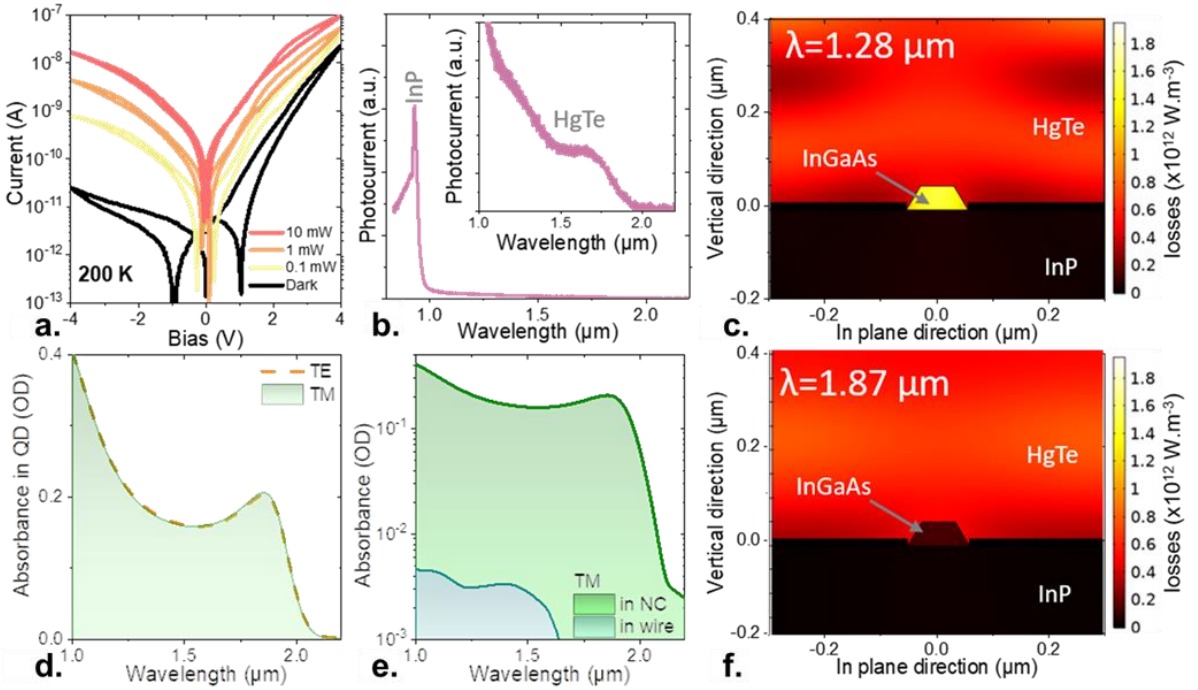

Figure 39 Spectroscopic properties of the photocurrent. a. I-V curves of the hybrid structure in the dark and under illumination by a laser diode (λ=1.55 µm). The indicated power is the one from the laser diode. b. Photocurrent spectrum for the hybrid structure. The inset is a zoom on the spectral range corresponding to the band edge of HgTe. c. Absorption map of the hybrid structure at 1.28 µm (below InGaAs band gap). d. Simulated absorption of the hybrid structure along the TE and TM polarization. e. Simulated absorption of the hybrid structure along the TM polarization within the InGaAs wires and within the HgTe NCs. f. Absorption map of the hybrid structure at 1.87 µm (above InGaAs band gap). Maps from part c and f are simulated in TE polarization.

In the former case, substantial absorption losses occur within the InGaAs nanowire. However, it is important to note that the InGaAs nanowire array have a thickness of around 50 nm, constituting a relatively small volume within the overall structure. Consequently, the absorption attributed to the InGaAs accounts for only a minor fraction of the total absorption, as depicted in Figure 39e. This further substantiates the decoupling of the absorption and transport properties within this hybrid structure.

The HgTe NC film predominantly drives the absorption in the SWIR regime, while the InGaAs nanowires primarily govern the transport behavior by acting as a unipolar barrier that facilitates the extraction of photogenerated electrons. The limited absorption exhibited by the InGaAs further elucidates the absence of polarization in the overall absorption profile, despite the nanowires'-oriented structure, as illustrated in Figure 39c.

3.2-3 High electrical bandwidth hybrid photodetector

The sensing capabilities of the InGaAs/HgTe hybrid infrared detector are then investigated to assess its performance. When the device is illuminated, the responsivity is directly proportional to the applied bias. Notably, the magnitude of responsivity shows minimal dependence on the bias polarity, as evidenced in Figure 40a, reaching a maximum value of 16 $mA.W^{-1}$ at -4 V. In contrast, the dark current, observed in the I-V curve (refer to Figure 40a), exhibits strong dependence on the bias polarity. Therefore, the optimal operational condition, leading to the largest current modulation, is achieved with a substantial reverse bias of -4 V for this diode.

Upon cooling the device from 300 K to 200 K, the responsivity experiences a two-fold reduction, as illustrated in Figure 40b, while the dark current undergoes a significant decrease

of three orders of magnitude. In the nanocrystal array, charge conduction occurs through a hopping mechanism, resulting in the thermal activation of both carrier density and mobility. During illumination, the carrier density is determined by the incident photon flux, thus making the temperature dependence of the response predominantly governed by the thermal activation of carrier mobility.

Furthermore, the responsivity is contingent upon the incident photon flux, whereby the photocurrent scales as $P^{0.63}$, with P representing the incident power. Notably, larger responses are measured under weaker irradiations, as demonstrated in Figure 40c. This trend is due to the occurrence of different recombination mechanisms.

The inset of Figure 40d provides evidence that the noise in the device follows a 1/f characteristic.[89,212] This observation suggests that the primary source of noise originates from the transport within the nanocrystal array. In high-mobility III-V semiconductor films, white noise components such as shot and thermal noises are typically associated with charge conduction, whereas 1/f noise is more prevalent in the NC array.

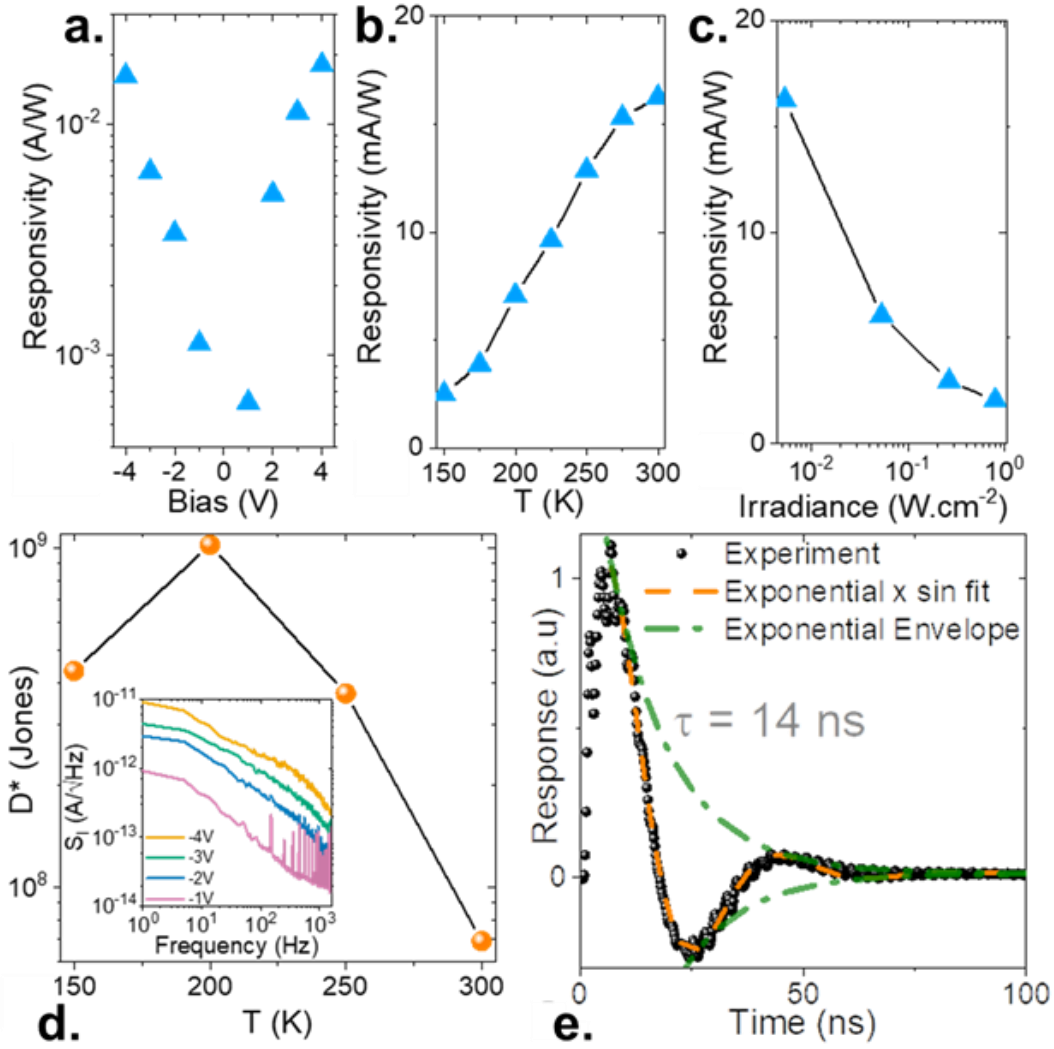

Figure 40 Photodetection performance of the hybrid structure. a. Responsivity at 300 K of the hybrid structure as a function of the applied bias, under illumination by a laser diode at 1.55 µm with an irradiance of 5x10^{-3} W.cm^{-2}. b. Responsivity of the hybrid structure as a function of the temperature, under -4 V under an irradiance of 5x10^{-3} W.cm^{-2} at 1.55 µm. c. Responsivity of the hybrid structure as a function of the incident irradiance power, at 300 K under -4 V. d.

Specific detectivity under -4 V as a function of the operating temperature for a signal modulated at 1 kHz. The inset is the noise current spectral density as a function of the signal frequency, while the device is operated under various biases. e. Photocurrent response of the hybrid structure to a 1 ns pulse of light at 1.57 µm. The data are fitted by the product of an exponential decay curve with a sinus curve accounting for the imperfectly impedance matching of the device with the acquisition scope. Exponential decay time is estimated to be ≈14 ns.

The detectivity of the diode at room temperature is measured to be $7x10^7$ Jones. Under a reverse bias of -4 V, at a temperature of 200 K, the detectivity increases to 10^9 Jones. These measurements are obtained with a cut-off wavelength of 2 µm and a signal modulation frequency of 1 kHz. While the detectivity achieved in this diode is modest compared to state-of-the-art diodes based on HgTe NCs, which can achieve detectivity levels of 10^{11} Jones[40,42,221] at similar wavelengths and room temperature, it is comparable to the detectivity reported for HgTe NC layers coupled to graphene, falling within the range of 10^8 – 10^9 Jones[77,222]. The limitation in detectivity can be attributed to the absence of open circuit voltage (V_{OC}) in this approach, which prevents zero-volt operation.

However, the planar geometry of this device, in contrast to vertical geometry diodes, offers advantages such as reduced capacitance, enabling fast operation. When illuminated with a 1 ns pulse at 1.57 µm, this device exhibits an exponential decay of the signal with a characteristic decay time of 14 ns, as depicted in Figure 40e. This response time is almost two orders of magnitude faster than that reported for vertical diodes. Therefore, while our device may have a weaker signal-to-noise ratio, it compensates for it with a higher device bandwidth, making its time-response suitable for LiDAR applications.

3.3 Toward a MWIR-sensitized InGaAs photodetector

Traditionally, the design of infrared sensors has pitted epitaxially grown narrow band gap semiconductors against their colloidal counterparts. However, in the previous section, we have demonstrated the feasibility of Van der Waals heterostructures using these two semiconductor types. Our proposed device utilizes a unique geometry in which high-mobility n-type InGaAs nanowires serve as electron extractors from a p-type HgTe nanocrystal array. This design challenges the prevailing notion that such configurations are limited to 2D layered materials, where nanocrystals function solely as light sensitizers on the surface. By combining epitaxially and colloidally grown semiconductors, we can leverage the advantages of both approaches. This strategy has proven effective in extending the spectral response of InGaAs technology towards longer wavelengths, while simultaneously circumventing the constraints associated with epitaxial growth techniques.

In order to develop a mid-wavelength infrared (MWIR) detector, this work aims to combine two distinct concepts of my thesis. The first concept, introduced in the second chapter, involves the utilization of a hybrid structure comprising HgSe and HgTe nanocrystals. This hybrid structure offers advantages in achieving mid-infrared absorption while addressing challenges associated with degenerate doping in NCs, such as high dark current and bolometric response. The hybrid structure will be employed to sensitize an array of InGaAs nanowires, thereby facilitating the design of an MWIR photodiode.

Furthermore, the integration of bulk semiconductors with NCs can prove beneficial in overcoming the limitations associated with doping control in colloidal particles. It is worth noting that the band alignment of infrared-absorbing IV-VI[170,223] and II-VI[49] semiconductor NCs remains relatively unexplored. Consequently, considering the NC/bulk heterostructure as a potential approach becomes highly significant in designing an NC-based p-n junction, as achieving ambipolar operation in these materials is otherwise challenging unless a ligand exchange is performed.[174]

This study aims to explore the advancement of a photodiode that operates within the mid-wave infrared (MWIR) spectrum. The device architecture involves the integration of an array of InGaAs nanowires as the hole transporting material, coupled with HgSe nanocrystals

(NCs) serving as the MWIR absorbers. Unlike the previous research discussed earlier, the primary objective of this investigation is to expand the spectral sensitivity of bulk semiconductors to encompass longer wavelengths, with a specific focus on achieving a cutoff wavelength of 5 µm. However, this objective presents notable challenges due to the heightened interfacial barrier encountered during the charge transfer process.

3.3-1 Fabrication of the InGaAs – HgSe/HgTe heterostructure

The growth of InGaAs is carried out by our collaborator, L. Desplanque, at IEMN in Lille. The fabrication procedure for the growth of the nanowire is the same as the one described in the previous section for the InGaAs/HgTe hybrid. The difference in the following device is that the InGaAs nanowires are p-doped with a targeted Beryllium atom density of $5x10^{18}$ cm^{-3}.

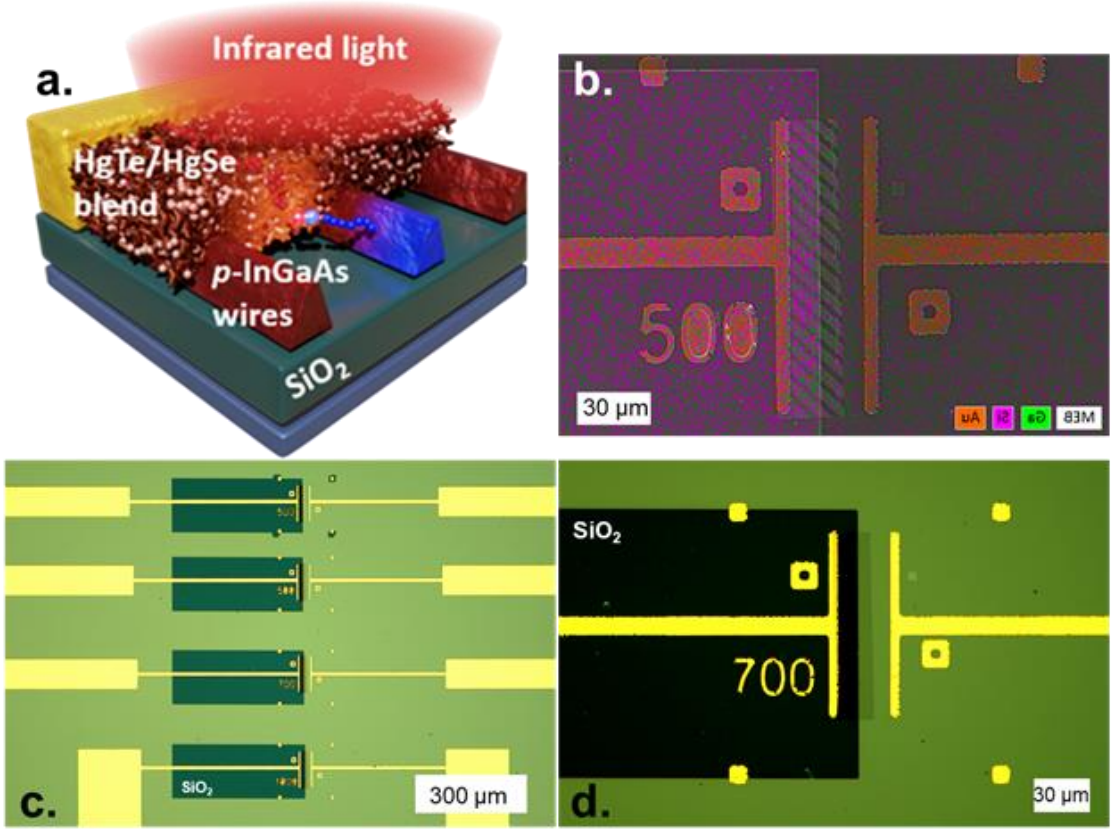

Figure 41 InGaAs – HgSe/HgTe hybrid infrared photodetector. a. Schematic of the device with the InGaAs nanowires coated with the HgSe/HgTe mixture. b. Super-imposed energy dispersive X-ray spectroscopy mapping for Ga, Si and Au. The map was acquired with an EDX coupled to a scanning electron microscope (SEM) at a 10 kV bias. Low magnification (c.) and high magnification db) images of the wires connected to the electrodes. Electrodes appear in yellow. The darker areas are made of SiO_2, which prevents direct connection of the NC array to the metallic electrode connected to the wire. The InGaAs wires appear dark green and are only connected to the left electrode.

Following the growth of InGaAs, I proceed to the fabrication procedure with the subsequent steps. Firstly, the sample is dipped in an ammonia solution to prevent any oxidation of the InGaAs nanowires. Then, to create metallic gold contacts, an optical lithography technique is employed, and the gold is deposited using thermal evaporation until a thickness of 150 nm is achieved. The InGaAs nanowires are electrically connected to one of the gold electrodes while remaining isolated from the second electrode. During this lithography step, achieving precise alignment between the gold contact and the nanowire array proves challenging, resulting in an approximate distance of 10 µm between them. The electrode that

is in contact with the nanowire array is then encapsulated beneath a layer of silica to ensure that charge conduction primarily occurs through the nanowires, as illustrated in Figure 41b-c.

The silica layer, or SiO2 patch, is patterned using e-beam lithography and deposited through sputtering, resulting in a thickness of 100 nm. This thickness ensures the insulation of the electrode connected to the nanowire array from the nanocrystals, thereby maintaining the desired electrical isolation, while enforcing the current to flow through the nanowire array.

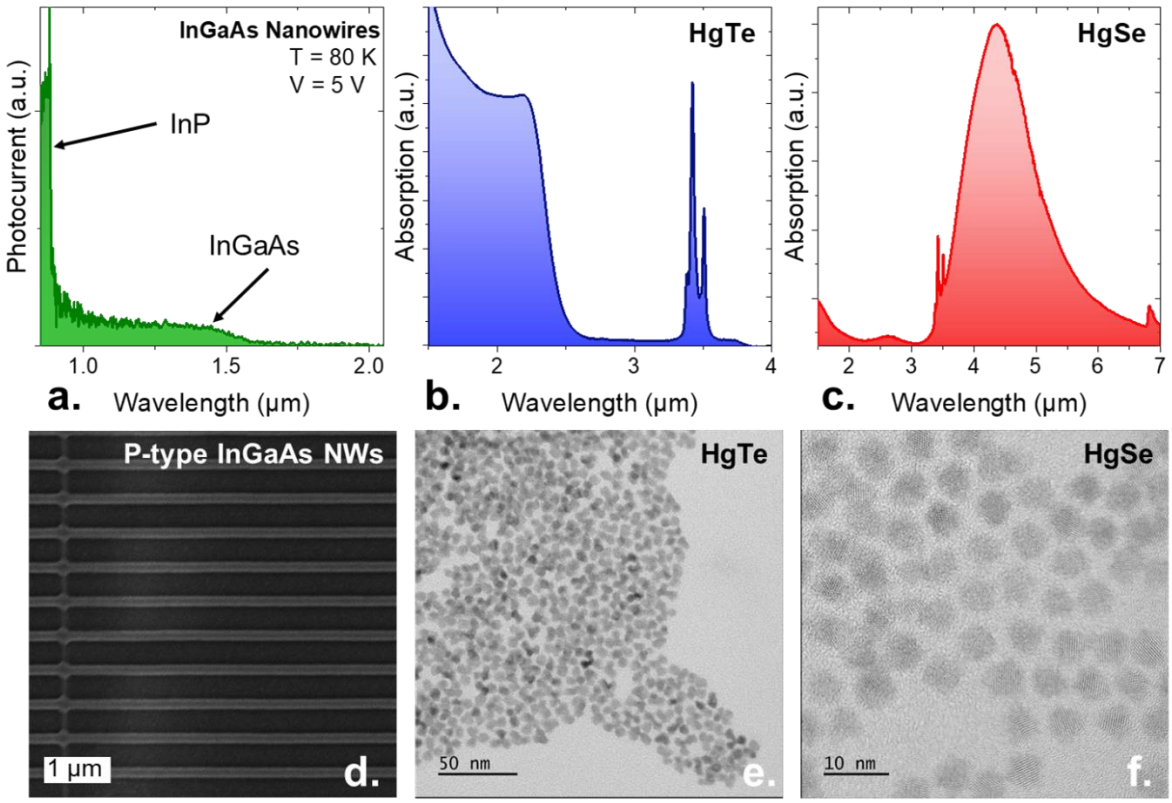

Figure 42 Mid-wave infrared absorbing material properties. a. Photocurrent spectrum of the InGaAs nanowires at 80K under 5 V bias. b. and c. are absorption spectra of HgTe NCs and HgSe NCs respectively. d. SEM image of the InGaAs nanowires. e. and f. are TEM images of HgTe NCs and HgSe NCs respectively.

The subsequent steps involve the growth of HgTe[31] and HgSe[57] nanocrystals using established procedures outlined in the previous chapters of this manuscript. The optical properties of the constituent materials in the mixed-dimensional van der Waals heterostructure are presented in Figure 42. A specific device featuring an array of InGaAs nanowires connected to both electrodes is fabricated to investigate its optical characteristics. The photocurrent spectrum of InGaAs, depicted in Figure 42a, reveals a cut-off wavelength of approximately 1.5 μm at 80 K. Notably, HgTe nanocrystals exhibit a branched morphology, whereas HgSe nanocrystals appear quasi-spherical, as evident from the transmission microscopy images shown in Figure 42e-f. The absorption spectrum of HgTe nanocrystals, illustrated in Figure 42b, displays a band edge in the extended short-wavelength infrared (eSWIR) region at 2.5 μm. At longer wavelengths, around 3.5 μm, the narrow doublet arising from the C-H resonance can be attributed to the dodecanethiol capping ligand. In the case of HgSe nanocrystals, the primary contribution to absorption arises from the intraband transition, with a cut-off wavelength of approximately 5 μm. A minor signal at higher energies (below 2 μm) is also observed, likely resulting from the mostly bleached interband transition. This suggests a doping level of approximately 2 electrons per dot for HgSe nanocrystals. Subsequently, these nanocrystals are blended in an optimized ratio, roughly 1:1, based on empirical determinations. As previously explained, this ratio ensures that the presence of HgTe

is sufficient to prevent percolation within HgSe array, leading to improved transport properties characterized by reduced dark current, rapid response, and increased activation energy. The HgSe/HgTe blend then undergoes a liquid-phase ligand exchange process using a mixture of thiol and mercury ions, resulting in the formation of a photoconductive film. Finally, a film of the HgSe/HgTe blend is deposited onto the InGaAs nanowire array through spin-coating, achieving a thickness within the range of 300 to 400 nm.

3.3-2 Design of a planar p-n junction in the mid-infrared

The objective of this study is to develop a mid-wave infrared (MWIR) photodiode by combining an array of InGaAs nanowires with a blend of HgSe/HgTe nanocrystals in a mixed-dimensional van der Waals heterostructure. This hybrid device aims to engineer carrier wave-functions at the device level, enabling the formation of a p-n junction. Similar to its short-wave infrared counterpart discussed in the previous section, this photodetector aims to decouple the optical and transport properties. The high-mobility InGaAs nanowires are responsible for driving the transport of photogenerated holes, while the HgSe/HgTe nanocrystals facilitate mid-infrared absorption through their intraband transition. To investigate these properties, we conducted a spectroscopic analysis of the InGaAs-HgSe/HgTe hybrid. Theoretical calculations of absorption maps and spectra were performed by G. Vincent using the Finite Element Method (FEM) with COMSOL software.

Figure 43a presents the simulated absorption map of the hybrid structure, revealing that the absorption is primarily governed by the contributions of the HgSe and HgTe nanocrystals. The intraband absorption of HgSe nanocrystals is observed in the range of 4 – 5 µm, while the interband contribution of HgTe nanocrystals is observed at higher energies around 2.5 µm. A small bump corresponding to a resonant O-H bond indicates the effectiveness of the ligand exchange procedure. The InGaAs nanowires, constituting a small volume within the structure (50 nm thick), exhibit negligible absorption and induce no polarization. A gradual decrease in absorption is observed at higher energies due to the InP substrate, which still possesses a small imaginary component in its complex refractive index above 1 µm.[224] This absorption feature can be attributed to the relatively high thickness of the InP layer (400 µm in the simulation).

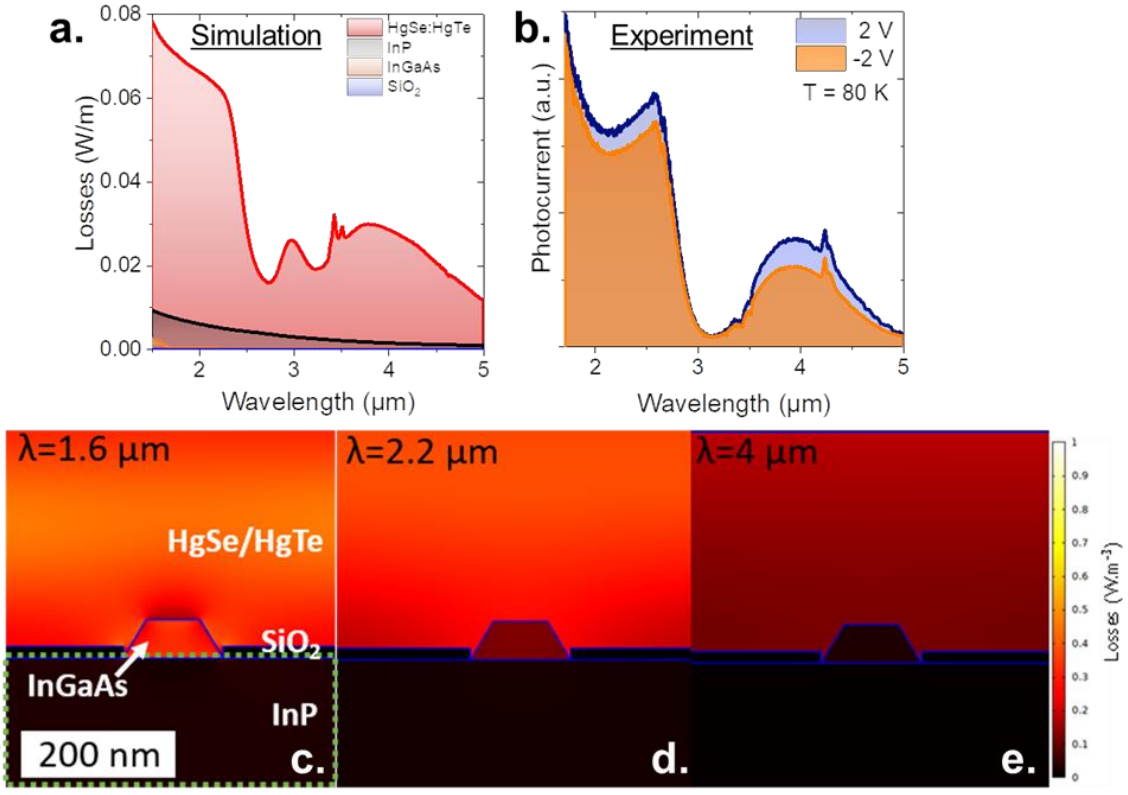

Figure 43 Spectroscopic properties of the photocurrent. a. Simulated absorption spectra of the hybrid structure under TM polarization withing the different materials of the structure. b. Photocurrent spectra of the hybrid structure at 80 K under reversed and forward biases. c. e. and e. are simulated absorption maps under TM polarization at 1.6 µm (below InGaAs bandgap), 2.2 µm (above InGaAs bandgap) and 4 µm (at the intraband), respectively.

To experimentally validate these properties, photocurrent spectra of the hybrid structure were measured under various applied biases at 80 K, as shown in Figure 43b. The photocurrent spectrum is predominantly determined by the HgSe and HgTe nanocrystals, encompassing both intraband and interband contributions. Notably, the O-H contribution, present in the absorption spectra, is absent in the photocurrent spectra as the ligands do not participate in the photoconductive process. The energy splitting between the HgTe and HgSe features is reduced compared to the absorption spectra depicted in Figure 43a due to the redshift of the HgTe[29,126] intraband transition and blueshift of the HgSe[57] intraband transition upon cooling. Furthermore, a distinct increase in photocurrent below 1.7 µm is observed, which can be attributed to the efficient conduction of photogenerated holes through the high-mobility InGaAs nanowires[225] ($\mu_{p-InGaAs} \approx 100\ cm^2.V^{-1}.s^{-1} >> \mu_{NC}$). The device geometry facilitates the transfer of MWIR photocurrent originating from HgSe absorption towards the InGaAs nanowires. The combined theoretical and experimental investigation of the hybrid spectroscopic properties confirms the mid-infrared sensitization of III-V InGaAs nanowires through an HgSe/HgTe nanocrystal matrix.

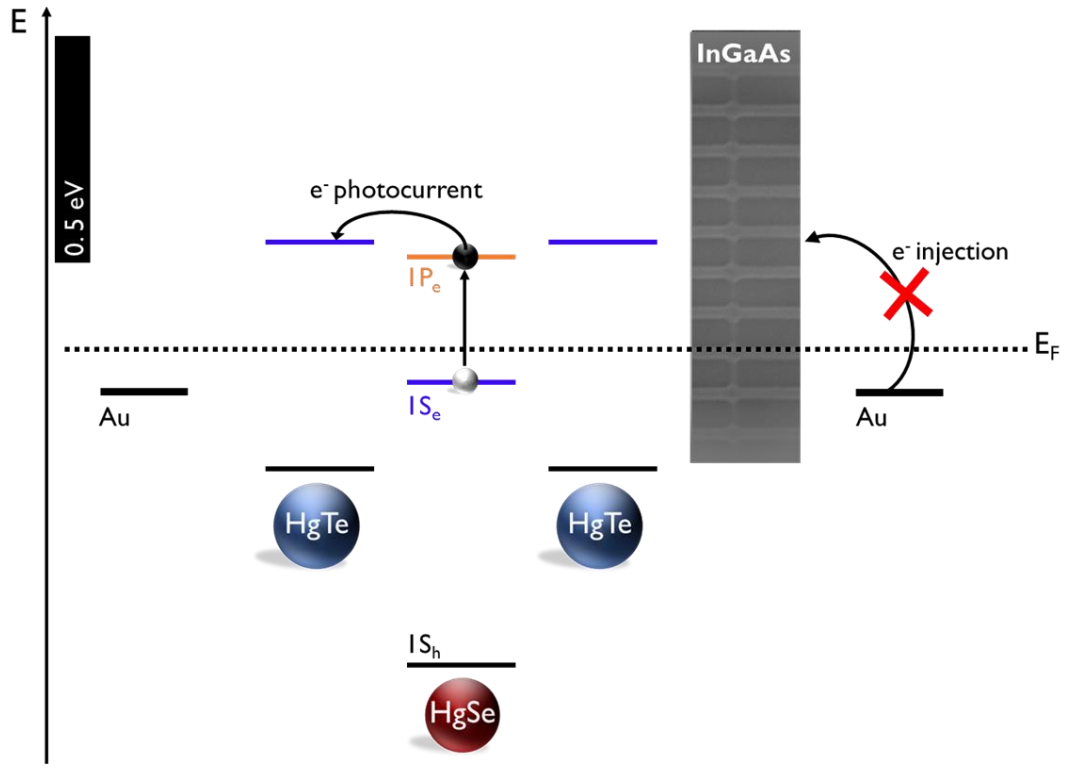

Figure 44 Energy diagram of the MWIR sensitized InGaAs photodetector. The dashed line corresponds to the Fermi level. The black rectangle corresponds to the energy scale.

The investigation of the transport properties of the InGaAs - HgSe/HgTe infrared photodetector aims to elucidate the presence of a planar p-n junction. To unveil the device's operation, it is crucial to understand the band alignment within the hybrid structure. Livache *et al*.[106], through photoemission measurements, have previously determined the relative positioning of HgSe and HgTe. InGaAs has been doped with Be, resulting in a p-type behavior and positioning the Fermi level in the lower portion of the InGaAs band gap. InGaAs possesses a band gap of 0.75 eV, while HgTe has a band gap of 0.5 eV. In the case of HgTe, the material is quasi-intrinsic[88,226], as illustrated in Figure 44a, implying that the Fermi level roughly resides

in the middle of the band gap. If InGaAs were to be intrinsic, it would establish a 125 meV offset barrier for both electrons and holes. The hole doping of InGaAs shifts the Fermi level towards the valence band, thereby rendering it quasi-degenerate with HgTe. The substantial disparity in band gaps generates a barrier in the conduction band, as proposed in Figure 44.

The transport properties of the hybrid MWIR photodetector are presented in Figure 45. Electrically, the device exhibits diode-like behavior with a strongly rectifying current-voltage (IV) curve, as depicted in Figure 45c. This demonstrates the advantageous characteristics of the III-V nanowires compared to a device employing gold electrodes. In this system, the p-doped InGaAs nanowires serve as a unipolar barrier, effectively blocking the flow of electrons. Remarkably, the rectifying behavior persists even at room temperature, which sets it apart from most MWIR diodes based on nanocrystals that lose rectification outside of cryogenic temperatures.[40]

Additionally, the transport properties exhibit a significant dependence on temperature, making sample cooling a viable strategy for reducing the dark current, in contrast to a pristine array of degenerately doped nanocrystals.[106,170,180,210] The evolution of the dark current with temperature is depicted in Figure 45b. The rapid decrease at higher temperatures is fitted with an Arrhenius model, resulting in an extracted activation energy of 163 meV. Notably, this represents the highest reported value for transport in intraband particles at this wavelength, underscoring the advantages offered by our device geometry.

Figure 45b illustrates the absence of open-circuit voltage under illumination of a QCL matching the intraband absorption. This absence of V_{OC} has been discussed for the previous hybrid InGaAs/HgTe, and hampers device operation under a 0 V bias. Nevertheless, this approach maintains a rectifying I-V curve for the dark current, and low levels of dark current are sustained even under significant negative reverse bias conditions (even at -5 V). This stands in contrast to most diodes based on HgTe NCs, where the current asymmetry is typically lost above 0.4 V.[106,170,180,210]

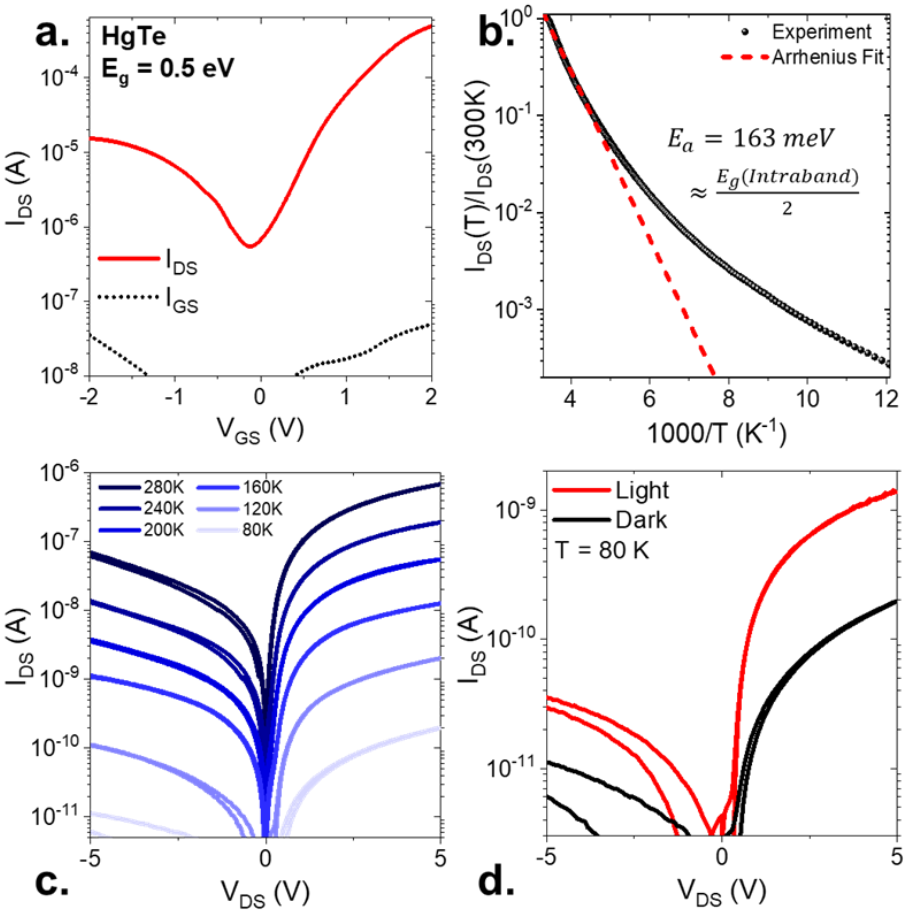

Figure 45 Transport properties of the hybrid structure. a. Electrolytic field-effect transistor measurement of HgTe nanocrystals with a 0.5 eV bandgap. The transfer curve reveals a rise of conduction under both electron and holes injection, suggesting an ambipolar behavior. b. Evolution of the dark current as a function of the temperature for the hybrid structure. An Arrhenius model is used to fit the exponential decay, giving an extracted activation energy of 163 meV. c. I-V curves under dark conditions, at various temperatures for the heterostructure. d. I-V of the hybrid structure under dark and illumination of a QCL at 4.42 µm (with an output power of 12 mW).

3.3-3 Detection performances of the MWIR photodiode

The infrared sensing performance of the InGaAs – HgSe/HgTe hybrid detector is systematically investigated. The responsivity of the device exhibits a temperature-dependent behavior, with values ranging from 6 $mA.W^{-1}$ at room temperature to approximately one order of magnitude lower at cryogenic temperatures of 80 K, as illustrated in Figure 46a. This decrease in responsivity with decreasing temperature can be attributed to the thermal activation of mobility associated with hopping conduction. The limited responsivity observed in the device can be primarily attributed to the absence of a light management strategy, resulting in suboptimal overall absorption efficiency. This deficiency is due to the reduced volume fraction of HgSe nanocrystals involved in intraband absorption, as elucidated in the preceding chapter. To assess the time response characteristics, a quantum cascade laser (QCL) emitting at a wavelength of 4.4 µm, corresponding to the intraband absorption of the hybrid detector, is employed. The time-response analysis, depicted in Figure 46b, reveals a rapid intraband absorption process occurring within a timescale of less than 100 µs, highlighting the significantly faster dynamics compared to an array comprising solely intraband absorbers.

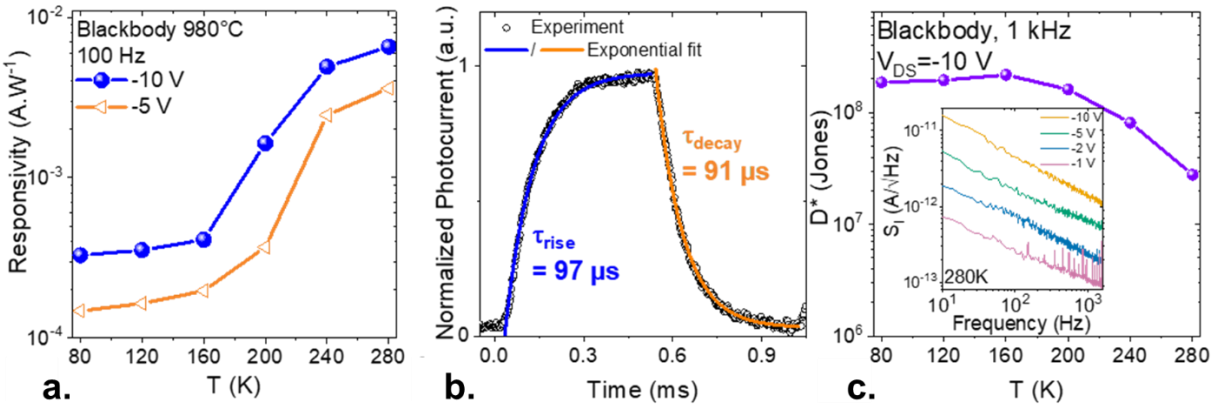

Figure 46 MWIR detection performances from the hybrid structure. a. Responsivity of the heterostructure as a function of the temperature under -5 V and -10 V with a blackbody illumination. b. Photocurrent response from the hybrid structure to a 1 kHz optically chopped quantum cascade laser (QCL) at 4.42 µm. Data are fitted using exponential decays. c. Specific detectivity under – 10 V as a function of the operating temperature. The inset is the noise current spectral density at 280 K as a function of the signal frequency under various biases.

The noise characteristics of the InGaAs – HgSe/HgTe hybrid detector are primarily governed by a 1/f noise contribution, as indicated by the inset in Figure 46c. The detectivity of the device, which quantifies its ability to detect weak signals, is approximately $2x10^8$ Jones at 80 K. Although this value is one order of magnitude lower than the best intraband devices[106,174,210], it maintains this level of performance up to 200 K. In contrast, the detectivity of the same HgSe/HgTe blend is reduced by a factor of 10 when the temperature is increased from 80 K to 160 K, as demonstrated in the previous chapter. This suggests that the utilization of InGaAs for charge extraction in the hybrid detector offers the advantage of enhanced operating temperature capabilities, thereby reducing constraints on device size, weight, and power consumption.

3.4 Conclusion

The field of nanocrystal heterostructures has attracted significant attention in recent years due to their distinct properties and potential applications, particularly in high-performance light-emitting diodes (LEDs) for displays. The ability to combine nanocrystals with different properties has opened up exciting avenues for advanced device design and improved performance. While most heterostructures have traditionally relied on core-shell configurations, recent advancements in controlled assembly techniques have facilitated the integration of nanocrystals with different compositions and sizes, resulting in hybrid materials with enhanced optoelectronic properties.

In the early 2010s, the concept of mixed-dimensional van der Waals (vdW) heterostructures extended the scope of nanocrystal heterostructures to include 2D layered materials, offering exceptional responsivity. For a considerable period, the design of infrared photodetectors has pitted narrow bandgap III-V semiconductors against their colloidal II-VI counterparts. However, in this chapter, instead of opposing these two technologies, we have demonstrated the extension of the mixed-dimensional vdW heterostructure concept to bulk InGaAs by precisely engineering the carrier wave-functions at the device level. We have presented two hybrid detectors comprising an array of InGaAs nanowires and mercury chalcogenide nanocrystals, aiming to enhance the spectral response of the former while alleviating the constraints imposed by epitaxial lattice matching.

The first hybrid detector relies on the coupling of HgTe nanocrystals with an array of InGaAs wires. In this configuration, high-mobility n-doped InGaAs nanowires serve as electron extractors from a p-doped HgTe matrix. The hybrid detector effectively decouples the transport and absorption properties, utilizing nanocrystals with a size optimized to achieve a 2 µm cut-wavelength, while InGaAs facilitates the transport of the photogenerated carriers. The heterostructure is carefully designed to establish a p-n junction at the interface between the two materials. We have demonstrated, for the first time, synergistic properties arising from the combination of bulk 1D InGaAs and colloidal nanocrystals, characterized by a high activation energy (400 meV) and strong rectification behavior. The specific detectivity (10^9 Jones at 200 K) is relatively modest compared to state-of-the-art nanocrystal-based photodiodes but is offset by a high electrical bandwidth almost reaching the GHz range.

The second hybrid detector follows a similar approach as the first one but utilizes a blend of HgSe and HgTe nanocrystals to achieve mid-wavelength infrared (MWIR) absorption, primarily leveraging the intraband transition of HgSe. This strategy simplifies the design of nanocrystal-based infrared photodiodes in a spectral range where the band alignment remains predominantly unknown. Additionally, this device maintains a high signal-to-noise ratio up to 200 K, whereas other intraband-based devices can only operate at cryogenic temperatures. In both hybrid detectors presented in this chapter, the absence of V_{OC} impedes operation at 0 V, thus limiting the signal-to-noise ratio. We attribute this lack of V_{OC} to the introduction of a large shunt resistance by the nanocrystal matrix and suboptimal transport characteristics for the photogenerated carriers.

Having established the concept of coupling, we will demonstrate its applicability to more efficient geometries. In the subsequent chapter, we will delve into the integration of HgTe nanocrystals into an advanced infrared technology known as an infrared camera. Specifically, we will employ in situ and operando photoemission microscopy to gain a comprehensive understanding of the device's operation.

4 Exploring *in-operando* and *in-situ* a short-wave infrared camera based on HgTe nanocrystals

This chapter presents the development of the most advanced infrared device, compared to the ones of the previous chapters, which were more exploratory. Specifically, advancements in the design and implementation of an infrared camera based on HgTe nanocrystals will be discussed. Notably, this imager will undergo *in-situ* and *in-operando* investigations to probe its energy and photocurrent landscapes. This innovative approach represents a crucial departure from the conventional practice of studying the material and the device independently, instead focusing on the material within the context of the device itself. The experimental procedures involve the production of the ROIC by New Imaging Technologies. The characterization of the HgTe-based camera is a joint effort between our group and David Darson from LPENS. Photoemission measurements are conducted at the ANTARES and TEMPO beamlines of the synchrotron SOLEIL. Data processing of XPS data have been performed by Mariarosa Cavallo. The electrostatic simulations are conducted by Tung Huu Dang at INSP. Photocurrent microscopy is performed at ONERA with the assistance of Baptiste Fix and Grégory Vincent. Finally, the nanoparticle growth is carried out by Yoann Prado at INSP.

Related article:

- ***Khalili, A**.; Cavallo, M.; Bossavit, E.; Alchaar, R.; Dang, T. H.; Dabard, C.; Zhang, H.; Ledos, N.; Parahyba, V.; Potet, P.; Utterback, J. K.; Prado, Y.; Silly, M. G.; Dudin, P.; Avila, J.; Pierucci, D.; Lhuillier, E. In Situ Mapping of the Vectorial Electric Field within a Nanocrystal-Based Focal Plane Array Using Photoemission Microscopy, **2023**, (Submitted).*

.

4 Exploring *in-operando* and *in-situ* a short-wave infrared camera based on HgTe nanocrystals 87
4.1 Focal plane array based on HgTe nanocrystals 88
4.1-1 Toward cost-efficient infrared cameras 88
4.1-2 NC-based camera operated in a photoconductive mode 90
4.2 Inside an HgTe-based readout circuit 92
4.2-1 Fabrication of a model 92
4.2-2 Transport characterization 93
4.3 In-situ mapping of a HgTe-based focal plane array 95
4.3-1 X-ray Photoemission Spectroscopy: history and principle 96
4.3-2 Energy landscape of HgTe-based camera 99
4.3-3 Revealing the photocurrent spatial distribution in HgTe-based FPA 103
4.4 Conclusion 107

Infrared nanocrystal-based sensors have witnessed notable progress in recent years, facilitating their integration into a wide array of novel and innovative applications. These next-generation applications are gradually entering everyday life, including LiDAR systems in autonomous vehicles, sensors in smart homes and buildings, and agricultural monitoring systems. As new industries join into the infrared domain, there is a growing emphasis on cost-efficiency rather than high performance. In this context, existing technologies based on epitaxially grown semiconductors are unable to meet the rising demand due to their inherent high cost and limited throughput. Throughout this manuscript, it has become increasingly apparent that nanocrystals emerge as the optimal candidate for the development of cost-effective infrared sensors.

In the subsequent chapter, we will explore the integration of HgTe nanocrystals into an infrared camera featuring photoconductive operation. Through a collaborative effort with NIT, we will showcase the achievement of high-quality images using this nanocrystal-based imaging system. Furthermore, we will delve into the *in-operando* and *in-situ* investigation of the active material within the device, aiming to unravel its operational mechanisms beyond the overall device response. In particular, we will illustrate the utility of photoemission microscopy in probing the energy landscape of the HgTe-based imaging array.[227]

4.1 Focal plane array based on HgTe nanocrystals

The short-wave infrared (SWIR) range of 1 – 2.5 µm is the key spectral range for emerging civilian applications. Presently, the industry-leading technology in this range relies on InGaAs semiconductor materials. However, the growth of InGaAs materials constitutes a substantial portion of the final cost of the focal plane array (FPA). Moreover, the integration of the active layer with the read-out integrated circuit (ROIC) necessitates a complex hybridization process, involving the use of small indium bumps or copper bumps[228] to establish electrical connectivity between the absorbing semiconductor and the ROIC. This step not only increases costs but also poses challenges in reducing pixel size, although smaller pixel pitches approaching the diffraction limit offer enhanced imager quality.[229]

Given the already established nature of this technology, its roadmap does not present a clear path for significant cost reduction. Consequently, in the subsequent section, we will introduce a short-wave infrared camera based on HgTe nanocrystals. Specifically, we will outline the fabrication procedure employed for such a camera and elucidate the developments implemented to achieve high-quality images.

4.1-1 Toward cost-efficient infrared cameras

The developments made on the HgTe-based infrared camera are done in collaboration with New Imaging Technologies[230] (NIT) and D. Darson from Laboratoire de Physique de l'Ecole Normale Supérieure (LPENS).

In the short-wave infrared (SWIR) range, nanocrystal-based infrared cameras using PbS nanocrystals have already been successfully demonstrated and have gained global market presence through companies such as IMEC[231], SWIR Vision System[140], and STMicroelectronics[232]. However, the utilization of PbS nanocrystals poses challenges when addressing wavelengths above 1.5 µm due to its 0.41 eV bandgap, leading to a substantial increase in dark current. In this context, HgTe nanocrystals have been employed in collaboration with NIT and LPENS to develop the first generation of infrared cameras.

The initial implementation of HgTe-based infrared cameras operates in a photoconductive mode, with the nanocrystals designed to mimic the InGaAs cutoff wavelength of 1.7 µm. The photoconductive geometry of the camera is relatively straightforward, facilitating a smooth integration as the first-generation imager. The selected infrared region of interest, the SWIR range, offers convenient accessibility, featuring bandgap energies that are notably higher compared to those of the MWIR or LWIR. Consequently, the presence of thermally

activated carriers is significantly reduced, eliminating the need for a cooling system, which would otherwise substantially increase the camera's cost.

The photoconductive HgTe camera used in this work incorporates the ROIC *NIT1601 Quantum C* developed by New Imaging Technologies. The fabrication process of the ROIC is outlined in Figure 47. The *NIT1601 Quantum C* model the third generation of ROIC developed as a joint effort between our group and NIT. This model has been specifically tailored to ensure compatibility with the deposition of HgTe nanocrystals,[233] and the implementations will be detailed in the following.

NIT ensures the fabrication of the readout integrated circuit. To begin, the ROICs in VGA format (640x512 pixels) with a pixel pitch of 15 µm are manufactured using a Silicon foundry, as illustrated in Figure 47a. Subsequently, chemical mechanical planarization (CMP) is employed to polish the wafers, resulting in a flat surface, as shown in Figure 47b. CMP is a technique that combines chemical etching and mechanical abrasion to attain a flat surface. During CMP, a chemical slurry[234] is applied onto the surface while it is simultaneously polished with a rotating pad, as illustrated in Figure 47b. The chemical agents in the slurry selectively dissolve the surface material, while the mechanical action of the pad helps eliminate any remaining irregularities, resulting in a smoother surface. This importance holds true for nanocrystals as well, as the quality of the film directly affects the sensing performance. It is worth noting that a non-flat surface of the ROIC leads to the formation of cracks and thickness variations in the nanocrystal film, as depicted in Figure 48b. Furthermore, when a thick film, typically exceeding 400 nm, dries, it tends to develop cracks to a certain extent. Therefore, the use of a thin film (200 nm) in combination with the CMP step is of utmost importance to achieve a high-quality film that meets the desired performance criteria, as shown in Figure 48a.

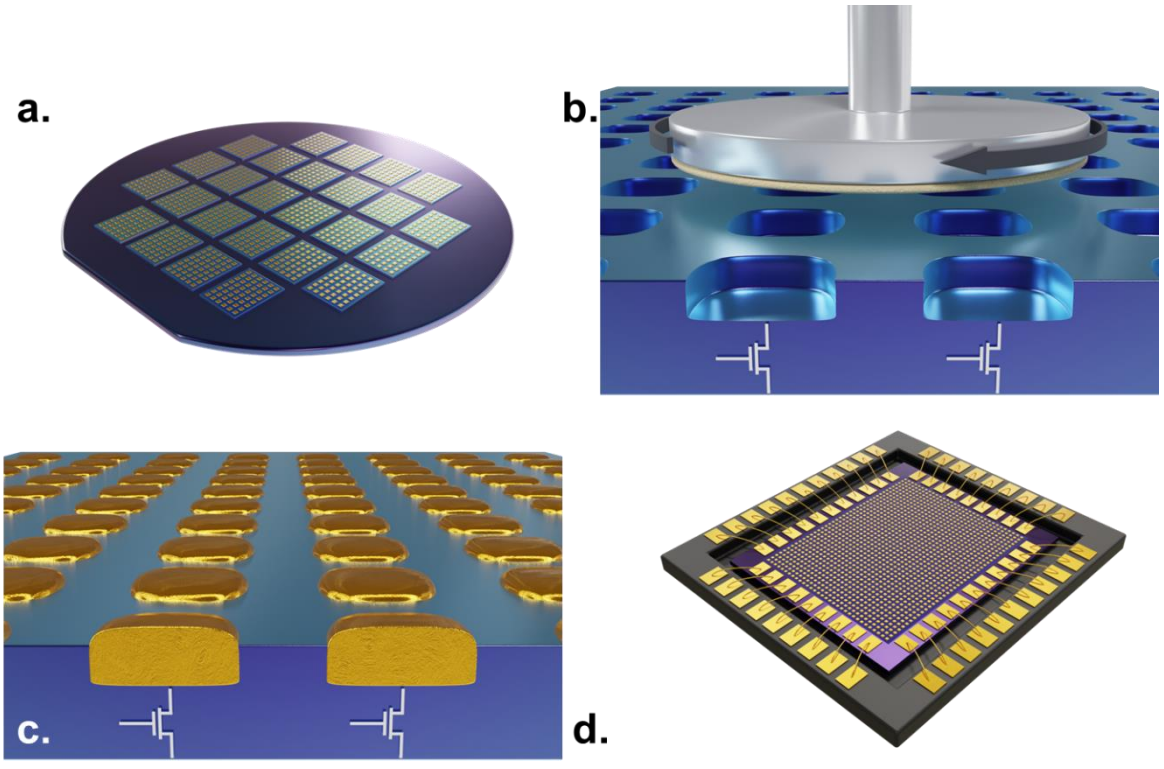

Figure 47 Fabrication of readout integrated circuit model NIT1601 Quantum C. a. A VGA format ROIC array is grown in a Si foundry on an 8-inch wafer. b. This wafer is then polished throughout a chemical mechanical planarization step to obtain a flat surface. c. Electrode contacts are grown with top gold plating to minimize amalgam formation with HgTe NCs deposited later. d. The wafer is then sliced and packaged in a CLCC.

Following this, an electrode is grown on each pixel, with the thickness chosen slightly larger than that of the dielectric surface to prevent any discontinuities in the nanocrystal film, as depicted in Figure 47c. Finally, the readout circuits are sliced and packaged onto a ceramic leadless chip carrier (CLCC), as presented in Figure 47d.

HgTe nanocrystals are grown with a size of approximately 6 – 8 nm, which corresponds to a cutoff wavelength of 1.7 µm. This specific infrared region aligns well with the emerging applications that demand cost-effective sensors. To render the HgTe nanocrystals photoconductive, they undergo processing in the form of an ink comprising a mixture of mercury salt ($HgCl_2$) and mercaptoethanol (MPOH). The concentration of the ink is set at approximately 250 $mg.ml^{-1}$ to ensure a film thickness of 200 nm through the employment of spin-coating. This concentration, along with the parameters governing the speed of spin-coating, has been carefully optimized to establish a reproducible process, which is crucial for a successful transition to industrial-scale production. Our observations indicate that employing a higher ink concentration, typically around 500 $mg.ml^{-1}$, yields thicker films exceeding 400 nm. However, this higher concentration leads to colloidal instability of the ink, resulting in the aggregation of nanoparticles and the formation of a gel-like substance. Therefore, we have chosen to hold to the initial ink concentration to achieve a HgTe ink that remains colloidally stable.

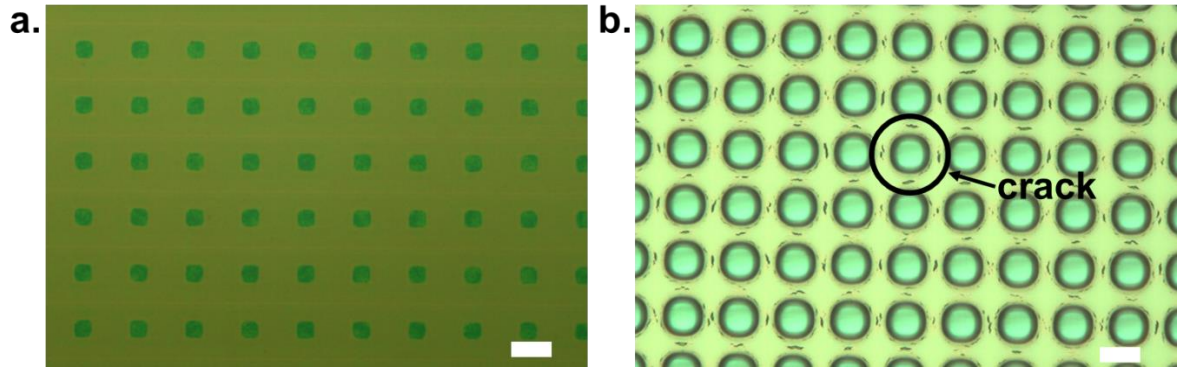

Figure 48 Thickness effect on the nanocrystal film quality. a. Optical microscopy image of a ROIC coated with a thin film HgTe NCs of around 200 nm. b. Optical microscopy image of a ROIC coated with a thick HgTe NC film of approximately 400 nm. There is a formation of discontinuities (cracks) around pixels. White rectangles on both pictures are the scale bar corresponding to 10 µm.

4.1-2 NC-based camera operated in a photoconductive mode

The main objective of a readout integrated circuit is to collect, amplify, and process the electrical signals generated by the active material in response to incident light. In the photoconductive mode, the ROIC functions by applying a voltage across the photoconductive material. The ROIC model used in this study, the *NIT1601 Quantum C*, is specifically designed to operate in this photoconductive mode, which allows for an in-plane polarization with a checkerboard distribution. In practical terms, a bias voltage is applied to alternate pixels, resulting in an effective half VGA format. However, through a software-based approach, a full VGA image can be reconstructed by combining two identical images with inversed checkerboard distributions.

The results presented in Figure 49 exhibit infrared images obtained using the HgTe-based imager with a cutoff wavelength of 1.7 µm. To achieve these images, HgTe nanocrystals were deposited in a single step using spin-coating, resulting in a high-quality film that directly translates to high image quality. As depicted in Figure 49, the infrared pictures exhibit remarkable uniformity, with minimal occurrence of dead pixels, mainly located at the edges due to border effects. These effects could be mitigated by reducing the film thickness.

Figure 49 Short-infrared images captures with the HgTe-based camera. a. Picture of the Eiffel Tower in Paris. b. Picture of the Louvre Museum in Paris. c. Image captured in Paris of trees. d. Same picture as (c) with an addition longpass filter at a cut-on wavelength of 1400 nm.

Figure 49 demonstrates the feasibility of passive imaging in the short-infrared range using the HgTe camera. The scene captured in Figure 49 exclusively relies on natural sunlight for illumination. Furthermore, Figure 49d was obtained using a longpass filter (FEL) with a cut-on wavelength of 1400 nm, providing evidence that the captured images result from infrared radiation and not residual silicon absorption from the CMOS or the visible response of NCs. Additionally, an observable difference in contrast between Figure 49c and d can be discerned, with the tree's leaves appearing darker in the FEL image due to water absorption beyond 1.4 µm.

Low noise electronics compatible with the employed ROICs have been developed by David Darson at LPENS. These electronics are integrated into a vacuum chamber along with a double Peltier stage, enabling effective cooling of the detector to temperatures as low as -40 °C. In collaboration with D. Darson, we conducted a characterization of the HgTe-based infrared camera, which revealed an EQE of approximately 4 – 5%. The camera achieved a frame rate of 200 frames per second (fps), and this rate can be increased up to 340 fps by selecting a specific region of interest (ROI) within the image (640x200 pixels).[44] However, it is important to note that the main limitation of the photoconductive mode is the dark current level, which restricts the integration time to 1 ms at room temperature in the first generation of camera.

The next challenge will certainly involve the development of an alternative device geometry based on a vertical colloidal stack. This configuration will enable the operation of the ROIC at 0 V or reduced polarization, leading to a significant reduction in dark current and subsequently improving the signal-to-noise ratio. To realize a vertical stack, it is imperative to

determine the electronic structure of each material and gain a deeper comprehension of the active material's properties beyond the overall response of the device. In the subsequent sections, I will delve into the investigation of the energy and photocurrent landscape of the HgTe-based short-wave infrared camera through *in-situ* and *in-operando* techniques. The latter are based on photoemission and photocurrent microscopy. The aim is to developed new tools to probe the material within the context of the device itself (*in-operando*).

4.2 Inside an HgTe-based readout circuit

Understanding the material properties of nanocrystals is crucial for the design and development of highly efficient infrared sensors. For the first time, we have demonstrated the first generation of HgTe-based camera providing highly uniform SWIR images. Nonetheless, to fully exploit the potential of nanocrystals in the design of ROICs, it is imperative to delve into their intrinsic material properties and investigate their behavior at the sub-µm level, corresponding to the pixel size. To facilitate this exploration, a device that mimics the ROIC architecture has been developed, enabling subsequent *in-situ* and *in-operando* experimental investigations. In the following section, we will elaborate on the fabrication process of the ROIC model and discuss the characterization of its transport properties.

4.2-1 Fabrication of a model

The fabrication of the focal plane array-like structure is carried out in the cleanroom of Institut des Nanosciences de Paris. Figure 50 describes the different steps of the fabrication procedure. The fabrication process of the device initiates with the cleaning of the glass substrate. Firstly, the substrate undergoes sonication in acetone, followed by rinsing with isopropanol, and subsequent drying using N_2 gas. To ensure optimal cleanliness, a final cleaning step is executed employing an O_2 plasma treatment, as shown in Figure 50a.

To enhance adhesion, an adhesion promoter TI PRIME is spin-coated onto the substrate and subsequently baked at 120 °C for a duration of 2 minutes. Subsequently, a photoresist layer AZ5214E is uniformly spin-coated onto the substrate and baked at 110 °C for 90 seconds to perform optical lithography.

The substrate is then exposed to ultraviolet (UV) light through a precisely positioned pattern mask for 1.5 s. Following exposure, the resist film is baked at 125 °C for 2 minutes for the inversion of the resist pattern. Subsequently, a flood exposure lasting 40 s is carried out. The resist is then developed by immersing the substrate in a bath of AZ726 developer 30 s, followed by rinsing with pure water and gentle drying using N_2 gas. To eliminate any remaining resist residues, the patterned substrate is subjected to 5 minutes of oxygen plasma treatment.

Next, a thin film consisting of chromium (5 nm) and gold (100 nm) is deposited onto the patterned substrate using thermal evaporation. The lift-off process is carried out by immersing the film in acetone for a duration of 1 hour, resulting in the removal of the resist layer and leaving behind the desired gold electrode pattern. The resulting device structure consists of 8 pixels, each with a size of 6x6 μm^2, and a pitch of 15 µm, as the focal plane array of *NIT1601 Quantum C* used in the previous section, as shown in Figure 50b and d.

Following a rinsing of the sample with acetone and isopropanol, the adhesion promoter and resist deposition steps are repeated for the subsequent phase of fabrication. In this phase, a second chromium mask is used to expose the sample for a specific duration of 1.5 seconds. Similar to the previous step, the resist inversion process (comprising annealing and flood exposure) is executed, followed by development in AZ726 developer for 30 seconds and rinsing in pure water.

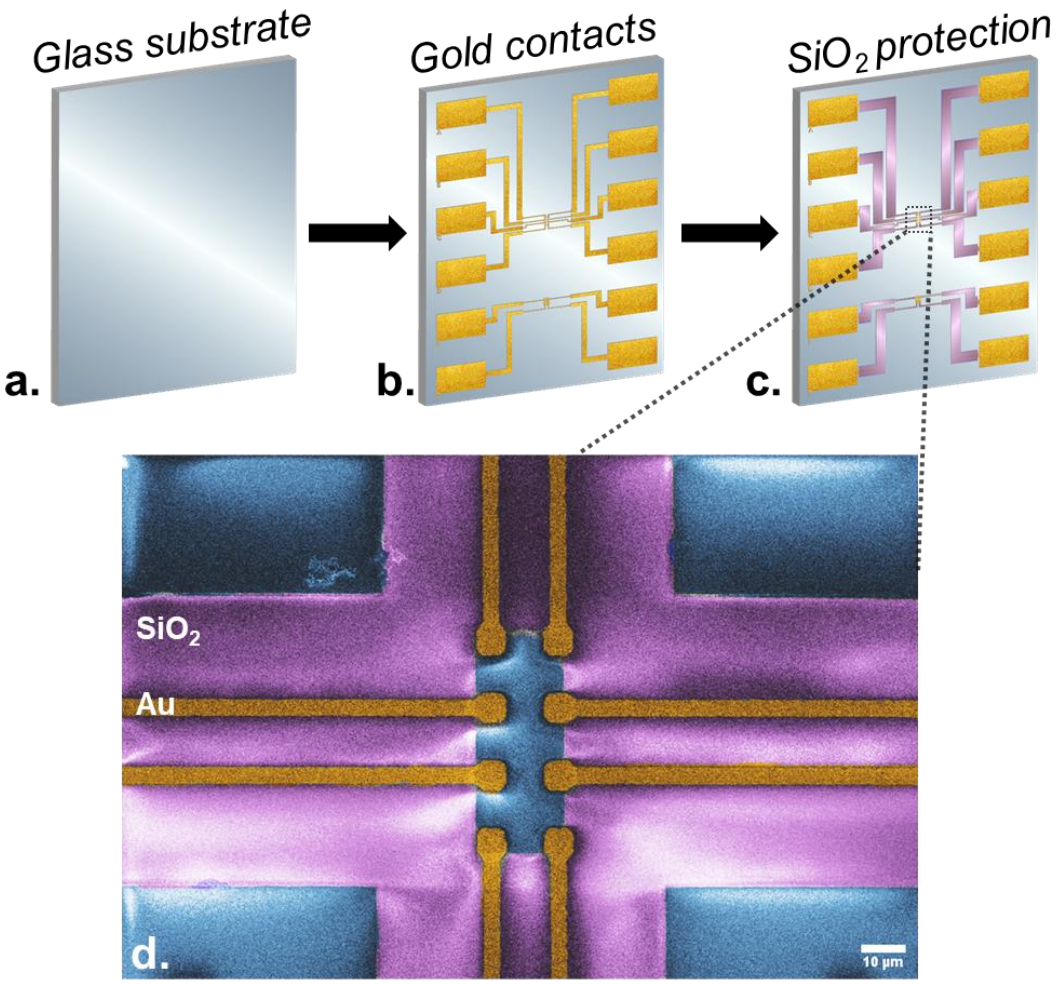

Figure 50 Main fabrication steps for the focal plane array-like device. Deposition on a glass substrate (a.) of the gold metallic contacts after U-V lithography (b.). c. Sputtering of SiO_2 after a second U-V lithography. d. False-colored optical microcopy image of the focal plane array-like structure with 15 µm pixel pitch. Substrate is blue, silica appears purple and gold contact are goldy.

The patterned sample is then introduced into an Alcatel sputtering chamber for the deposition of a 100 nm layer of SiOx. This deposition process spans approximately 50 minutes. Finally, any remaining resist is removed by immersing the sample overnight in acetone. The electrode contacts are intentionally buried beneath this layer of silica to ensure their exclusion from the photocharge collection process. As a result, only the electrode tips, corresponding to the pixels, are electrically active, mirroring the operational principle observed in the actual ROIC, as depicted in Figure 50c and d.

Finally, a film of HgTe nanocrystals ink with a cut-off wavelength at 1.7 µm is deposited on the patterned sample throughout a spin-coating process. The ink concentration and the spin-coating parameters have been optimized to reach a final film thickness of 200 nm, which aligns with the thickness utilized in the practical implementation of the ROIC.

4.2-2 Transport characterization

Before delving into spatial mapping of the energy and photocurrent landscape, the focal plane array-like device has been characterized in terms of performance for SWIR sensing.

The dark current has been measured across a range of temperature, extending down to 150 K, as depicted in Figure 51a. Under 2 V operation at 250 K, the resulting current density reaches approximately 500 $\mu A.cm^{-2}$. Notably, as the temperature is progressively reduced from

room temperature to 200 K, the current experiences a significant reduction of two orders of magnitude, accompanied by a corresponding 260 meV activation energy, as illustrated in Figure 51b. It is worth noting that this activation energy is slightly lower than the characteristic value of half the band gap ($E_G/2 = 350\ meV$), which suggests that the primary mechanism influencing carrier density is the balance between generation and recombination.

Figure 51c presents the responsivity characteristics of the device under broadband blackbody illumination at a temperature of 980°C. The responsivity values exhibit an increase with larger electric fields or higher operating temperatures. As stated in the introduction chapter, the responsivity is closely linked to the external quantum efficiency (EQE) and is given by the expression $R = (EQE \cdot e)/h\nu$, where e represents the charge of a proton and $h\nu$ corresponds to the energy of the incident photon. Therefore, responsivity values exceeding approximately 2 A·W^{-1} at 1.7 µm correspond to EQE values above 100%, indicating the presence of photogain[45,74,76] in the system.

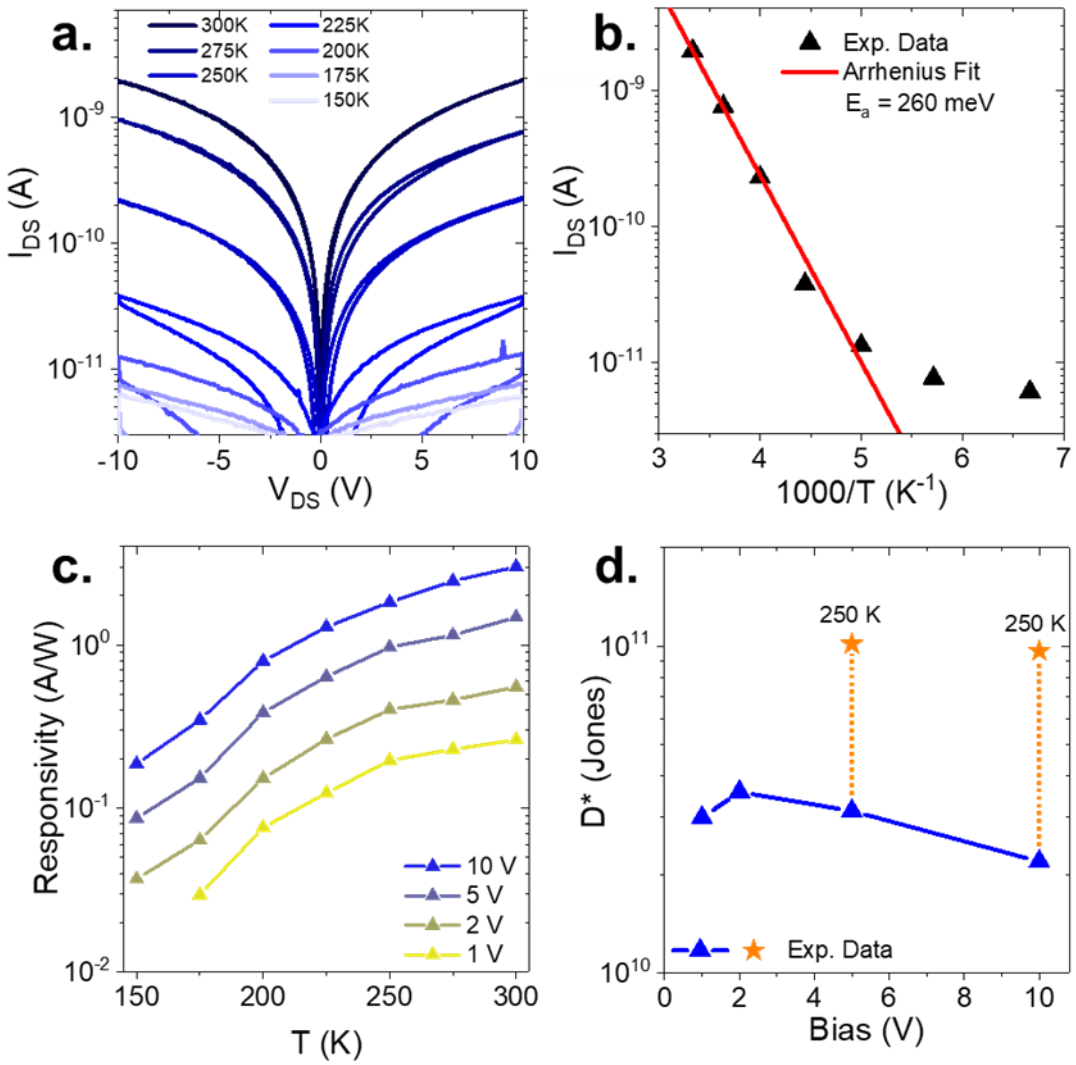

Figure 51 Focal plane array-like structure and performances for SWIR detection. a. IV curves from the FPA-like device at various temperatures. Darker curves correspond to higher temperatures. b. Current as a function of the temperature (scatter) and its Arrhenius fit (red line). c. Responsivity as function of the temperature under various applied biases. d. Detectivity as function of the applied bias at room temperature and at 250 K.

We have seen in the second chapter that HgTe with a band-edge at 1.7 µm exhibits a p-type behavior, which may appear counterintuitive considering that the effective mass of holes

in HgTe is 25 times greater than that of electrons.[29] Under illumination, charge transport primarily occurs through photo-generated holes, while electrons, due to their reduced mobility, exhibit behavior reminiscent of trapping. Once a hole reaches an electrode, it is reinjected into the film by the opposing electrode to ensure the electroneutrality of the sample. This process continues until the slower electrons undergo recombination. This mechanism, called photogain, generates multiple holes per absorbed photon, contributing to the significant photoresponse observed in our device.

Figure 52 shows the noise current density of the device and demonstrates a dominant 1/f behavior, as expected for a photoconductive device based on nanocrystals.[89,212] At room temperature, the noise exhibits a substantial increase of over one order of magnitude when the bias voltage is increased from 1 to 10 V, as clearly demonstrated in Figure 52a.

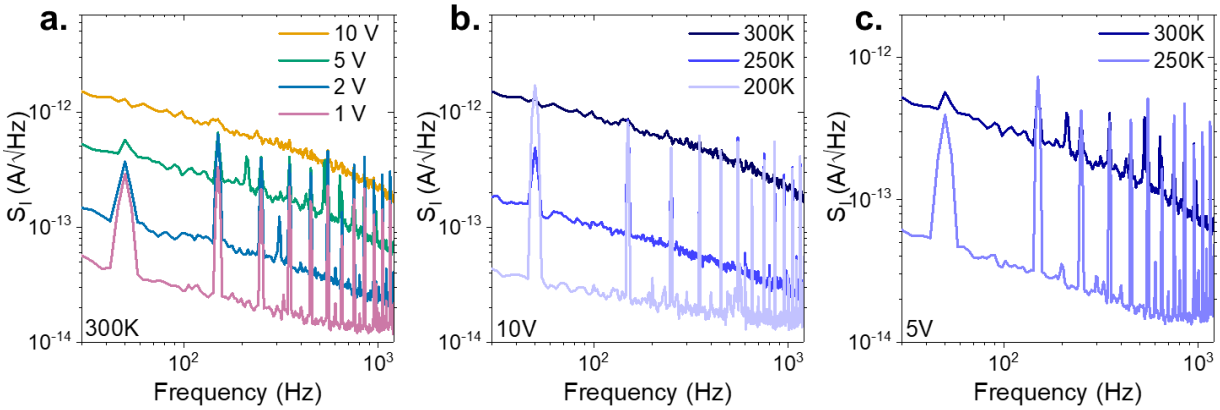

Figure 52 Noise current spectral density of the FPA-like structure under various biases at room temperature (a.) and for different temperatures at 10 V (b.) and 5 V (c.).

Additionally, when the detector is cooled from 300 to 200 K while maintaining a fixed voltage, the noise experiences a significant reduction of nearly one order of magnitude, as illustrated in Figure 52b-c. These observed trends align with expectations, considering that the noise in such a system is closely associated with the dark current, which is highly influenced by temperature and polarization factors. The resulting detectivity value at room temperature is maximized at a potential of 2 V, reaching 4×10^{10} Jones. At a temperature of 250 K, the detectivity further improves, reaching 10^{11} Jones, as depicted in Figure 2e. The achieved detectivity values closely approach the targeted performance levels for short-wave infrared applications, specifically around 10^{11} Jones at room temperature and 10^{12} Jones when operating at lower temperatures.[43]

4.3 In-situ mapping of a HgTe-based focal plane array

Until now, advancements in the field of infrared sensing and imaging have consistently been tied to the comprehension of material properties. For instance, when examining PbS photodiodes, systematic measurements[209] were conducted to elucidate the interplay between surface ligands, associated dipoles, and the energy of the band relative to the Fermi level. Similarly, efforts have been undertaken to unveil the band alignment[88,220,226] and complex optical index[139] of HgTe nanocrystals, with the objective of facilitating the rational design of diode stacks. However, prior investigations primarily relied on *non-operando* techniques like optical spectroscopy, electrochemistry, and conventional photoemission. Regrettably, these methods failed to account for the influence of applied electrical fields on the diode and the dielectric environment surrounding it, which is not vacuum, thereby potentially allowing for interactions and charge transfers. While this approach is sufficient for initial device development, it has now become imperative to embrace *in-situ* investigation of the electronic structure *in-operando* conditions.

In this following section, we harness the capabilities of photoemission microscopy as a means to unveil the *operando* electronic properties of a focal plane array. This particular technique has been previously employed by Cavallo *et al.* to probe the scalar energy landscape of a nanocrystal-based field-effect transistor[67,235] and photodiode[236]. Significantly, it has provided invaluable insights into the phenomenon of surface band bending at the interface between the nanocrystal semiconductor and the electrode. By doing so, it has not only provided direct evidence of the impact of gate bias on band alignment but has also laid bare the inherent potential of a diode. Within the context of our work, we undertake an investigation of how photoemission microscopy can be judiciously employed to reveal the distribution of vectorial electric fields in a structure similar to a focal plane array during its operational phase. The findings arising from this investigation will bear considerable significance for the future modeling and design of advanced devices, most notably infrared imagers. The last part of this work will be devoted to the first attempt of performing *in-situ* and *in-operando* photocurrent mapping using scanning near-field optical microscopy.

4.3-1 X-ray Photoemission Spectroscopy: history and principle

X-ray Photoemission Spectroscopy (XPS) is a powerful technique used to probe the electronic and chemical properties of material surfaces. It provides valuable information about the elemental composition, chemical state, and electronic structure of materials.The principle of XPS is based on the photoelectric effect discovered by Hertz[237] in 1887, where X-ray photons are used to excite electrons in a material, causing them to be emitted from the surface. The energy and intensity of the emitted electrons are measured to extract valuable information about the material.

The development of XPS as a technique for surface analysis began in the 1960s. Kai Siegbahn, a Swedish physicist at Uppsala, made significant contributions to the understanding and application of XPS. In 1954, he recorded the first high-energy-resolution XPS spectrum of cleaved sodium chloride (NaCl).[238] A decade later, in 1967, a comprehensive study on XPS was published by Siegbahn, which garnered immediate recognition for its analytical utility. Siegbahn referred to this technique as Electron Spectroscopy for Chemical Analysis (ESCA).[239] Notably, in collaboration with Siegbahn, a group of engineers from Hewlett-Packard (HP) in the USA developed the first commercial monochromatic XPS instrument in 1969. Furthermore, Siegbahn's comprehensive contributions to XPS and its applications were acknowledged twelve years later when he was awarded the Nobel Prize.[240]

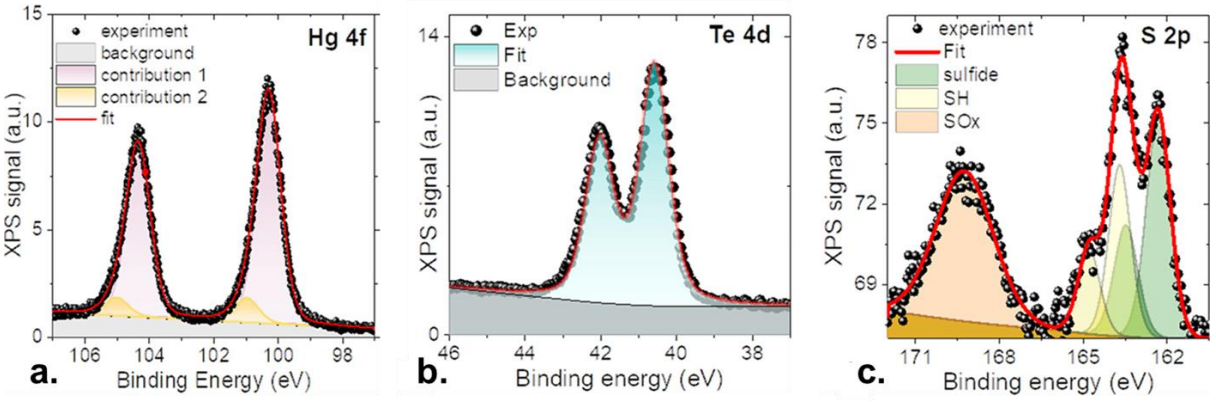

Figure 53 Surface chemistry of HgTe probed by X-ray photoemission spectroscopy. a. Hg 4f core levels for HgTe with a cut-off wavelength at 1.7 µm (the photon energy is hv = 1253 eV). b. Te 4d core levels for the same device (acquired with a hv = 1486 eV). c. S 2p core levels for the same device (hv = 1486 eV). Adapted from ref.[241]

The XPS process begins with the irradiation of the sample surface using X-ray photons. These X-rays possess energies in the range of a few hundred to several thousand electron volts (eV), corresponding to the binding energies of electrons in the material. Therefore, under

such X-ray illumination, electrons can be stripped from the material. The emitted electrons, known as photoelectrons, carry information about the electronic structure of the material. The energy of the photoelectrons is directly related to the difference between the binding energy of the electron in the atom and the energy of the incident X-ray photon. By measuring the kinetic energy and intensity of the emitted electrons, its binding energy BE can be determined as $BE = h\nu - KE - W_{FA}$, where $h\nu$ is the photon energy, KE is the kinetic energy, and W_{FA} is the work-function of the analyzer.

Moreover, XPS offers significant scientific value by enabling the analysis of the energy distribution of photoelectrons, thereby providing essential chemical information. The binding energy of an electron is inherently influenced by its chemical surroundings, enabling the identification of distinct chemical states (redox state or chemical environment) of an element based on their characteristic binding energies. Consequently, XPS facilitates the determination of both the chemical composition and the specific chemical bonding states existing within a given material. As shown in Figure 53, the core level analysis of the predominant element in HgTe nanocrystals investigated in this study is presented. The resolved spectrum of the Te core level (Figure 53b) demonstrates a single distinct contribution. In contrast, the Hg 4f spectrum (Figure 53a) exhibits two distinct contributions,[241] which can be attributed to the interaction of Hg with Te (HgTe) and Hg with sulfur (HgS) originating from the ligands, specifically mercapthoethanol.[64,242] The structure of the S 2p states (Figure 53c) appears to be more intricate, displaying at least three distinct contributions, indicating a potential oxidation of the sulfur atoms present in the ligands.

In the early stages of XPS development, the technique was primarily used to investigate the elemental composition of materials. It provided valuable insights into the surface chemistry of solids, especially in the fields of catalysis and surface science. Over time, advancements in instrumentation and data analysis techniques enabled the characterization of more complex chemical states and the electronic structure of materials. The introduction of synchrotron radiation as a source of X-rays greatly enhanced the capabilities of XPS. Synchrotron-based XPS allowed for higher photon flux and tunable energy (*i.e.*, tunable escape depth), enabling more precise measurements and the investigation of a wider range of materials. It also facilitated the development of XPS-based techniques such as angle-resolved XPS (ARPES), providing additional insights into the electronic structure of materials. Today, XPS is widely used in various fields, including materials science, surface chemistry, catalysis, nanotechnology, and environmental science. It has become an essential tool for studying the surface properties of materials and revealing their electronic structure.

Throughout the course of my thesis, I have attended multiple experimental sessions at the SOLEIL synchrotron facility. These sessions were conducted approximately biannually and focused on the acquisition of photoemission data using TEMPO[243] and ANTARES beamlines. These beamlines are used for investigations involving soft X-ray photons within the energy range of 20 to 1500 eV. The results of these experimental sessions will be comprehensively presented in the subsequent subsection. While here, we will elaborate on the experimental parameters and conditions employed during these sessions.

In the context of this research work, we have initially conducted non-spatially resolved measurements on HgTe NCs with a cut-off wavelength of 1.7 µm. To facilitate such measurements, a thin film of HgTe NC ink is spin-coated onto a silicon substrate that had been pre-coated with an 80 nm layer of gold. This coating allows to avoid any chemical interaction between the gold substrate and HgTe NCs. Then, during the experimental procedure, X-ray radiation interacts with the material, resulting in the ejection of photoelectrons from the surface and subsequently inducing a charge imbalance with photoholes left behind. This charge imbalance causes an excess of charge, resulting in an increase of the BE due to coulombic interactions by holes. Consequently, the presence of the gold coating allows for the dissipation of the charge excess, thereby ensuring the charge neutrality within the system.

The prepared sample is then introduced into a dedicated preparation chamber, wherein it undergoes a degassing process under a vacuum level below 10^{-9} mbar, for at least 2 hours,

which is crucial to remove any oxygen or carbon contamination. Following the degassing process, the sample is transferred to the analysis chamber for further investigation. The acquisition of the signal is achieved through the utilization of an MBS A-1 photoelectron analyzer, which is a two-dimensional detector capable of amplifying incoming electrons and discriminating them based on their respective kinetic energies.

The data acquisition process is conducted using a constant pass energy of 50 eV within the electron detector. The pass energy refers to the energy range within which the photoelectrons are allowed to pass before reaching the electron analyzer. It plays a fundamental role in determining both the energy resolution and sensitivity of the experimental setup. Subsequently, the photon energy is adjusted at 150 eV to enable the acquisition of valence band and work function, and at 700 eV for the analysis of core levels. At lower photon energy levels (150 eV), the device is predominantly probed at its surface in comparison to higher energy photons (700 eV), while having a greater signal at lower binding energies (BE). However, it is important to note that this necessitates calibration whenever there is a change in photon energy. The determination of the work function involves the application of an 18 V bias between the sample and the analyzer in order to let low energy electrons enter the analyzer. The Fermi energy is calibrated using a gold substrate, where the incident photon energy is determined by measuring the second order of the Au core level peaks. To establish a reference point, the Fermi edge is measured, and its binding energy is set as the zero-energy-point. This calibration shift is subsequently applied to all XPS spectra acquired using the same pass energy, ensuring consistency and accuracy throughout the analysis.

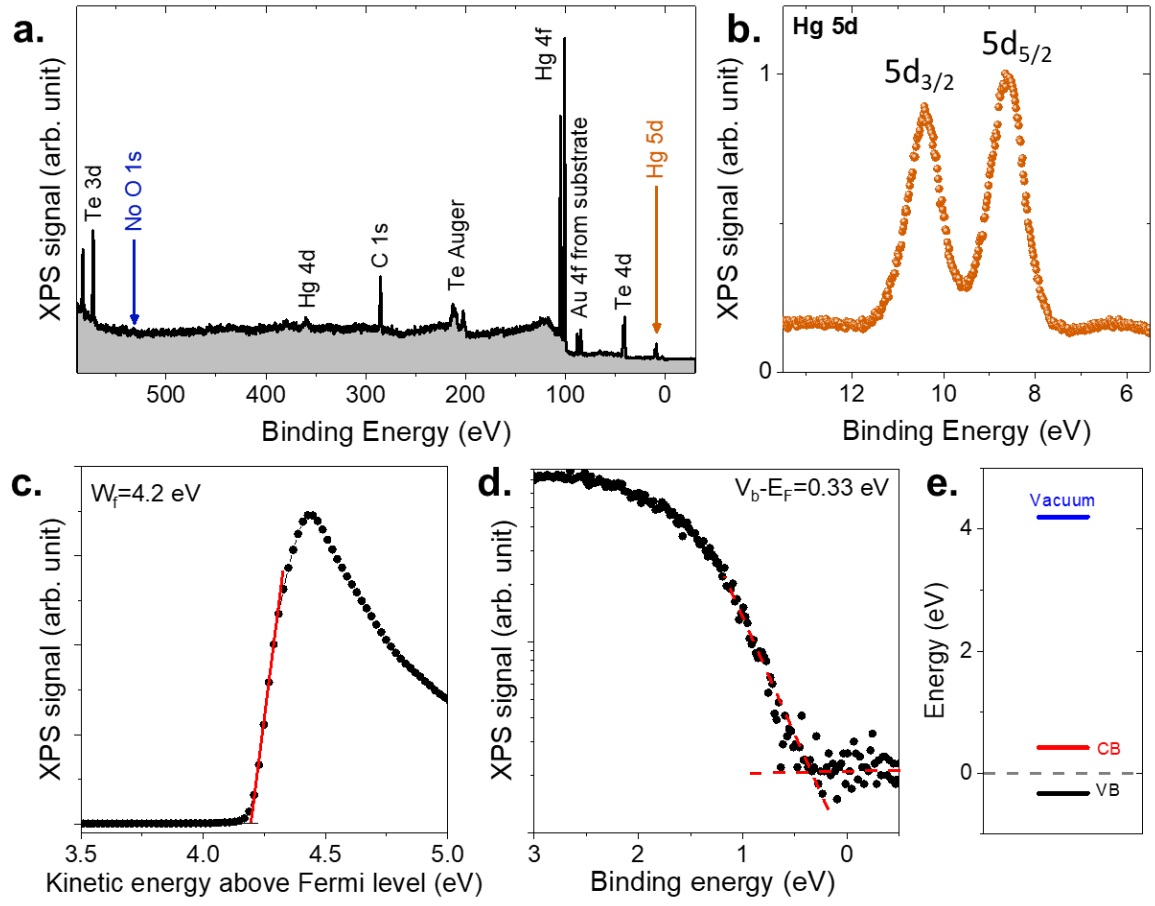

Figure 54 X-ray photoemission spectroscopy of HgTe NC thin film. a. Overview spectrum acquired at hv=700 eV. Contribution from gold is due to its presence in the substrate (used to prevent sample charging). b. XPS spectrum of the Hg 5d state. c. XPS spectrum of the of the secondary electron cut-off. d. XPS of the valence band. e. Reconstructed electronic spectrum of the HgTe NC used in device considering an optical band gap of 0.7 eV.

Figure 54a presents the photoemission survey spectrum obtained by employing identical film preparation procedures to ensure the representativeness of the NC film with respect to the device. The survey spectrum reveals discernible contributions from Hg and Te, while the presence of the Au 4f state can be attributed to the gold substrate, which mitigates charging effects. Furthermore, a minor carbon contribution originating from the mercaptoethanol ligands is observed. Conversely, peaks associated with S and Cl exhibit weak cross-sections or occur in very small quantities, rendering them undetectable. Notably, despite the ambient conditions during film preparation, no significant oxygen contribution (BE(O1s) = 532 eV) is evidenced. This observation aligns with a recent report by Zhang *et al.*,[241] which emphasizes the limited propensity of HgTe nanocrystals for oxidation. This absence of oxidation is of paramount importance to ensure the pristine state of the valence band and its freedom from oxide contributions, which is critical for photoemission microscopy investigations.

Furthermore, an investigation of the valence band state reveals its position to be 0.3 eV below the Fermi level, as illustrated in Figure 54d and e. This particular arrangement locates the Fermi level within the lower portion of the band gap, providing a plausible explanation for the observed p-type conduction. Additionally, this determined value can be correlated with the thermal activation energy associated with hole activation. Despite the material not being strictly intrinsic, the significant depth of the Fermi level within the band gap reinforces the material's relevance for photodetection. Finally, through the measurement of the low energy cut-off of secondary electrons, we determine the material's work function to be approximately 4.2 eV, and by coupling this information to infrared spectroscopy to determine HgTe bandgap value, a reconstructed energy diagram on an absolute energy scale is proposed, as presented in Figure 54e. Here, Coulombic correction to bandgap (few tens of meV) are neglected as they fall within the experiment resolution.

Following this run, we have conducted spatially resolved photoemission experiments at the ANTARES beamline of the SOLEIL synchrotron. The experimental setup involves using the focal plane array-like device described in the previous section. This device features 8 gold pixels measuring 6x6 µm² each, with a pitch of 15 µm, coated with a 200 nm thick film of HgTe ink.

Linearly horizontally polarized photons with an energy of 95 eV are employed throughout the investigation. Similar to the TEMPO beamline, we use the MBS A-1 hemispherical electron analyzer[244] to discriminate the photoelectrons based on their kinetic energy. The measurements are conducted at a temperature of 250 K (similar to the NC-based device), with an energy resolution of 30 meV and a remarkable spatial resolution as low as 700 nm.

To enable bias application, the ROIC-like device is mounted on the *in-operando* sample holder of the ANTARES beamline, with direct grounding achieved through the manipulator. In order to evaluate the energy shift across the map, photoemission spectra are acquired specifically for the Hg 5d state and subsequently averaged over a small number of points (5 or 10) within the region of interest. Finally, the binding energy is calibrated by measuring the Fermi edge of a gold substrate mounted to the same sample holder as the device.

4.3-2 Energy landscape of HgTe-based camera

After characterizing the electronic structure of HgTe, the next step involves employing X-ray photoemission microscopy to unveil the spatial distribution of the applied electric field within the focal plane array-like device. This is achieved by utilizing a Fresnel zone plate in conjunction with the synchrotron beam, which enables the focusing of the beam from a conventional scale of 100 µm to 700 nm. This range corresponds to the pixel size of the device and remains two orders of magnitude larger than the size of the nanocrystals, effectively preventing any discrete charge effects. It is important to note that although photoemission

microscopy provides a lower resolution compared to transmission electron microscopy techniques like 4D STEM[245,246], which have also been utilized for mapping the vectorial electric field of devices, it offers the distinct advantage of imposing minimal constraints on device updates.

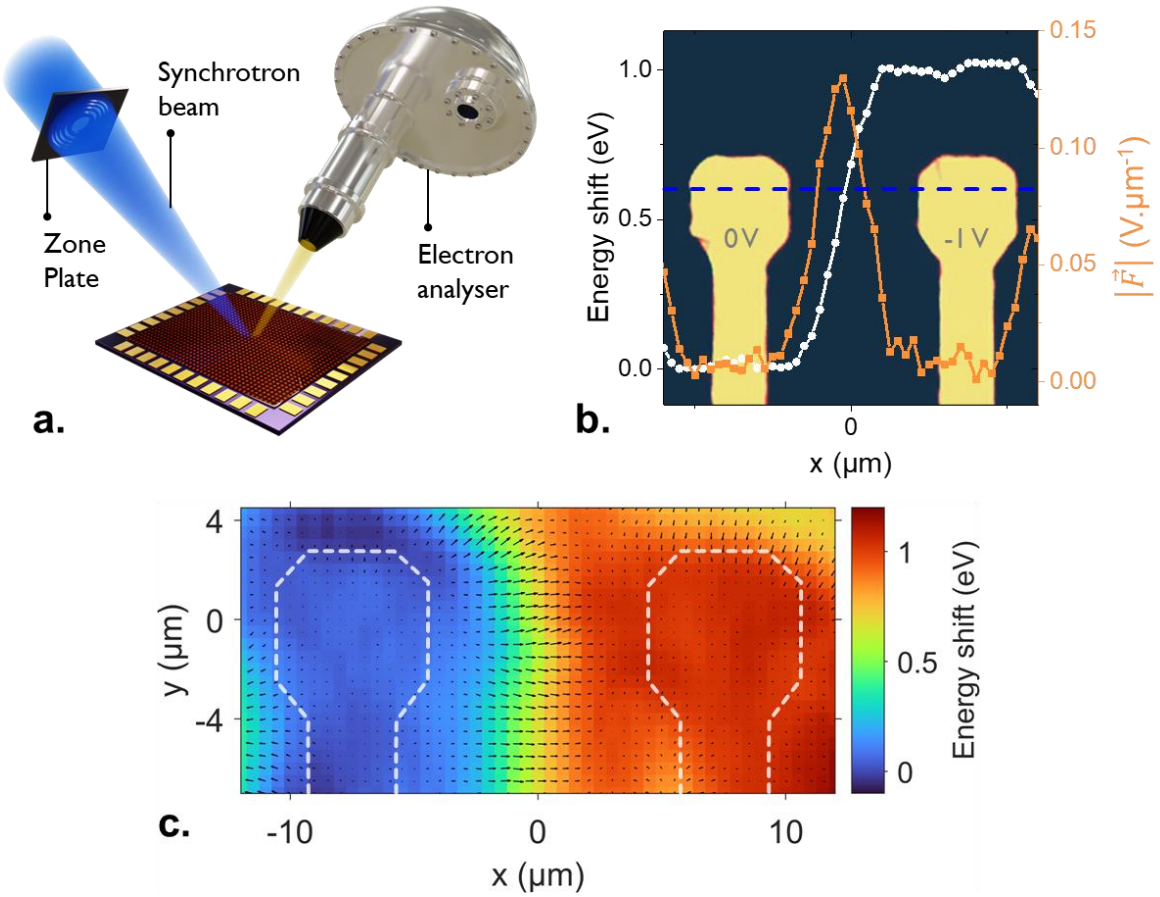

Figure 55 X-ray photoemission microscopy applied to a focal plane array-like device. a. Schematic of the photoemission microscopy setup. b. Energy shift for the Hg 5d state (white line) across the area between two pixels (blue dashed line) as 1 V is applied over them. The profile is obtained by subtracting the profile with grounded electrodes. The orange plot corresponds to the electric field value across the area between two pixels (blue dashed line). A microscopy image of the device is added as background. c. Energy shift mapping (color map) for the Hg 5d state over the area between two pixels as 1 V is applied between them. On top of it, an arrow map indicating the direction and modulus of the electric field as obtained from the gradient of the kinetic energy map.

A systematic raster scanning procedure is employed to scan each point of the sample in front of an electron analyzer, allowing for the acquisition of a photoemission spectrum at every position. The resulting dataset forms a three-dimensional matrix that represents the photoemission intensity as a function of kinetic energy and the (X;Y) coordinates in the sample plane. In combination with the scanning mode, the microscope allows for the *operando* examination of the device by enabling the direct application of bias within the analysis chamber.

Subsequently, the photoemission spectrum of the Hg 5d state is analyzed for each individual point by fitting it with a double Gaussian curve, facilitating the determination of its binding energy. A schematic depiction of the experimental setup is presented in Figure 55a. As demonstrated by recent works by Cavallo *et al.*[67,235,236], this method proves effective in monitoring the bias drop, as shown in Figure 55b. The nearly linear decline in bias between adjacent pixels indicates a monotonous electric field, aligning with the anticipated behavior exhibited by diffusive transport mechanisms commonly observed in nanocrystalline materials,

where conduction primarily occurs through hopping processes.[247,248] In contrast, a bias drop concentrated near the edge contact would be indicative of ballistic transport phenomena.

Within the focal plane array-like structure, the representation of the energy drop as a one-dimensional plot fails to capture the full distribution of the electric field vector ($\vec{F}$). The focal plane array-like device exhibits a two-dimensional distribution of the electric field around each pixel due to its specific geometric configuration. Through the implementation of high-resolution mapping of the energy landscape, it becomes feasible to extract the gradient of the energy landscape. Considering that $\vec{F} = -\nabla V$, where V represents the electric potential, it is possible to establish a direct relationship between the experimental data and the electric field as:

$$\vec{F} = +\nabla KE = \frac{\partial KE}{\partial x}\hat{x} + \frac{\partial KE}{\partial y}\hat{y}$$

where KE denotes the profile of measured kinetic energy. Figure 55c illustrates the mapping of the electric field between two pixels. As expected, the electric potential V remains constant (equipotential) above the metallic electrodes, resulting in an effectively negligible electric field (≈ 0). However, it is noteworthy that the electric field extends beyond the immediate vicinity between the pixels, implying that transport will take place over a larger spatial extent.

In order to gain deeper insights into the experimental distribution of the electric field, electrostatic simulations were conducted by T.H. Dang using Comsol software. The simulation inputs are provided in Table 4. Performing a 3D electrostatic simulation of the device poses certain challenges due to the significant differences in device dimensions along the thickness (200 nm), necessitating a fine mesh, as well as within the plane (15 µm period). Consequently, to simplify the problem, 2D simulations were carried out from both a top and side view, as depicted in Figure 56 and 57.

Table 4 Input parameters for electrostatic simulation on Comsol software.

Material	Electrical conductivity ($S.m^{-1}$)	Relative permittivity
Air	10^{-14}	1
Au	$44x10^{6}$	1
HgTe NC film	1	12
SiO_2	10^{-12}	2.56

For the simulations, the focal plane array-like device was modeled using its nominal structure, with square-shaped electrodes and HgTe present only between the electrodes. In Figure 56b, it can be observed that while the overall electrostatic field closely approximates its average value, a distinct tip effect is evident at the metal-semiconductor interface and particularly at the corners of the electrodes. This observation diverges from the experimental findings, where the field is null on electrode edges and gradually increases from the vicinity of the electrode, reaching a maximum in the central region between the electrodes.

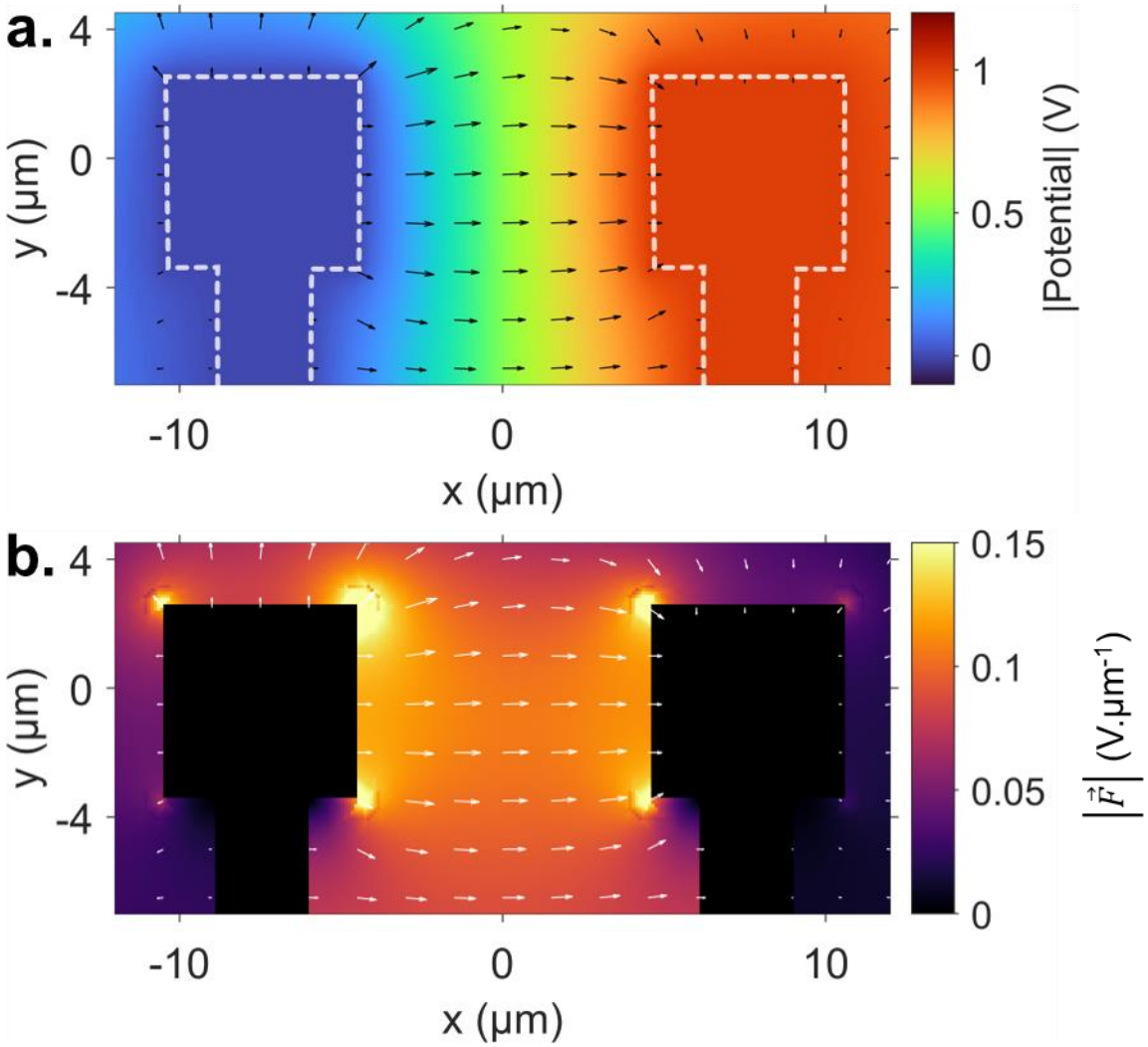

Figure 56 Top view 2D simulation of the electrostatic field assuming a nominal structure. a. Simulated top view of the electrostatic potential map and derived vectorial mapping. (b)

. To mitigate this tip effect, it is necessary to consider a smoother electrode shape with rounded edges and corners. Furthermore, it is important to take into account that the probed field is obtained within the HgTe film rather than in air, as shown in Figure 57. In this scenario, the tip effect is suppressed, and consistent with the experimental observations, a rise in the electric field is observed from the electrodes.

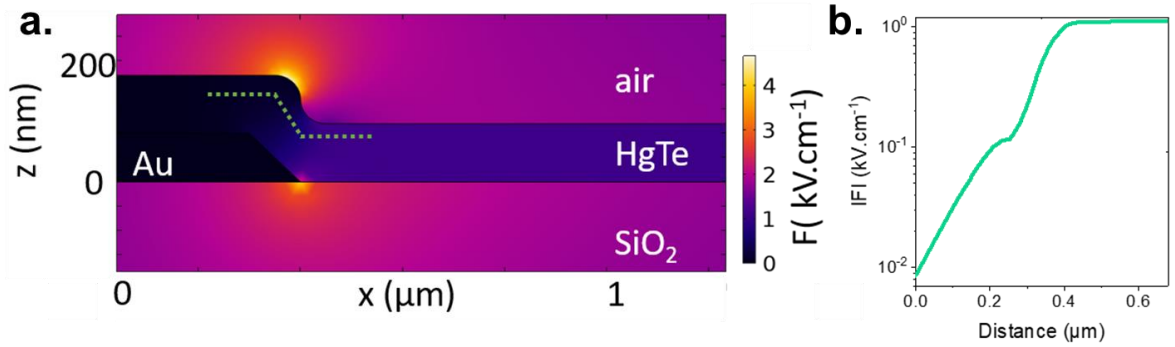

Figure 57 Side view 2D simulation of the electric field in the HgTe film assuming some conformality for the film. a. Simulated side view of the electrostatic field map. b. electrostatic field magnitude along the dashed line shown in part a.

Within the region of interest in the structure, specifically at its center, where the electric field is at its maximum value, experimental measurements yield a magnitude of 1.2 kV.cm^{-1}. This measurement closely corresponds to the average value calculated by dividing the applied bias by the distance between the electrodes ($V/L \approx 1$ kV.cm^{-1}). However, it should be noted that the distribution of the electrostatic field magnitude exhibits a notable broadness, as depicted in Figure 58.

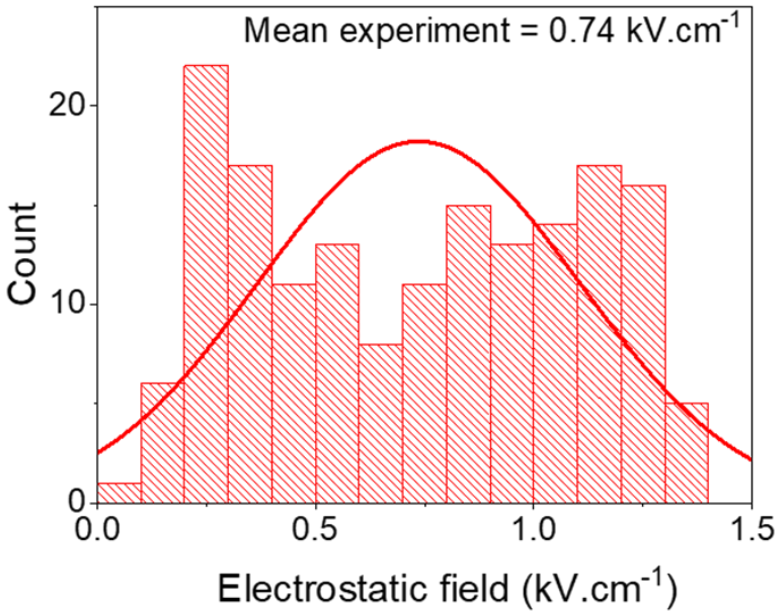

Figure 58 Experimental electrostatic electric field histogram in the area between the two pixels.

The presence of such a broad distribution presents additional complexities in transport modeling, as the diffusion length is also influenced by the magnitude of the electric field.[249–253] Nevertheless, a higher field in regions distant from the electrode facilitates charge collection, as compared to a scenario where the field is more uniformly distributed and charge collection in the vicinity of the electrode is favored.

The determination of the vectorial distribution of the electric field is of significant importance in precisely defining the optically active region of a device, a critical parameter for assessing its performance. In the subsequent investigation, we will extend our analysis beyond the examination of electronic structure by employing Scanning Near-field Optical Microscopy (SNOM) to map *in-operando* the photocurrent of the focal plane array-like device.

4.3-3 Revealing the photocurrent spatial distribution in HgTe-based FPA

Mapping the photocurrent in nanocrystal-based devices holds significant relevance in understanding their optoelectronic properties and optimizing their performance. By visualizing the spatial distribution of the photocurrent, valuable insights can be gained into the mechanisms governing charge transport, recombination, and collection within the device structure. This information is crucial for identifying and addressing potential limitations and optimizing device designs. Scanning Near-field Optical Microscopy (SNOM) is a powerful technique combing the capabilities of near-field microscopy with optical spectroscopy, enabling the simultaneous visualization and characterization of the electromagnetic field distribution and the photocurrent response. In the following, we will elaborate upon the fundamental principle of SNOM and discuss about the preliminary results obtained.

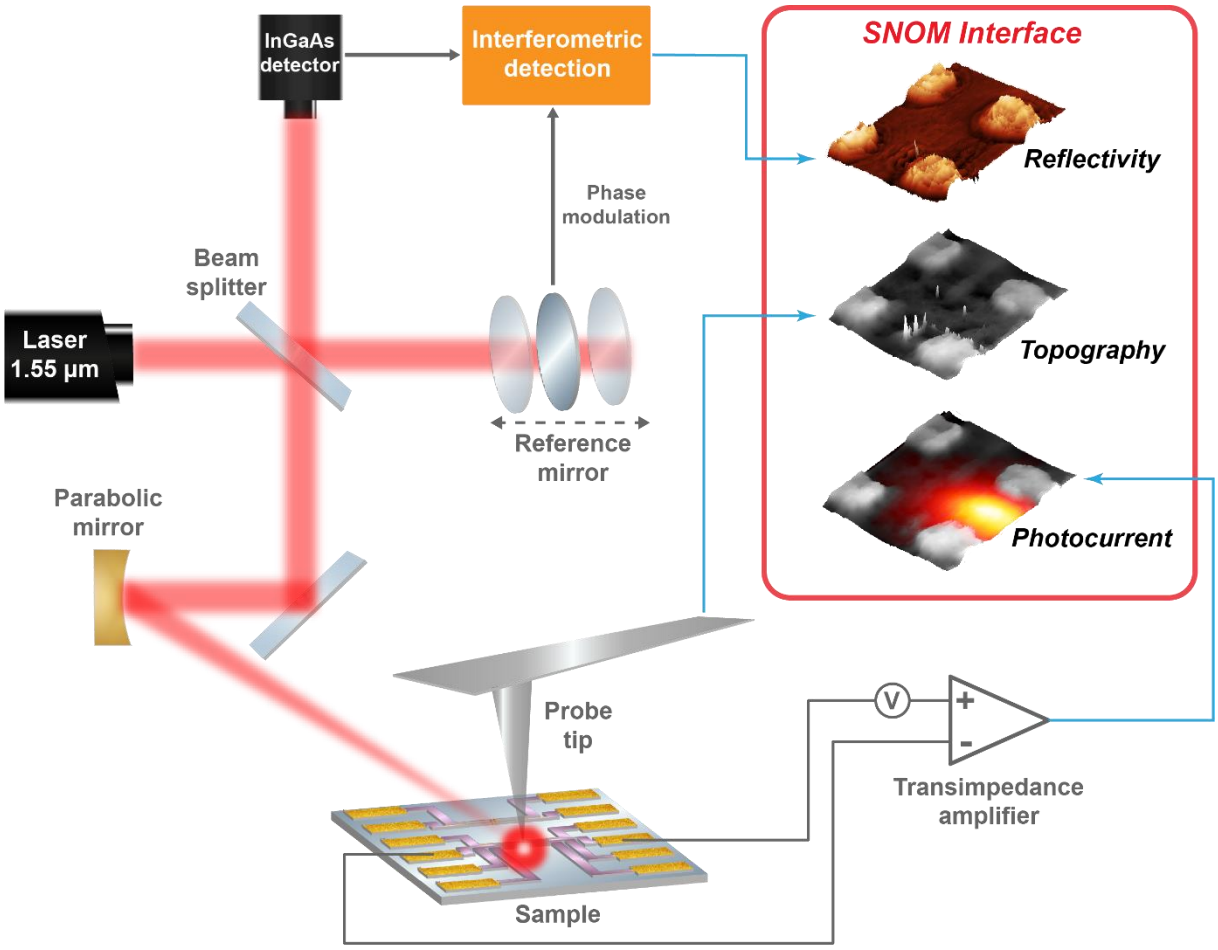

Figure 59 Experimental setup of scanning near-field optical microscopy for photocurrent distribution.

In SNOM, a subwavelength-sized probe tip is used to scan across the surface of the device under illumination at the desired wavelength. The probe tip, typically coated with a metal layer, behaves as an antenna, resulting in a local increase of the electric field concentration at its apex. As the tip approaches the sample surface, the evanescent electromagnetic field at the tip apex interacts with the sample, leading to a local increase of charge generation. Consequently, the total generated photocurrent consists of two components: the current generated by the focused light beam and the current generated at the tip apex. Due to the oscillating motion of the tip at a frequency Ω above the sample surface, the tip-induced photocurrent is also modulated. By scanning the sample beneath the illuminated tip and recording the demodulated photocurrent at the first and second harmonics of Ω, the magnitude and spatial distribution of the local charge generation can be determined. These changes in electrical properties are directly correlated with the local optoelectronic properties of the device. The spatial resolution in SNOM exhibits a direct correlation with the dimensions of the probe tip, enabling achievable resolutions as fine as 20 nm. This surpasses the resolution capabilities of photoemission microscopy by more than one order of magnitude, while approaching the size scale of nanocrystals.

To obtain a complete photocurrent map, the SNOM system scans the probe tip across the device surface in a raster pattern. At each point, the photocurrent is measured, resulting in a two-dimensional image that represents the spatial distribution of the photocurrent across the surface. The high spatial resolution of SNOM is achieved by exploiting the subwavelength-sized probe tip. This enables the visualization of nanoscale features and the identification of localized variations in the photocurrent response. Additionally, by controlling the polarization,

wavelength, and intensity of the incident light, SNOM allows for the study of the dependence of the photocurrent on these parameters, providing insights into the light-matter interactions within the infrared detector.

Throughout the research conducted in this chapter, an investigation is carried out to analyze the local distribution of photocurrent in the focal plane array-like infrared device. This experimental investigation has been conducted in collaboration with Baptiste Fix and Grégory Vincent in their laboratory at ONERA. To simulate the configuration of the SWIR camera discussed in the initial section of this chapter, a deposition of HgTe nanocrystal ink with a thickness of 200 nm is performed on the FPA-like device. To prevent any mechanical damage on the NC film during the extensive raster scanning process, a thin layer of polymethyl methacrylate (PMMA) with a typical thickness of 30 nm is deposited as a protective coating. The thickness of the PMMA layer is sufficiently small compared to to the typical optical relevant length, such as the absorption depth, in order to maintain the viability of a near-field approach.

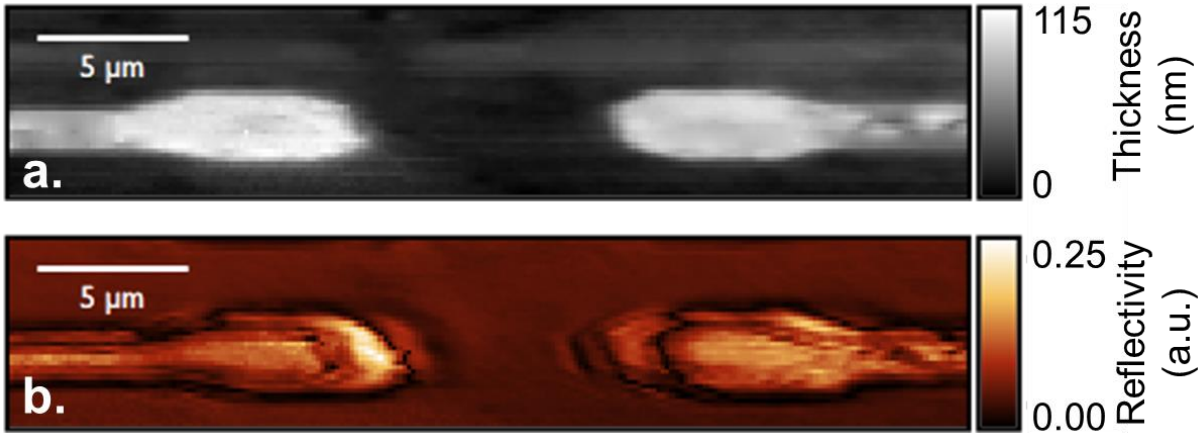

Figure 60 Investigation of the FPA-like device optical properties with scanning near-field optical microscopy. a. Topography map of the FPA-like device acquired with a tip tapping frequency of 80 kHz. b. Reflectivity map of the FPA-like sample demodulated at the second harmonic of the reference signal (tapping frequency) as $2\Omega = 160\ kHz$*, to suppress any far-field contributions. Both maps have a spatial resolution of 160 nm along X direction and 400 nm along Y direction.*

Figure 59 illustrates the experimental setup for SNOM measurement. A laser operating at a wavelength of 1550 nm serves as the light source in this SNOM experiment. The laser emits a linearly polarized beam, which is precisely focused onto the metallic probe tip at an average incident angle of 60°. The probe tip itself possesses a radius of approximately 10 nm and oscillates with a tapping frequency denoted as Ω, operating at around 80 kHz. The tapping amplitude is maintained at 50 nm. In order to capture the scattered light, an InGaAs detector is employed to detect and measure the sample's reflectivity, allowing for the reconstruction of reflectivity maps. The selection of the tapping frequency takes into consideration the electrical bandwidth of the transimpedance amplifier used in this experimental setup. Subsequently, the change in electrical signal resulting from light absorption is acquired through lock-in detection, where the reference signal corresponds to the tapping frequency. The output signal acquired corresponds to the photovoltage. To effectively eliminate contributions from the far-field background, the acquired signal is demodulated at the second harmonic of the tapping frequency, specifically at 2Ω (160 kHz). The photocurrent maps have a spatial resolution of 160 nm along the X direction and 400 nm along the Y direction. The spatial resolution in this case is determined by the dimensions of the window (32x20 µm²), the number of data points collected in each direction, and the integration time per point (26 ms in this case). Achieving a high-resolution map can be time-consuming, with acquisition times exceeding 10 hours at very fine resolutions. In this particular investigation, we chose to acquire multiple maps by varying different parameters, explaining a moderate spatial resolution of 160x400 nm².

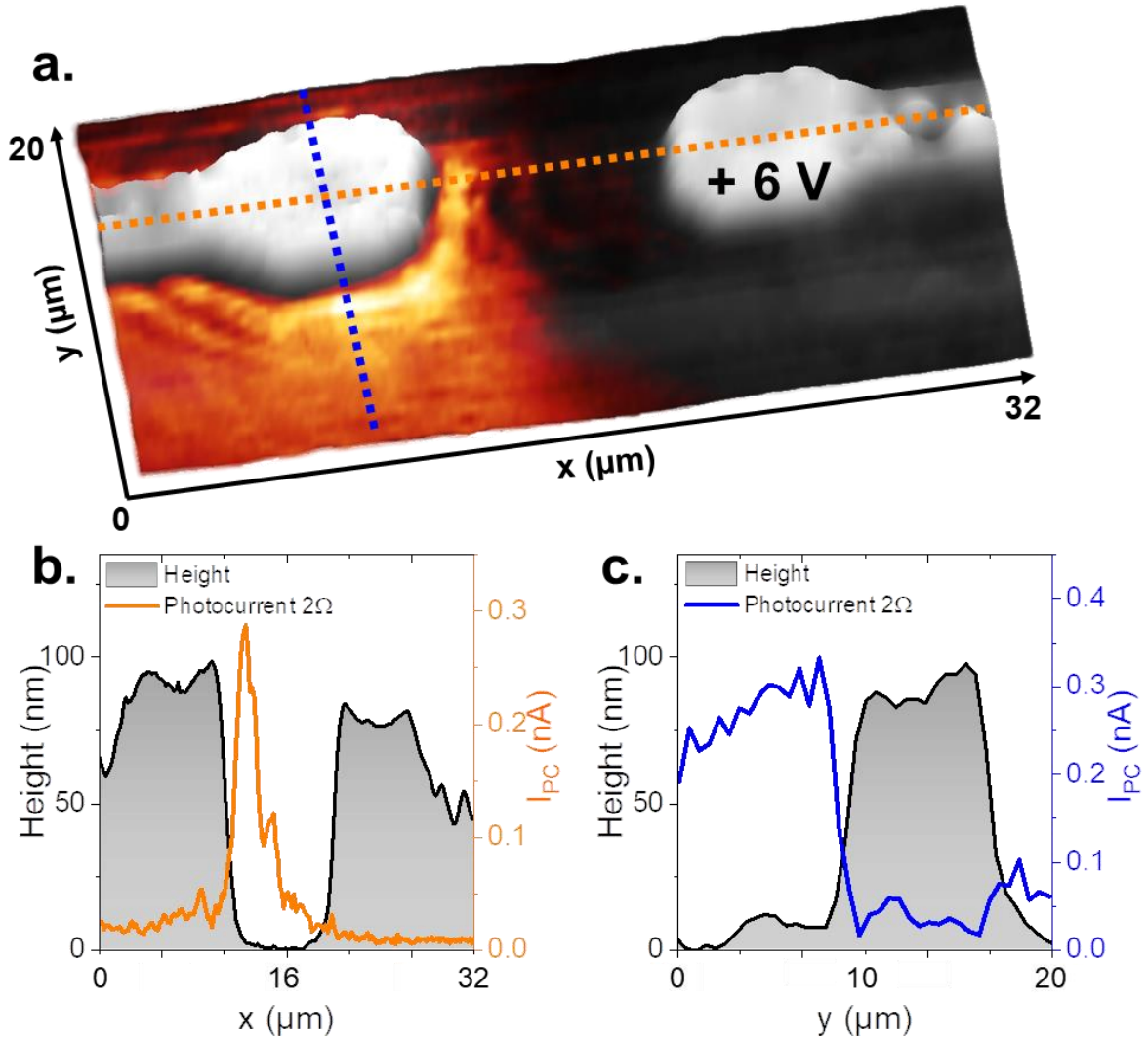

Figure 61 Mapping of the photocurrent distribution within a focal plane array-like device under a polarization of +6 V. a. Combined representation of the topography map and the corresponding photocurrent distribution in the FPA-like device. The intensity of the photocurrent is depicted using a color gradient, where darker shades indicate low photocurrent intensity, while brighter orange shades denote higher amplitude of the photocurrent. The orange and blue lines in (a) correspond to the line profiles examined in graphs (b) and (c) respectively. b. Extracted values for the thickness (depicted in black) and the photocurrent (shown in orange) presented along the horizontal profile scan. The photocurrent is extracted at the tip tapping frequency 2Ω (160 kHz). c. Extracted values for the thickness (shown in black) and the photocurrent (represented in blue) are displayed along the vertical profile scan. The photocurrent is extracted at the tip tapping frequency 2Ω (160 kHz).

The optical properties of the FPA-like device are initially explored through the mapping of its reflectivity across a pixel array period, as illustrated in Figure 60b. The reflectivity exhibits a homogeneous distribution across the nanocrystal region and attains its maximum value on top of the gold electrodes. This observation aligns with expectations, as the gold electrodes are known to exhibit total reflection of the incident light. The examination of this reflectivity map serves as an initial step when conducting photocurrent mapping, as it ensures a proper alignment of the system. Comparable to conventional Atomic Force Microscopy (AFM), SNOM enables the retrieval of the device's topography, as demonstrated in Figure 60a. The obtained topographic map corresponds well with the fabrication process of the FPA-like device, where

the gold electrodes have a thickness of approximately 100 nm. Furthermore, the topography can be visualized in a three-dimensional representation, as depicted in Figure 61a, revealing that the pixels exhibit rounded corners rather than perfect squares. This characteristic further explains considering rounded corners in the electrostatic simulation of the electric field, as discussed in the previous subsection.

The investigation of the photocurrent distribution in the FPA-like device involves the application of a potential of 6 V to one of the pixels while the other pixel is grounded, as depicted in Figure 61a. A distinct asymmetry in the photocurrent distribution becomes evident, with a concentration near the grounded electrode. Furthermore, it should be noted that the distribution of photocurrent extends across the entire pixel rather than being confined solely to the region between the two pixels.

To quantitatively analyze the photocurrent, its values are extracted along horizontal and vertical line profiles, as illustrated in Figure 61b and Figure 61c, respectively. Along the horizontal line between the two pixels, the photocurrent attains its maximum at the very edge of the pixel and decreases as the distance increases, as demonstrated in Figure 61b. The decay length is determined by fitting a single exponential function and is found to be approximately 1.7 µm. Similarly, along the vertical line along the grounded pixel, the photocurrent exhibits a maximum at the edge and decays with increasing distance.

Prior to delving into speculative analysis, it is imperative to replicate the SNOM experiments multiple times to validate the observed photocurrent asymmetry. The results presented in this chapter are based on a single device and have not been replicated with other samples. This challenge is inherent to the feasibility of near-field techniques on nanocrystal-based devices. Certainly, the sample preparation for this technique presents challenges, as it necessitates sufficient robustness to endure the raster scans of the tip. This explains our utilization of a thin PMMA layer, which allows for a near-field approach while ensuring the preservation of sample integrity. Moreover, a parasitic electrical bias coming from the probe tip is possible and should be tracked in future experiments. Therefore, it is of utmost importance to conduct photocurrent mapping on a few additional devices to verify the observed photocurrent distribution. The integration of photocurrent and photoemission spectroscopy for *in-situ* and *in-operando* investigations of the active layer in HgTe-based devices represents a novel approach in the field of nanocrystals and would significantly contribute to the development of advanced infrared devices.

4.4 Conclusion

The spectral range of 1 – 2.5 µm, known as SWIR, holds significant importance for emerging civilian applications. As the infrared market attracts participation from new industries, the demand for efficient and cost-effective sensors intensifies. In this context, in collaboration with NIT and LPENS, we have successfully developed a SWIR camera using HgTe nanocrystals, which exhibits a cut-off wavelength at 1.7 µm. The employed ROIC functions in a photoconductive mode, yielding high-quality images from the HgTe-based imager. Notably, the imager achieves an EQE of 4 – 5%. Moving forward, a significant challenge lies in operating the ROIC in a photovoltaic mode, allowing for a 0 V operation that would substantially enhance the camera's sensitivity.

The integration of nanocrystals into advanced devices, such as photodiodes, necessitates the establishment of experimental techniques capable of unraveling the material properties within a realistic dielectric environment during operation. In the initial phase of this work, we have successfully fabricated a device that mimics the behavior of the ROIC and conducted a characterization of its transport properties. The FPA-like device exhibits an EQE exceeding 100%, which signifies the presence of photogain.[45,74,76] Furthermore, the detectivity at room temperature reaches a value of $4x10^{10}$ Jones, which is in close proximity to the required performance levels for SWIR applications.

Subsequently, we have successfully showcased the efficacy of scanning photoemission microscopy as a pertinent technique not only for probing the energy landscape of the device *in-operando* but also for revealing the vectorial distribution of the electric field, which cannot be described by a scalar parameter in this device. The method exhibits a remarkable versatility, as it has been successfully implemented across diverse device geometries, including field-effect transistors, diodes, and now focal-plane arrays. This underscores the broad applicability and generality of the approach in providing valuable insights into the optoelectronics properties of various nanoscale devices.

Lastly, in the last part of this work, we began an initial effort to elucidate the spatial distribution of photocurrent within a HgTe-based focal-plane array FPA through the use of Scanning Near-field Optical Microscopy. This technique reveals the underlying mechanisms that govern charge transport, recombination, and collection within the architecture of the device. The next step is to verify the reproducibility of the observed photocurrent distribution across multiple samples of the FPA-like device.

By combining the comprehensive 2D mapping outcomes obtained through photoemission microscopy, simulation tools, and the utilization of nanoprobes for photocurrent mapping, it becomes conceivable to establish a correlation linking the static energy landscape to conduction at the mesoscopic scale. This critical effort would facilitate the integration of HgTe nanocrystals into highly advanced infrared technologies, driving the field towards unprecedented levels of sophistication and performance.

Conclusion and perspectives

Over the course of the past three decades, the field of nanocrystals has undergone a rapid evolution, involving various aspects such as precise size and doping control during growth, the establishment of photoconduction within nanocrystal arrays, and the integration of nanocrystals into advanced devices, such as cameras. Within the context of this manuscript, it has become evident that mercury chalcogenides (HgX) nanocrystals represent a promising and viable alternative to conventional epitaxially grown semiconductors for the realization of high-performance and cost-effective infrared sensors. Throughout the course of my PhD thesis, I have explored innovative concepts relating to both the material properties of nanocrystals and the design of complex device geometries, with a particular focus on enhancing the light-matter coupling.

The second chapter focused on employing intraband absorption in nanocrystals, combined with a strategic approach to light management, for the development of a HOT mid-infrared photodetector. To achieve this, a hybrid material consisting of HgSe/HgTe NCs was used, acting as a dye-sensitized infrared sensor, wherein intraband absorption is decoupled from transport properties. The hybrid material uses HgSe nanocrystals to maintain intraband absorption in the MWIR, while simultaneously decreasing dark current, increasing activation energy, and enhancing time-response through the incorporation of HgTe NCs. Collaboratively, with D. Boschetto from LOA, we unveiled the charge transfer mechanism between HgSe and HgTe nanocrystals via transient reflectivity measurements, revealing a hopping time range of 30 to 50 ps. However, the integration of a HgSe/HgTe mixture in the detector led to a decrease in the volume fraction of HgSe, subsequently reducing intraband absorption. To address this challenge, an optical resonator based on guided-mode resonance was specifically designed to enhance intraband absorption. Consequently, the MWIR detector achieved state-of-the-art performance, with a detectivity of 10^9 Jones at 80 K.

The third chapter focused on the integration of mixed-dimensional van der Waals heterostructures comprising HgX nanocrystals and bulk InGaAs. Notably, this research pursued a novel approach by using the combined strengths of both materials, rather than pitting them. Initially, the coupling of InGaAs nanowires with HgTe nanocrystals was explored to develop a planar photodiode. This investigation revealed synergistic properties in the SWIR, characterized by high activation energy and great rectification behavior. Building upon these findings, the wavelength range was further extended to the MWIR by employing the hybrid material HgSe/HgTe, introduced in the second chapter. This strategic approach simplified the design of nanocrystal-based infrared photodiodes within a spectral range where the precise band alignment remains largely unknown.

The last part of this manuscript was dedicated to the investigation of the most advanced infrared device, surpassing the capabilities of the devices discussed in previous chapters. Specifically, an HgTe-based imager, developed through a collaborative effort between our research group and New Imaging Technologies, was exposed to *in-situ* and *in-operando* operations to unveil its energy and photocurrent landscapes. This innovative approach represents a critical departure from conventional practices, as it focuses on studying the material within the context of the device itself, rather than treating them as separate entities. To gain insights into the imager's behavior, a device mimicking its characteristics was developed, enabling the utilization of XPS microscopy to reveal the vectorial distribution of the electric field. Furthermore, preliminary results of the photocurrent distribution within the imager were presented, employing a near-field approach achieved through SNOM.

In the following, we present a list of perspectives closely aligned with the research conducted throughout my PhD thesis:

- The integration of the HgSe/HgTe hybrid material in a photodiode with a dedicated focus on the light-matter coupling management strategy. To achieve this, the GMR nanostructures would need to be redesigned to match the vertical architecture. For

instance, a metallic grid structure could be employed as a replacement for conventional conductive oxide electrodes (e.g., ITO, FTO), while simultaneously inducing a resonance effect.

- The lack of open-circuit voltage (V_{OC}) in the mixed-dimensional vdW structure made of HgX NCs and InGaAs NWs dramatically impedes the sensing performance of the device. The interface resistance of the device needs to be tuned in function of the series resistance. To overcome this challenge, the nanowire geometry needs to be substituted with a conventional InGaAs channel to enhance the surface area of the heterojunction. Furthermore, reducing the distance between the gold contact and the InGaAs layer is crucial, and transitioning to a vertical geometry represents the most optimal approach to achieve this.

- The achievement of high-quality SWIR images with nanocrystals has been demonstrated through the implementation of an HgTe-based camera operating in a photoconductive mode. Moving forward, the next challenge is the integration of a photodiode structure onto the ROIC. This integration would enable a reduced bias application, thereby substantially enhancing the signal-to-noise ratio.

- Additional iterations of the SNOM experiment should be performed in order to validate the reproducibility of the observed photocurrent distribution in the HgTe-based focal plane array. Then, by merging the 2D mapping data obtained from XPS microscopy and SNOM, a deeper understanding of the active material properties beyond its overall response can be achieved. This would facilitate the integration of HgTe nanocrystals into advanced infrared technologies, thereby propelling the field towards the level of maturity of epitaxially grown semiconductors.

Appendix

1. From the nanocrystal growth to a thin film deposition

Chemicals used during this thesis*:* Mercury chloride ($HgCl_2$, Sigma-Aldrich, 99%), mercury acetate ($Hg(OAc)_2$, Alfa Aesar, >98%), Mercury compounds are highly toxic. Handle them with special care. tellurium powder (Te, Sigma-Aldrich, 99.99%), selenium powder (Se, Alfa Aesar, >99%), trioctylphosphine (TOP, Alfa Aesar, 90%), oleylamine (OLA, Acros, 80-90%), dodecanethiol (DDT, Sigma-Aldrich, 98%), acetone (VWR), isopropanol (IPA, VWR), ethanol absolute anhydrous (EtOH, VWR), methanol (VWR, >98%), hexane (VWR, 99%), 2-mercaptoethanol (MPOH, Merck, >99%), N,N dimethylformamide (DMF, VWR), toluene (VWR, 99.8%), methylisobutylketone (MIBK, VWR, >98.5%), ammonia (NH_3, 30%, Carlo Erba Reagents). All chemicals are used without further purification except oleylamine that is centrifuged before use. **Mercury compounds are highly toxic and must me handled with special care**.

1 M TOP:Te*:* 2.54 g of Te powder are mixed in 20 mL of TOP in a three neck flask. The flask is kept under vacuum at room temperature for 5 min and then the temperature is raised to 100 °C. Furthermore, degassing of flask is conducted for the next 20 min. The atmosphere is switched to nitrogen and the temperature is raised to 275 °C. The solution is stirred until a clear orange coloration is obtained. The flask is cooled down to room temperature and the color change to yellow. Finally, this solution is transferred to a nitrogen filled glove box for storage.

1 M TOP:Se precursor: 1.54 g of Se powder is sonicated in 20 mL of TOP until a colorless solution is obtained

HgSe NCs with a band-edge at 2200 cm^{-1}: In a 50 mL three neck flask, 500 mg of $Hg(OAc)_2$, 10 mL of oleic acid and 25 mL of oleylamine are degassed under vacuum at 85 °C. Meanwhile, 1.6 mL of TOP:Se (1 M) are extracted from the glove box. After the atmosphere is switched to N_2 and the temperature stabilized at 100 °C, the TOP:Se solution is quickly injected. After 3 min, 1 mL of DDT (6.6 mmol) is injected and a water bath is used to quickly decrease the temperature. The content of the flask is split over 2 centrifuge tubes and EtOH is added. After centrifugation, the formed pellets are redispersed in one centrifuge tube with toluene and one drop of DDT. The solution is precipitated a second time using ethanol. Again, the formed pellet is redispersed in toluene and one drop of DDT. At this step the CQDs are centrifuged in pure toluene to get rid of the lamellar phases. The solid phase is discarded. The stable phase is transferred in a weighted tube and finally precipitated using methanol. The solid is dried under vacuum for 30 min (in glove box vacuum chamber). Finally, CQDs are redispersed with a 50 $mg.mL^{-1}$ concentration in toluene.

HgTe NCs with a band-edge at 4000 cm^{-1}: In a 100 mL three neck flask, 543 mg of $HgCl_2$ and 50 mL of oleylamine are degassed under vacuum at 110 °C. Meanwhile, 2 mL of TOP:Te (1 M) are extracted from the glove box and mixed with 8 mL of oleylamine. After the atmosphere is switched to N_2 and the temperature stabilized at 80 °C, the TOP:Te solution is quickly injected. After 3 min, 10 mL of a mixture of DDT in toluene (10% of DDT) is injected and a water bath is used to quickly decrease the temperature. The content of the flask is split over 4 centrifuge tubes and MeOH is added. After centrifugation, the formed pellets are redispersed in one centrifuge tube with toluene. The solution is precipitated a second time using ethanol. Again, the formed pellet is redispersed in toluene. At this step the CQDs are centrifuged in pure toluene to get rid of the lamellar phases. The solid phase is discarded. The stable phase is transferred in a weighted tube and finally precipitated using methanol. The solid is dried under vacuum for 30 min (in glove box vacuum chamber). Finally, CQDs are redispersed with a 50 $mg.mL^{-1}$ concentration in toluene.

HgTe NCs with band-edge at 6000 cm^{-1}: In a 100 mL three-neck flask, 540 mg of $HgCl_2$ and 50 mL of oleylamine were degassed under vacuum at 110 °C. At this stage, the solution was yellow and clear. Meanwhile, 2 mL of TOP:Te (1 M) was extracted from the glove box and was mixed with 8 mL of oleylamine. The atmosphere was switched to N_2 and the temperature was set at 58 °C. The TOP:Te solution was quickly injected and the solution turned dark after 3 min, 10 mL of a mixture of 10% DDT in toluene was injected and a water bath was used to quickly decrease the temperature. The content of the flask was split over 4 tubes and MeOH was added. After centrifugation, the formed pellets were redispersed in one tube with toluene. The solution was precipitated a second time with absolute EtOH. Again, the formed pellet was redispersed in toluene. At this step, the CQDs were centrifuged in pure toluene to remove the lamellar phase. The solid phase was discarded. The stable phase is transferred in a weighted falcon and finally precipitated using ethanol. Finally, CQDs are redispersed with a 50 $mg.mL^{-1}$ concentration in toluene.

HgX ink: 3 mL of the CQD solution in toluene (0.9 OD at 400 nm after a 500x dilution) is mixed with 1.2 mL of exchange solution (15 mg $HgCl_2$, 9 mL DMF, 1 mL MPOH) and 0.8 mL of DMF. The solution is vortexed and sonicated for 3 min to help the ligand exchange. Then, the solution is precipitated by adding toluene and centrifuged at 6000 rpm for 3 min. The supernatant is discarded and the QDs are dried under vacuum. Finally, the NCs are redispersed in 250 µL of DMF, centrifuged for 2 min at 6000 rpm and filtered through a 0.22 µm PTFE filter. The HgX ink can be deposited *via* spin-coating. The typical speed parameters for a 200 nm thickness follows a two-step procedure: 1000 rpm/500 $rpm.s^{-1}$ for 120 s followed by 3000 rpm/500 $rpm.s^{-1}$ for 60 s.

2. Fabrication of electrodes

General procedure for optical and e-beam lithography: Here, we give a general process, which is very typical to all the procedures I used to fabricate each device presented throughout this manuscript. There would only be minor differences between each device fabrication, as the thickness of the metallic contacts, the dose for e-beam lithography, or the material deposited after the lithography step.

The sample is rinsed with acetone and isopropanol. An adhesion primer (TI-PRIME) is spin-coated onto the substrate and annealed for 2 min at 120 °C before AZ5214E photo-resist is spin-coated and baked at 110 °C for 90s. A MJB4 mask-aligner is used to exposed the sample to UV light for 1.5 s through a lithography mask. Then the sample is baked 2 min at 125 °C to invert the resist and flood-exposed for 40 s. The sample is dipped 30 s in a solution of AZ726 developer before being rinsed in pure water for 15 s. The patterned substrate is dried and cleaned with 5 min of oxygen plasma to remove resist residues. In a thermal evaporator, 5 nm of chromium are deposited as an adhesion promoter before 150 nm of gold are evaporated. Lift-off is conducted in an acetone bath for at least 1 h. Then, the substrate is rinsed with isopropanol before a layer of A6 PMMA 950 is spin-coated and baked 15 min at 150 °C. The sample is transferred in a Zeiss Supra 40 SEM with Raith ELPHYS Quantum device for electron beam lithography. The operating bias is set to 20 kV and the aperture to 20 µm. The current is measured at 100 pA. The dose is set at 260 $\mu C.cm^{-2}$. The PMMA is developed by dipping the film in a solution of MIBK:isopropanol (1:3) for 50 s and rinsed in pure isopropanol for 20 s. We then place the sample in an Alcatel sputtering chamber for a 50 min deposition of 100 nm of SiO_x. The lift-off is performed by dipping the film in acetone overnight.

List of publications

Journal Articles

2023

1. **Khalili, A**.; Cavallo, M.; Dang, T. H.; Dabard, C.; Zhang, H.; Bossavit, E.; Abadie, C.; Prado, Y.; Xu, X. Z.; Ithurria, S.; Vincent, G.; Coinon, C.; Desplanque, L.; Lhuillier, E. Mid-Wave Infrared Sensitized InGaAs Using Intraband Transition in Doped Colloidal II–VI Nanocrystals. *The Journal of Chemical Physics* 2023, *158*, 094702.

2. **Khalili, A**.; Cavallo, M.; Bossavit, E.; Alchaar, R.; Dang, T. H.; Dabard, C.; Zhang, H.; Ledos, N.; Parahyba, V.; Potet, P.; Utterback, J. K.; Prado, Y.; Silly, M. G.; Dudin, P.; Avila, J.; Pierucci, D.; Lhuillier, E. In Situ Mapping of the Vectorial Electric Field within a Nanocrystal-Based Focal Plane Array Using Photoemission Microscopy. *ACS Appl. Electron. Mater.* 2023, *5*, 4377–4384.

3. Alchaar, R.; Dabard, C.; Mastrippolito, D.; Bossavit, E.; Dang, T. H.; Cavallo, M.; **Khalili, A**.; Zhang, H.; Domenach, L.; Ledos, N.; et al. On the Suitable Choice of Metal for HgTe Nanocrystal-Based Photodiode: To Amalgam or Not to Amalgam. *J. Phys. Chem. C* 2023.

4. Cavallo, M.; Alchaar, R.; Bossavit, E.; Zhang, H.; Dang, T. H.; **Khalili, A**.; Prado, Y.; Silly, M. G.; Utterback, J. K.; Ithurria, S.; Dudin, P.; Avila, J.; Pierucci, D.; Lhuillier, E. Inside a Nanocrystal-Based Photodiode Using Photoemission Microscopy. *Nanoscale* 2023, *15*, 9440–9448.

5. Cavallo, M.; Bossavit, E.; Matzen, S.; Maroutian, T.; Alchaar, R.; Dang, T. H.; **Khalili, A**.; Dabard, C.; Zhang, H.; Prado, Y.; Abadie, C.; Utterback, J. K.; Dayen, J. F.; Silly, M. G.; Dudin, P.; Avila, J.; Lhuillier, E.; Pierucci, D. Coupling Ferroelectric to Colloidal Nanocrystals as a Generic Strategy to Engineer the Carrier Density Landscape. *Advanced Functional Materials* 2023.

6. Cavallo, M.; Bossavit, E.; Zhang, H.; Dabard, C.; Dang, T. H.; **Khalili, A**.; Abadie, C.; Alchaar, R.; Mastrippolito, D.; Prado, Y.; Becerra, L.; Rosticher, M.; Silly, M. G.; Utterback, J. K.; Ithurria, S.; Avila, J.; Pierucci, D.; Lhuillier, E. Mapping the Energy Landscape from a Nanocrystal-Based Field Effect Transistor under Operation Using Nanobeam Photoemission Spectroscopy. *Nano Lett.* 2023.

7. Dang, T. H.; Abadie, C.; Chu, A.; Cavallo, M.; **Khalili, A**.; Dabard, C.; Bossavit, E.; Zhang, H.; Prado, Y.; Pierucci, D.; Utterback, J. K.; Todorov, Y.; Sirtori, C.; Jaeck, J.; Vincent, G.; Vasanelli, A.; Fix, B.; Lhuillier, E. Bias Reconfigurable Photoresponse of an Infrared Nanocrystal Film Integrated into a Coupled Fabry-Perot Resonator. *ACS Photonics* 2023, *10*, 1601–1607.

8. Lhuillier, E.; Dang, T. H.; Cavallo, M.; Abadie, C.; **Khalili, A**.; Gréboval, C. Electronic Structure of Mercury Chalcogenides Nanocrystals. In *Handbook of II-VI Semiconductor-Based Sensors and Radiation Detectors: Volume 1, Materials and Technology*; Korotcenkov, G., Ed.; Springer International Publishing: Cham, 2023; pp 133–156.

9. Lhuillier, E.; Dang, T. H.; Cavallo, M.; Abadie, C.; **Khalili, A**.; Peterson, J. C.; Gréboval, C. Infrared Sensing Using Mercury Chalcogenide Nanocrystals. In *Handbook of II-VI*

Semiconductor-Based Sensors and Radiation Detectors: Volume 2, Photodetectors; Korotcenkov, G., Ed.; Springer International Publishing: Cham, 2023; pp 155–181.

10. Pierini, S.; Abadie, C.; Dang, T. H.; **Khalili, A**.; Zhang, H.; Cavallo, M.; Prado, Y.; Gallas, B.; Ithurria, S.; Sauvage, S.; Dayen, J. F.; Vincent, G.; Lhuillier, E. Lithium-Ion Glass Gating of HgTe Nanocrystal Film with Designed Light-Matter Coupling. *Materials* 2023, *16*, 2335.

11. Zhang, H.; Guilloux, V.; Bossavit, E.; Fu, N.; Dabard, C.; Cavallo, M.; Dang, T. H.; **Khalili, A**.; Abadie, C.; Alchaar, R.; Gréboval, C.; Xu, X. Z.; Utterback, J. K.; Pierucci, D.; Ithurria, S.; Climente, J. I.; Barisien, T.; Lhuillier, E. Visible and Infrared Nanocrystal-Based Light Modulator with CMOS Compatible Bias Operation. *ACS Photonics* 202**3**, *10*, 430–436.

12. Dabard, C.; Bossavit, E.; Dang, T. H.; Ledos, N.; Cavallo, M.; **Khalili, A**.; Zhang, H.; Alchaar, R.; Patriarche, G.; Vasanelli, A.; Diroll, B. T.; Degiron, A.; Lhuillier, E.; Ithurria, S. Electroluminescence and Plasmon-Assisted Directional Photoluminescence from 2D HgTe Nanoplatelets. *J. Phys. Chem. C* 2023, *127*, 14847–14855.

13. Bossavit, E.; Dang, T. H.; He, P.; Cavallo, M.; **Khalili, A**.; Dabard, C.; Zhang, H.; Gacemi, D.; Silly, M. G.; Abadie, C.; Gallas, B.; Pierucci, D.; Todorov, Y.; Sirtori, C.; Diroll, B. T.; Degiron, A.; Lhuillier, E.; Vasanelli, A. Plasmon-Assisted Directional Infrared Photoluminescence of HgTe Nanocrystals. *Advanced Optical Materials n/a*, 2300863.

14. Alchaar, R.; **Khalili, A**.; Ledos, N.; Dang, T. H.; Lebreton, M.; Cavallo, M.; Bossavit, E.; Zhang, H.; Prado, Y.; Lafosse, X.; Parahyba, V.; Potet, P.; Darson, D.; Lhuillier, E. Focal Plane Array Based on HgTe Nanocrystals with Photovoltaic Operation in the Short-Wave Infrared. *Applied Physics Letters* 2023, *123*, 051108.

15. Dang, T. H.; Cavallo, M.; **Khalili, A**.; Dabard, C.; Bossavit, E.; Zhang, H.; Ledos, N.; Prado, Y.; Lafosse, X.; Abadie, C.; Gacemi, D.; Ithurria, S.; Vincent, G.; Todorov, Y.; Sirtori, C.; Vasanelli, A.; Lhuillier, E. Multiresonant Grating to Replace Transparent Conductive Oxide Electrode for Bias Selected Filtering of Infrared Photoresponse. *Nano Lett.* 2023.

2022

16. **Khalili, A**.; Weis, M.; Mizrahi, S. G.; Chu, A.; Dang, T. H.; Abadie, C.; Gréboval, C.; Dabard, C.; Prado, Y.; Xu, X. Z.; Péronne, E.; Livache, C.; Ithurria, S.; Patriarche, G.; Ramade, J.; Vincent, G.; Boschetto, D.; Lhuillier, E. Guided-Mode Resonator Coupled with Nanocrystal Intraband Absorption. *ACS Photonics* 2022, *9*, 985–993.

17. **Khalili, A**.; Abadie, C.; Dang, T. H.; Chu, A.; Izquierdo, E.; Dabard, C.; Gréboval, C.; Cavallo, M.; Zhang, H.; Pierini, S.; Prado, Y.; Xu, X. Z.; Ithurria, S.; Vincent, G.; Coinon, C.; Desplanque, L.; Lhuillier, E. Colloidal II–VI—Epitaxial III–V Heterostructure: A Strategy to Expand InGaAs Spectral Response. *Appl. Phys. Lett.* 2022, *120*, 051101.

18. Abadie, C.; Paggi, L.; Fabas, A.; **Khalili, A**.; Dang, T. H.; Dabard, C.; Cavallo, M.; Alchaar, R.; Zhang, H.; Prado, Y.; et al. Helmholtz Resonator Applied to Nanocrystal-Based Infrared Sensing. *Nano Lett.* 2022, *22*, 8779–8785.

19. Bossavit, E.; Qu, J.; Abadie, C.; Dabard, C.; Dang, T.; Izquierdo, E.; **Khalili, A**.; Gréboval, C.; Chu, A.; Pierini, S.; Cavallo, M.; Prado, Y.; Parahyba, V.; Xu, X. Z.; Decamps-Mandine, A.; Silly, M.; Ithurria, S.; Lhuillier, E. Optimized Infrared LED and Its Use in an All-HgTe Nanocrystal-Based Active Imaging Setup. *Advanced Optical Materials* 2022, *10*, 2101755.

20. Chehaibou, B.; Izquierdo, E.; Chu, A.; Abadie, C.; Cavallo, M.; **Khalili, A**.; Dang, T. H.; Gréboval, C.; Xu, X. Z.; Ithurria, S.; Vincent, G.; Gallas, B.; Mugny, G.; Arnaud, A.; Lhuillier, E.; Delerue, C. The Complex Optical Index of PbS Nanocrystal Thin Films and Their Use for Short Wave Infrared Sensor Design. *Nanoscale* 2022, *14*, 2711–2721.

21. Dang, T. H.; Abadie, C.; **Khalili, A**.; Gréboval, C.; Zhang, H.; Prado, Y.; Xu, X. Z.; Gacemi, D.; Descamps-Mandine, A.; Ithurria, S.; Todorov, Y.; Sirtori, C.; Vasanelli, A.; Lhuillier, E. Broadband Enhancement of Mid-Wave Infrared Absorption in a Multi-Resonant Nanocrystal-Based Device. *Advanced Optical Materials* 2022, *10*, 2200297.

22. Dang, T. H.; **Khalili, A**.; Abadie, C.; Gréboval, C.; Cavallo, M.; Zhang, H.; Bossavit, E.; Utterback, J. K.; Dandeu, E.; Prado, Y.; Vincent, G.; Ithurria, S.; Todorov, Y.; Sirtori, C.; Vasanelli, A.; Lhuillier, E. Nanocrystal-Based Active Photonics Device through Spatial Design of Light-Matter Coupling. *ACS Photonics* 2022, *9*, 2528–2535.

23. Gréboval, C.; Darson, D.; Parahyba, V.; Alchaar, R.; Abadie, C.; Noguier, V.; Ferré, S.; Izquierdo, E.; **Khalili, A**.; Prado, Y.; Potet, P.; Lhuillier, E. Photoconductive Focal Plane Array Based on HgTe Quantum Dots for Fast and Cost-Effective Short-Wave Infrared Imaging. *Nanoscale* **2022**, *14*, 9359–9368.

24. Gréboval, C.; Izquierdo, E.; Abadie, C.; **Khalili, A**.; Cavallo, M.; Chu, A.; Dang, T. H.; Zhang, H.; Lafosse, X.; Rosticher, M.; Xu, X. Z.; Descamps-Mandine, A.; Ouerghi, A.; Silly, M. G.; Ithurria, S.; Lhuillier, E. HgTe Nanocrystal-Based Photodiode for Extended Short-Wave Infrared Sensing with Optimized Electron Extraction and Injection. *ACS Appl. Nano Mater.* 2022, *5*, 8602–8611.

25. Pierini, S.; Capitani, F.; Scimeca, M.; Kozlov, S.; Pierucci, D.; Alchaar, R.; Abadie, C.; **Khalili, A**.; Cavallo, M.; Dang, T. H.; et al. Vanishing Confinement Regime in Terahertz HgTe Nanocrystals Studied under Extreme Conditions of Temperature and Pressure. *J. Phys. Chem. Lett.* 2022, *13*, 6919–6926.

26. Rastogi, P.; Izquierdo, E.; Gréboval, C.; Cavallo, M.; Chu, A.; Dang, T. H.; **Khalili, A**.; Abadie, C.; Alchaar, R.; Pierini, S.; et al. Extended Short-Wave Photodiode Based on CdSe/HgTe/Ag2Te Stack with High Internal Efficiency. *J. Phys. Chem. C* 2022, *126*, 13720–13728.

27. Zhang, H.; Alchaar, R.; Prado, Y.; **Khalili, A**.; Gréboval, C.; Cavallo, M.; Bossavit, E.; Dabard, C.; Dang, T. H.; Abadie, C.; et al. Material Perspective on HgTe Nanocrystal-Based Short-Wave Infrared Focal Plane Arrays. *Chem. Mater.* 2022, *34*, 10964–10972.

2021

28. Chee, S.-S.; Gréboval, C.; Magalhaes, D. V.; Ramade, J.; Chu, A.; Qu, J.; Rastogi, P.; **Khalili, A**.; Dang, T. H.; Dabard, C.; Prado, Y.; Patriarche, G.; Chaste, J.; Rosticher, M.; Bals, S.; Delerue, C.; Lhuillier, E. Correlating Structure and Detection Properties in HgTe Nanocrystal Films. *Nano Lett.* 2021, *21*, 4145–4151.

29. Dabard, C.; Planelles, J.; Po, H.; Izquierdo, E.; Makke, L.; Gréboval, C.; Moghaddam, N.; **Khalili, A**.; Dang, T. H.; Chu, A.; et al. Optimized Cation Exchange for Mercury Chalcogenide 2D Nanoplatelets and Its Application for Alloys. *Chem. Mater.* **2021**, *33*, 9252–9261.

30. Dang, T. H.; Vasanelli, A.; Todorov, Y.; Sirtori, C.; Prado, Y.; Chu, A.; Gréboval, C.; **Khalili, A**.; Cruguel, H.; Delerue, C.; Vincent, G.; Lhuillier, E. Bias Tunable Spectral Response of Nanocrystal Array in a Plasmonic Cavity. *Nano Lett.* 2021, *21*, 6671–6677.

31. Gréboval, C.; Chu, A.; Magalhaes, D. V.; Ramade, J.; Qu, J.; Rastogi, P.; **Khalili, A**.; Chee, S.-S.; Aubin, H.; Vincent, G.; Bals, S.; Delerue, C.; Lhuillier, E. Ferroelectric Gating of Narrow Band-Gap Nanocrystal Arrays with Enhanced Light–Matter Coupling. *ACS Photonics* 2021, *8*, 259–268.

32. Gréboval, C.; Dabard, C.; Konstantinov, N.; Cavallo, M.; Chee, S.-S.; Chu, A.; Dang, T. H.; **Khalili, A**.; Izquierdo, E.; Prado, Y.; Majjad, H.; Xu, X. Z.; Dayen, J.-F.; Lhuillier, E. Split-Gate Photodiode Based on Graphene/HgTe Heterostructures with a Few Nanosecond Photoresponse. *ACS Appl. Electron. Mater.* 2021, *3*, 4681–4688.

33. Prado, Y.; Qu, J.; Gréboval, C.; Dabard, C.; Rastogi, P.; Chu, A.; **Khalili, A**.; Xu, X. Z.; Delerue, C.; Ithurria, S.; Lhuillier, E. Seeded Growth of HgTe Nanocrystals for Shape Control and Their Use in Narrow Infrared Electroluminescence. *Chem. Mater.* 2021, *33*, 2054–2061.

34. Rastogi, P.; Chu, A.; Dang, T. H.; Prado, Y.; Gréboval, C.; Qu, J.; Dabard, C.; **Khalili, A**.; Dandeu, E.; Fix, B.; Xu, X. Z.; Ithurria, S.; Vincent, G.; Gallas, B.; Lhuillier, E. Complex Optical Index of HgTe Nanocrystal Infrared Thin Films and Its Use for Short Wave Infrared Photodiode Design. *Advanced Optical Materials* 2021, *9*, 2002066.

2020

35. Gréboval, C.; Noumbé, U. N.; Chu, A.; Prado, Y.; **Khalili, A**.; Dabard, C.; Dang, T. H.; Colis, S.; Chaste, J.; Ouerghi, A.; Dayen, J.-F.; Lhuillier, E. Gate Tunable Vertical Geometry Phototransistor Based on Infrared HgTe Nanocrystals. *Appl. Phys. Lett.* 2020, *117*, 251104.

36. Gréboval, C.; Rastogi, P.; Qu, J.; Chu, A.; Ramade, J.; **Khalili, A**.; Dabard, C.; Dang, T. H.; Cruguel, H.; Ouerghi, A.; Witkowski, N.; Silly, M. G.; Lhuillier, E. Time-Resolved Photoemission to Unveil Electronic Coupling between Absorbing and Transport Layers in a Quantum Dot-Based Solar Cell. *J. Phys. Chem. C* 2020, *124*, 23400–23409.

37. Moghaddam, N.; Gréboval, C.; Qu, J.; Chu, A.; Rastogi, P.; Livache, C.; **Khalili, A**.; Xu, X. Z.; Baptiste, B.; Klotz, S.; Fishman, G.; Capitani, F.; Ithurria, S.; Sauvage, S.; Lhuillier, E. The Strong Confinement Regime in HgTe Two-Dimensional Nanoplatelets. *J. Phys. Chem. C* 2020, *124*, 23460–23468.

38. Qu, J.; Rastogi, P.; Gréboval, C.; Lagarde, D.; Chu, A.; Dabard, C.; **Khalili, A**.; Cruguel, H.; Robert, C.; Xu, X. Z.; Ithurria, S.; Silly, M. G.; Ferré, S.; Marie, X.; Lhuillier, E. Electroluminescence from HgTe Nanocrystals and Its Use for Active Imaging. *Nano Lett.* 2020, *20*, 6185–6190.

39. Rastogi, P.; Chu, A.; Gréboval, C.; Qu, J.; Noumbé, U. N.; Chee, S.-S.; Goyal, M**.; Khalili, A**.; Xu, X. Z.; Cruguel, H.; et al. Pushing Absorption of Perovskite Nanocrystals into the Infrared. *Nano Lett.* 2020, *20*, 3999–4006.

Communications

1. Design of a nanocrystal-based intraband photodetector with an enhanced light-matter coupling, Summer School Bad Honnef, **2021**, Poster.

2. Optical nanoresonator coupled to intraband transition for mid-infrared sensing, Infrared Workshop OCN, Paris, **2021**, Talk.

3. Intraband absorption coupled with an optical nanoresonator for mid-infrared sensing, NanoGe Spring Meeting, Online, **2022**, Talk.

4. Expansion of the InGaAs spectral response with HgTe nanocrystals, Workshop Bad Honnef, **2022**, Poster.

5. Extended SWIR imaging using colloidal nanocrystals, IR For Space Applications, Toulouse, **2023**, Talk.

References

(1) Herschel, W. XIV. Experiments on the Refrangibility of the Invisible Rays of the Sun. *Philos. Trans. R. Soc. Lond.* **1800**, *90*, 284–292.

(2) Langley, S. P. The Bolometer and Radiant Energy. *Proc. Am. Acad. Arts Sci.* **1880**, *16*, 342–358.

(3) Smith, W. Effect of Light on Selenium During the Passage of An Electric Current *. *Nature* **1873**, *7*, 303–303.

(4) Murray, C. B.; Norris, D. J.; Bawendi, M. G. Synthesis and Characterization of Nearly Monodisperse CdE (E = Sulfur, Selenium, Tellurium) Semiconductor Nanocrystallites. *J. Am. Chem. Soc.* **1993**, *115*, 8706–8715.

(5) Rogalski, A. Infrared Detectors: An Overview. *Infrared Phys. Technol.* **2002**, *43*, 187–210.

(6) Rogalski, A. *Infrared Detectors*; CRC Press, 2010.

(7) Rogalski, A. HgCdTe Infrared Detector Material: History, Status and Outlook. *Rep. Prog. Phys.* **2005**, *68*, 2267.

(8) Rogalski, A.; Martyniuk, P.; Kopytko, M. InAs/GaSb Type-II Superlattice Infrared Detectors: Future Prospect. *Appl. Phys. Rev.* **2017**, *4*, 031304.

(9) Rogalski, A. Quantum Well Photoconductors in Infrared Detector Technology. *J. Appl. Phys.* **2003**, *93*, 4355–4391.

(10) Levine, B. F.; Choi, K. K.; Bethea, C. G.; Walker, J.; Malik, R. J. Quantum Well Avalanche Multiplication Initiated by 10 µm Intersubband Absorption and Photoexcited Tunneling. *Appl. Phys. Lett.* **1987**, *51*, 934–936.

(11) Rode, D. L. Electron Transport in InSb, InAs, and InP. *Phys. Rev. B* **1971**, *3*, 3287–3299.

(12) Lawson, W. D.; Nielsen, S.; Putley, E. H.; Young, A. S. Preparation and Properties of HgTe and Mixed Crystals of HgTe-CdTe. *J. Phys. Chem. Solids* **1959**, *9*, 325–329.

(13) Rauscher, B. J.; Boehm, N.; Cagiano, S.; Delo, G. S.; Foltz, R.; Greenhouse, M. A.; Hickey, M.; Hill, R. J.; Kan, E.; Lindler, D.; Mott, D. B.; Waczynski, A.; Wen, Y. New and Better Detectors for the JWST Near-Infrared Spectrograph. *Publ. Astron. Soc. Pac.* **2014**, *126*, 739.

(14) Peng, X.; Manna, L.; Yang, W.; Wickham, J.; Scher, E.; Kadavanich, A.; Alivisatos, A. P. Shape Control of CdSe Nanocrystals. *Nature* **2000**, *404*, 59–61.

(15) Ithurria, S.; Tessier, M. D.; Mahler, B.; Lobo, R. P. S. M.; Dubertret, B.; Efros, A. L. Colloidal Nanoplatelets with Two-Dimensional Electronic Structure. *Nat. Mater.* **2011**, *10*, 936–941.

(16) Leroy, S. Phosphors and Quantum Dots 2015: LED Downconverters for Lighting and Displays. *Yole Dev.* **2015**.

(17) Leroy, S. Quantum Dots and Wide Color Gamut Display Technologies. *Yole Dev.* **2017**.

(18) Bourzac, K. Quantum Dots Go on Display. *Nature* **2013**, *493*, 283–283.

(19) Huang, Y.-M.; Singh, K. J.; Liu, A.-C.; Lin, C.-C.; Chen, Z.; Wang, K.; Lin, Y.; Liu, Z.; Wu, T.; Kuo, H.-C. Advances in Quantum-Dot-Based Displays. *Nanomaterials* **2020**, *10*, 1327.

(20) Rogach, A. L.; Eychmüller, A.; Hickey, S. G.; Kershaw, S. V. Infrared-Emitting Colloidal Nanocrystals: Synthesis, Assembly, Spectroscopy, and Applications. *Small* **2007**, *3*, 536–557.

(21) Rogach, A.; Kershaw, S. V.; Burt, M.; Harrison, M. T.; Kornowski, A.; Eychmüller, A.; Weller, H. Colloidally Prepared HgTe Nanocrystals with Strong Room-Temperature Infrared Luminescence. *Adv. Mater.* **1999**, *11*, 552–555.

(22) Izquierdo, E.; Robin, A.; Keuleyan, S.; Lequeux, N.; Lhuillier, E.; Ithurria, S. Strongly Confined HgTe 2D Nanoplatelets as Narrow Near-Infrared Emitters. *J. Am. Chem. Soc.* **2016**, *138*, 10496–10501.

(23) Rogach, A. l.; Harrison, M. t.; Kershaw, S. v.; Kornowski, A.; Burt, M. g.; Eychmüller, A.; Weller, H. Colloidally Prepared CdHgTe and HgTe Quantum Dots with Strong Near-Infrared Luminescence. *Phys. Status Solidi B* **2001**, *224*, 153–158.
(24) Svane, A.; Christensen, N. E.; Cardona, M.; Chantis, A. N.; van Schilfgaarde, M.; Kotani, T. Quasiparticle Band Structures of HgS, HgSe, and HgTe. *Phys. Rev. B* **2011**, *84*, 205205.
(25) Dornhaus, R.; Nimtz, G.; Schlicht, B. *Narrow-Gap Semiconductors*; Springer Tracts in Modern Physics; Springer: Berlin, Heidelberg, 1983; Vol. 98.
(26) Berger, L. I. *Semiconductor Materials*; CRC Press, 1996.
(27) Sargent, E. H. Colloidal Quantum Dot Solar Cells. *Nat. Photonics* **2012**, *6*, 133–135.
(28) Pietryga, J. M.; Park, Y.-S.; Lim, J.; Fidler, A. F.; Bae, W. K.; Brovelli, S.; Klimov, V. I. Spectroscopic and Device Aspects of Nanocrystal Quantum Dots. *Chem. Rev.* **2016**, *116*, 10513–10622.
(29) Moghaddam, N.; Gréboval, C.; Qu, J.; Chu, A.; Rastogi, P.; Livache, C.; Khalili, A.; Xu, X. Z.; Baptiste, B.; Klotz, S.; Fishman, G.; Capitani, F.; Ithurria, S.; Sauvage, S.; Lhuillier, E. The Strong Confinement Regime in HgTe Two-Dimensional Nanoplatelets. *J. Phys. Chem. C* **2020**, *124*, 23460–23468.
(30) Kovalenko, M. V.; Kaufmann, E.; Pachinger, D.; Roither, J.; Huber, M.; Stangl, J.; Hesser, G.; Schäffler, F.; Heiss, W. Colloidal HgTe Nanocrystals with Widely Tunable Narrow Band Gap Energies: From Telecommunications to Molecular Vibrations. *J. Am. Chem. Soc.* **2006**, *128*, 3516–3517.
(31) Keuleyan, S.; Lhuillier, E.; Guyot-Sionnest, P. Synthesis of Colloidal HgTe Quantum Dots for Narrow Mid-IR Emission and Detection. *J. Am. Chem. Soc.* **2011**, *133*, 16422–16424.
(32) Shen, G.; Chen, M.; Guyot-Sionnest, P. Synthesis of Nonaggregating HgTe Colloidal Quantum Dots and the Emergence of Air-Stable n-Doping. *J. Phys. Chem. Lett.* **2017**, *8*, 2224–2228.
(33) Prado, Y.; Qu, J.; Gréboval, C.; Dabard, C.; Rastogi, P.; Chu, A.; Khalili, A.; Xu, X. Z.; Delerue, C.; Ithurria, S.; Lhuillier, E. Seeded Growth of HgTe Nanocrystals for Shape Control and Their Use in Narrow Infrared Electroluminescence. *Chem. Mater.* **2021**, *33*, 2054–2061.
(34) Böberl, M.; Kovalenko, M. V.; Gamerith, S.; List, E. J. W.; Heiss, W. Inkjet-Printed Nanocrystal Photodetectors Operating up to 3 μm Wavelengths. *Adv. Mater.* **2007**, *19*, 3574–3578.
(35) Huo, N.; Gupta, S.; Konstantatos, G. MoS_2–HgTe Quantum Dot Hybrid Photodetectors beyond 2 Um. *Adv. Mater.* **2017**, *29*, 1606576.
(36) Kim, D.-W.; Jang, J.; Kim, H.; Cho, K.; Kim, S. Electrical Characteristics of HgTe Nanocrystal-Based Thin Film Transistors Fabricated on Flexible Plastic Substrates. *Thin Solid Films* **2008**, *516*, 7715–7719.
(37) Chen, M.; Yu, H.; Kershaw, S. V.; Xu, H.; Gupta, S.; Hetsch, F.; Rogach, A. L.; Zhao, N. Fast, Air-Stable Infrared Photodetectors Based on Spray-Deposited Aqueous HgTe Quantum Dots. *Adv. Funct. Mater.* **2014**, *24*, 53–59.
(38) Lhuillier, E.; Keuleyan, S.; Rekemeyer, P.; Guyot-Sionnest, P. Thermal Properties of Mid-Infrared Colloidal Quantum Dot Detectors. *J. Appl. Phys.* **2011**, *110*, 033110.
(39) Keuleyan, S.; Lhuillier, E.; Brajuskovic, V.; Guyot-Sionnest, P. Mid-Infrared HgTe Colloidal Quantum Dot Photodetectors. *Nat. Photonics* **2011**, *5*, 489–493.
(40) Ackerman, M. M.; Tang, X.; Guyot-Sionnest, P. Fast and Sensitive Colloidal Quantum Dot Mid-Wave Infrared Photodetectors. *ACS Nano* **2018**, *12*, 7264–7271.
(41) Tang, X.; Ackerman, M. M.; Chen, M.; Guyot-Sionnest, P. Dual-Band Infrared Imaging Using Stacked Colloidal Quantum Dot Photodiodes. *Nat. Photonics* **2019**, *13*, 277–282.
(42) Gréboval, C.; Izquierdo, E.; Abadie, C.; Khalili, A.; Cavallo, M.; Chu, A.; Dang, T. H.; Zhang, H.; Lafosse, X.; Rosticher, M.; Xu, X. Z.; Descamps-Mandine, A.; Ouerghi, A.; Silly, M. G.; Ithurria, S.; Lhuillier, E. HgTe Nanocrystal-Based Photodiode for Extended Short-Wave Infrared Sensing with Optimized Electron Extraction and Injection. *ACS Appl. Nano Mater.* **2022**, *5*, 8602–8611.

(43) Rastogi, P.; Izquierdo, E.; Gréboval, C.; Cavallo, M.; Chu, A.; Dang, T. H.; Khalili, A.; Abadie, C.; Alchaar, R.; Pierini, S.; et al. Extended Short-Wave Photodiode Based on CdSe/HgTe/Ag_2Te Stack with High Internal Efficiency. *J. Phys. Chem. C* **2022**, *126*, 13720–13728.
(44) Gréboval, C.; Darson, D.; Parahyba, V.; Alchaar, R.; Abadie, C.; Noguier, V.; Ferré, S.; Izquierdo, E.; Khalili, A.; Prado, Y.; Potet, P.; Lhuillier, E. Photoconductive Focal Plane Array Based on HgTe Quantum Dots for Fast and Cost-Effective Short-Wave Infrared Imaging. *Nanoscale* **2022**, *14*, 9359–9368.
(45) Zhang, S.; Bi, C.; Qin, T.; Liu, Y.; Cao, J.; Song, J.; Huo, Y.; Chen, M.; Hao, Q.; Tang, X. Wafer-Scale Fabrication of CMOS-Compatible Trapping-Mode Infrared Imagers with Colloidal Quantum Dots. *ACS Photonics* **2023**, *10*, 673–682.
(46) Buurma, C.; Pimpinella, R. E.; Ciani, A. J.; Feldman, J. S.; Grein, C. H.; Guyot-Sionnest, P. MWIR Imaging with Low Cost Colloidal Quantum Dot Films. In *Optical Sensing, Imaging, and Photon Counting: Nanostructured Devices and Applications 2016*; SPIE, 2016; Vol. 9933, p 993303.
(47) Ciani, A. J.; Pimpinella, R. E.; Grein, C. H.; Guyot-Sionnest, P. Colloidal Quantum Dots for Low-Cost MWIR Imaging. In *Infrared Technology and Applications XLII*; SPIE, 2016; Vol. 9819, pp 333–341.
(48) Keuleyan, S.; Kohler, J.; Guyot-Sionnest, P. Photoluminescence of Mid-Infrared HgTe Colloidal Quantum Dots. *J. Phys. Chem. C* **2014**, *118*, 2749–2753.
(49) Gréboval, C.; Chu, A.; Goubet, N.; Livache, C.; Ithurria, S.; Lhuillier, E. Mercury Chalcogenide Quantum Dots: Material Perspective for Device Integration. *Chem. Rev.* **2021**, *121*, 3627–3700.
(50) Liu, H.; Keuleyan, S.; Guyot-Sionnest, P. N- and p-Type HgTe Quantum Dot Films. *J. Phys. Chem. C* **2012**, *116*, 1344–1349.
(51) Wang, C.; Shim, M.; Guyot-Sionnest, P. Electrochromic Nanocrystal Quantum Dots. *Science* **2001**, *291*, 2390–2392.
(52) Wehrenberg, B. L.; Guyot-Sionnest, P. Electron and Hole Injection in PbSe Quantum Dot Films. *J. Am. Chem. Soc.* **2003**, *125*, 7806–7807.
(53) Jeong, K. S.; Guyot-Sionnest, P. Mid-Infrared Photoluminescence of CdS and CdSe Colloidal Quantum Dots. *ACS Nano* **2016**, *10*, 2225–2231.
(54) Jeong, K. S.; Deng, Z.; Keuleyan, S.; Liu, H.; Guyot-Sionnest, P. Air-Stable n-Doped Colloidal HgS Quantum Dots. *J. Phys. Chem. Lett.* **2014**, *5*, 1139–1143.
(55) Deng, Z.; Jeong, K. S.; Guyot-Sionnest, P. Colloidal Quantum Dots Intraband Photodetectors. *ACS Nano* **2014**, *8*, 11707–11714.
(56) Oh, S. J.; Berry, N. E.; Choi, J.-H.; Gaulding, E. A.; Paik, T.; Hong, S.-H.; Murray, C. B.; Kagan, C. R. Stoichiometric Control of Lead Chalcogenide Nanocrystal Solids to Enhance Their Electronic and Optoelectronic Device Performance. *ACS Nano* **2013**, *7*, 2413–2421.
(57) Lhuillier, E.; Scarafagio, M.; Hease, P.; Nadal, B.; Aubin, H.; Xu, X. Z.; Lequeux, N.; Patriarche, G.; Ithurria, S.; Dubertret, B. Infrared Photodetection Based on Colloidal Quantum-Dot Films with High Mobility and Optical Absorption up to THz. *Nano Lett.* **2016**, *16*, 1282–1286.
(58) Guyot-Sionnest, P. Electrical Transport in Colloidal Quantum Dot Films. *J. Phys. Chem. Lett.* **2012**, *3*, 1169–1175.
(59) Morgan, N. Y.; Leatherdale, C. A.; Drndić, M.; Jarosz, M. V.; Kastner, M. A.; Bawendi, M. Electronic Transport in Films of Colloidal CdSe Nanocrystals. *Phys. Rev. B* **2002**, *66*, 075339.
(60) Yu, D.; Wang, C.; Guyot-Sionnest, P. N-Type Conducting CdSe Nanocrystal Solids. *Science* **2003**, *300*, 1277–1280.
(61) Talapin, D. V.; Murray, C. B. PbSe Nanocrystal Solids for N- and p-Channel Thin Film Field-Effect Transistors. *Science* **2005**, *310*, 86–89.
(62) Nag, A.; Kovalenko, M. V.; Lee, J.-S.; Liu, W.; Spokoyny, B.; Talapin, D. V. Metal-Free Inorganic Ligands for Colloidal Nanocrystals: S^{2-}, HS^-, Se^{2-}, HSe^-, Te^{2-}, HTe^-, TeS_3^{2-}, OH^-, and NH^{2-} as Surface Ligands. *J. Am. Chem. Soc.* **2011**, *133*, 10612–10620.

(63) Tang, J.; Kemp, K. W.; Hoogland, S.; Jeong, K. S.; Liu, H.; Levina, L.; Furukawa, M.; Wang, X.; Debnath, R.; Cha, D.; Chou, K. W.; Fischer, A.; Amassian, A.; Asbury, J. B.; Sargent, E. H. Colloidal-Quantum-Dot Photovoltaics Using Atomic-Ligand Passivation. *Nat. Mater.* **2011**, *10*, 765–771.
(64) Chen, M.; Lan, X.; Tang, X.; Wang, Y.; Hudson, M. H.; Talapin, D. V.; Guyot-Sionnest, P. High Carrier Mobility in HgTe Quantum Dot Solids Improves Mid-IR Photodetectors. *ACS Photonics* **2019**, *6*, 2358–2365.
(65) Chen, M.; Shen, G.; Guyot-Sionnest, P. State-Resolved Mobility of 1 $Cm^2/(Vs)$ with HgSe Quantum Dot Films. *J. Phys. Chem. Lett.* **2020**, *11*, 2303–2307.
(66) Lhuillier, E.; Keuleyan, S.; Zolotavin, P.; Guyot-Sionnest, P. Mid-Infrared HgTe/As_2S_3 Field Effect Transistors and Photodetectors. *Adv. Mater.* **2013**, *25*, 137–141.
(67) Cavallo, M.; Bossavit, E.; Zhang, H.; Dabard, C.; Dang, T. H.; Khalili, A.; Abadie, C.; Alchaar, R.; Mastrippolito, D.; Prado, Y.; Becerra, L.; Rosticher, M.; Silly, M. G.; Utterback, J. K.; Ithurria, S.; Avila, J.; Pierucci, D.; Lhuillier, E. Mapping the Energy Landscape from a Nanocrystal-Based Field Effect Transistor under Operation Using Nanobeam Photoemission Spectroscopy. *Nano Lett.* **2023**, *23*, 1363–1370.
(68) Lenard, P. On Cathode Rays. *Nobel Lect.* **1906**.
(69) Schultz, M. L.; Morton, G. A. Photoconduction in Germanium and Silicon. *Proc. IRE* **1955**, *43*, 1819–1828.
(70) Jagtap, A.; Goubet, N.; Livache, C.; Chu, A.; Martinez, B.; Gréboval, C.; Qu, J.; Dandeu, E.; Becerra, L.; Witkowski, N.; Ithurria, S.; Mathevet, F.; Silly, M. G.; Dubertret, B.; Lhuillier, E. Short Wave Infrared Devices Based on HgTe Nanocrystals with Air Stable Performances. *J. Phys. Chem. C* **2018**, *122*, 14979–14985.
(71) Cryer, M. E.; Halpert, J. E. 300 Nm Spectral Resolution in the Mid-Infrared with Robust, High Responsivity Flexible Colloidal Quantum Dot Devices at Room Temperature. *ACS Photonics* **2018**, *5*, 3009–3015.
(72) Lhuillier, E.; Dayen, J.-F.; Thomas, D. O.; Robin, A.; Doudin, B.; Dubertret, B. Nanoplatelets Bridging a Nanotrench: A New Architecture for Photodetectors with Increased Sensitivity. *Nano Lett.* **2015**, *15*, 1736–1742.
(73) Wang, H.; Lhuillier, E.; Yu, Q.; Zimmers, A.; Dubertret, B.; Ulysse, C.; Aubin, H. Transport in a Single Self-Doped Nanocrystal. *ACS Nano* **2017**, *11*, 1222–1229.
(74) Konstantatos, G.; Sargent, E. H. PbS Colloidal Quantum Dot Photoconductive Photodetectors: Transport, Traps, and Gain. *Appl. Phys. Lett.* **2007**, *91*, 173505.
(75) Liu, Y.; Gibbs, M.; Perkins, C. L.; Tolentino, J.; Zarghami, M. H.; Bustamante, J. Jr.; Law, M. Robust, Functional Nanocrystal Solids by Infilling with Atomic Layer Deposition. *Nano Lett.* **2011**, *11*, 5349–5355.
(76) Chu, A.; Gréboval, C.; Prado, Y.; Majjad, H.; Delerue, C.; Dayen, J.-F.; Vincent, G.; Lhuillier, E. Infrared Photoconduction at the Diffusion Length Limit in HgTe Nanocrystal Arrays. *Nat. Commun.* **2021**, *12*, 1794.
(77) Noumbé, U. N.; Gréboval, C.; Livache, C.; Chu, A.; Majjad, H.; Parra López, L. E.; Mouafo, L. D. N.; Doudin, B.; Berciaud, S.; Chaste, J.; Ouerghi, A.; Lhuillier, E.; Dayen, J.-F. Reconfigurable 2D/0D p–n Graphene/HgTe Nanocrystal Heterostructure for Infrared Detection. *ACS Nano* **2020**, *14*, 4567–4576.
(78) Gréboval, C.; Noumbe, U.; Goubet, N.; Livache, C.; Ramade, J.; Qu, J.; Chu, A.; Martinez, B.; Prado, Y.; Ithurria, S.; Ouerghi, A.; Aubin, H.; Dayen, J.-F.; Lhuillier, E. Field-Effect Transistor and Photo-Transistor of Narrow-Band-Gap Nanocrystal Arrays Using Ionic Glasses. *Nano Lett.* **2019**, *19*, 3981–3986.
(79) Chen, M.; Lu, H.; Abdelazim, N. M.; Zhu, Y.; Wang, Z.; Ren, W.; Kershaw, S. V.; Rogach, A. L.; Zhao, N. Mercury Telluride Quantum Dot Based Phototransistor Enabling High-Sensitivity Room-Temperature Photodetection at 2000 Nm. *ACS Nano* **2017**, *11*, 5614–5622.
(80) Konstantatos, G.; Badioli, M.; Gaudreau, L.; Osmond, J.; Bernechea, M.; de Arquer, F. P. G.; Gatti, F.; Koppens, F. H. L. Hybrid Graphene–Quantum Dot Phototransistors with Ultrahigh Gain. *Nat. Nanotechnol.* **2012**, *7*, 363–368.

(81) Becquerel, E. *Mémoire Sur Les Effets Électriques Sous l'influence Des Rayons Solaires*; 1839.
(82) Becquerel, E. *Mémoire Sur Le Rayonnement Chimique*; 1842.
(83) Chapin, D. M.; Fuller, C. S.; Pearson, G. L. A New Silicon P-n Junction Photocell for Converting Solar Radiation into Electrical Power. *J. Appl. Phys.* **1954**, *25*, 676–677.
(84) Dang, T. H. Multiresonant Grating to Replace Transparent Conductive Oxide Electrode for Bias Selected Filtering of Infrared Photoresponse. **2023**, (Submitted).
(85) Gréboval, C.; Izquierdo, E.; Livache, C.; Martinez, B.; Dufour, M.; Goubet, N.; Moghaddam, N.; Qu, J.; Chu, A.; Ramade, J.; Aubin, H.; Cruguel, H.; Silly, M.; Lhuillier, E.; Ithurria, S. Impact of Dimensionality and Confinement on the Electronic Properties of Mercury Chalcogenide Nanocrystals. *Nanoscale* **2019**, *11*, 3905–3915.
(86) Gréboval, C.; Rastogi, P.; Qu, J.; Chu, A.; Ramade, J.; Khalili, A.; Dabard, C.; Dang, T. H.; Cruguel, H.; Ouerghi, A.; Witkowski, N.; Silly, M. G.; Lhuillier, E. Time-Resolved Photoemission to Unveil Electronic Coupling between Absorbing and Transport Layers in a Quantum Dot-Based Solar Cell. *J. Phys. Chem. C* **2020**, *124*, 23400–23409.
(87) Brown, P. R.; Kim, D.; Lunt, R. R.; Zhao, N.; Bawendi, M. G.; Grossman, J. C.; Bulović, V. Energy Level Modification in Lead Sulfide Quantum Dot Thin Films through Ligand Exchange. *ACS Nano* **2014**, *8*, 5863–5872.
(88) Chen, M.; Guyot-Sionnest, P. Reversible Electrochemistry of Mercury Chalcogenide Colloidal Quantum Dot Films. *ACS Nano* **2017**, *11*, 4165–4173.
(89) Liu, H.; Lhuillier, E.; Guyot-Sionnest, P. 1/f Noise in Semiconductor and Metal Nanocrystal Solids. *J. Appl. Phys.* **2014**, *115*, 154309.
(90) Hooge, F. N. The Relation between 1/*f* Noise and Number of Electrons. *Phys. B Condens. Matter* **1990**, *162*, 344–352.
(91) Esaki, L.; Tsu, R. Superlattice and Negative Differential Conductivity in Semiconductors. *IBM J. Res. Dev.* **1970**, *14*, 61–65.
(92) Levine, B. F. Quantum-well Infrared Photodetectors. *J. Appl. Phys.* **1993**, *74*, R1–R81.
(93) Faist, J.; Capasso, F.; Sivco, D. L.; Sirtori, C.; Hutchinson, A. L.; Cho, A. Y. Quantum Cascade Laser. *Science* **1994**, *264*, 553–556.
(94) Hines, M. A.; Guyot-Sionnest, P. Synthesis and Characterization of Strongly Luminescing ZnS-Capped CdSe Nanocrystals. *J. Phys. Chem.* **1996**, *100*, 468–471.
(95) Kortan, A. R.; Hull, R.; Opila, R. L.; Bawendi, M. G.; Steigerwald, M. L.; Carroll, P. J.; Brus, L. E. Nucleation and Growth of CdSe on ZnS Quantum Crystallite Seeds, and Vice Versa, in Inverse Micelle Media. *J. Am. Chem. Soc.* **1990**, *112*, 1327–1332.
(96) Justo, Y.; Geiregat, P.; van Hoecke, K.; Vanhaecke, F.; De Mello Donega, C.; Hens, Z. Optical Properties of PbS/CdS Core/Shell Quantum Dots. *J. Phys. Chem. C* **2013**, *117*, 20171–20177.
(97) Sagar, L. K.; Walravens, W.; Zhao, Q.; Vantomme, A.; Geiregat, P.; Hens, Z. PbS/CdS Core/Shell Quantum Dots by Additive, Layer-by-Layer Shell Growth. *Chem. Mater.* **2016**, *28*, 6953–6959.
(98) Sagar, L. K.; Walravens, W.; Maes, J.; Geiregat, P.; Hens, Z. HgSe/CdE (E = S, Se) Core/Shell Nanocrystals by Colloidal Atomic Layer Deposition. *J. Phys. Chem. C* **2017**, *121*, 13816–13822.
(99) Deng, Z.; Guyot-Sionnest, P. Intraband Luminescence from HgSe/CdS Core/Shell Quantum Dots. *ACS Nano* **2016**, *10*, 2121–2127.
(100) Kamath, A.; Melnychuk, C.; Guyot-Sionnest, P. Toward Bright Mid-Infrared Emitters: Thick-Shell n-Type HgSe/CdS Nanocrystals. *J. Am. Chem. Soc.* **2021**, *143*, 19567–19575.
(101) Shen, G.; Guyot-Sionnest, P. HgS and HgS/CdS Colloidal Quantum Dots with Infrared Intraband Transitions and Emergence of a Surface Plasmon. *J. Phys. Chem. C* **2016**, *120*, 11744–11753.
(102) Lifshitz, E.; Brumer, M.; Kigel, A.; Sashchiuk, A.; Bashouti, M.; Sirota, M.; Galun, E.; Burshtein, Z.; Le Quang, A. Q.; Ledoux-Rak, I.; Zyss, J. Air-Stable PbSe/PbS and PbSe/$PbSe_xS_{1-x}$ Core−shell Nanocrystal Quantum Dots and Their Applications. *J. Phys. Chem. B* **2006**, *110*, 25356–25365.

(103) Bartnik, A. C.; Wise, F. W.; Kigel, A.; Lifshitz, E. Electronic Structure of PbSe/PbS Core-Shell Quantum Dots. *Phys. Rev. B* **2007**, *75*, 245424.
(104) Ivanov, S. A.; Piryatinski, A.; Nanda, J.; Tretiak, S.; Zavadil, K. R.; Wallace, W. O.; Werder, D.; Klimov, V. I. Type-II Core/Shell CdS/ZnSe Nanocrystals: Synthesis, Electronic Structures, and Spectroscopic Properties. *J. Am. Chem. Soc.* **2007**, *129*, 11708–11719.
(105) Kim, S.; Fisher, B.; Eisler, H.-J.; Bawendi, M. Type-II Quantum Dots: CdTe/CdSe (Core/Shell) and CdSe/ZnTe (Core/Shell) Heterostructures. *J. Am. Chem. Soc.* **2003**, *125*, 11466–11467.
(106) Livache, C.; Martinez, B.; Goubet, N.; Gréboval, C.; Qu, J.; Chu, A.; Royer, S.; Ithurria, S.; Silly, M. G.; Dubertret, B.; Lhuillier, E. A Colloidal Quantum Dot Infrared Photodetector and Its Use for Intraband Detection. *Nat. Commun.* **2019**, *10*, 2125.
(107) Yang, Z.; Fan, J. Z.; Proppe, A. H.; Arquer, F. P. G. de; Rossouw, D.; Voznyy, O.; Lan, X.; Liu, M.; Walters, G.; Quintero-Bermudez, R.; Sun, B.; Hoogland, S.; Botton, G. A.; Kelley, S. O.; Sargent, E. H. Mixed-Quantum-Dot Solar Cells. *Nat. Commun.* **2017**, *8*, 1325.
(108) Sun, B.; Ouellette, O.; García de Arquer, F. P.; Voznyy, O.; Kim, Y.; Wei, M.; Proppe, A. H.; Saidaminov, M. I.; Xu, J.; Liu, M.; et al. Multibandgap Quantum Dot Ensembles for Solar-Matched Infrared Energy Harvesting. *Nat. Commun.* **2018**, *9*, 4003.
(109) Pradhan, S.; Di Stasio, F.; Bi, Y.; Gupta, S.; Christodoulou, S.; Stavrinadis, A.; Konstantatos, G. High-Efficiency Colloidal Quantum Dot Infrared Light-Emitting Diodes via Engineering at the Supra-Nanocrystalline Level. *Nat. Nanotechnol.* **2019**, *14*, 72–79.
(110) Yang, H.; Wong, E.; Zhao, T.; Lee, J. D.; Xin, H. L.; Chi, M.; Fleury, B.; Tang, H.-Y.; Gaulding, E. A.; Kagan, C. R.; Murray, C. B. Charge Transport Modulation in PbSe Nanocrystal Solids by Au_xAg_{1-x} Nanoparticle Doping. *ACS Nano* **2018**, *12*, 9091–9100.
(111) Koppens, F. H. L.; Mueller, T.; Avouris, P.; Ferrari, A. C.; Vitiello, M. S.; Polini, M. Photodetectors Based on Graphene, Other Two-Dimensional Materials and Hybrid Systems. *Nat. Nanotechnol.* **2014**, *9*, 780–793.
(112) Geim, A. K.; Grigorieva, I. V. Van Der Waals Heterostructures. *Nature* **2013**, *499*, 419–425.
(113) Khalili, A.; Abadie, C.; Dang, T. H.; Chu, A.; Izquierdo, E.; Dabard, C.; Gréboval, C.; Cavallo, M.; Zhang, H.; Pierini, S.; Prado, Y.; Xu, X. Z.; Ithurria, S.; Vincent, G.; Coinon, C.; Desplanque, L.; Lhuillier, E. Colloidal II–VI—Epitaxial III–V Heterostructure: A Strategy to Expand InGaAs Spectral Response. *Appl. Phys. Lett.* **2022**, *120*, 051101.
(114) Khalili, A.; Cavallo, M.; Dang, T. H.; Dabard, C.; Zhang, H.; Bossavit, E.; Abadie, C.; Prado, Y.; Xu, X. Z.; Ithurria, S.; Vincent, G.; Coinon, C.; Desplanque, L.; Lhuillier, E. Mid-Wave Infrared Sensitized InGaAs Using Intraband Transition in Doped Colloidal II–VI Nanocrystals. *J. Chem. Phys.* **2023**, *158*, 094702.
(115) Goossen, K. W.; Lyon, S. A. Grating Enhanced Quantum Well Detector. *Appl. Phys. Lett.* **1985**, *47*, 1257–1259.
(116) Goossen, K. W.; Lyon, S. A.; Alavi, K. Grating Enhancement of Quantum Well Detector Response. *Appl. Phys. Lett.* **1988**, *53*, 1027–1029.
(117) Hasnain, G.; Levine, B. F.; Bethea, C. G.; Logan, R. A.; Walker, J.; Malik, R. J. GaAs/AlGaAs Multiquantum Well Infrared Detector Arrays Using Etched Gratings. *Appl. Phys. Lett.* **1989**, *54*, 2515–2517.
(118) Andersson, J. Y.; Lundqvist, L. Grating-coupled Quantum-well Infrared Detectors: Theory and Performance. *J. Appl. Phys.* **1992**, *71*, 3600–3610.
(119) Sarusi, G.; Levine, B. F.; Pearton, S. J.; Bandara, K. M. S.; Leibenguth, R. E.; Andersson, J. Y. Optimization of Two Dimensional Gratings for Very Long Wavelength Quantum Well Infrared Photodetectors. *J. Appl. Phys.* **1994**, *76*, 4989–4994.
(120) Andersson, J. Y.; Lundqvist, L.; Paska, Z. F. Quantum Efficiency Enhancement of AlGaAs/GaAs Quantum Well Infrared Detectors Using a Waveguide with a Grating Coupler. *Appl. Phys. Lett.* **1991**, *58*, 2264–2266.

(121) Chen, C. J.; Choi, K. K.; Tidrow, M. Z.; Tsui, D. C. Corrugated Quantum Well Infrared Photodetectors for Normal Incident Light Coupling. *Appl. Phys. Lett.* **1996**, *68*, 1446–1448.
(122) Chen, C. J.; Choi, K. K.; Chang, W. H.; Tsui, D. C. Performance of Corrugated Quantum Well Infrared Photodetectors. *Appl. Phys. Lett.* **1997**, *71*, 3045–3047.
(123) Forrai, D. P.; Endres, D. W.; Choi, K. K.; O'Neill, J. J. Corrugated QWIP for Tactical Army Applications. *Def. Tech. Inf. Cent. ARMY Res. LAB ADELPHI MD*.
(124) Kovalenko, M. V.; Scheele, M.; Talapin, D. V. Colloidal Nanocrystals with Molecular Metal Chalcogenide Surface Ligands. *Science* **2009**, *324*, 1417–1420.
(125) Dolzhnikov, D. S.; Zhang, H.; Jang, J.; Son, J. S.; Panthani, M. G.; Shibata, T.; Chattopadhyay, S.; Talapin, D. V. Composition-Matched Molecular "Solders" for Semiconductors. *Science* **2015**, *347*, 425–428.
(126) Lhuillier, E.; Keuleyan, S.; Guyot-Sionnest, P. Optical Properties of HgTe Colloidal Quantum Dots. *Nanotechnology* **2012**, *23*, 175705.
(127) Beck, F. J.; Stavrinadis, A.; Diedenhofen, S. L.; Lasanta, T.; Konstantatos, G. Surface Plasmon Polariton Couplers for Light Trapping in Thin-Film Absorbers and Their Application to Colloidal Quantum Dot Optoelectronics. *ACS Photonics* **2014**, *1*, 1197–1205.
(128) Diedenhofen, S. L.; Kufer, D.; Lasanta, T.; Konstantatos, G. Integrated Colloidal Quantum Dot Photodetectors with Color-Tunable Plasmonic Nanofocusing Lenses. *Light Sci. Appl.* **2015**, *4*, e234–e234.
(129) Baek, S.-W.; Ouellette, O.; Jo, J. W.; Choi, J.; Seo, K.-W.; Kim, J.; Sun, B.; Lee, S.-H.; Choi, M.-J.; Nam, D.-H.; Quan, L. N.; Kang, J.; Hoogland, S.; García de Arquer, F. P.; Lee, J.-Y.; Sargent, Edward. H. Infrared Cavity-Enhanced Colloidal Quantum Dot Photovoltaics Employing Asymmetric Multilayer Electrodes. *ACS Energy Lett.* **2018**, *3*, 2908–2913.
(130) Prins, F.; Kim, D. K.; Cui, J.; De Leo, E.; Spiegel, L. L.; McPeak, K. M.; Norris, D. J. Direct Patterning of Colloidal Quantum-Dot Thin Films for Enhanced and Spectrally Selective Out-Coupling of Emission. *Nano Lett.* **2017**, *17*, 1319–1325.
(131) Le-Van, Q.; Le Roux, X.; Aassime, A.; Degiron, A. Electrically Driven Optical Metamaterials. *Nat. Commun.* **2016**, *7*, 12017.
(132) Konstantatos, G.; Sargent, E. H. Nanostructured Materials for Photon Detection. *Nat. Nanotechnol.* **2010**, *5*, 391–400.
(133) Schuller, J. A.; Barnard, E. S.; Cai, W.; Jun, Y. C.; White, J. S.; Brongersma, M. L. Plasmonics for Extreme Light Concentration and Manipulation. *Nat. Mater.* **2010**, *9*, 193–204.
(134) Yifat, Y.; Ackerman, M.; Guyot-Sionnest, P. Mid-IR Colloidal Quantum Dot Detectors Enhanced by Optical Nano-Antennas. *Appl. Phys. Lett.* **2017**, *110*, 041106.
(135) Tang, X.; Wu, G. fu; Lai, K. W. C. Plasmon Resonance Enhanced Colloidal HgSe Quantum Dot Filterless Narrowband Photodetectors for Mid-Wave Infrared. *J. Mater. Chem. C* **2017**, *5*, 362–369.
(136) Chu, A.; Gréboval, C.; Goubet, N.; Martinez, B.; Livache, C.; Qu, J.; Rastogi, P.; Bresciani, F. A.; Prado, Y.; Suffit, S.; Ithurria, S.; Vincent, G.; Lhuillier, E. Near Unity Absorption in Nanocrystal Based Short Wave Infrared Photodetectors Using Guided Mode Resonators. *ACS Photonics* **2019**, *6*, 2553–2561.
(137) Chen, M.; Shao, L.; Kershaw, S. V.; Yu, H.; Wang, J.; Rogach, A. L.; Zhao, N. Photocurrent Enhancement of HgTe Quantum Dot Photodiodes by Plasmonic Gold Nanorod Structures. *ACS Nano* **2014**, *8*, 8208–8216.
(138) Tang, X.; Ackerman, M. M.; Guyot-Sionnest, P. Thermal Imaging with Plasmon Resonance Enhanced HgTe Colloidal Quantum Dot Photovoltaic Devices. *ACS Nano* **2018**, *12*, 7362–7370.
(139) Rastogi, P.; Chu, A.; Dang, T. H.; Prado, Y.; Gréboval, C.; Qu, J.; Dabard, C.; Khalili, A.; Dandeu, E.; Fix, B.; Xu, X. Z.; Ithurria, S.; Vincent, G.; Gallas, B.; Lhuillier, E. Complex Optical Index of HgTe Nanocrystal Infrared Thin Films and Its Use for Short Wave Infrared Photodiode Design. *Adv. Opt. Mater.* **2021**, *9*, 2002066.

(140) www.swirvisionsystems.com (accessed May 3, 2023).
(141) www.imec-int.com (accessed May 3, 2023).
(142) www.emberion.com (accessed May 3, 2023).
(143) Tang, X.; Ackerman, M. M.; Shen, G.; Guyot-Sionnest, P. Towards Infrared Electronic Eyes: Flexible Colloidal Quantum Dot Photovoltaic Detectors Enhanced by Resonant Cavity. *Small* **2019**, *15*, 1804920.
(144) Urayama, J.; Norris, T. B.; Singh, J.; Bhattacharya, P. Observation of Phonon Bottleneck in Quantum Dot Electronic Relaxation. *Phys. Rev. Lett.* **2001**, *86*, 4930–4933.
(145) Arakawa, Y.; Sakaki, H. Multidimensional Quantum Well Laser and Temperature Dependence of Its Threshold Current. *Appl. Phys. Lett.* **1982**, *40*, 939–941.
(146) Liu, H. C.; Gao, M.; McCaffrey, J.; Wasilewski, Z. R.; Fafard, S. Quantum Dot Infrared Photodetectors. *Appl. Phys. Lett.* **2001**, *78*, 79–81.
(147) Maimon, S.; Finkman, E.; Bahir, G.; Schacham, S. E.; Garcia, J. M.; Petroff, P. M. Intersublevel Transitions in InAs/GaAs Quantum Dots Infrared Photodetectors. *Appl. Phys. Lett.* **1998**, *73*, 2003–2005.
(148) Sauvage, S.; Boucaud, P.; Julien, F. H.; Gérard, J.-M.; Marzin, J.-Y. Infrared Spectroscopy of Intraband Transitions in Self-Organized InAs/GaAs Quantum Dots. *J. Appl. Phys.* **1997**, *82*, 3396–3401.
(149) Phillips, J.; Kamath, K.; Bhattacharya, P. Far-Infrared Photoconductivity in Self-Organized InAs Quantum Dots. *Appl. Phys. Lett.* **1998**, *72*, 2020–2022.
(150) Krishna, S. Quantum Dots-in-a-Well Infrared Photodetectors. *J. Phys. Appl. Phys.* **2005**, *38*, 2142.
(151) Krishna, S.; Raghavan, S.; von Winckel, G.; Rotella, P.; Stintz, A.; Morath, C. P.; Le, D.; Kennerly, S. W. Two Color InAs/InGaAs Dots-in-a-Well Detector with Background-Limited Performance at 91 K. *Appl. Phys. Lett.* **2003**, *82*, 2574–2576.
(152) Gendron, L.; Carras, M.; Huynh, A.; Ortiz, V.; Koeniguer, C.; Berger, V. Quantum Cascade Photodetector. *Appl. Phys. Lett.* **2004**, *85*, 2824–2826.
(153) DIRECTIVE 2011/65/EU OF THE EUROPEAN PARLIAMENT AND OF THE COUNCIL of 8 June 2011 on the Restriction of the Use of Certain Hazardous Substances in Electrical and Electronic Equipment. *Off. J. Eur. Union* **2011**.
(154) Gunapala, S. D.; Bandara, S. V.; Hill, C. J.; Ting, D. Z.; Liu, J. K.; Rafol, S. B.; Blazejewski, E. R.; Mumolo, J. M.; Keo, S. A.; Krishna, S.; Chang, Y.-C.; Shott, C. A. Demonstration of 640×512 Pixels Long-Wavelength Infrared (LWIR) Quantum Dot Infrared Photodetector (QDIP) Imaging Focal Plane Array. *Infrared Phys. Technol.* **2007**, *50*, 149–155.
(155) Jiang, J.; Mi, K.; Tsao, S.; Zhang, W.; Lim, H.; O'Sullivan, T.; Sills, T.; Razeghi, M.; Brown, G. J.; Tidrow, M. Z. Demonstration of a 256×256 Middle-Wavelength Infrared Focal Plane Array Based on InGaAs/InGaP Quantum Dot Infrared Photodetectors. *Appl. Phys. Lett.* **2004**, *84*, 2232–2234.
(156) Krishna, S.; Forman, D.; Annamalai, S.; Dowd, P.; Varangis, P.; Tumolillo, T., Jr; Gray, A.; Zilko, J.; Sun, K.; Liu, M.; Campbell, J.; Carothers, D. Demonstration of a 320×256 Two-Color Focal Plane Array Using InAs/InGaAs Quantum Dots in Well Detectors. *Appl. Phys. Lett.* **2005**, *86*, 193501.
(157) Bois, P.; Guériaux, V.; l'Isle, N. B. de; Manissadjian, A.; Facoetti, H.; Marcadet, X.; Costard, E.; Nedelcu, A. QWIP Status and Future Trends at Thales. In *Quantum Sensing and Nanophotonic Devices IX*; SPIE, 2012; Vol. 8268, pp 566–576.
(158) Kimata, M. Uncooled Infrared Focal Plane Arrays. *IEEJ Trans. Electr. Electron. Eng.* **2018**, *13*, 4–12.
(159) Kokkoniemi, R.; Girard, J.-P.; Hazra, D.; Laitinen, A.; Govenius, J.; Lake, R. E.; Sallinen, I.; Vesterinen, V.; Partanen, M.; Tan, J. Y.; Chan, K. W.; Tan, K. Y.; Hakonen, P.; Möttönen, M. Bolometer Operating at the Threshold for Circuit Quantum Electrodynamics. *Nature* **2020**, *586*, 47–51.
(160) Laurent, L.; Yon, J.-J.; Moulet, J.-S.; Roukes, M.; Duraffourg, L. 12-Um-Pitch Electromechanical Resonator for Thermal Sensing. *Phys. Rev. Appl.* **2018**, *9*, 024016.
(161) www.flir.fr/browse/industrial/handheld-thermal-cameras/ (accessed May 3, 2023).

(162) Lu, H.; Carroll, G. M.; Neale, N. R.; Beard, M. C. Infrared Quantum Dots: Progress, Challenges, and Opportunities. *ACS Nano* **2019**, *13*, 939–953.
(163) Guyot-Sionnest, P.; Ackerman, M. M.; Tang, X. Colloidal Quantum Dots for Infrared Detection beyond Silicon. *J. Chem. Phys.* **2019**, *151*, 060901.
(164) Sahu, A.; Khare, A.; Deng, D. D.; Norris, D. J. Quantum Confinement in Silver Selenide Semiconductor Nanocrystals. *Chem. Commun.* **2012**, *48*, 5458–5460.
(165) Sahu, A.; Qi, L.; Kang, M. S.; Deng, D.; Norris, D. J. Facile Synthesis of Silver Chalcogenide (Ag_2E; E = Se, S, Te) Semiconductor Nanocrystals. *J. Am. Chem. Soc.* **2011**, *133*, 6509–6512.
(166) Qu, J.; Goubet, N.; Livache, C.; Martinez, B.; Amelot, D.; Gréboval, C.; Chu, A.; Ramade, J.; Cruguel, H.; Ithurria, S.; Silly, M. G.; Lhuillier, E. Intraband Mid-Infrared Transitions in Ag_2Se Nanocrystals: Potential and Limitations for Hg-Free Low-Cost Photodetection. *J. Phys. Chem. C* **2018**, *122*, 18161–18167.
(167) Guyot-Sionnest, P.; Hines, M. A. Intraband Transitions in Semiconductor Nanocrystals. *Appl. Phys. Lett.* **1998**, *72*, 686–688.
(168) Wehrenberg, B. L.; Wang, C.; Guyot-Sionnest, P. Interband and Intraband Optical Studies of PbSe Colloidal Quantum Dots. *J. Phys. Chem. B* **2002**, *106*, 10634–10640.
(169) Kroupa, D. M.; Hughes, B. K.; Miller, E. M.; Moore, D. T.; Anderson, N. C.; Chernomordik, B. D.; Nozik, A. J.; Beard, M. C. Synthesis and Spectroscopy of Silver-Doped PbSe Quantum Dots. *J. Am. Chem. Soc.* **2017**, *139*, 10382–10394.
(170) Ramiro, I.; Özdemir, O.; Christodoulou, S.; Gupta, S.; Dalmases, M.; Torre, I.; Konstantatos, G. Mid- and Long-Wave Infrared Optoelectronics via Intraband Transitions in PbS Colloidal Quantum Dots. *Nano Lett.* **2020**, *20*, 1003–1008.
(171) Robin, A.; Livache, C.; Ithurria, S.; Lacaze, E.; Dubertret, B.; Lhuillier, E. Surface Control of Doping in Self-Doped Nanocrystals. *ACS Appl. Mater. Interfaces* **2016**, *8*, 27122–27128.
(172) Martinez, B.; Livache, C.; Notemgnou Mouafo, L. D.; Goubet, N.; Keuleyan, S.; Cruguel, H.; Ithurria, S.; Aubin, H.; Ouerghi, A.; Doudin, B.; Lacaze, E.; Dubertret, B.; Silly, M. G.; Lobo, R. P. S. M.; Dayen, J.-F.; Lhuillier, E. HgSe Self-Doped Nanocrystals as a Platform to Investigate the Effects of Vanishing Confinement. *ACS Appl. Mater. Interfaces* **2017**, *9*, 36173–36180.
(173) Kroupa, D. M.; Vörös, M.; Brawand, N. P.; McNichols, B. W.; Miller, E. M.; Gu, J.; Nozik, A. J.; Sellinger, A.; Galli, G.; Beard, M. C. Tuning Colloidal Quantum Dot Band Edge Positions through Solution-Phase Surface Chemistry Modification. *Nat. Commun.* **2017**, *8*, 15257.
(174) Chen, M.; Hao, Q.; Luo, Y.; Tang, X. Mid-Infrared Intraband Photodetector via High Carrier Mobility HgSe Colloidal Quantum Dots. *ACS Nano* **2022**, *16*, 11027–11035.
(175) Talapin, D. V.; Lee, J.-S.; Kovalenko, M. V.; Shevchenko, E. V. Prospects of Colloidal Nanocrystals for Electronic and Optoelectronic Applications. *Chem. Rev.* **2010**, *110*, 389–458.
(176) Hafiz, S. B.; Scimeca, M. R.; Zhao, P.; Paredes, I. J.; Sahu, A.; Ko, D.-K. Silver Selenide Colloidal Quantum Dots for Mid-Wavelength Infrared Photodetection. *ACS Appl. Nano Mater.* **2019**, *2*, 1631–1636.
(177) Hafiz, S. B.; Al Mahfuz, M. M.; Ko, D.-K. Vertically Stacked Intraband Quantum Dot Devices for Mid-Wavelength Infrared Photodetection. *ACS Appl. Mater. Interfaces* **2021**, *13*, 937–943.
(178) Park, M.; Choi, D.; Choi, Y.; Shin, H.; Jeong, K. S. Mid-Infrared Intraband Transition of Metal Excess Colloidal Ag_2Se Nanocrystals. *ACS Photonics* **2018**, *5*, 1907–1911.
(179) Delga, A. 8 - Quantum Cascade Detectors: A Review. In *Mid-infrared Optoelectronics*; Tournié, E., Cerutti, L., Eds.; Woodhead Publishing Series in Electronic and Optical Materials; Woodhead Publishing, 2020; pp 337–377.
(180) Goubet, N.; Livache, C.; Martinez, B.; Xu, X. Z.; Ithurria, S.; Royer, S.; Cruguel, H.; Patriarche, G.; Ouerghi, A.; Silly, M.; Dubertret, B.; Lhuillier, E. Wave-Function Engineering in HgSe/HgTe Colloidal Heterostructures To Enhance Mid-Infrared Photoconductive Properties. *Nano Lett.* **2018**, *18*, 4590–4597.

(181) Livache, C.; Goubet, N.; Gréboval, C.; Martinez, B.; Ramade, J.; Qu, J.; Triboulin, A.; Cruguel, H.; Baptiste, B.; Klotz, S.; Fishman, G.; Sauvage, S.; Capitani, F.; Lhuillier, E. Effect of Pressure on Interband and Intraband Transition of Mercury Chalcogenide Quantum Dots. *J. Phys. Chem. C* **2019**, *123*, 13122–13130.
(182) Ruppert, M.; Bui, H.; Sagar, L. K.; Geiregat, P.; Hens, Z.; Bester, G.; Huse, N. Intraband Dynamics of Mid-Infrared HgTe Quantum Dots. *Nanoscale* **2022**, *14*, 4123–4130.
(183) Guyot-Sionnest, P.; Shim, M.; Matranga, C.; Hines, M. Intraband Relaxation in CdSe Quantum Dots. *Phys. Rev. B* **1999**, *60*, R2181–R2184.
(184) Apretna, T.; Massabeau, S.; Gréboval, C.; Goubet, N.; Tignon, J.; Dhillon, S.; Carosella, F.; Ferreira, R.; Lhuillier, E.; Mangeney, J. Few Picosecond Dynamics of Intraband Transitions in THz HgTe Nanocrystals. *Nanophotonics* **2021**, *10*, 2753–2763.
(185) Fan, J. Z.; Vafaie, M.; Bertens, K.; Sytnyk, M.; Pina, J. M.; Sagar, L. K.; Ouellette, O.; Proppe, A. H.; Rasouli, A. S.; Gao, Y.; Baek, S.-W.; Chen, B.; Laquai, F.; Hoogland, S.; Arquer, F. P. G. de; Heiss, W.; Sargent, E. H. Micron Thick Colloidal Quantum Dot Solids. *Nano Lett.* **2020**, *20*, 5284–5291.
(186) Lan, X.; Chen, M.; Hudson, M. H.; Kamysbayev, V.; Wang, Y.; Guyot-Sionnest, P.; Talapin, D. V. Quantum Dot Solids Showing State-Resolved Band-like Transport. *Nat. Mater.* **2020**, *19*, 323–329.
(187) Heine, C.; Morf, R. H. Submicrometer Gratings for Solar Energy Applications. *Appl. Opt.* **1995**, *34*, 2476–2482.
(188) Sai, H.; Fujiwara, H.; Kondo, M. Back Surface Reflectors with Periodic Textures Fabricated by Self-Ordering Process for Light Trapping in Thin-Film Microcrystalline Silicon Solar Cells. *Sol. Energy Mater. Sol. Cells* **2009**, *93*, 1087–1090.
(189) Zhu, J.; Yu, Z.; Burkhard, G. F.; Hsu, C.-M.; Connor, S. T.; Xu, Y.; Wang, Q.; McGehee, M.; Fan, S.; Cui, Y. Optical Absorption Enhancement in Amorphous Silicon Nanowire and Nanocone Arrays. *Nano Lett.* **2009**, *9*, 279–282.
(190) Vanecek, M.; Babchenko, O.; Purkrt, A.; Holovsky, J.; Neykova, N.; Poruba, A.; Remes, Z.; Meier, J.; Kroll, U. Nanostructured Three-Dimensional Thin Film Silicon Solar Cells with Very High Efficiency Potential. *Appl. Phys. Lett.* **2011**, *98*, 163503.
(191) Massiot, I.; Vandamme, N.; Bardou, N.; Dupuis, C.; Lemaître, A.; Guillemoles, J.-F.; Collin, S. Metal Nanogrid for Broadband Multiresonant Light-Harvesting in Ultrathin GaAs Layers. *ACS Photonics* **2014**, *1*, 878–884.
(192) Verdun, M.; Portier, B.; Jaworowicz, K.; Jaeck, J.; Lelarge, F.; Guilet, S.; Dupuis, C.; Haïdar, R.; Pardo, F.; Pelouard, J.-L. Guided-Mode Resonator for Thin InGaAs P-i-N Short-Wave Infrared Photo-Diode. *Appl. Phys. Lett.* **2016**, *108*, 053501.
(193) Derkacs, D.; Lim, S. H.; Matheu, P.; Mar, W.; Yu, E. T. Improved Performance of Amorphous Silicon Solar Cells via Scattering from Surface Plasmon Polaritons in Nearby Metallic Nanoparticles. *Appl. Phys. Lett.* **2006**, *89*, 093103.
(194) Nakayama, K.; Tanabe, K.; Atwater, H. A. Plasmonic Nanoparticle Enhanced Light Absorption in GaAs Solar Cells. *Appl. Phys. Lett.* **2008**, *93*, 121904.
(195) Ouyang, Z.; Pillai, S.; Beck, F.; Kunz, O.; Varlamov, S.; Catchpole, K. R.; Campbell, P.; Green, M. A. Effective Light Trapping in Polycrystalline Silicon Thin-Film Solar Cells by Means of Rear Localized Surface Plasmons. *Appl. Phys. Lett.* **2010**, *96*, 261109.
(196) Wu, J.-L.; Chen, F.-C.; Hsiao, Y.-S.; Chien, F.-C.; Chen, P.; Kuo, C.-H.; Huang, M. H.; Hsu, C.-S. Surface Plasmonic Effects of Metallic Nanoparticles on the Performance of Polymer Bulk Heterojunction Solar Cells. *ACS Nano* **2011**, *5*, 959–967.
(197) Chen, H.-L.; Cattoni, A.; De Lépinau, R.; Walker, A. W.; Höhn, O.; Lackner, D.; Siefer, G.; Faustini, M.; Vandamme, N.; Goffard, J.; Behaghel, B.; Dupuis, C.; Bardou, N.; Dimroth, F.; Collin, S. A 19.9%-Efficient Ultrathin Solar Cell Based on a 205 Nm Thick Gaas Absorber and a Silver Nanostructured Back Mirror. *Nat. Energy* **2019**, *4*, 761–767.
(198) Hunsperger, R. G. *Integrated Optics: Theory and Technology*; Tamir, T., Lotsch, H. K. V., Series Eds.; Springer Series in Optical Sciences; Springer: Berlin, Heidelberg, 1991; Vol. 33.
(199) Wang, S. S.; Magnusson, R.; Bagby, J. S.; Moharam, M. G. Guided-Mode Resonances in Planar Dielectric-Layer Diffraction Gratings. *JOSA A* **1990**, *7*, 1470–1474.

(200) Wang, S. S.; Magnusson, R. Theory and Applications of Guided-Mode Resonance Filters. *Appl. Opt.* **1993**, *32*, 2606–2613.
(201) Magnusson, R.; Wang, S. S. New Principle for Optical Filters. *Appl. Phys. Lett.* **1992**, *61*, 1022–1024.
(202) Gréboval, C.; Chu, A.; Magalhaes, D. V.; Ramade, J.; Qu, J.; Rastogi, P.; Khalili, A.; Chee, S.-S.; Aubin, H.; Vincent, G.; Bals, S.; Delerue, C.; Lhuillier, E. Ferroelectric Gating of Narrow Band-Gap Nanocrystal Arrays with Enhanced Light–Matter Coupling. *ACS Photonics* **2021**, *8*, 259–268.
(203) Rastogi, P.; Chu, A.; Gréboval, C.; Qu, J.; Noumbé, U. N.; Chee, S.-S.; Goyal, M.; Khalili, A.; Xu, X. Z.; Cruguel, H.; et al. Pushing Absorption of Perovskite Nanocrystals into the Infrared. *Nano Lett.* **2020**, *20*, 3999–4006.
(204) Lemarchand, F.; Sentenac, A.; Giovannini, H. Increasing the Angular Tolerance of Resonant Grating Filters with Doubly Periodic Structures. *Opt. Lett.* **1998**, *23*, 1149–1151.
(205) Lemarchand, F.; Sentenac, A.; Cambril, E.; Giovannini, H. Study of the Resonant Behaviour of Waveguide Gratings: Increasing the Angular Tolerance of Guided-Mode Filters. *J. Opt. Pure Appl. Opt.* **1999**, *1*, 545.
(206) Sakat, E.; Héron, S.; Bouchon, P.; Vincent, G.; Pardo, F.; Collin, S.; Pelouard, J.-L.; Haïdar, R. Metal–Dielectric Bi-Atomic Structure for Angular-Tolerant Spectral Filtering. *Opt. Lett.* **2013**, *38*, 425–427.
(207) Hugonin, J. P.; Lalanne, P. RETICOLO Software for Grating Analysis. arXiv January 8, 2023.
(208) Moharam, M. G.; Grann, E. B.; Pommet, D. A.; Gaylord, T. K. Formulation for Stable and Efficient Implementation of the Rigorous Coupled-Wave Analysis of Binary Gratings. *JOSA A* **1995**, *12*, 1068–1076.
(209) Chehaibou, B.; Izquierdo, E.; Chu, A.; Abadie, C.; Cavallo, M.; Khalili, A.; Dang, T. H.; Gréboval, C.; Xu, X. Z.; Ithurria, S.; Vincent, G.; Gallas, B.; Mugny, G.; Arnaud, A.; Lhuillier, E.; Delerue, C. The Complex Optical Index of PbS Nanocrystal Thin Films and Their Use for Short Wave Infrared Sensor Design. *Nanoscale* **2022**, *14*, 2711–2721.
(210) Khalili, A.; Weis, M.; Mizrahi, S. G.; Chu, A.; Dang, T. H.; Abadie, C.; Gréboval, C.; Dabard, C.; Prado, Y.; Xu, X. Z.; Péronne, E.; Livache, C.; Ithurria, S.; Patriarche, G.; Ramade, J.; Vincent, G.; Boschetto, D.; Lhuillier, E. Guided-Mode Resonator Coupled with Nanocrystal Intraband Absorption. *ACS Photonics* **2022**, *9*, 985–993.
(211) Hafiz, S. B.; Al Mahfuz, M. M.; Lee, S.; Ko, D.-K. Midwavelength Infrared p–n Heterojunction Diodes Based on Intraband Colloidal Quantum Dots. *ACS Appl. Mater. Interfaces* **2021**, *13*, 49043–49049.
(212) Lai, Y.; Li, H.; Kim, D. K.; Diroll, B. T.; Murray, C. B.; Kagan, C. R. Low-Frequency (1/f) Noise in Nanocrystal Field-Effect Transistors. *ACS Nano* **2014**, *8*, 9664–9672.
(213) Novoselov, K. S.; Geim, A. K.; Morozov, S. V.; Jiang, D.; Zhang, Y.; Dubonos, S. V.; Grigorieva, I. V.; Firsov, A. A. Electric Field Effect in Atomically Thin Carbon Films. *Science* **2004**, *306*, 666–669.
(214) Jariwala, D.; Marks, T. J.; Hersam, M. C. Mixed-Dimensional van Der Waals Heterostructures. *Nat. Mater.* **2017**, *16*, 170–181.
(215) Dean, C. R.; Young, A. F.; Meric, I.; Lee, C.; Wang, L.; Sorgenfrei, S.; Watanabe, K.; Taniguchi, T.; Kim, P.; Shepard, K. L.; Hone, J. Boron Nitride Substrates for High-Quality Graphene Electronics. *Nat. Nanotechnol.* **2010**, *5*, 722–726.
(216) Masala, S.; Adinolfi, V.; Sun, J.-P.; Gobbo, S. D.; Voznyy, O.; Kramer, I. J.; Hill, I. G.; Sargent, E. H. The Silicon:Colloidal Quantum Dot Heterojunction. *Adv. Mater.* **2015**, *27*, 7445–7450.
(217) Bucamp, A.; Coinon, C.; Codron, J.-L.; Troadec, D.; Wallart, X.; Desplanque, L. Buffer Free InGaAs Quantum Well and In-Plane Nanostructures on InP Grown by Atomic Hydrogen Assisted MBE. *J. Cryst. Growth* **2019**, *512*, 11–15.
(218) Chuang, C.-H. M.; Brown, P. R.; Bulović, V.; Bawendi, M. G. Improved Performance and Stability in Quantum Dot Solar Cells through Band Alignment Engineering. *Nat. Mater.* **2014**, *13*, 796–801.

(219) Bucamp, A.; Coinon, C.; Troadec, D.; Lepilliet, S.; Patriarche, G.; Wallart, X.; Desplanque, L. Gate Length Dependent Transport Properties of In-Plane Core-Shell Nanowires with Raised Contacts. *Nano Res.* **2020**, *13*, 61–66.
(220) Chu, A.; Martinez, B.; Ferré, S.; Noguier, V.; Gréboval, C.; Livache, C.; Qu, J.; Prado, Y.; Casaretto, N.; Goubet, N.; Cruguel, H.; Dudy, L.; Silly, M. G.; Vincent, G.; Lhuillier, E. HgTe Nanocrystals for SWIR Detection and Their Integration up to the Focal Plane Array. *ACS Appl. Mater. Interfaces* **2019**, *11*, 33116–33123.
(221) Dong, Y.; Chen, M.; Yiu, W. K.; Zhu, Q.; Zhou, G.; Kershaw, S. V.; Ke, N.; Wong, C. P.; Rogach, A. L.; Zhao, N. Solution Processed Hybrid Polymer: HgTe Quantum Dot Phototransistor with High Sensitivity and Fast Infrared Response up to 2400 Nm at Room Temperature. *Adv. Sci.* **2020**, *7*, 2000068.
(222) Grotevent, M. J.; Hail, C. U.; Yakunin, S.; Bachmann, D.; Calame, M.; Poulikakos, D.; Kovalenko, M. V.; Shorubalko, I. Colloidal HgTe Quantum Dot/Graphene Phototransistor with a Spectral Sensitivity beyond 3 Mm. *Adv. Sci.* **2021**, *8*, 2003360.
(223) Ramiro, I.; Kundu, B.; Dalmases, M.; Özdemir, O.; Pedrosa, M.; Konstantatos, G. Size- and Temperature-Dependent Intraband Optical Properties of Heavily n-Doped PbS Colloidal Quantum Dot Solid-State Films. *ACS Nano* **2020**, *14*, 7161–7169.
(224) Adachi, S. Optical Dispersion Relations for GaP, GaAs, GaSb, InP, InAs, InSb, $Al_xGa_{1-x}As$, and $In_{1-x}Ga_xAs_yP_{1-y}$. *J. Appl. Phys.* **1989**, *66*, 6030–6040.
(225) Godey, S.; Dhellemmes, S.; Wilk, A.; Zaknoune, M.; Mollot, F. CBr_4 and Be Heavily Doped InGaAs Grown in a Production MBE System. *J. Cryst. Growth* **2005**, *278*, 600–603.
(226) Jagtap, A.; Martinez, B.; Goubet, N.; Chu, A.; Livache, C.; Gréboval, C.; Ramade, J.; Amelot, D.; Trousset, P.; Triboulin, A.; Ithurria, S.; Silly, M. G.; Dubertret, B.; Lhuillier, E. Design of a Unipolar Barrier for a Nanocrystal-Based Short-Wave Infrared Photodiode. *ACS Photonics* **2018**, *5*, 4569–4576.
(227) Khalili, A.; Cavallo, M.; Bossavit, E.; Alchaar, R.; Dang, T. H.; Dabard, C.; Zhang, H.; Ledos, N.; Parahyba, V.; Potet, P.; Utterback, J. K.; Prado, Y.; Silly, M. G.; Dudin, P.; Avila, J.; Pierucci, D.; Lhuillier, E. In Situ Mapping of the Vectorial Electric Field within a Nanocrystal-Based Focal Plane Array Using Photoemission Microscopy. **2023**, (Submitted).
(228) Manda, S.; Matsumoto, R.; Saito, S.; Maruyama, S.; Minari, H.; Hirano, T.; Takachi, T.; Fujii, N.; Yamamoto, Y.; Zaizen, Y.; Hirano, T.; Iwamoto, H. High-Definition Visible-SWIR InGaAs Image Sensor Using Cu-Cu Bonding of III-V to Silicon Wafer. In *2019 IEEE International Electron Devices Meeting (IEDM)*; 2019; p 16.7.1-16.7.4.
(229) Lee, J.; Georgitzikis, E.; Li, Y.; Lin, Z.; Park, J.; Lieberman, I.; Cheyns, D.; Jayapala, M.; Lambrechts, A.; Thijs, S.; Stahl, R.; Malinowski, P. E. Imaging in Short-Wave Infrared with 1.82 µm Pixel Pitch Quantum Dot Image Sensor. In *2020 IEEE International Electron Devices Meeting (IEDM)*; 2020; p 16.5.1-16.5.4.
(230) www.new-imaging-technologies.com (accessed May 3, 2023).
(231) Georgitzikis, E.; Malinowski, P. E.; Li, Y.; Maes, J.; Hagelsieb, L. M.; Guerrieri, S.; Hens, Z.; Heremans, P.; Cheyns, D. Integration of PbS Quantum Dot Photodiodes on Silicon for NIR Imaging. *IEEE Sens. J.* **2020**, *20*, 6841–6848.
(232) Steckel, J. S.; Josse, E.; Pattantyus-Abraham, A. G.; Bidaud, M.; Mortini, B.; Bilgen, H.; Arnaud, O.; Allegret-Maret, S.; Saguin, F.; Mazet, L.; et al. 1.62 µm Global Shutter Quantum Dot Image Sensor Optimized for near and Shortwave Infrared. In *2021 IEEE International Electron Devices Meeting (IEDM)*; 2021; p 23.4.1-23.4.4.
(233) Alchaar, R.; Dabard, C.; Mastrippolito, D.; Bossavit, E.; Dang, T. H.; Cavallo, M.; Khalili, A.; Zhang, H.; Domenach, L.; Ledos, N.; et al. On the Suitable Choice of Metal for HgTe Nanocrystal-Based Photodiode: To Amalgam or Not to Amalgam. *J. Phys. Chem. C* **2023**.
(234) Krishnan, M.; Nalaskowski, J. W.; Cook, L. M. Chemical Mechanical Planarization: Slurry Chemistry, Materials, and Mechanisms. *Chem. Rev.* **2010**, *110*, 178–204.
(235) Cavallo, M.; Bossavit, E.; Matzen, S.; Maroutian, T.; Alchaar, R.; Dang, T. H.; Khalili, A.; Dabard, C.; Zhang, H.; Prado, Y.; Abadie, C.; Utterback, J. K.; Dayen, J. F.; Silly, M. G.;

Dudin, P.; Avila, J.; Lhuillier, E.; Pierucci, D. Coupling Ferroelectric to Colloidal Nanocrystals as a Generic Strategy to Engineer the Carrier Density Landscape. *Adv. Funct. Mater.* **2023**, 2300846.

(236) Cavallo, M.; Alchaar, R.; Bossavit, E.; Zhang, H.; Dang, T. H.; Khalili, A.; Prado, Y.; Silly, M. G.; Utterback, J. K.; Ithurria, S.; Dudin, P.; Avila, J.; Pierucci, D.; Lhuillier, E. Inside a Nanocrystal-Based Photodiode Using Photoemission Microscopy. *Nanoscale* **2023**, *15*, 9440–9448.

(237) Hertz, H. Ueber Einen Einfluss Des Ultravioletten Lichtes Auf Die Electrische Entladung. *Ann. Phys.* **1887**, *267*, 983–1000.

(238) Siegbahn, K.; Edvarson, K. β-Ray Spectroscopy in the Precision Range of 1 : 105. *Nucl. Phys.* **1956**, *1*, 137–159.

(239) *ESCA Atomic, Molecular and Solid State Structure Studies by Means of Electron Spectroscopy: Presented to the Royal Society of S#ience of Uppsala, Dec. 3rd, 1965*; Kungliga Vetenskaps-Societeten; Almqvist & Wiksell: Uppsala, 1967.

(240) Siegbahn, K. Electron Spectroscopy for Atoms, Molecules and Condensed Matter. *Nobel Lect.* **1981**.

(241) Zhang, H.; Alchaar, R.; Prado, Y.; Khalili, A.; Gréboval, C.; Cavallo, M.; Bossavit, E.; Dabard, C.; Dang, T. H.; Abadie, C.; et al. Material Perspective on HgTe Nanocrystal-Based Short-Wave Infrared Focal Plane Arrays. *Chem. Mater.* **2022**, *34*, 10964–10972.

(242) Martinez, B.; Ramade, J.; Livache, C.; Goubet, N.; Chu, A.; Gréboval, C.; Qu, J.; Watkins, W. L.; Becerra, L.; Dandeu, E.; Fave, J. L.; Méthivier, C.; Lacaze, E.; Lhuillier, E. HgTe Nanocrystal Inks for Extended Short-Wave Infrared Detection. *Adv. Opt. Mater.* **2019**, *7*, 1900348.

(243) Polack, F.; Silly, M.; Chauvet, C.; Lagarde, B.; Bergeard, N.; Izquierdo, M.; Chubar, O.; Krizmancic, D.; Ribbens, M.; Duval, J. -P.; Basset, C.; Kubsky, S.; Sirotti, F. TEMPO: A New Insertion Device Beamline at SOLEIL for Time Resolved Photoelectron Spectroscopy Experiments on Solids and Interfaces. *AIP Conf. Proc.* **2010**, *1234*, 185–188.

(244) Avila, J.; Razado-Colambo, I.; Lorcy, S.; Lagarde, B.; Giorgetta, J.-L.; Polack, F.; Asensio, M. C. Antares, a Scanning Photoemission Microscopy Beamline at Soleil. *J. Phys. Conf. Ser.* **2013**, *425*, 192023.

(245) Wang, Y.-Y.; Yuan, R.; Wang, S.; Wang, Z.; Jin, Q. Internal Electric Field Profiling of 2D P-N Junctions of Semiconductor Devices by 4D STEM and Dual Lens Electron Holography. *Microsc. Today* **2022**, *30*, 24–29.

(246) da Silva, B. C.; Sadre Momtaz, Z.; Monroy, E.; Okuno, H.; Rouviere, J.-L.; Cooper, D.; Den Hertog, M. I. Assessment of Active Dopants and p–n Junction Abruptness Using in Situ Biased 4D-STEM. *Nano Lett.* **2022**, *22*, 9544–9550.

(247) Ella, L.; Rozen, A.; Birkbeck, J.; Ben-Shalom, M.; Perello, D.; Zultak, J.; Taniguchi, T.; Watanabe, K.; Geim, A. K.; Ilani, S.; Sulpizio, J. A. Simultaneous Voltage and Current Density Imaging of Flowing Electrons in Two Dimensions. *Nat. Nanotechnol.* **2019**, *14*, 480–487.

(248) Hofmann, P. Accessing the Spectral Function of in Operando Devices by Angle-Resolved Photoemission Spectroscopy. *AVS Quantum Sci.* **2021**, *3*, 021101.

(249) Nenashev, A. V.; Jansson, F.; Baranovskii, S. D.; Österbacka, R.; Dvurechenskii, A. V.; Gebhard, F. Effect of Electric Field on Diffusion in Disordered Materials. I. One-Dimensional Hopping Transport. *Phys. Rev. B* **2010**, *81*, 115203.

(250) Nenashev, A. V.; Jansson, F.; Baranovskii, S. D.; Österbacka, R.; Dvurechenskii, A. V.; Gebhard, F. Effect of Electric Field on Diffusion in Disordered Materials. II. Two- and Three-Dimensional Hopping Transport. *Phys. Rev. B* **2010**, *81*, 115204.

(251) Richert, R.; Pautmeier, L.; Bässler, H. Diffusion and Drift of Charge Carriers in a Random Potential: Deviation from Einstein's Law. *Phys. Rev. Lett.* **1989**, *63*, 547–550.

(252) Arkhipov, V. I.; Bässler, H. A Model of Weak-Field Quasi-Equilibrium Hopping Transport in Disordered Materials. *Philos. Mag. Lett.* **1993**, *67*, 343–349.

(253) Xing, Y.; Yazdani, N.; Lin, W. M. M.; Yarema, M.; Zahn, R.; Wood, V. Effect of Positional Disorders on Charge Transport in Nanocrystal Quantum Dot Thin Films. *ACS Appl. Electron. Mater.* **2022**, *4*, 631–642.

Adrien Khalili Lazarjani October 4th, 2023

Subject: Advancing Nanocrystal-based Infrared Imaging: Exploring Novel Strategies in the Design and Characterization

Abstract: The infrared region is a part of the electromagnetic spectrum with wavelengths longer than those of visible light. This spectral domain provides complementary information to the visible range, and finds application in various fields such as defense, astronomy, and emerging civilian technologies including LiDAR in autonomous vehicles, or face recognition in our smartphones. While the silicon-based sensing technology rules over the visible market, its equivalent has yet to be developed in the infrared. Colloidal nanocrystals offer a promising avenue for the realization of high-performance and cost-effective infrared sensors. These chemically synthetized crystalline objects exhibit quantum confinement effects, resulting in size-tunable optical properties. Among infrared absorbing nanocrystals, I have specifically used mercury chalcogenides (HgX) nanocrystals that can address the entire infrared range from the visible to the THz region. Over the course of my thesis, I have explored innovative concepts relating to both the material properties of nanocrystals and the design of complex device geometries with enhanced light-matter coupling. In particular, I have proposed different approaches to uncouple optical and transport properties in HgX-based photodetectors, aiming to achieve state-of-the-art sensing performances. Furthermore, I have pursued a novel strategy based on *in-operando* measurements, which focus on studying the material within the context of the device itself, rather than regarding them as separate entities.

Keywords: Infrared, nanocrystals, optoelectronics, heterostructures, imagery

Sujet : Avancement de l'Imagerie Infrarouge basée sur les Nanocristaux : Exploration de Stratégies Novatrices dans la Conception et la Caractérisation

Résumé : L'infrarouge est une région spectre électromagnétique avec des longueurs d'onde plus longues que celles de la lumière visible. Cette gamme spectrale fournit des informations complémentaires au domaine visible, et trouve des applications dans divers domaines tels que la défense, l'astronomie, et les technologies civiles émergentes dont le LiDAR dans les véhicules autonomes, ou la reconnaissance faciale dans nos smartphones. Alors que la technologie de détection à base de silicium règne sur le marché du visible, son équivalent reste à développer dans l'infrarouge. Les nanocristaux colloïdaux offrent une voie prometteuse pour la réalisation de capteurs infrarouges performants et économiques. Ces objets cristallins synthétisés chimiquement présentent des effets de confinement quantique, qui permettent d'ajuster leurs propriétés optiques avec leur taille. Parmi les nanocristaux absorbant l'infrarouge, j'ai utilisé des nanocristaux de chalcogénures de mercure (HgX) qui peuvent adresser toute la gamme infrarouge du visible à la région THz. Au cours de ma thèse, j'ai exploré des concepts innovants liés à la fois aux propriétés matérielles des nanocristaux et à la conception de géométries de dispositifs complexes avec un couplage lumière-matière exalté. En particulier, j'ai proposé différentes approches pour découpler les propriétés optiques et de conduction dans les photodétecteurs à base de nanocristaux HgX, afin d'atteindre des performances de détection de pointe. De plus, j'ai entrepris une nouvelle approche en utilisant des mesures *in-operando*, axées sur l'étude du matériau dans le contexte du dispositif lui-même, plutôt que de les considérer comme des entités distinctes.

Mots clés : Infrarouge, nanocristaux, optoélectronique, hétérostructures, imagerie